Superconductivity and localization in one-dimensional InSb and InAs nanowires

Juan Carlos Estrada Saldaña

Juan Carlos Estrada Saldaña. Superconductivity and localization in one-dimensional InSb and InAs nanowires. Superconductivity [cond-mat.supr-con]. Université Grenoble Alpes, 2017. English. NNT : 2017GREAY038 . tel-01705583

HAL Id: tel-01705583
https://theses.hal.science/tel-01705583

Submitted on 9 Feb 2018

Communauté
UNIVERSITÉ Grenoble Alpes

THÈSE

Pour obtenir le grade de

DOCTEUR DE la Communauté UNIVERSITÉ GRENOBLE ALPES

Spécialité : **Physique de la Matière Condensée et du Rayonnement**

Arrêté ministériel : 7 août 2006

Présentée par

Juan Carlos ESTRADA SALDAÑA

Thèse dirigée par **Silvano DE FRANCESCHI**

préparée au sein **du Laboratoire de Transport Electronique Quantique et Supraconductivité,**
du Service de Photonique, Electronique et Ingénierie Quantiques,
de l'Institut Nanosciences et Cryogénie,
du CEA Grenoble
et de **l'Ecole Doctorale de Physique de Grenoble**

Supraconductivité et localisation dans des nanofils unidimensionnels d'InSb et d'InAs

Thèse soutenue publiquement le **9 Juin 2017**,
devant le jury composé de :

Pascal SIMON
Laboratoire de Physique des Solides / Université Paris Sud, Président
Jesper NYGARD
Niels Bohr Institute and Nano-Science Center, Rapporteur
Francesco GIAZOTTO
NEST Istituto Nanoscienze-CNR and Scuola Normale Superiore, Rapporteur
Vincent BOUCHIAT
Institut Néel / CNRS-Grenoble, Examinateur

Superconductivity and localization in one-dimensional InSb and InAs nanowires

To the ones I love.

Résumé

Dans ma thèse, j'ai étudié le transport électronique quantique dans des nanofils semiconducteurs couplés aux supraconducteurs, avec le but de comprendre les conditions nécessaires pour observer des états liés de Majorana. De manière inattendue, au cours de mes expériences j'ai trouvé des exemples notables de l'omniprésence de la localisation spatiale des électrons dans des nanofils apparemment balistiques et unidimensionnels (1D). Ses effets peuvent imiter des signatures d'unidimensionnalité, d'hélicité et des états liés de Majorana, jetant un doute sur leur interprétation.

La conductance d'un nanofil 1D est quantifiée et censée montrer des plateaux a des multiples entiers du quantum de conductance. Curieusement, le transport dans un nanofil d'InAs qui hébergeait une boite quantique à un seul niveau a montré qu'il pouvait *répliquer* les deux premiers plateaux résolus en spin. Une mesure du courant Josephson sous un champ magnétique a révélé les transitions d'état fondamental d'un électron qui occupait ce niveau et confirmé sa nature localisé.

Dans le régime hélicoïdal, une chute de la conductance est prédite au milieu de chaque plateau de conductance. De façon étonnante, des dispositifs à base de nanofils uniques d'InSb hébergeant une boite quantique qui conduisait en parallèle avec le canal 1D ont reproduit la même signature.

Enfin, la présence des états liés de Majorana, devrait être décelée par un pic à tension de biais nul (ZBP) lors d'une spectroscopie tunnel. Dans un des échantillons à deux canaux mentionnés précédemment, lorsque le canal unidimensionnel était fermé, un ZBP a émergé dans le gap supraconducteur sous un champ magnétique parallèle au nanofil. Ce ZBP a été attribué aux états liés d'Andreev de la boite quantique. Dans une expérience différente faite avec une jonction Josephson à base d'un nanofil d'InAs hébergeant une boite quantique, un ZBP relié au courant Josephson est apparu dans le gap supraconducteur comme le résultat d'une transition de l'état fondamental singlet de la boite quantique vers un état doublet.

Malgré la localisation, il a été possible d'extraire des informations significatives sur le régime 1D. Le rôle des grilles a été majeur dans la détermination des dégénérescences sous un champ magnétique des sous-bandes d'un nanofil d'InSb présentant deux canaux de conduction en parallèle. En jouant avec leurs tensions de seuil, effets orbitaux, et facteurs gyromagnétiques, la tension de grille pouvait changer les énergies des sous-bandes appartenant à chaque canal, de manière à les verrouiller ensemble. Grace à ce mécanisme, il a été possible d'observer un plateau à 2 e^2/h

jusque à de forts champs magnétiques sans aucune apparition d'un plateau à 1 e^2/h. La possible existence des deux fils quantiques dans un seul nanofil ouvre la voie à l'observation des états hélicoïdaux et des états liés de Majorana de nature fractionnel.

Dans l'ensemble, ces résultats pointent vers la nécessité d'une meilleure compréhension de la physique des dispositifs à base de nanofils d'InAs et d'InSb. Des études supplémentaires dans l'état supraconducteur et normal doivent être réalisées sur des dispositifs plus simples avec un faible nombre de grilles, avant de faire l'étude et manipulations des états liés de Majorana dans des systèmes plus complexes, dont les signatures de localisation pourraient être mieux cachées. Ces résultats originaux vont être publiés dans les mois qui suivent dans quatre articles différents.

Abstract

In my thesis, I studied low-temperature electronic transport in semiconductor nanowires coupled to superconductors, with the goal of understanding the requirements to observe Majorana bound states. Unexpectedly, I found dramatic examples of the pervasiveness of spatial *localization* of electrons even in seemingly ballistic one-dimensional (1D) nanowires. Localization could replicate signatures of one-dimensionality, helicity and Majorana bound states, casting a shadow of doubt on their interpretation.

1D nanowires are expected to show plateaus of quantized conductance. Curiously, transport through an InAs nanowire hosting a single-level quantum dot showed that it could *mimic* the first two spin-resolved plateaus. A measurement of the Josephson supercurrent under magnetic field revealed the ground-state transitions of an electron occupying this level, confirming its localized nature.

In the helical regime, a conductance dip is predicted to appear in each of the conductance plateaus. Surprisingly, InSb nanowire devices hosting a quantum dot conducting in *parallel* with a 1D channel reproduced this signature.

The presence of Majorana bound states, in turn, should be revealed by a zero-bias peak (ZBP) in tunnel spectroscopy. In one of the two-path devices mentioned above, when the 1D path was closed, a zero-bias peak emerged inside the superconducting gap under a magnetic field parallel to the nanowire. This ZBP was related to trivial Andreev bound states from the quantum dot in *parallel* to the 1D channel. In a different experiment done in an InAs nanowire Josephson junction device hosting a quantum dot, a ZBP related to a Josephson supercurrent appeared inside of the superconducting gap as a result of a transition of the ground-state of the dot from a singlet to a doublet.

In spite of localization, it was possible to extract some meaningful information about the 1D regime. The role of the gates was major in determining the degeneracy of the subbands in an InSb nanowire with two 1D conduction paths in parallel under magnetic field. Through a direct influence on their threshold voltages, orbital effects, and g-factors, the gate voltage could shift the energies of the subbands and lock them together. Via this mechanism, it was possible to observe a 2 e^2/h plateau lasting until very large field without the appearance of a 1 e^2/h plateau. The possible existence of two quantum wires in a single nanowire opens the door for novel helical and

Majorana bound states of fractional nature.

Altogether, these results point to the need of a better understanding of the physics of simpler few-gates short-channel InAs and InSb nanowire superconducting and normal-state devices, before committing to the utterly complex devices that should be fabricated to study and manipulate Majorana bound states, in which signatures of localization could be better hidden. These original results will be published in the coming months in four different articles.

Contents

Acknowledgments

A PhD thesis is a lengthy marathon, sprinkled with moments of exhilarating sprinting and unexpected falls. Many people have helped me through these ups and downs. I am grateful to all of them for making this one-in-a-lifetime experience an unforgettable and cherished one.

First of all, I want to thank my family, for always supporting me. Papi, mami, Diego, gracias por todo. To my girlfriend, for her love and patience, for her unconditional support, for the travels and the adventures, for the lunches together between experiments, and for the interesting discussions about nanowires and physics. большое спасибо, Даша. To my friends, for taking me out of the lab in the weekends, and for giving me fresh perspectives about life. Among them, I specially thank Patrick Torresani for the four years that we shared an office and its extensive help in all matters, from French language corrections to Latex tips; and Eduardo J. H. Lee, for he was, besides a mentor, a reliable and loyal friend. To all my peruvian and South American friends in Grenoble, gracias!

I thank my supervisor, Silvano De Franceschi, for the time he spent mentoring me and the valuable lessons in physics, presentation-making and scientific-writing that he gave me. Thank you for giving me the freedom and the means to develop and pursue my own ideas, and for transmitting me your high integrity and sincerity as a scientist. For teaching me that one should always look for the alternative explanation of a experiment to avoid tricking oneself, and for making it natural to change my mind upon new evidence.

Besides Silvano, I also want to thank Eduardo Lee and Florian Vigneau for providing advices and corrections for this manuscript.

I thank Eduardo Lee and Jean-Pierre Cleuziou for their teachings of microfabrication techniques in the cleanroom, as well as cryogenics and device characterization in the lab. Their collaboration was invaluable during my PhD.

Thanks to the team of growers from Eindoven and Pisa for proving me with the InSb and InAs nanowires that I used in my thesis, and for the information which they so kindly provided. From Eindhoven, thanks to Diana Car, Sébastien Plissard and Erik Bakkers. From Pisa, thanks to Daniele Ercolani and Lucia Sorba. Additionally, thanks to Valentina Zannier and Jérémy David for the transmission electron microscopy images of the InAs nanowires.

Thanks to the theoreticians which whom I collaborated. Thanks to Rok Zitko and Ramon Aguado for the NRG modeling of the 0.7 anomaly in InAs nanowires, and for explaining me the theory in such a didactic way. Thanks to Zaiping Zeng and Yann-Michel Niquet for the simulation of the spin-orbit gap in 1D InSb nanowires, and for the modeling of two quantum wires in parallel in a single InSb nanowire.

I also want to thank all the people in the lab from the team of Silvano who helped me with the little and big problems that I faced, and who made my PhD life easier. Among these are Patrick Torresani, Eduardo Lee, Jean-Pierre Cleuziou, Romain Maurand, Raisei Mizoguchi, Florian Vigneau, Julien Renard and Moira Hocevar. I had a great team of brilliant and dedicated people. To Romain, in particular, for all the times that you passed by the dilution fridge with an optimistic mindset about what I was measuring.

Thanks to the people in the Pheliqs lab, in special Xavier Jehl, for his training in the bonding machine; Francois Lefloch and Max Hofheinz, for the discussions about Josephson junctions and for the fabrication tips; Marc Sanquer and Jean-Pascal Brison, for their kindness; Patricia, for helping me with the buffet; Iulian Matei and Jean-Michel Martinod, for their help in debugging the problems with the cryogenic equipment; and finally Michel, for crafting mechanical pieces for my experiments.

Thanks to Jean-Luc Thomassin for his advice and training in electron-beam lithography, and to Frederic Gustavo, for his advice and training in metal evaporation. Thank you both for your kindness and attention. Thanks to the rest of the technical staff in the PTA cleanroom, for providing me with their help and training when needed. Thanks to Laurent Cagnon and to Corinne Perret, for their training and help with the atomic layer deposition of hafnium oxide.

Finally, I want to express my sincere gratitude to the members of the Jury for reading my manuscript, for traveling to Grenoble to attend my defense, for their timely questions, and for their words of encouragement.

Chapter 1

Introduction

1.1 Context

Hybrid devices made of a semiconductor nanowire coupled to a superconductor have received a tremendous boost of popularity in the last five years, thanks to experiments announcing the observation of Majorana bound states [1][2]. These devices may be used one day as the physical platforms for topological quantum computation [3].

Majorana bound states (MBS) are quasiparticles predicted to emerge in nanowires with helical states coupled to an s-wave superconductor [4]. These quasiparticles receive their name from their elementary-particle counterparts, predicted by Ettore Majorana in 1937 as an elegant solution of the Dirac equation [5]. They are supposed to be massless, spinless and chargeless. Moreover, they are their *own* antiparticle. Because of these interesting and unusual properties, they are actively searched in particle accelerators [6]. So far, this search has not been successful.

MBS, on the other hand, are not exactly fermions [7]. They were first predicted by Kitaev in a model of a one-dimensional (1D) chain of spinless electrons with inter-site hopping and superconducting pairing [8].

In this model, MBS can be obtained by "cutting" an electron -or a hole- in half, which merely means writing the creation operator of one fermion in terms of two Majorana operators. Because of this, Majorana quasiparticles always come in pairs, an in the chain model two Majorana quasiparticles produce one electron per site. Kitaev demonstrated that there existed a *topological phase* in which two unpaired Majorana states could exist at the sites in the two edges of the chain, at zero energy. These are the interesting states, since they belong to the same fermion but are non-local -i.e., they are spatially separated by the length of the whole chain.

It was realized later that the Kitaev chain Hamiltonian could be entirely mapped to the Hamiltonian of a nanowire with spin-orbit coupling, Zeeman energy, a 1D dispersion, and an adjustable chemical potential, coupled to a conventional superconductor with singlet pairing [4]. Since all the physical requirements listed above can be obtained in principle with materials that were believed to be well-understood, this proposal gained a considerable interest. In this proposal, once the nanowire is in an effectively spinless helical state, it enters the topological phase. In this phase, two unpaired zero-energy Majorana states are bound to the boundaries between the trivial and the topological phases in the nanowire.

These states can be probed by tunnel spectroscopy [9], which is extremely sensitive to nearby states -by a factor exponentially decaying with the distance from the tunnel probe. A device for doing this can consist on an InSb or an InAs nanowire attached to a superconductor (S) and a tunnel probe [1]. The tunnel probe can be, for example, a normal (N) metal in contact with one end of the nanowire (NW), and the tunnel barrier can be obtained by electrostatic gating. This device can be thought of as a voltage-biased S-NW-N junction.

Once tuned to the helical regime, a voltage-biased spectroscopy of one of the topological nanowire edges is done. At zero magnetic field, a low-bias V - dI/dV curve would show the density of states (DOS) of the *induced* superconducting gap in the nanowire. Under an increasing magnetic field parallel to the nanowire, the gap should first close with a slope given by the g-factor of the nanowire and then *re-open*. This re-opening of the gap comes with a zero-bias peak of 2 e^2/h conductance, associated with tunneling through a zero-energy Majorana state in the end of the topological nanowire that is being probed.

1.2 Challenges of the experiment to observe Majorana bound states

There is nothing trivial with an experiment designed to search for MBS. From a materials point of view, the requirements are stringent. For obtaining helical states, the nanowire needs to be ballistic and one-dimensional over $\sim 1\ \mu$m, and have a strong spin-orbit coupling. In addition, in order to enter the topological Majorana regime, the nanowire has to be coupled to a superconductor with a large enough critical field, and to have a large g-factor to avoid losing superconductivity before entering the topological regime. If a clear signature of MBS is wanted, the proximity effect needs to result in a hard induced gap -i.e., a gap virtually free of quasiparticle states.

An additional challenge is placing the chemical potential of the $\sim 1\ \mu$m-long section of the nanowire under the superconductor in the topological regime. This is further complicated by the presence of defects (essentially charge traps), which will tend to localize electrons [10]. This type of disorder could be compensated by the use of many gates.

The zero-bias peak signature of MBS can in turn be replicated by other mechanisms, among which localization in the form naturally-occurring quantum dots is perhaps the most damming. For instance, zero-bias peaks unrelated to MBS have been found in a dot with a soft gap [11], and in a dot displaying Andreev bound states that crossed zero-energy at a quantum phase transition [12].

1.3 This thesis

One question that remains is if *other* signatures related to one-dimensional transport, helical states and Majorana bound states can be *replicated* by quantum dots, and thus raise the possibility that they may be unrelated to these three more exotic regimes. The ever-increasing complexity of the devices used in Majorana experiments in nanowires is certainly not going to aid in making that distinction. My trust is that, by gaining a more robust understanding of the background physics of simpler devices, the experiments aiming for the observation of Majorana bound states will be benefited.

The driving idea of my thesis has been to investigate the effects of a strong magnetic field on the transport characteristic of a one-dimensional nanowire attached to superconducting contacts, with the goal of understanding some basic properties underlying the search for MBS in a nanowire strongly coupled to a superconductor. With the limited amount of time that I had, I restricted beforehand my attention to two main questions. First, to understand the 1D transport properties of InAs and InSb nanowires, including the helical regime. Second, to study the Josephson effect through a 1D nanowire under an external magnetic field.

To this aim, I fabricated two-terminal S-NW-S devices of channel length below the mean free path of electrons (200 - 450 nm), on which I performed low-temperature transport measurements. Artistic views of some of these devices are given in Figure 1.1. These devices revealed that spatial localization of electrons is *ubiquitous* in both InAs and InSb nanowires. Localization occurs even in devices showing clear signs of conductance quantization that hint to the ballistic 1D nature of the nanowires. Localization affects both the normal and the superconducting state transport through these nanowires, leading to novel and interesting effects.

Localization can appear at low charge density, in which case it will distort a tunnel spectroscopy performed on these nanowires, which is essential for probing MBS in the most recurrent experiment realized in the past. It can also show as a quantum dot conducting in parallel to a 1D path, producing false-positives for helical states and even MBS.

I also found that electrostatic gates could play roles not previously known. In an InSb nanowire, the gates can tune the degeneracy of the subbands of two quantum wires coexisting in the same nanowire. In an InAs nanowire hosting a quantum dot, a gate affecting its energy levels and their coupling to the leads can produce a behavior resembling conductance quantization. In both types of nanowires, the need to use gates may lead to unwanted camel-shaped band profiles that localize electrons.

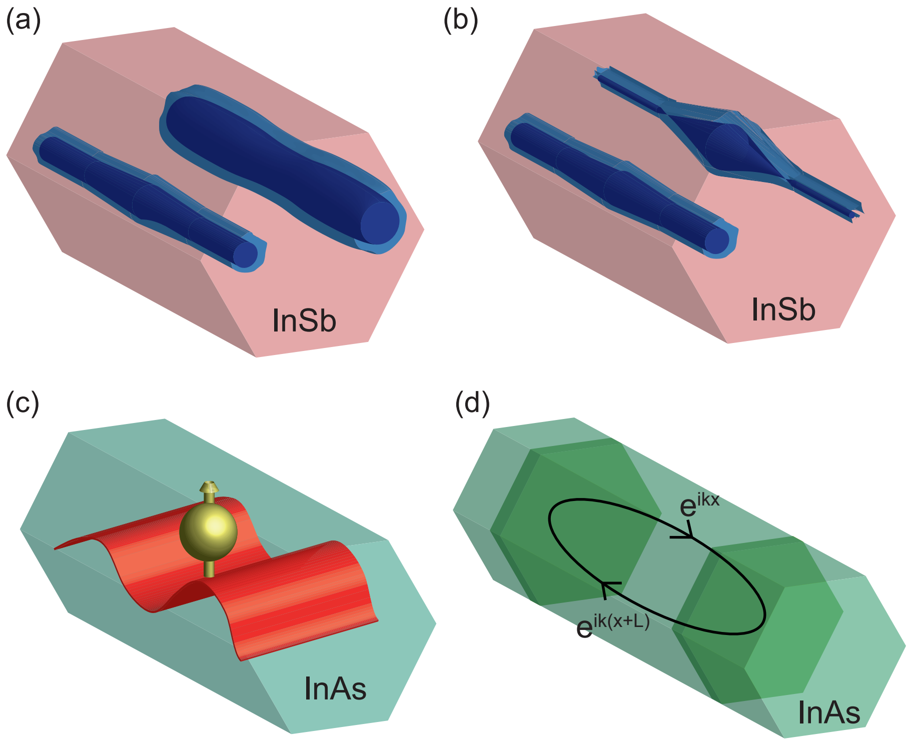

Figure 1.1: Artistic view of the channel of some of the nanowire devices measured in this thesis. **(a)** Two parallel 1D paths of transport in a single InSb nanowire. The electron gases are shown in blue. Normal-state measurements done in this device are shown in Chapter 3. **(b)** A 1D path in parallel with a quantum dot path in a single InSb nanowire. Normal-state measurements of this device are discussed in Chapter 3. A zero-bias anomaly emerging with magnetic field in the superconducting-state of this device is shown in Chapter 4. **(c)** Localization of an electron at the onset of 1D conduction by a camel-shaped band edge (shown in red) in an InAs nanowire (depicted in green). Normal and superconducting-state measurements of this device are shown in Chapter 5. **(d)** InAs nanowire quantum point contact with Fabry-Pérot resonances induced by stacking faults in the channel. Normal and superconducting-state measurements of this device are shown in Chapter 4.

These properties could reflect on the superconducting transport. In the case of the InAs nanowire just mentioned, localization affects the magnetic field behavior of the Josephson current. This is similar to the case of Zeeman-split Andreev bound states discussed before, but happens in a more transparent and symmetric regime.

This thesis is organized as follows. In Chapter 2 I present some of the theory that I will use in the next chapters. This is done from the point of view of an experimentalist, with a strong focus in the intuitive rather than the abstract and rigorous side of it.

In Chapter 3, I discuss transport through 0D and 1D objects in parallel in InSb nanowires which displayed conductance quantization. First, I describe the experimental situation of a quantum wire conducting in parallel with a quantum dot, within the same nanowire. Then, I discuss the more interesting case of two quantum wires conducting in parallel in the same nanowire, given its implications for the observation of fractional helical and MBS [13]. Both systems may produce conductance signatures that resemble the expected trademark of helical states.

Next, in Chapter 4, I do a comparison of the superconducting transport, particularly the gap spectroscopy and the Josephson current, across many devices. These comprise InAs and InSb nanowires hosting quantum point contacts or quantum dots, coupled to a few superconductor materials, including aluminum, vanadium, tantalum and niobium/tantalum bilayers. When possible, I provide numbers for the hardness of the superconducting gap and the I_cR_n product. A hard gap and a large I_cR_n are important figures of merit when choosing the best possible system to host MBS.

I also show that it is possible to obtain a quantized supercurrent correlated to quantized conductance in an InSb nanowire device, and how this is not the case when the conductance of the plateaus is altered by Fabry-Pérot resonances in an InAs nanowire. I also do superconducting-state measurements in the InSb nanowire device that hosted a quantum dot in parallel to a quantum wire, and show how a zero-bias peak from Andreev bound states in the dot emerges with magnetic field inside of the superconducting gap. This feature, surprisingly reminiscent of the trademark of MBS, alerts us of the fact that dots hiding in seemingly ballistic systems may trick us into believing the wrong interpretation.

In Chapter 5, I present measurements of an InAs-nanowire Josephson-juntion with high critical field superconducting tantalum (Ta) contacts. In the normal state, the observation of plateaus of quantized conductance could trick one to believe that a ballistic 1D channel was involved. However, upon closer inspection evidence of localization was discovered. In the superconducting regime, an unprecedented behavior of the supercurrent under magnetic field was explored, when the localized state was spin-resolved. Supercurrent re-emergence provoked by the Zeeman energy revealed a quantum phase transition (QPT) of the ground-state of the dot.

In Chapter 6 I present the follow-up of these last findings. In a different InAs nanowire device, equipped with two gates and having a better-defined, high-impedance quantum dot, I manage to reproduce the QPT revealed by the supercurrent under magnetic field observed in the more transparent system of Chapter 5. I take the experiment of Chapter 5 one step further, by controlling the field at which the QPT occurs via a gate voltage. I show that for a tunnel coupling low enough, the supercurrent can be zero at zero field, and emerge as a zero-bias peak when the field is increased. This mechanism can therefore reproduce the signature of MBS in an S-NW-S junction.

The main message that I want to convey in my thesis is that there is still a lot of preliminary work to do in understanding the 1D regime in a simple two-terminal nanowire device before attempting to understand the topological one. Even though both paths of research can and should develop in parallel, as it is indeed the case, progress could be made quicker if the basic processes are first fully grasped.

Chapter 2

Basic concepts

In this chapter I will present the main concepts that I will use to interpret the experimental data that I have acquired during my PhD.

2.1 Quantum point contacts

A quantum point contact (QPC) is a small 1D constriction between two large electron [1] reservoirs. Transverse confinement of electrons results in the presence of N subbands. There is no confinement in the direction of transport, and therefore in this direction electrons will behave like planar waves.

As the constriction is opened, the number of subbands through which transport can occur will progressively increase. At zero magnetic field, every spin-degenerate subband will contribute by a quantum of conductance G_0=2 e^2/h to the total conductance of the system -where the factor 2 accounts for a two-fold spin-degeneracy. The transport signature of a QPC is therefore a set of conductance plateaus in multiples of 2 e^2/h. If there is elastic scattering in the constriction, the conductance will be given by equation 2.1, where T is transmission of an electron through the constriction [15].

$$G = G_0 N T \tag{2.1}$$

QPCs have been observed in both metallic and semiconductor systems. In metals, in order to obtain a few open channels, the size of the constriction must be in the atomic scale. This has been achieved by scanning tunnel microscopy [16] and mechanically-controllable break junctions [17]. In semiconductors, on the other hand, the few-channel regime can be obtained with a constriction in the tenths of nanometers range, which is a size accessible by current nanolithography techniques. Moreover, the number of open channels can be tuned by a gate, which is not possible in the case

---

[1] Hole QPCs have been demonstrated as well [14].

of metals. QPCs in semiconductors were first demonstrated in GaAs/AlGaAs two-dimensional gases (2DEGs) [18], and more recently, in semiconductor nanowires [19][20][21].

Figure 2.1**a** (left) shows a qualitative subband dispersion -assumed to be parabolic- in a QPC without spin-orbit interaction, and the expected zero-temperature conductance trace (right) as a function of the chemical potential μ, which can be tuned by a gate. Two subbands (tagged 1 and 2) give raise to two plateaus. The size of the first plateau provides the energy spacing ΔE between the first and the second subbands. In nanowires, however, some subbands may be degenerate at zero-field. In those cases, the number of degenerate subbands will be reflected in the conductance characteristic [19].

Zeeman and orbital effects

Under an external magnetic field, the spin-degeneracy of the subbands will be lifted by the Zeeman effect. Every spin-resolved subband will contribute by $G_0/2$ to the conductance, producing half-integer plateaus. Figure 3.20**b** (left) shows a cartoon of how a finite magnetic field affects the subband dispersion of Figure 3.20**a** (left). The subbands split symmetrically with respect to the zero-field case by the Zeeman energy $E_z = |g|\mu_B B$, where μ is the Bohr magneton and g is the g-factor of the electrons in the confined crystal. The expected zero-temperature conductance trace is also indicated in 2.1**b** (right). Four half-plateaus at 1 e^2/h are drawn, together with the Zeeman energies of the subbands 1 and 2 for a general case where $|g_1|$ is different from $|g_2|$. In InSb and InAs nanowires, given their large g-factor, the Zeeman effect is strong at moderate magnetic fields.

A magnetic field oriented perpendicular to the axis of the nanowire will also have an orbital effect -Landau diamagnetism- in the subbands. The orbital effect is a result of the electrons engaging in cyclotron motion, which will result in skipping motion at the walls of the nanowire. This effect will shift the subbands towards larger energy by different amounts. Figure 2.1**c** shows the effect of the Zeeman energy and the orbital effect on the subbands (left) and on the conductance (right). In general, subbands will cross at high magnetic field and become degenerate because of both effects. If the field is large enough, the orbital effect will flatten the subbands in the bulk of the nanowire (low k), and edge states will emerge in the walls (high k) [22][23]. This is not shown in Figure 2.1**c**.

A magnetic field may also reduce the backscattering, increasing the transparency of the subbands in a nanowire [20].

The 0.7 anomaly

QPCs obtained in two-dimensional gases by the split-gate technique show a recurrent conductance feature. This feature consists in the reduction of the conductance at the onset of the 2 e^2/h plateau, down to a value of $\sim 0.7\times 2\ e^2/h$. Because of that, this feature is usually known as the *the 0.7*

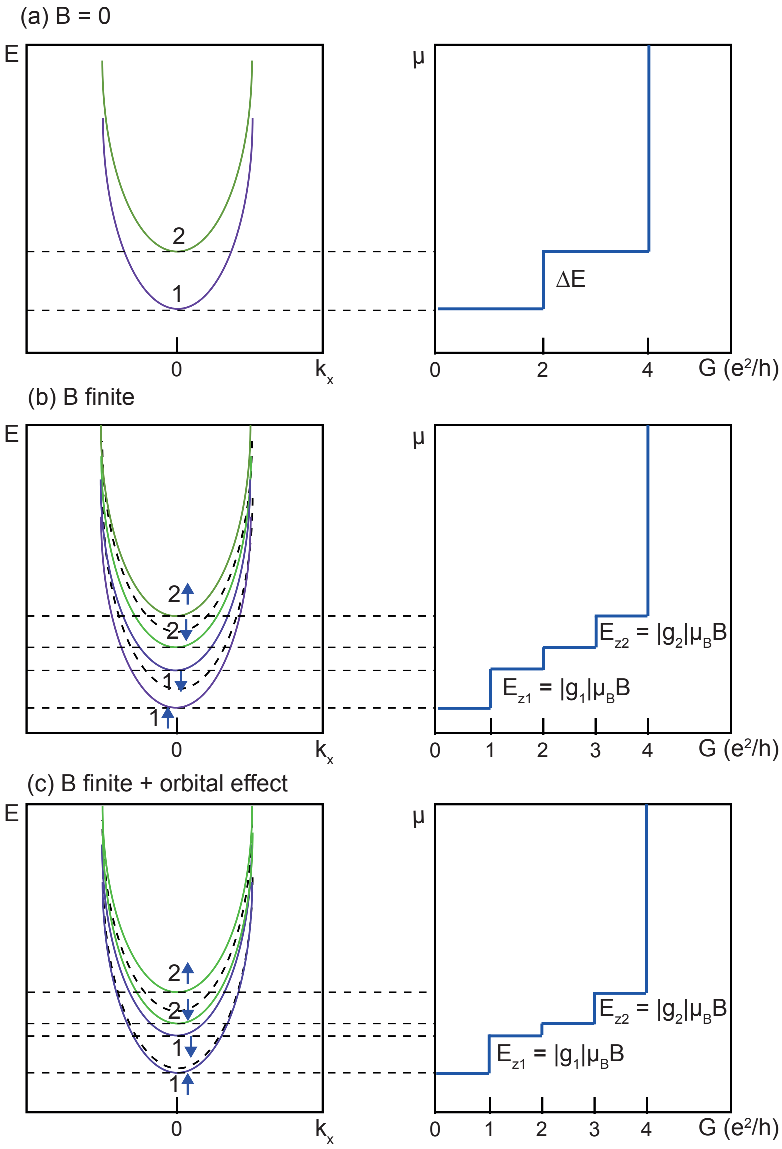

Figure 2.1: Subband dispersion of a quantum point contact without spin-orbit interaction (left panels) and corresponding conductance characteristic (right panels), for **(a)** zero magnetic field, **(b)** finite field producing a Zeeman splitting and **(c)** finite field oriented perpendicular to the axis of the nanowire, producing a Zeeman splitting and an orbital effect.

anomaly. Its origin is somewhat controversial, but it is agreed that it cannot come from simple single-particle physics [24]. One of the leading explanations resides in the Kondo effect arising from spatial localization of electrons [25][26][27][28][29].

The 0.7 anomaly has specific signatures as the magnetic field, temperature and bias voltage are varied [24]. Upon applying an external magnetic field, the 0.7×2 e^2/h conductance feature evolves towards 1 e^2/h. Lowering the temperature leads in turn to an increase of the conductance in the 0.7

structure. Additionally, a voltage-biased conductance trace in the 0.7 anomaly "shoulder" shows an intriguing zero-bias peak. The phenomenology is certainly not limited to these characteristics; however, these are the ones universally attached to the feature.

Until now, the 0.7 anomaly has not been reported in semiconductor nanowires. However, the same many-body physics that gives raise to the 0.7 anomaly in 2DEG QPCs could in principle operate in nanowire QPCs. Moreover, additional localization possibilities occur in the latter systems, as will be shown later.

2.2 Helical states

The zero-field subband dispersion of a nanowire QPC changes if the nanowire has a finite Rashba spin-orbit coupling [30][31][32]. Figure 2.2**a** (left) shows a sketch of the nanowire laying on a substrate. The asymmetry in the out-of-plane direction in this device can lead to the Rashba interaction, and can be aided by the effect of an out-of-plane electric field applied by a gate. Electrons moving in the crystal across this electric field will feel an effective Rashba magnetic field B_{SO}. The dispersion modified by the spin-orbit interaction is shown qualitatively in Figure 2.2**a** (center). The subbands shift in k-vector, but they stay degenerate in energy. Therefore, the change (right) is not reflected in the conductance characteristic, which stays unmodified with respect to the case without spin-orbit coupling. The crossing of the k-shifted subbands sets the energy E_{SO} of the spin-orbit interaction.

If a magnetic field is applied in a direction parallel to B_{SO}, the subbands will Zeeman-split 2.2**b** (center). In this case, the conductance (right) will not change from the case without spin-orbit interaction.

However, if the field is applied in a direction parallel to the axis of the nanowire -i.e., perpendicular to B_{SO}-, the shifted bands of Figure 2.2**a** (center) will anticross at zero k-vector as a result of spin mixing. This will open a pseudogap whose magnitude is given by the Zeeman energy and whose visibility upon raising the magnetic field depends on the strength of the Rashba interaction. Known as spin-orbit gap or helical gap -and identified here as Δ_{SO}-, this pseudogap is preceded by a hill-shaped dispersion of height $\sim E_{SO}$ at $k = 0$. At a large Zeeman energy, the hill feature vanishes monotonically as there is no more spin mixing. The case portrayed in Figure 2.2**c** (center) is that of $E_z = E_{SO}$, in which both Δ_{SO} and E_{SO} are equally and thus optimally visible.

The subband sections in the energy range corresponding to the spin-orbit gap are called *helical states*. They are effectively spinless, as right movers have one spin-projection and left-movers have another. Their spin projections are sketched in Figure 2.2**c** (center) by blue arrows. The corresponding conductance characteristic, sketched in Figure 2.2**c** (right), will show a dip when the chemical potential is placed at the spin-orbit gap.

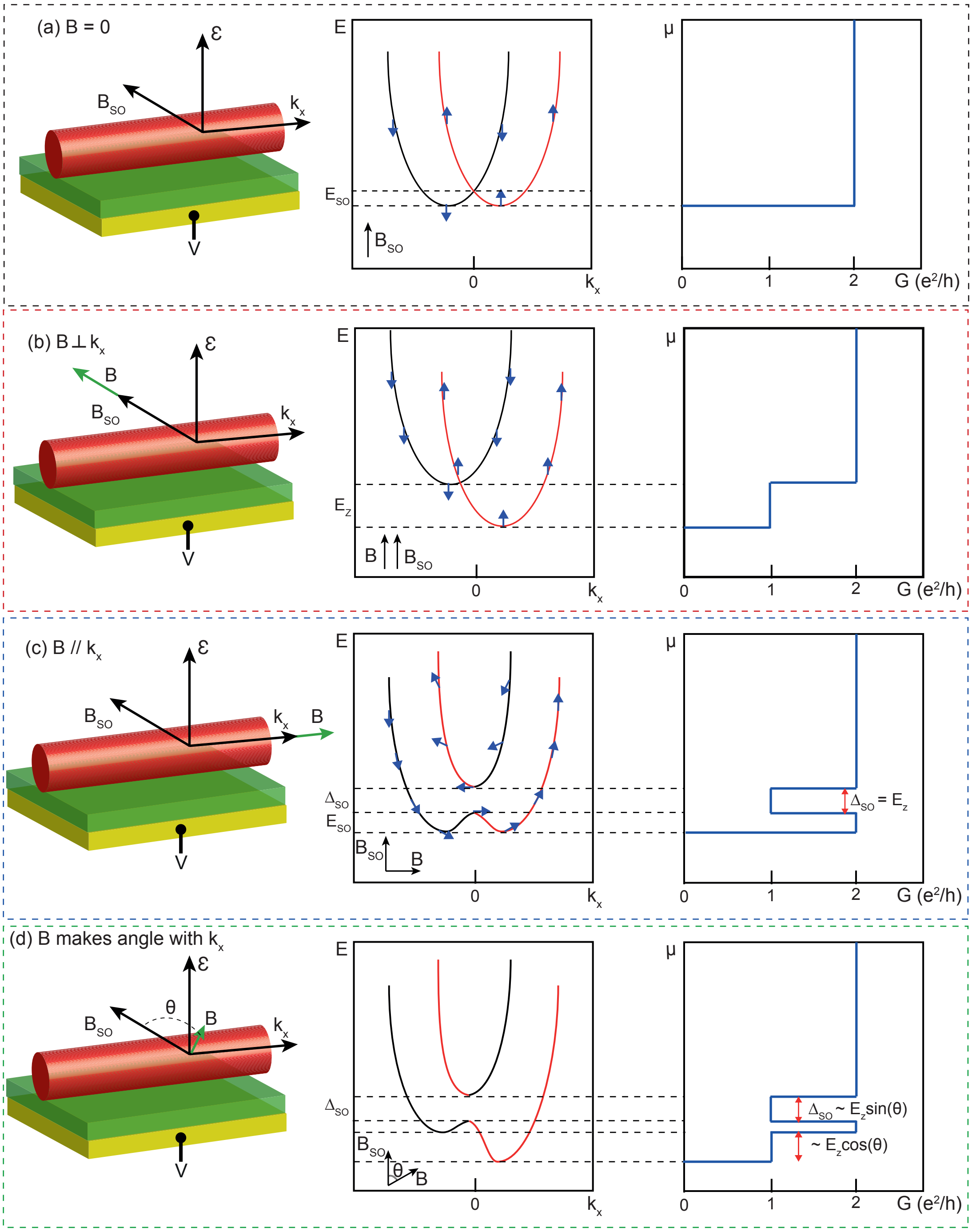

Figure 2.2: Sketch of a nanowire QPC with wavector k_x, electric field ε, spin-orbit effective field B_{SO} and external magnetic field B indicated (left); corresponding subband dispersion (center) and corresponding conductance characteristic (right), for **(a)** zero magnetic field; **(b)** field oriented parallel to B_{SO}; **(c)** field oriented perpendicular to B_{SO}; and **(d)** field oriented in the plane of k_x and B_{SO}, and at an angle θ with respect to B_{SO}. The blue arrows indicate the spin-projection given by B and B_{SO}

If the magnetic field orientation is still in the plane of the substrate but at an angle θ with respect to B_{SO}, then the component of the field that is perpendicular to B_{SO} will produce a mixing and give raise to a helical gap as in Figure 2.2**c** (center), while the component that is parallel to B_{SO} will split the two bands -without mixing- as in Figure 2.2**b** (center). This intermediate situation is portrayed in Figure 2.2**d**. This time, the conductance characteristic will not only show a dip at the spin-orbit gap, but also a plateau at 1 e^2/h of width $\sim E_z cos(\theta)$, when the chemical potential is placed at the bottom of the spin-polarized subband [33][34].

2.3 Quantum dots

Quantum dots are zero-dimensional boxes of electrons. In analogy to an atom, they exhibit discrete levels separated by an energy ΔE -as opposed to subbands. The low effective mass in III-V semiconductor materials allows to achieve a sizable ΔE of a few meV for confinement sizes in the tenths of nanometers range, which is accessible at low temperature.

In virtue of its small size, which provides it with a small capacitance, a quantum dot connected to electron reservoirs experiences a phenomenon called Coulomb blockade. When an electron occupies a state of the dot, an incoming electron is blocked from entering unless a bias-voltage V ~ U or a gate voltage V ~ U+ΔE are applied, where U = e^2/C is the charging energy of the occupying electron. The blocking of the passage of more electrons means that the current is zero at V < U. Coulomb blockade offers the possibility of having a single electron state with complete certainty.

For odd occupation number, the ground-state of the dot in the simplest case is a spin doublet. For even, its ground-state is instead a singlet. Shell-filling of a dot by a gate voltage gives rise to peaks of conductance -known as Coulomb peaks-, whenever the necessary U -or ΔE+U, for singlets- for adding an extra electron is reached. If a map of the conductance as a function of the bias and gate voltage is made, a diamond-shaped pattern is obtained, known as Coulomb diamonds [35][36].

If the quantum dot has a finite coupling Γ to the leads, which means that part of its wavefunction is delocalized, then electrons can tunnel through the dot by virtual processes, even in the blockaded state. Known collectively as cotunneling processes, these virtual processes can occur elastically or inelastically [37]. The difference between these two processes is that the latter requires an energy excitation of the quantum dot.

When Γ ~ U, a single electron spin sitting in a state can be screened by an antiferromagnetic coupling -mediated by cotunneling- to the electrons in the leads. This phenomenon is known as the Kondo effect. The ground-state of the dot, which would be a doublet without these correlations, changes to a many-body singlet [38]. The Kondo effect enhances the zero-bias conductance in the otherwise blocked regime of a Coulomb diamond, in which the state of the dot is occupied on average by one electron. The enhancement occurs on a scale set by T_K, the Kondo temperature. At T $\ll T_K$, and for symmetric tunnel-coupling to the leads, the Kondo-enhanced conductance in the diamond can reach the unitary conductance -i.e., 2 e^2/h [39].

When $\Gamma \gg$ U, the charge blockade is no longer effective. For symmetric tunnel couplings to the leads, Coulomb peaks merge in pairs forming Breit-Wigner resonances with a peak conductance of 2 e^2/h [35].

The ubiquity of quantum dots in InAs and InSb nanowire devices is well-known. In these nanowires, quantum dots can appear naturally [40] or be purposely engineered [41]. In both cases, the walls of the nanowire localize the motion of electrons in two of three spatial dimensions. In *naturally formed* quantum dots, the third and last degree of translational freedom, along the nanowire axis, can be confined by defects in the nanowire, poor contacts to the leads, and surface potentials [42][43].

In *engineered* quantum dots, confinement in the axial direction is imposed by artificially created tunnel barriers. Such barriers can be formed by band engineering through axial semiconductor heterostructuring or doping [44][45]. Alternatively, they can be induced by electrostatic gating. Many-gates devices allow the possibility to address individually the properties of a quantum dot, including its tunnel coupling to each of the leads, its level position, and even the number of dots in series in an individual nanowire [41]. This increased level of sophistication has eventually led to the realization of spin-orbit qubits in these systems [46][47].

It is interesting to point out that nanowires are not the only 1D-like objects in which quantum dots can spontaneously arise. Carbon nanotubes, which are few-nanometers-thick rolls of one-atom-thick layers of carbon atoms, and which can stretch to several tenths of micrometer in length, can also host these types of zero-dimensional systems in-spite of their quasi-1D structure [48].

2.4 Advantages of InAs and InSb nanowires for low-dimensional transport

Nanowires are elongated crystalline objects with diameters typically between a few tenths and a few hundredths of nanometer and lengths of several microns. They can be fabricated out of many materials, including semiconductors [49], metals [50], superconductors [51], and ferromagnets [52]. To obtain the highest degree of control of the crystal structure, they are usually grown by a bottom-up technique -often based on the vapor-liquid-solid mechanism [53]-, though they can also be etched down from a bulk material [54] or carved within a template [55]. Nanowire growth is a very active field of research.

This versatility of material choice, coupled with the crystal perfection that can be achieved, turns nanowires into interesting platforms for performing experiments of quantum electron transport through low-dimensional systems [56].

A compelling material selection with this aim in mind is a semiconductor of very low doping and of small band-gap. A small semiconductor band-gap is important to obtain an ohmic contact between a metal and the nanowire, if one wants to use carriers from the conduction band -though not the *only* factor [57]. Besides, a small band-gap semiconductor has a low effective mass [58]. For a given nanowire diameter, this leads to a large subband spacing if the nanowire is one-dimensional, or a large energy-level spacing if it behaves as a quantum dot. If the semiconductor also has low doping, it is possible to obtain low charge densities [59]. Additionally, a semiconductor material has the advantage that its charge density can be tuned through gating by capacitive coupling [60].

Some compound semiconductors made of elements from the columns III and V of the periodic table, such as InAs and InSb, fulfill the small band-gap requirement [58]. Nanowires made of these two semiconductors in particular have been intensively researched in transport, due to their large g-factor and their strong spin-orbit interaction.

In the bulk, the g-factor (g) of InAs is -15, whereas that of InSb is -51.3 [61]. In nanowires, larger values have been achieved in some works. In InAs nanowires, $|g|$ was shown to be as large as 18 [62], whilst in InSb nanowires it attained the mind-blowing value of 70 [63]. The free electron value, in comparison, is slightly larger than 2 [64]. A large g-factor is useful for some spin experiments, because the Zeeman energy $E_z = |g|\mu_B B$ (for a spin S = 1/2 state) will be significant at a small magnetic field B.

A strong spin-orbit coupling, on the other hand, can contribute in the mixing of electron states and be useful to couple electric fields to electron spins [65]. Even though InAs and InSb nanowires are commonly named as "strong spin-orbit coupling nanowires", the reality is that the size of the spin orbit interaction varies a lot depending on the way it is estimated.

Theoretical calculations in InAs and InSb nanowires with one-dimensional dispersion estimate the helical spin-orbit gap in the tenths of μeV [2]. Recent works claiming the experimental observation of the helical spin-orbit gap, on the other hand, place it at around 6.5 meV for InSb nanowires [33] and 2.5 meV for InAs nanowires [66]. Weak anti-localization measurements have yielded more modest values of 0.25 - 1 meV for InSb nanowires [67] and 0.1 meV for InAs nanowires [66]. Direct spectroscopy of singlet-triplet anti-crossings in quantum dots has determined a spin-orbit splitting of around 0.25 meV [68] in InAs nanowires and a similar value in InSb nanowires [65]. Small differences between these values are expected, since the details of the electric field contributing to the Rashba spin-orbit coupling will depend on the device itself. Moreover, nanowires with small confinement in the axial direction -as in the case of 1D nanowires- are expected to have a mixture

---

[2] Self consistent tight-binding atomistic calculations by Zaiping Zeng, from INAC/CEA Grenoble, done for a 20 nm InAs nanowire, estimate it to be under 0.1 meV. Non-self consistent tight-binding atomistic calculations done for a 100 nm InSb nanowire also estimate it below 0.1 meV.

of Rashba and Dresselhaus spin-orbit coupling [3] [69]. If the spin-orbit gap is too small, it may only be observable at low field; i.e., before the spin-polarizing Zeeman field dominates.

2.5 Mechanisms leading to zero and one-dimensional transport in nanowires

1D transport in nanowires has just been recently obtained thanks to the crystal quality achieved and the improvements in contact-making. Even then, QPCs in 2DEGs have the upper-hand in the quality and number of the conductance plateaus observed. While the best-ever reported case of conductance quantization has shown two plateaus at zero field in InSb nanowires [19], clean 2DEGs in GaAs/AlGaAs heterostructures routinely display more than ten plateaus [18]. The main reason is the large mean free path of 2DEGs, which stems from the fact that they are buried, an thus protected from surface charges and oxidation. The mean free path of InSb and InAs nanowires is of the order of 300 nm, which is much smaller than that of high-quality 2DEGs.

In a non-ideal world, quantum dots and quantum point contacts can coexist in the same nanowire. In understanding the mechanisms that can lead to zero and one-dimensional transport in nanowires, it is possible to learn what to consider in designing a device that favors one instead of the other.

Figure 2.3 shows simplified schemes of a two-terminal nanowire junction illustrating four mechanisms that favor the observation of conductance quantization at low temperature. The nanowire is drawn in black and the leads in green. The first case, depicted in Figure 2.3**a**, is the ideal one. The nanowire acts as an electron waveguide of transparency T = 1. All the drop in conductance happens at the contacts, which are drawn in blue, corresponding to a case where the nanowire was etched from the top to remove its native oxide before depositing metal. If the contacts have a limited transparency, a Fabry-Pérot cavity is obtained and the conductance will show oscillations on top of the plateaus.

The second case, displayed in Figure 2.3**b**, depicts the situation when there is a scatterer in the nanowire. In one-dimension, the scatterer only produces backscattering, and the transmission is reduced from 1.

We go back now to the ideal case, but in a situation where a gate voltage is applied and its the *only* source of electric potential. This potential might be used, for instance, to change the chemical potential of the nanowire and observe conductance plateaus. Figure 2.3**c** shows this case.

---

[3] InAs and InSb nanowires used in transport have a wurzite and a zinc-blende crystalline structure, respectively. In these crystals, a Dresselhaus-type of spin-orbit coupling is expected. However, InSb nanowires grown in the [111] direction should lack the necessary inversion asymmetry needed for a Dresselhaus-type of spin-orbit coupling, and thus only the Rashba-type should remain [33].

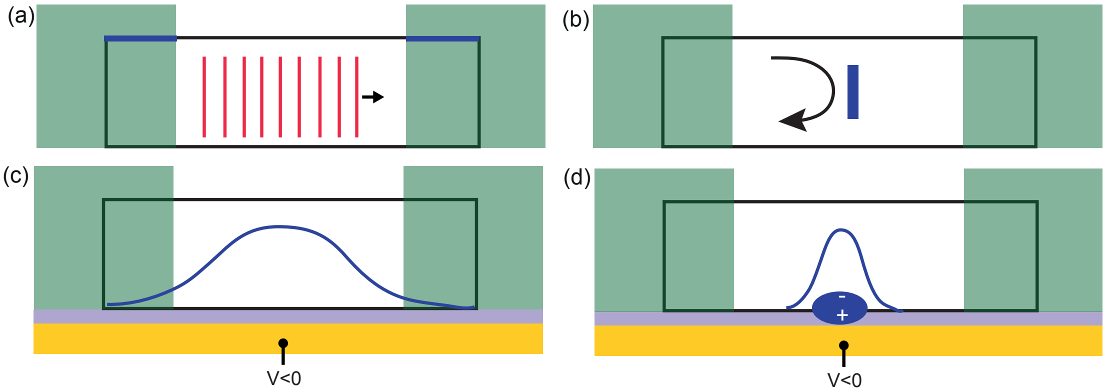

Figure 2.3: Scheme of a two-terminal nanowire junction illustrating mechanisms that favor conductance quantization at low temperature. **(a)** Electron plane waves -depicted by red lines- through a defect-free nanowire with high transparency contacts. **(b)** A defect in the nanowire increases backscattering and can alter the quantization of the plateaus by reducing the transmission T. **(c)** A large local gate produces an electric constriction in the middle of the nanowire (i.e. a quantum point contact), but it does not alter the potential below the contacts due to screening. The spatial profile of the bottom of the lowest subband is sketched by a blue curve. **(d)** Dipolar molecules -like water- sharpen the potential, resulting in a sharper spatial profile.

The nanowire sections below the contacts are assumed populated with many subbands acting as reservoirs. Moreover, the subband profile changes adiabatically over the length of the nanowire, which should improve the visibility of the conductance plateaus [28][32].

A sharper potential could have been obtained if the screening by the contacts was more effective, or if there were water molecules on the substrate before the nanowire was deposited, as illustrated in Figure 2.3**d**. A sharp potential deteriorates the visibility of the plateaus [32][70][28]. In general, any charge in the surface of the nanowire or trapped in the dielectric will alter the electric potential seen by the nanowire and thus alter the subband profile in unpredictable ways.

The mechanisms that lead to electron localization -i.e., quantum dots- are more numerous. It is possible to classify them in two types: spontaneous localization and localization due to gate-induced tunnel barriers. Figure 2.4 shows simplified schemes of a two-terminal nanowire junction illustrating a few of these mechanisms. The left panels are examples of spontaneous localization, while the right ones are examples of gate-induced localization. Figure 2.4**a** shows that, if tunnel barriers exist at the nanowire / metal interfaces (drawn in blue), a quantum dot will form in the whole channel (red-dashed circle) [71].

As it is illustrated in the scheme of Figure 2.4**b**, localization can also occur by defects (drawn in blue) within the nanowire [72] -stacking faults, for instance [43]. Figure 2.4**c** shows a last example, in which a charge $-|Q|$ lays on top of -or within- the native oxide [73][74][75] of the nanowire and depletes the channel locally [42][10]. This may result in a quantum dot formed below the charge (red-dashed circle).

The lesson learned from these schemes is that, if one does not have a pristine nanowire with clean contact interfaces, plus a clean substrate and an environment free of charges, then localization will happen spontaneously and in an unpredictable way.

Gates have been routinely used to form quantum dots in nanowires in the past [41][46][47]. They also need to be used to form and tune a QPC in the nanowire [19][20][21]. An example of a gate-induced quantum dot is shown in Figure 2.4**d**. The electric potential from the gates spatially modifies the profile of the bottom of the lowest subband -which is drawn in blue. A camel-shape conduction band such as the one shown in this scheme can lead to the formation of a quantum dot (red-dashed circle). Anther example of gate-induced localization is shown in Figure 2.4**e**. As explained before, the screening of the potential of the gates does not allow to alter the subband profile below the metallic leads. An unknown number of subbands may reside there. If these sections are naturally depleted, then applying a positive voltage will lead to the confinement of a quantum dot in the channel of the nanowire. Depending on the doping concentration and profile of the nanowire, many other cases may exist. This fact coupled with the various degrees of crystal perfection, contact perfection and the number of nearby charges that may exist, result in significant mesoscopic variations from device to device.

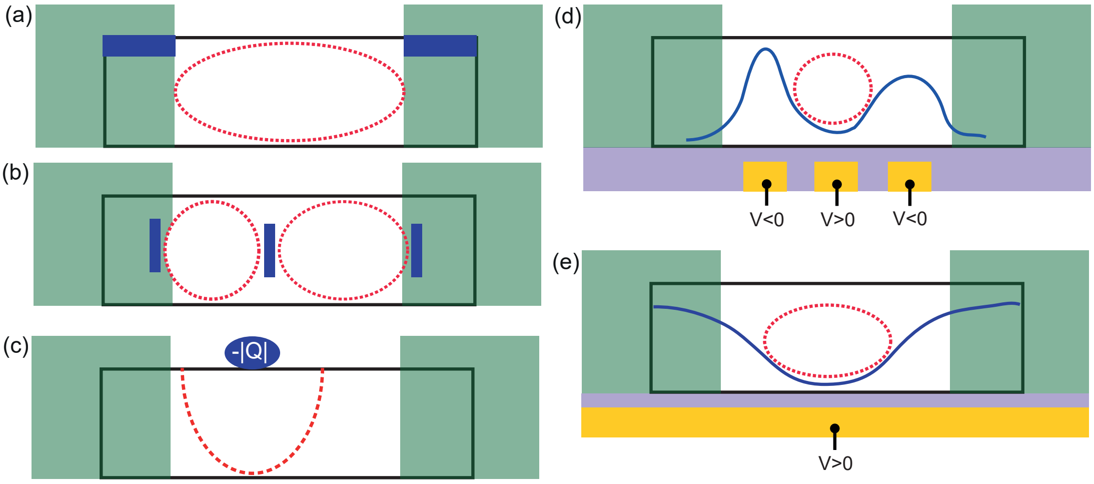

Figure 2.4: Scheme of a two terminal nanowire junction illustrating mechanisms that lead to quantum dot formation, either naturally **(a,b,c)** or by gates **(d,e)**. **(a)** Barriers in the contacts -in blue- lead to the formation of a quantum dot of the size of the channel -indicated by a red-dashed circle- in a defect-free nanowire. **(b)** Three defects in the nanowire induce natural barriers that confine two quantum dots. **(c)** A charge $-|Q|$ sitting on top of the native oxide of the nanowire depletes the channel locally, confining a dot -red-dashed line. **(d)** Local gates are needed to open the channel of the junction and change its chemical potential to measure conductance plateaus, but they can also electrically confine one or more quantum dots. If the electric potential produces a camel-shaped subband profile, a dot will be confined. **(e)** If the nanowire sections under the contacts are nearly depleted and one or a few subbands act as reservoirs. These sections cannot be tuned by the gate potential because the metallic leads screen it. Certain configurations can electrically confine a quantum dot, like the one depicted.

To study superconductivity through a truly one-dimensional nanowire, and maximize the chances of success, it is thus better to work with short-channel junctions (i.e., shorter than the mean free path). Indeed, the observation of ballistic transport requires the channel of the nanowire to be shorter than the mean free path. Unfortunately, real-life nanowires are not homogeneous enough to guarantee a universal value of the mean-free path, which means that one does not know in principle how short should the junction be. If this were the only consideration into account, then it would be desirable to fabricate the shortest junctions possible for ensuring ballistic transport.

However, in reality there are other issues to consider. Very short junctions (L<100 nm) have poor gate effect because of the screening of the metallic leads and are a challenge in lithography. Hence, a compromise in-between needs to be found. We eventually opted for channel lengths of a few hundredths of nm.

Even if the nanowire is ballistic, it may have its conductance hindered by the transparency of the contacts. Thus, transparent contacts are a must whenever conductance quantization is sought for.

2.6 The proximity effect

Superconductors are a macroscopic manifestation of quantum mechanics. In the BCS superconductors [4], the interaction of the electrons with the ions of the crystal lattice produces an attractive potential that, at a temperature below a critical temperature T_c, can result in the pairing of two electrons with opposite spin and momentum forming so-called Cooper pairs. In a piece of superconductor, a sizable portion of the free electrons will be involved in Cooper pair formation, and all will be described by the same macroscopic wavefunction. The aforementioned attractive potential will open a gap at the Fermi energy, protecting the superconducting state from dissipation and producing a hole-particle symmetry [76].

A superconductor can provide a normal conductor with superconducting properties, such as the Meissner effect and an induced -and renormalized- superconducting gap [77]. Andreev recognized that the microscopic origin of this phenomenon, known as the proximity effect, laid in the coherent retro-reflection of electron as holes in the normal-superconductor (NS) interface. Figure 2.5**a** depicts schematically this mechanism, known as Andreev Reflection. It also shows schematically the profile of the gap across the NS junction, following the calculation of Ref. [78]. The coherent pairing of electrons with retro-reflected holes in the N-lead induces a gap in the normal side (proximity effect), while the leakage of quasiparticles into the S-lead reduces the gap in the superconducting side (inverse proximity effect). The proximity effect in NS junctions has been corroborated by direct measurements of the local DOS in the normal metal side [79][80].

---

[4] BCS meaning that they can be described by the Bardeen–Cooper–Schrieffer theory, as opposed to unconventional superconductors.

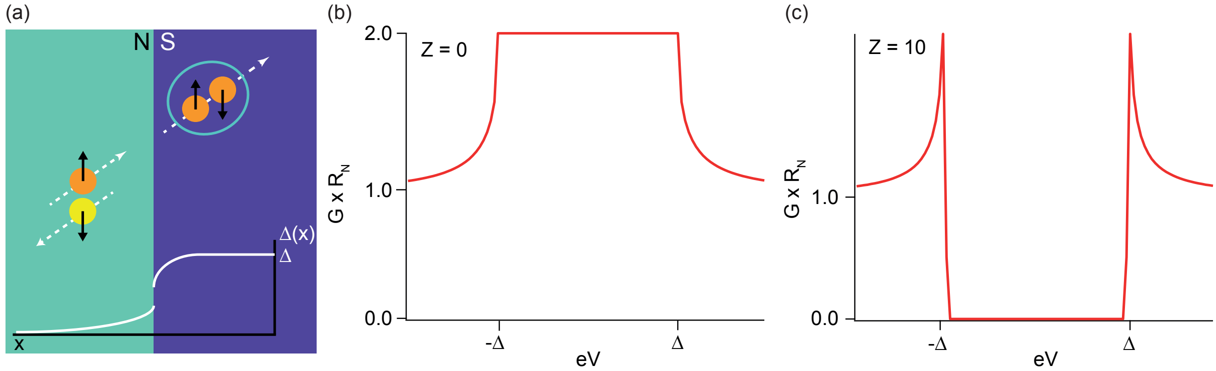

Figure 2.5: **(a)** Scheme of Andreev reflection in a NS junction. An electron (orange dot) impinges on the S surface and gets retro-reflected as a hole by the gap -after penetrating a distance $\sim \xi_S$ into the S-side. The electron and hole stay paired coherently in the N-side up to a distance ξ_N from the interface. In the bottom of the scheme, a cartoon of the gap profile across the junction is shown (adapted from Ref. [78]). The jump of Δ(x) at the interface depends on the barrier strength. **(b,c)** Calculation of the product of the conductance (G) and the normal resistance (R_N) using the theory of Blonder, Thinkham and Klapwijk [81] for a one-dimensional NS junction at zero temperature, for barrier strength Z = 0 (fully transparent) and Z = 10 (opaque).

A barrier at the NS interface will greatly modify the conductance measured through the NS junction [81]. When the barrier is transparent, the zero temperature product of the differential conductance and the normal-state resistance of the junction can reach 2 for bias-voltages $|V| \leq \Delta$, where Δ is the superconductor gap. If the barrier is opaque, though, the differential conductance will reflect the gaped DOS of the parent superconductor, approaching zero inside the gap. Figures 2.5**b,c** show plots of these two cases for a barrier strength Z = 0 and Z = 10, calculated with the formalism developed for zero temperature in a 1D NS junction in Ref. [81].

2.7 Hardness of the gap in superconductor/nanowire junctions

In a superconductor/nanowire (S-NW) junction, a proximity effect should in principle be established -as in an NS junction- if there are enough electrons available at the Fermi level. As explained above, however, a "hard" gap -i.e., a gap with virtually no subgap quasiparticle states- can only be measured correctly in the low-tunnel coupling regime, when the barrier at the S-NW interface is opaque (large Z) and there is negligible Andreev reflection.

Even in this situation, a S-NW junction can still present a soft gap [1]. A soft gap is named in this way because it has a non-zero DOS at $|eV| < \Delta$. The measured gap may also be reduced with respect to that of the parent superconductor. The opposite of this is a hard gap, for which the subgap DOS is very small. The *hardness* of the gap can be quantified as the ratio between the normal -above the gap- differential conductance G_N and the zero-bias subgap differential conductance G_S.

Takei et al. studied theoretically the influence on the hardness of the gap of interface inhomogeneities, magnetic and non-magnetic disorder in the nanowire, temperature and dissipative quasiparticle broadening [82]. They concluded that interface roughness was the main culprit in the softness of the gap, by effectively producing spatial fluctuations in the induced gap.

Researchers at Delft and Copenhagen recently managed to produce hard gaps in short superconductor/nanowire/normal (S-NW-N) metal junctions by improving the S-NW interface. In the case of the Delft group, the improvement came by passivation of the surface of an InSb nanowire with sulfur, and by using a wetting under-layer of NbTi before sputtering of the NbTiN superconductor [83][84]. In the case of the Copenhagen group, a thin aluminum (Al) layer was epitaxially grown in-situ on the surface of freshly-grown InAs nanowires, inside a MBE chamber [85]. However, Lee et al. at Grenoble have also obtained almost as hard gaps with either Al and vanadium through in-situ Ar^+ etching of the native oxide of InAs nanowires [11][12], showing that harsher surface treatments may still give good results.

In all of these cases it is difficult to tell if the induced gap in the nanowire improved significantly, as the channels were short (i.e., less than 300 nm), and it is generally hard to estimate accurately the coherence length of superconductivity in the proximitized nanowire. The issue is complicated by two factors. Firstly, the S-NW interface of lowest impedance can be anywhere below the superconductor deposited on the nanowire. Secondly, Cooper pairs can tunnel -or cotunnel- *directly* through the quantum dot or the QPC in the nanowire from one contact to the other, or they can diffuse if the disorder is important. Given that induced gaps with a Δ value similar to the parent superconductor have been obtained in the cases cited above, the possibility of direct tunneling without proximity is not farfetched. Andreev correlated electron-hole pairs could also leak through a short distance in the nanowire, and *then* tunnel to the other contact. In these conditions, the measured gap will be a truly induced one.

2.8 Gap spectroscopy in S-quantum dot-N junctions

Nanowires can naturally host quantum dots, as explained before. It is therefore appropriate to discuss the well-known and well-studied case of a quantum dot coupled to a superconducting and a normal lead (i.e., an S-QD-N junction).

In a S-QD-N junction, two regimes of interest for gap spectroscopy may be distinguished: 1) A dot badly-coupled to both leads ($\Gamma \ll$ U) and 2) A dot well-coupled to the S lead but badly-coupled to the N lead ($\Gamma_N \ll \Gamma_S$ and $\Gamma_N + \Gamma_S = \Gamma \lesssim$ U). In both cases, the tunneling of Cooper pairs is suppressed by the charging energy U, since two electrons cannot occupy the dot at the same time.

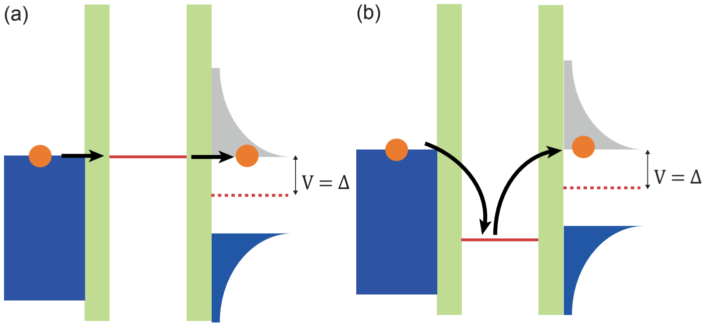

Figure 2.6: Schemes of transport mechanisms through a symmetric S-QD-N junction in the $\Gamma \ll U$ regime, at a bias voltage V >∼ Δ. **(a)** Sequential tunneling of a quasiparticle through a resonant dot level. **(b)** Cotunneling of a quasiparticle when a level of the dot is not resonant. Adapted from Ref. [86] for an N-QD-S case.

In the first case, quasiparticles can still pass in two ways. The first way involves the tunneling of a quasiparticle from the Fermi level of the metal through a resonant level of the dot. The gap of the superconductor cannot be breached by this quasiparticle, since it would involve the formation of a Cooper pair via a retro-reflected hole, violating the two-electrons rule stated above. Therefore, the voltage applied on the junction $|V|$ needs to be larger than Δ, provided that a gate can be used to compensate for the level spacing and U of the dot as shown in Figure 2.6**a**. The second way occurs when a level of the dot is not resonant, and it involves the cotunneling of the quasiparticle in a second order process shown in the scheme of Figure 2.6**b**.

Andreev bound states

In the second case, when the junction is asymmetrically coupled to the leads and Γ <∼ U, the de-pairing interaction of the spin of the electron with the BCS condensate will produce a pair of subgap states named Andreev bound states (ABS) or Shiba states in the literature [5] [87][12].

The physics of Shiba states in quantum dots is well-described in Refs. [87] and [12]. When a single electron is sitting on a level of the dot, it can adopt one of the following ground-states: 1) a spin-doublet $|d\rangle$ or 2) a spin-singlet $|s\rangle$. In turn, the singlet can be either BCS-like (when $\Delta \gg U$) or Kondo-like (when $U \gg \Delta$). The former arises via superpositions of a doubly-occupied and an empty states of the dot, while the latter is a consequence of the Kondo correlations between the spins of the quasiparticles at the S-lead and the single electron spin sitting in the dot level. There is no clear boundary in-between.

The energy of the ABS can be tuned by changing the ratio between the Kondo temperature T_K and Δ [89][87]. In a voltage-biased configuration, the states can move from V ∼ Δ at $T_K \ll \Delta$

---

[5] In S-N-S junctions, ABS arise as standing waves produced by successive Andreev reflections at the two NS interfaces, and should not be confused with the quantum dot case mentioned here.

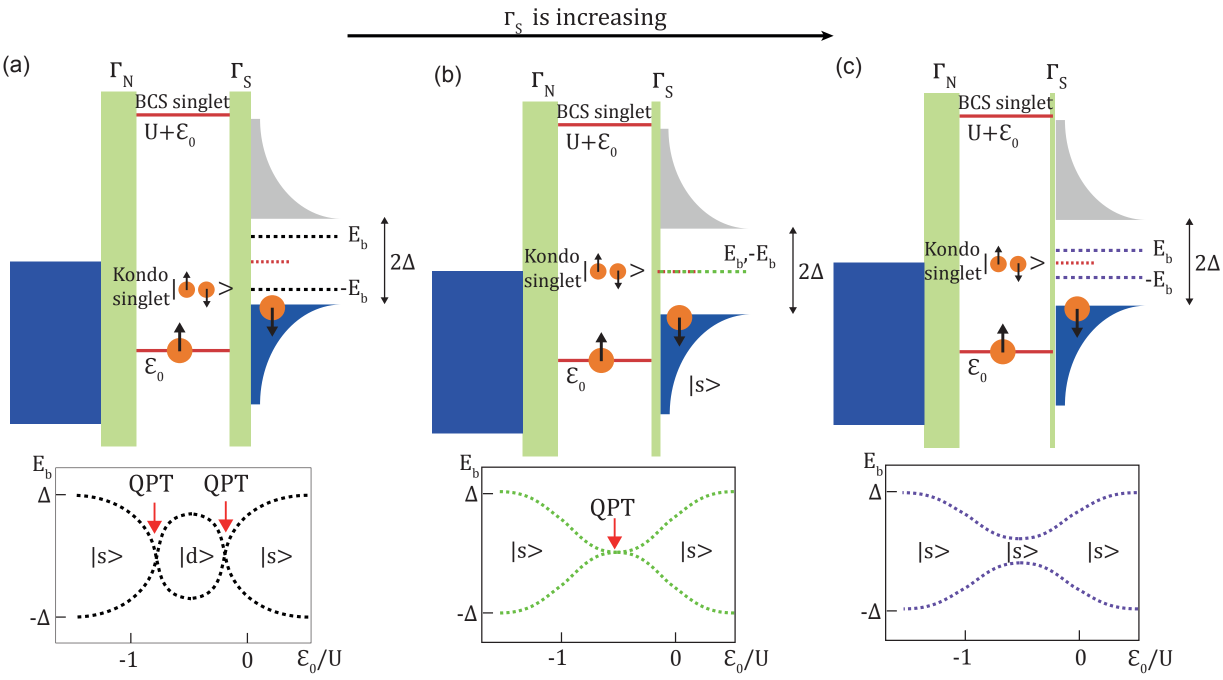

Figure 2.7: Schemes of transport mechanisms through an asymmetric S-QD-N junction in the $\Gamma_N < \Gamma_S$ and $\Gamma \lesssim$ U regime (upper panels) and corresponding dependence of the Andreev bound states (ABS) E_b and -E_b on the ratio of the level position of the dot with respect to the charging energy (ε_0/U). Γ_S is increasing from the left to the right panels. **(a)** At small Γ_S, the ground-state is a spin-doublet when the dot level is singly occupied, and the excited state is a Kondo singlet (KS) formed by the correlation of the electron spin from the dot and the quasiparticles from the S-lead (upper panel). A BCS singlet ground-state is only accessible when the dot level is not occupied or doubly occupied-, when the charging energy U is compensated by a gate voltage. In the two doublet - BCS singlet boundaries, a quantum phase transition (QPT) arises (bottom panel). **(b)** When Γ_S is larger, such that $T_K >\sim \Delta$, the Kondo correlations favor a KS ground-state, producing a QPT (bottom panel). The two ABS merge at the QPT when they cross the Fermi energy. **(c)** At an even larger Γ_S, the ABS drift apart and the KS ground-state is firmly established. Figures adapted from Refs. [87], [12] and [88].

(indicating a doublet ground-state) to nearly zero-bias at $T_K \sim \Delta$. When $T_K > \Delta$, a quantum phase transition (QPT) will occur as soon as the ABS cross the Fermi energy, leading to a zero-bias peak in the conductance of the S-QD-N junction. In the QPT, the ground-state of the dot changes from a doublet to a Kondo singlet. Since T_K depends on many dot parameters, the energy of the ABS can be conveniently modified by a gate voltage (which changes Γ, U, and level position ε_0 [88][90][12]) or a magnetic field (which reduces Δ and splits the doublet state [12]). And example of how the QPT is achieved by varying Γ_S or ε_0 is given in Figure 2.7.

2.9 Gap spectroscopy in S-quantum dot-S junctions

In S-QD-S junctions, the picture described above is complicated by the fact that there is a second superconducting gap with which the dot could in principle form ABS. However, for an asymmetric junction ($\Gamma_L \ll \Gamma_R$), the badly-coupled lead (i.e., Γ_L) will work as a tunnel probe for the ABS that form by the same mechanism as in the S-QD-N case in the strongly-coupled lead (i.e., Γ_R) [91][92][93].

Therefore, if the probing gap is clean of states, the ABS should appear as conductance peaks at an energy eV = $\Delta + E_b$ and -$\Delta - E_b$, and should be followed by negative differential conductance (NDC). Weaker peaks are also expected at $\Delta - E_b$ and -$\Delta + E_b$ [91]. However, if there is residual DOS at the Fermi level of the probing gap, then a couple of extra peaks related to the same ABS should emerge in the voltage-biased conductance characteristic at E_b and -E_b [11].

In the symmetric ($\Gamma_L = \Gamma_R$) and low-coupling regime ($\Gamma \ll$ U), one lead will tunnel-probe the other one via the weakly-coupled dot, leading to a conductance characteristic in which the BCS peaks are seen at eV = $\pm|2\Delta|$, without NDC. The processes depicted in Figure 2.6 will also be involved in this case.

However, if the coupling is larger ($\Gamma \sim$ U), and the junction is still symmetric, quasiparticles can be carried from one lead to the other via multiple Andreev reflections (MAR). MAR appear as conductance peaks at $eV = 2\Delta/n$ (where n=1,2,3,...). As the asymmetry between Γ_L and Γ_R increases, an ABS regime can be recovered [91].

2.10 Josephson effect in S-quantum dot-S junctions

S-QD-S junctions can also carry a supercurrent when the coupling of the junction to the leads is intermediate ($\Gamma \lesssim$ U) to large ($\Gamma \gg$ U). A supercurrent is a non-dissipative current of Cooper pairs that can pass through a piece of superconductor. A supercurrent can also pass if the superconductor is cut in the middle by a so-called weak-link, which can be a thin insulator, a sub-micron piece of metal, a geometrical constriction, or any other non-superconducting thin medium -including a semiconductor nanowire. The latter phenomenon, known as the Josephson effect, happens when there is sufficient overlap between the macroscopic wavefunctions $\Psi_L e^{i\phi_L}$ and $\Psi_R e^{i\phi_R}$ of the two separated pieces of superconductor [76].

The magnitude of the supercurrent depends on the phase difference $\phi = \phi_L$ - ϕ_R via the relationship shown in equation 2.2. In this equation, I_c is named the *critical current*. It is the maximum supercurrent that can pass through the junction before it is rendered dissipative.

$$I_s = I_c sin(\phi) \tag{2.2}$$

When a quantum dot is bridging two superconductors, the passage of Cooper pairs will be made difficult by the charging energy U in the dot. When $\Gamma \gg$ U, the charging energy is not a problem though, and Cooper pairs can pass resonantly if there is a dot level aligned with the leads. In this non-interacting regime, if a level is not aligned, Cooper pairs can still pass by cotunneling, though the magnitude of the supercurrent will be weaker. A supercurrent transistor has been reported in this way before [94]. In this work, the magnitude of the supercurrent was tuned by a gate voltage that changed the level position of the dot.

When $\Gamma \lesssim$ U, Cooper pairs need to break into their constituent electrons in order to pass through the interacting dot [86]. If $T_K \ll \Delta$ and the dot level is occupied by a single electron, the cotunneling processes that allow the passage of Cooper pairs will result in an *inverted* supercurrent, with an additional π phase-shift in equation 2.2 [95]. In this case, the ground-state of the dot will be a doublet. Conversely, if $T_K \gg \Delta$, Kondo correlations between the impurity spin and the quasiparticles of the leads will ensure a Kondo singlet ground-state, as in the ABS case stated above. When $T_K \gtrsim \Delta$, a QPT happens [96].

2.11 Josephson effect in S-quantum point contact-S junctions

In Ref. [97], it was calculated that the critical current through a QPC should be *quantized* as in the expression given by equation 2.3. This relation is valid for a QPC with fully transparent contacts and in the short junction limit, when the superconducting coherence length $\xi_N = \hbar v_F / \pi\Delta$ is longer than the channel length.

$$I_c = N\frac{2e^2}{h}\frac{\pi\Delta}{e} \tag{2.3}$$

2.12 Zero-bias peak and Majorana bound states in S-nanowire-S devices

In the introduction to this thesis, I mentioned the possibility of obtaining MBS in a long 1D nanowire with strong spin-orbit coupling, endowed with superconducting correlations through its contact with a high critical field superconductor [4]. I also mentioned a tunnel spectroscopy experiment with which one could probe a MBS in the boundary of a topological section of the nanowire [1][9]. In this experiment, one would simply attach a normal lead to the proximitized nanowire, forming a N - NW - S junction.

In a V - dI/dV measurement in this device, a zero-bias peak (ZBP) is expected to emerge when a strong enough magnetic field is oriented parallel to the nanowire, to maximize the spin-mixing given by the Rashba interaction. The magnitude of the field needed is given by $E_z = \sqrt{\Delta^2 + \mu^2}$, where E_z is the Zeeman energy and μ is the chemical potential in the topological section. The peak will vanish when the Rashba interaction becomes dominated by the Zeeman energy at large enough field, and the spin-mixing becomes negligible.

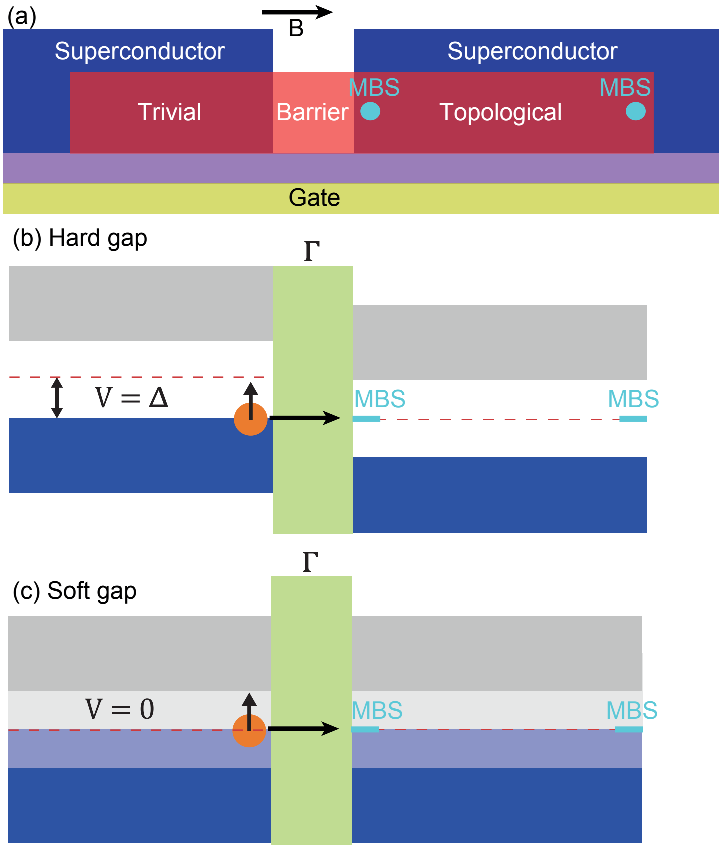

Figure 2.8: **(a)** Scheme of a S-NW-S device in which a section of the nanowire (in red) below the right lead has entered the topological regime, while the section under the left lead remains trivial. This could be due to different chemical potentials in these two sections. The nanowire section not covered by metal -i.e., the channel- has been depleted by a gate voltage and acts as a barrier. Two MBS are depicted by blue dots in the boundaries of the topological section. The magnetic field (B) orientation necessary for achieving the topological regime is indicated by a black arrow. **(b)** Low-energy semiconductor-type band scheme. When the induced gap in the nanowire is hard, the left section of the nanowire can be used to probe by tunnel spectroscopy the leftmost MBS on the right section, as long as a bias V = ±Δ is applied. **(c)** If the gap is soft, the leftmost MBS can also be probed at zero-bias.

In a S - NW - S junction, one could also use one of the S-leads as a tunnel probe of the MBS sitting in the proximitized section of the nanowire below the other lead, in the event that it can be turned topological. Such device is shown in Figure 2.8**a**. If the probing gap is hard, a voltage $|V|$ = Δ would need to be applied to transfer electrons from the quasiparticle band of the tunnel probe to the leftmost MBS at zero energy in the topological section of the nanowire, as shown in Figure

2.8**b**. Instead of a ZBP emerging with field, one would see in this case a couple of peaks at V = ±Δ, followed by negative differential conductance.

However, if the probing gap is soft, such as in the case of Figure 2.8**c**, electrons at the Fermi level could tunnel from the left lead to the MBS at V = 0, producing a ZBP in the conductance as in the case of a N - NW - S device. However, the ZBP would be joined by additional peaks at V = ±Δ. These peaks arise from the tunneling of quasiparticles in the BCS band of the probing lead to the MBS.

The practical complications of this type of experiment have been highlighted in the introduction of this thesis. There is an additional complication, which is the Josephson effect. The Josephson effect can produce a ZBP, as a result of the passage of current through the junction with no applied voltage. It has been assumed that the absence of a Josephson effect in Coulomb blockaded diamonds at zero field would mean that at high magnetic field there would certainly not be any remaining possibility of the development of a Josephson effect [98]. However, in Chapter 6 I show that a supercurrent-related ZBP can also emerge with magnetic field -without any ZBP at zero field- if there is a quantum dot confined between the two S-leads.

In Section 4.5 of Chapter 4 I will show a second additional complication, which comes from the existence of a quantum dot in parallel with the 1D electron gas in the nanowire (as demonstrated in Chapter 3). This dot may produce a ZBP emerging with a magnetic field oriented parallel to the nanowire.

Chapter 3

Parallel transport in InSb nanowires displaying conductance quantization

3.1 Introduction

One-dimensional (1D) semiconductor nanowires are interesting because they could host helical states and, if coupled to a superconductor, exotic Majorana bound states (MBS) [4][19][33][1].

InSb nanowires grown by the Eindhoven group are known for displaying conductance quantization at high magnetic field [20]. More recently, conductance plateaus were also demonstrated at zero magnetic field, under special fabrication conditions [19]. The same nanowires have been used to show the first signature of Majorana bound states [1], and they may possibly host helical states [33].

In this Chapter, I will show by means of transport measurements that, surprisingly, a single InSb nanowire can have two parallel conduction paths. First, I will discuss the case of a nanowire with a 1D channel in parallel to a quantum dot channel. Then, I will present a nanowire with two 1D parallel channels.

If confirmed by undergoing theoretical simulations, these measurements will have profound implications for experiments seeking helical states and MBS in these nanowires.

3.2 Quantum wire in parallel with a quantum dot

The two-terminal InSb nanowire device whose measurements are described and discussed in this section was fabricated using a tetra-layer of titanium (Ti), aluminum (Al), vanadium (V) and Al (of thicknesses, 2.5 nm, 10 nm, 100 nm and 10 nm, respectively) as metal contacts. Its subband profile and its chemical potential were controlled by a global backgate of Au separated from the

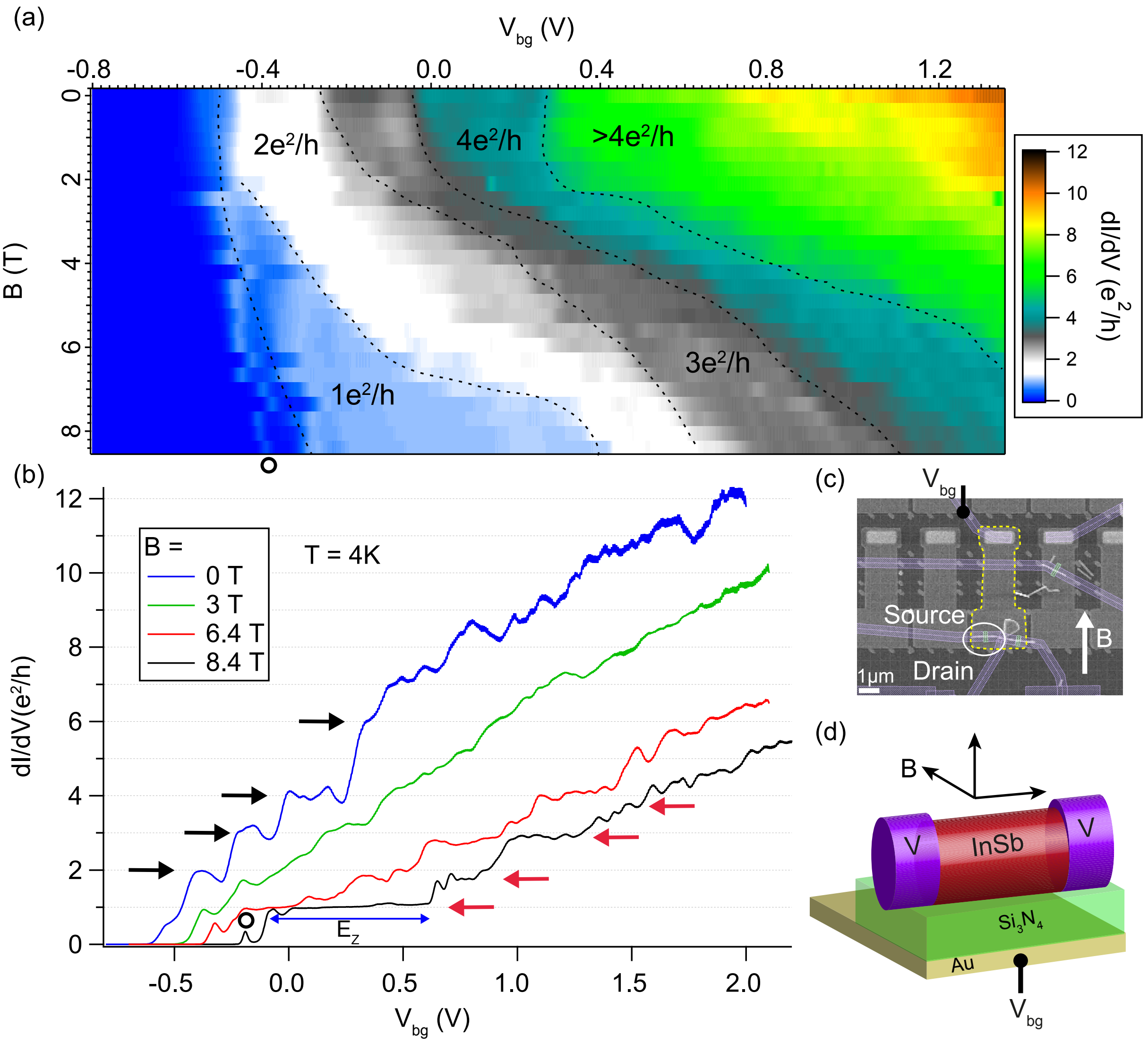

Figure 3.1: **(a)** Map of the zero-bias conductance as a function of the backgate and the magnetic field. Each plateau is labeled by its conductance. **(b)** Traces of zero-bias conductance as a function of the backgate, taken from **(a)**. The magnetic field at which each trace was taken is indicated in the legend. In **(b)**, black arrows point to the plateaus at 2 e^2/h, 3 e^2/h, 4 e^2/h and 6 e^2/h that are seen at B = 0 T, whilst the red arrows point to the plateaus at 1 e^2/h, 2 e^2/h, 3 e^2/h and 4 e^2/h seen at B = 8.4 T. In these two plots, a black circle points to a resonance near pinch-off. **(c)** SEM image of the device before metal deposition. The nanowire is encircled in white and situated on top a global gate, which is itself delimited by a yellow dashed line. The global gate is connected through an aperture opened by etching the Si_3N_4. The field was oriented in-plane and nearly perpendicular to the nanowire, as indicated in the image. **(d)** Scheme of the device. The field orientation is indicated.

device by 50 nm of silicon nitride (Si_3N_4) dielectric (for a SEM image of the device before metal deposition and a pertinent scheme, see Figures 3.1**c,d**). This combination of metals was used to take advantage of the good contacts of Al with InSb nanowires while retaining the high critical field and large gap of V. Ti was used as sticking layer for Al -at this moment we did not know that this was unnecessary- and V needed to be capped with Al to protect it from oxidation. The large total thickness of the metals deposited was chosen to fully cover the 100 nm - diameter nanowire. The channel of the nanowire in-between the two contacts was 200 nm long. For a full description of the microfabrication process of this type of device, please refer to Appendix A.

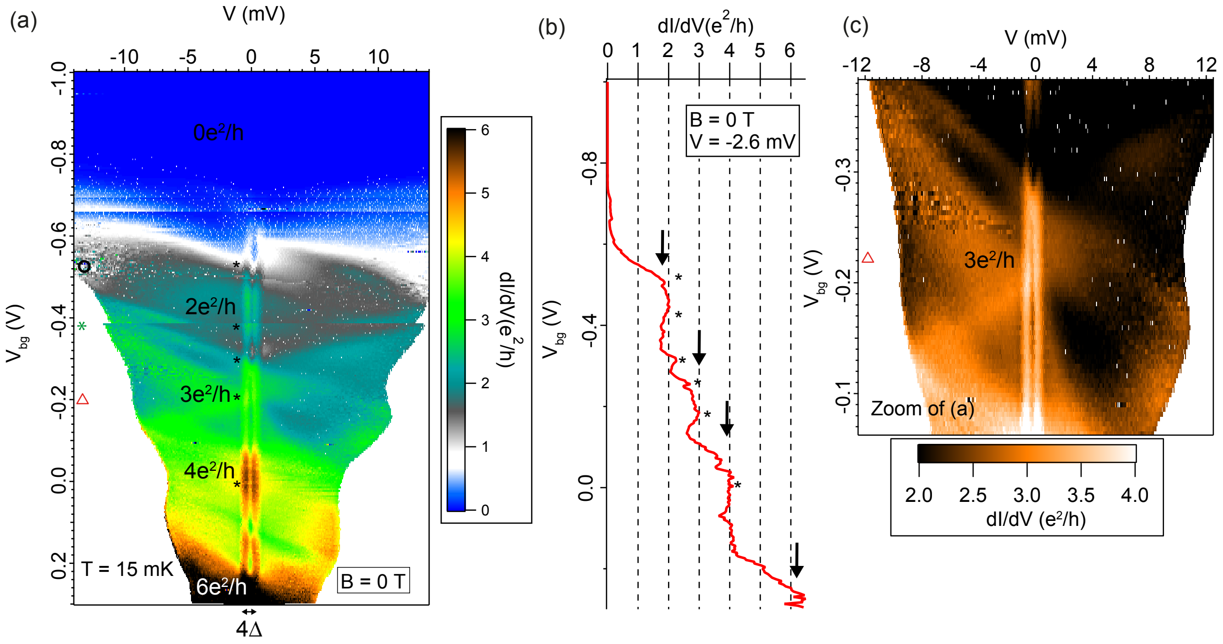

Figure 3.2: **(a)** Non-linear conductance map as a function of bias voltage V and backgate voltage V_{bg}, taken at B = 0 and T = 15 mK. Some values of conductance are indicated as an aid to identify plateaus. Black asterisks point to the crossing at zero bias of a few resonances. **(b)** Conductance cut at V = -2.6 mV from the map in **(a)**. Black arrows point to conductance plateaus.

Initial characterization

Figure 3.1**a** shows the evolution of the linear conductance with magnetic field at T = 4.2 K. At this temperature, Vanadium is no longer superconducting. Thus, this is a normal state measurement. From the accompanying plot in Figure 3.1**b**, which consists in cuts taken from 3.1**a** at a few magnetic fields, it can be readily seen that plateaus evolve as the magnetic field is increased. In the map 3.1**a**, these plateaus appear as color bands of light-blue, white, gray, and turquoise, which respectively correspond to 1 e^2/h, 2 e^2/h, 3 e^2/h and 4 e^2/h. At zero field, plateau-like structures can be seen at 2 e^2/h, 3 e^2/h, 4 e^2/h and possibly 6 e^2/h. All of these plateaus are expected for a nanowire with three spin-degenerate subbands, except for the one at 3 e^2/h. At B = 8.4 T, the linear conductance characteristic consists of a resonance (black circle) followed by a long 1 e^2/h plateau and small 2 e^2/h, 3 e^2/h and 4 e^2/h plateaus. The 1 e^2/h step is expected for non-degenerate spin-split subbands. Interestingly, the color bands in the map 3.1**a** bend noticeably with magnetic field, indicating a strong orbital effect. Orbital effects are indeed expected to be stronger when the field is applied perpendicular to the nanowire.

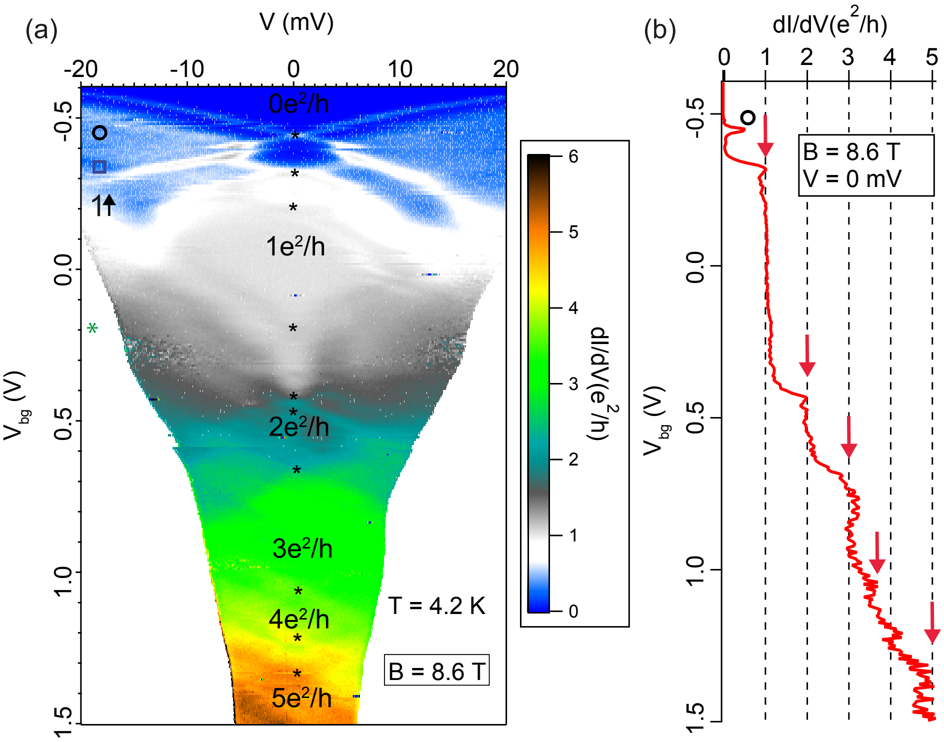

Figure 3.3: **(a)** Non-linear conductance map as a function of bias voltage V and backgate voltage V_{bg}, taken at B = 8.6 T and T = 4 K. The values of conductance of the first five plateaus are indicated. A few resonances are also indicated by a black asterisk. **(b)** Conductance cut at zero bias from the map in **(a)**. Red arrows point to conductance plateaus.

To gain some insight on the origin of the 3 e^2/h plateau at zero field, the non-linear conductance of the sample was measured. If the sample were truly 1D, at zero magnetic field a series of diamonds with flat conductance at multiples of 2 e^2/h would be observed [99]. Figure 3.2**a** shows a map of the conductance as a function of bias voltage V and backgate voltage V_{bg} at B = 0 and at T = 15 mK. To show that the same zero-bias characteristic still holds at this temperature as it did at T = 4.2 K, but to avoid the superconductivity of vanadium, a cut was taken at a voltage V = - 2.6 mV -i.e. well above 2Δ. This cut is shown in Figure 3.2**b**, and roughly shows the same plateaus as the trace at B = 0 and T = 4.2 K in Figure 3.1**a**.

Interestingly, although the linear conductance at B = 0 and T = 4.2 K showed plateau-like features, the non-linear conductance characteristic of Figure 3.2**a** is not quite the quantized conductance diamond structure expected for a series of subbands measured as a function of gate and bias voltage. Instead, super-imposed on the plateaus at 2 e^2/h and 4 e^2/h, there are a few sharp tilted lines resembling Coulomb resonances, which suspiciously points to electron localization. The 3 e^2/h plateau shown in the blue curve of Figure 3.1**b** does not correspond to a diamond of quantized conductance, but instead comes from one of such resonances. The origin of these super-imposed Coulomb resonances will be explained further below. In Figure 3.2**a** some of the resonances, including the one at 3 e^2/h, are indicated by black asterisks.

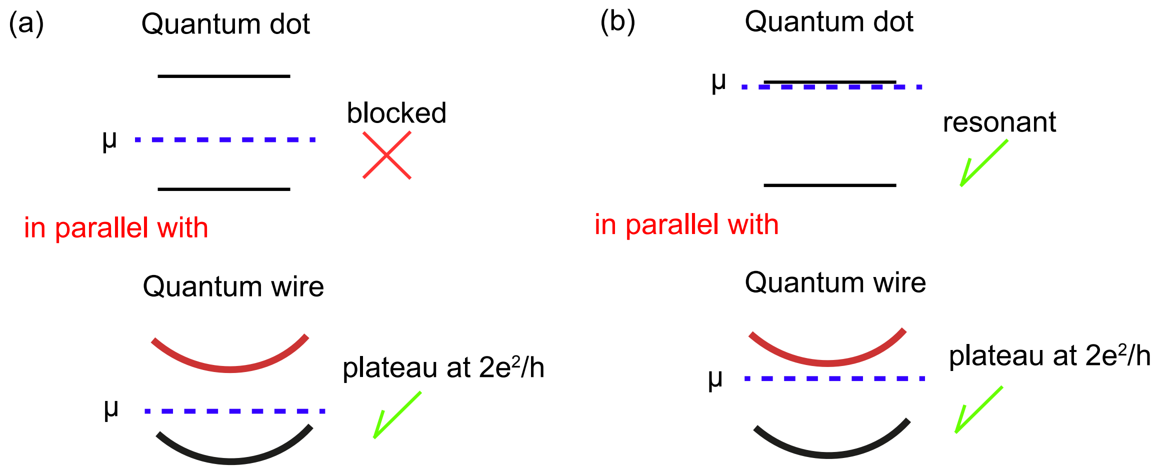

Figure 3.4: Schemes of transport through a quantum wire and a quantum dot in parallel with each other. **(a)** If the dot is in Coulomb blockade, only a plateau is seen in the conductance; otherwise, **(b)** if the dot is on resonance, a Coulomb peak on top of the plateau appears.

A similar non-linear conductance measurement as the one just described, but at a large field of B = 8.6 T and a temperature T = 4.2 K is shown in Figure 3.3**a**. Once again, if the sample were truly 1D, at large magnetic field a series of diamonds with flat conductance at multiples of 1 e^2/h should be seen. In this plot, similarly to the B = 0 case, there are a few resonances super-imposed on top of well-defined plateaus. The zero-bias crossings of some of these resonances are indicated with a black asterisk.

The fact that these resonances are on top of plateaus of quantized conductance may mean that there are *two parallel channels of transport*. Judging by the linear and non-linear conductance characteristics, these parallel channels would consist of a quantum point contact with 1D subbands and a quantum dot with discrete levels, as described in Figure 3.4**a,b**.

In the top of scheme 3.4**a**, the chemical potential of the leads with respect to the discrete levels of the quantum dot is depicted. Since the chemical potential is not aligned with any level, transport is in Coulomb blockade and there is no conductance contribution from the dot in this condition. On the other hand, for the same gate voltage, the chemical potential of the leads is above the edge of the first subband as depicted in the bottom of the scheme 3.4**a**. Thus, we expect

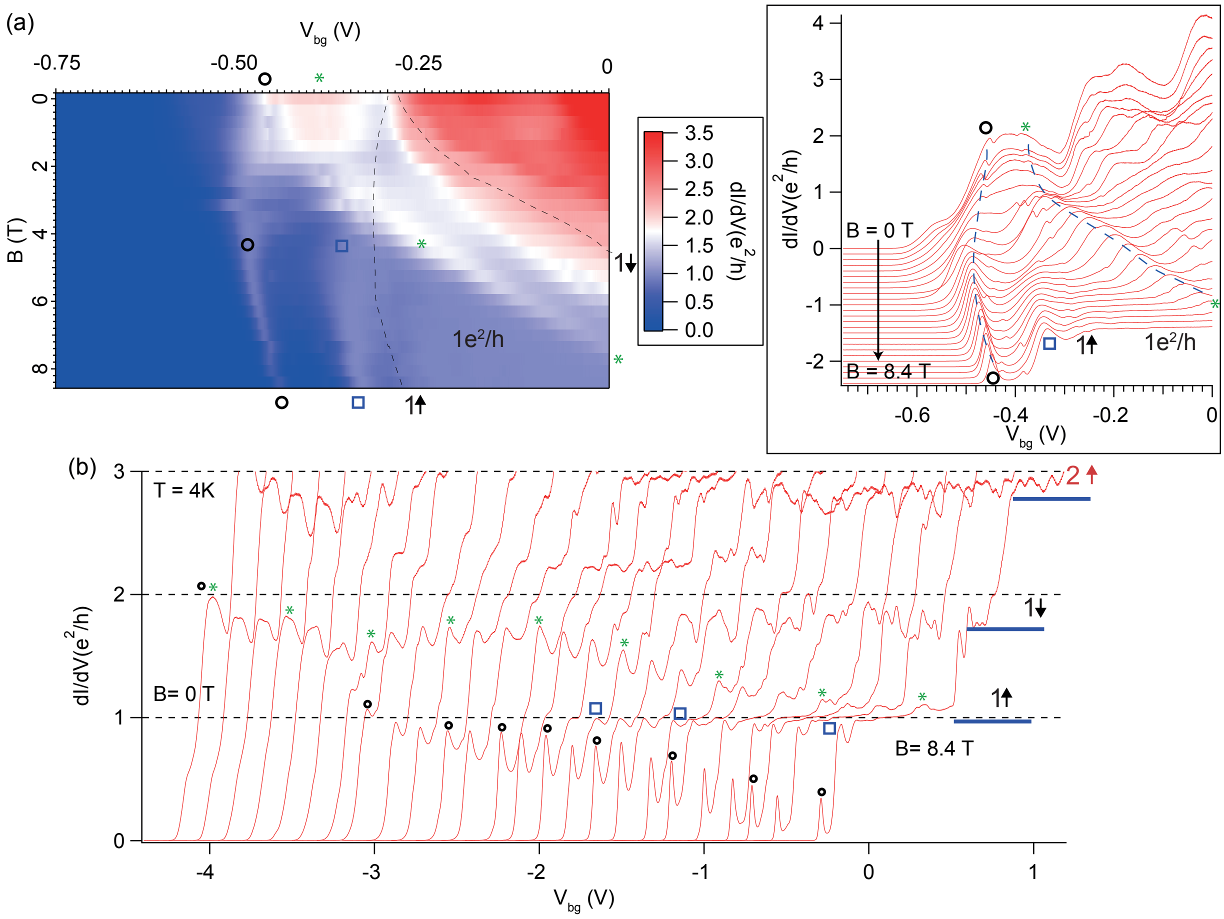

Figure 3.5: **(a)** Linear conductance map at T = 4.2 K as a function of the backgate voltage and the magnetic field, from B = 0 to B = 8.4 T, zoomed on the first quantized plateau. In this map, plateaus are indicated by their orbital number and spin species (either 1 ↑ or 1 ↓), while Coulomb resonances are indicated by squares, circles, and asterisks. A black dashed line was added a guide to follow the B-dependence of the bottom of the spin-split subbands. The inset on the right shows cut-lines from the map on the left. The magnetic field evolution of the two Coulomb peaks belonging to a 2 e^2/h Kondo resonance at zero field (black circle and green asterisk) are indicated by blue-dashed lines. The curves are offset by -0.1 e^2/h, starting from B = 0. **(b)** Linear conductance traces taken from the map in Figure 3.1**a**, from B = 0 to B = 8.4 T. These curves show the magnetic field evolution of the plateaus (blue parallel lines) and the Coulomb resonances on top of them (circles, asterisks and squares).

the conductance to be 2 e^2/h -or less, depending on the transparency-, since only one subband contributes to transport. In another gate condition, as depicted in the scheme 3.4**b**, one of the levels of the quantum dot is aligned with the chemical potential of the leads, leading to a removal of Coulomb blockade. This will result in a Coulomb peak on top of a 2 e^2/h plateau. This scheme of transport can be generalized to include many subbands in parallel with many quantum dot levels, which is much more likely the experimental case presented here.

Under a magnetic field, the Zeeman energy will split the spin-degenerate plateaus into half-integer plateaus, while shifting the Coulomb peaks of the parallel dot at the same time -depending on the ground state. It will also destroy Kondo correlations in the quantum dot, if the are any of these correlations present. Experimentally, the conductance of Kondo ridges will decrease as the magnetic field is raised. The orbital effect of the magnetic field will also shift both the Coulomb peaks and the plateaus.

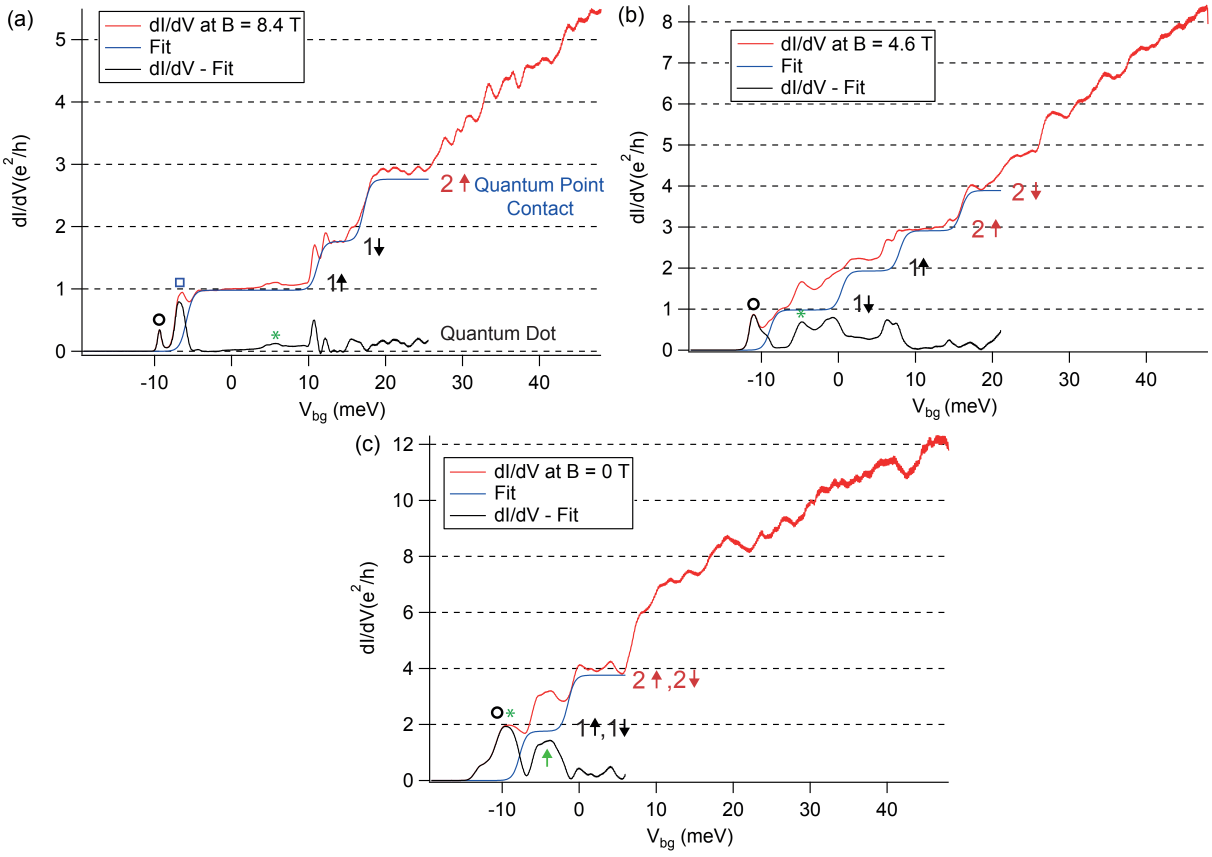

Figure 3.6: Linear conductance (dI/dV) curves as a function of voltage (red line) fitted by the saddle-point model (blue line), at T = 4.2 K and **(a)** B = 8.4 T, **(b)** B = 4.6 T and **(c)** B = 0. The black curve is a subtraction of the linear conductance minus the fitted curve. This method serves to deconvolve the quantum point contact conductance from the quantum dot conductance.

The map in Figure 3.1**a**, which showed the magnetic field evolution of the two-channels system, had a low gate-resolution and presented some charge switches, which made it difficult to follow the field evolution of each of the channels individually. A better-resolved and more stable measurement was retaken at T = 4.2 K, and appears in Figure 4.10**a**. The magnetic field evolution of some of the quantum dot levels and the first spin-resolved 1D subband are individually followed in Figure 4.10**a**. This figure shows a map of the linear conductance of the device at T = 4.2 K zoomed on the first plateau, as a function of backgate voltage and magnetic field. The field evolution of the levels can also be followed in the cut-lines shown in the right inset of Figure 4.10**a**, and in dI/dV vs. gate traces of Figure 4.10**b**, which were taken from the measurement at larger gate range shown in Figure 3.1**a**. The way in which dot levels were distinguished from subbands of the QPC will be discussed in short.

Let us first focus on the quantum dot Coulomb peaks. In the map of Figure 4.10**a**, three of these are indicated (at B = 0, B = 4.6 T and B = 8.4 T) by a black circle, a green asterisk, and a blue square [1]. They are also indicated in some of the traces of Figure 4.10**b**.

At B = 0, it can be seen that the Coulomb peaks indicated by the circle and the asterisk are overlapped and form a bump of conductance that nearly reaches $2e^2/h$. A charging energy U ~ 2.4 meV can be estimated based on the width of the bump. As the field is increased, though, the associated Coulomb peaks shift apart with a g-factor $|g| \sim 29$. The peak marked with a black circle becomes a sharp resonance at B = 8.4 T, while the peak marked by an asterisk crosses the $1\uparrow$ subband (at B ~ 3.5 T) and decreases in magnitude.

At large magnetic field (B > 5 T), another resonance -indicated by a blue square- becomes visible at the onset of the first spin-resolved subband. This resonance may be ascribed to a quantum dot that forms at the onset of the 1D path.

Now, let us switch the focus to the subbands. In the map and the cut-lines of Figure 4.10**a**, and in the traces of Figure 4.10**b**, the bottom of each of the spin-resolved components of the first and second subbands are indicated by their orbital number and spin species ($1\uparrow$, $1\downarrow$ and $2\uparrow$; $2\downarrow$ is out of range in these plots). Additionally, a black-dashed line was added in the map 4.10**a** as a visual aid to trace the magnetic evolution of the bottom of the spin-resolved subbands.

At intermediate field, the peaks of the quantum dot prevent the clear observation of some of the plateaus. However, at B = 8.4 T the orbital effect of the magnetic field has already pushed most of the peaks away from the first three plateaus, and they can be clearly observed. A blue horizontal line in Figure 4.10**b** gives the baseline conductance of each of the plateaus. At high magnetic field (i.e. B = 8.4 T), the $1e^2/h$ plateau has transparency equal to 1, while the $2e^2/h$ and $3e^2/h$ plateaus have a transparency slightly below 1.

Deconvolution of the quantum point contact and the quantum dot conductance

In order to deconvolve the conductance characteristics of the quantum dot and the quantum point contact, I fitted the linear conductance trace at B = 8.4 T with the saddle-point model (using the equations from ref. [99] at V = 0). This model was developed to explain the shape of the

---

[1] I also indicated the zero-bias gate position of these peaks in the charge stability diagrams of Figures 3.2 and 3.3, whenever they are visible.

conductance plateaus in QCPs in 2DEGs. Here, I just use it as a deconvolution tool, because this model produces plateaus, without making any claims that the potential of the nanowire is indeed a saddle.

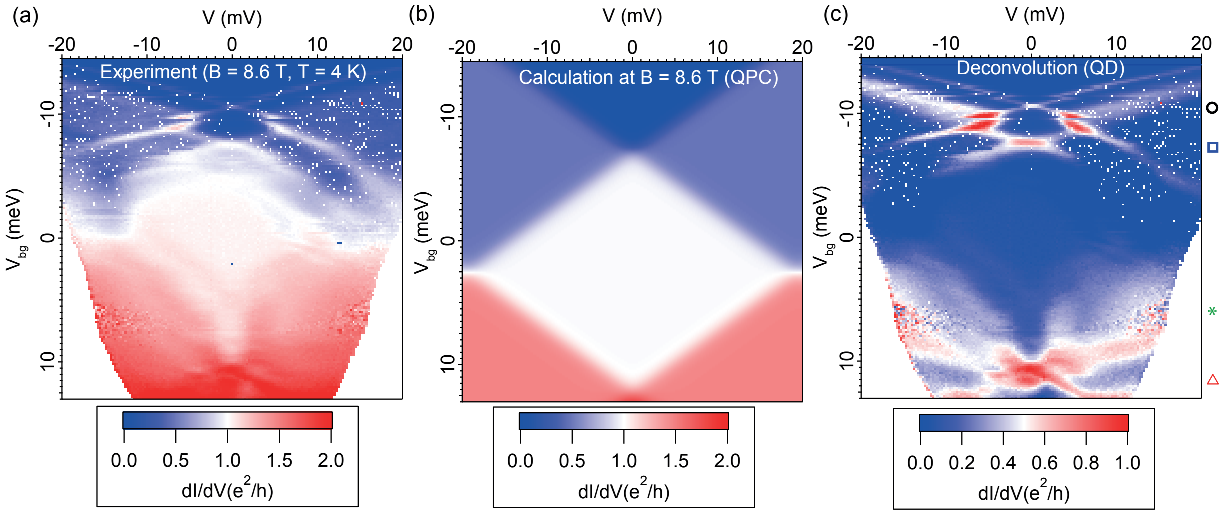

Figure 3.7: Deconvolution of the QPC non-linear conductance from the QD non-linear conductance. **(a)** Experimental conductance map at B = 8.6 T and T = 4 K, with the backgate voltage converted to energy by using the lever-arm of the device ($\alpha = 0.024$). **(b)** Saddle-point model calculation of the non-linear conductance with the parameters $\omega_x = 2.8$, $\omega_y = 0.5$ and $|g_1| = 41$. **(c)** Subtraction of the saddle-point model calculation from the experimental conductance. The quantum dot states are indicated by the same marks as before.

Figure 3.6**a** shows the experimental dI/dV trace at B = 8.4 T and T = 4 K (red line) and the fit (blue line). It also shows the *subtraction* (black line) of the fit from the experimental dI/dV trace. Note that, in these traces, the conductance has been converted to energy, with the aid of the lever-arm of the device ($\alpha = 0.024$). The parameters of this fit are $\omega_x = 2.8$, $\omega_y = 0.5$, $|g_1| = 41$ (g-factor of the first subband) and $|g_2| = 32$ (g-factor of the second subband).

The subtraction shows a series of Coulomb peaks, which I marked with the same code of circle, asterisk, square, and triangle as before. The ability to deconvolve the quantum dot and the QPC characteristics as shown here indicates that transport through these parallel channels is nearly classical -i.e., with negligible crosstalk. In other words, $G = G_{dot} + G_{QPC}$.

In Figure 3.6**b,c** I show a fit and a deconvolution of the experimental dI/dV traces at B = 4.6 T and B = 0, respectively, done with the same parameters as the one at B = 8.4 T. At B = 0, the quantum dot characteristic obtained from the deconvolution (black curve) shows two large and broad peaks, which can be identified as Kondo ridges. The first one, marked by a circle and an asterisk, reaches the unitary limit [39] and accounts for what seemed to be the $2e^2/h$ "plateau" at zero field. The second one, marked by a green arrow, accounts for the $3e^2/h$ "plateau" at zero field. At B = 4.6 T, the Kondo resonance indicated by the circle and the asterisk is split and the corresponding Coulomb peaks are separated by E_z+U. The valley conductance between the splitting peaks decreases as the field increases, which overall confirms the Kondo origin of these peaks.

It is important to stress that these fits are less accurate as the number of open one-dimensional channels increases, since it becomes harder to distinguish which features belong to the dot and which belong to the 1D channel. Moreover, when the gate voltage is raised to more positive values, the dot itself can become an open dot or a 1D system as a result of the increase in charge density. The highest accuracy is obtained at the first plateau, because of the ability to trivially distinguish dot and 1D features by their magnetic evolution only in this region. If the dot retained a low coupling over all gate voltages, and the QPC had sharp plateaus elsewhere, this would not be a problem, and the deconvolution could be used over larger gate ranges with equal accuracy. The fit is also less accurate towards zero field because larger backscattering is expected, which will produce resonances in the plateaus and prevent their clear distinction from dot-related resonances. Even in these conditions, it is at least possible to distinguish accurately the threshold voltages of both QPC and quantum dot thanks to their detailed field evolution.

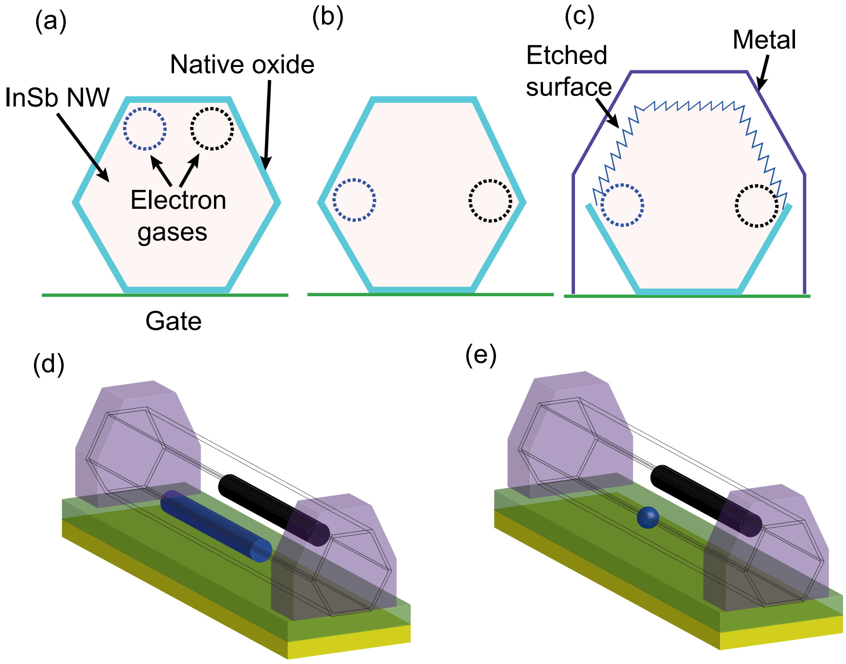

Figure 3.8: Hypothetical two 1D channels in parallel in an InSb nanowire with facets, at the **(a)** top or **(b)** middle facets (cross-sectional view), to be verified by self-consistent calculations such as those in Ref. [10]. **(c)** Cross-sectional view of the Ar$^+$-etched nanowire below the metallic leads. **(d)** 3D view of the nanowire device with two 1D electron gases (black and blue cylinders. **(e)** 1D electron gas in parallel (black cylinder) with a localized puddle of electrons (blue sphere). The quantum dot may form as a result of charges trapped in the native oxide of the nanowire.

As a final display of the power of this deconvolution technique, I also calculated the non-linear conductance with the saddle-point model (using the equations from ref. [99]) with the same parameters from the fit of the linear conductance at B = 8.4 T and T = 4 K. The calculation done for B = 8.6 T is shown in Figure 3.7**b**, while the experimental data taken at B = 8.6 T and T = 4 K is shown in Figure 3.7**a**. The deconvoluted quantum dot characteristic, obtained by subtracting the data of 3.7**a** minus the data of 3.7**b** is shown in Figure 3.7**c**. This Figure displays a series of Coulomb diamonds coming from the dot in parallel. The features get sharper towards negative gate voltages, proving that the backgate has an effect on the tunnel coupling of the dot to the leads.

Hypothetical physical platform for parallel transport

The QPC and the dot have comparable lever-arm parameters -implying that the ratio between the gate capacitive coupling and the total capacitive coupling is similar. Because of that, we can speculate that they lie in nearly-symmetric transverse positions in the nanowire, equidistant with respect to the gate. Ref. [10] demonstrated the formation of 1D edge channels symmetrically positioned on the top corners of a non-disordered Silicon nanowire with an oxide on top. Electrons in these channels could be localized into quantum dots by charges trapped in the oxide and by surface roughness. Inspired by the experimental observations presented in the current InSb nanowire device -and the one in the next section-, I propose the existence of two 1D electron gases between the oxidized facets of the nanowire as the underlying physical system that can give rise to parallel conduction in InSb nanowire devices.

This proposal, which stills needs to be verified by self-consistent calculations such as those of Ref. [10], is explained in the schemes of Figure 3.8. Schemes 3.8**a** and 3.8**b** show cross-sectional views of the faceted nanowire, with two examples of the position that corner channels -blue and black dashed circles- could assume. Given that the device shows electron accumulation -i.e., a negative gate voltage needs to be applied to push the electrons away and pinch-off the channels-, the most likely position for the channels is at the top facets. Scheme 3.8**c** shows a cross-sectional view of the nanowire below the metallic leads. The directional Ar^+ etching removes the native oxide of the nanowire only at the top, producing a rough surface that can be contacted by the metal. Hence, edge channels at the upper part of the nanowire have a better chance to be coupled to the leads. Scheme 3.8**d** shows an artist view of the two 1D electron gases in the nanowire channel -portrayed by blue and black cylinders. Scheme 3.8**d** depicts what could hypothetically happen to one of the gases when there is a charge trapped in the oxide of the nanowire, in the vicinity of the gas. In that case, the 1D corner path becomes a quantum dot, depicted as a blue sphere.

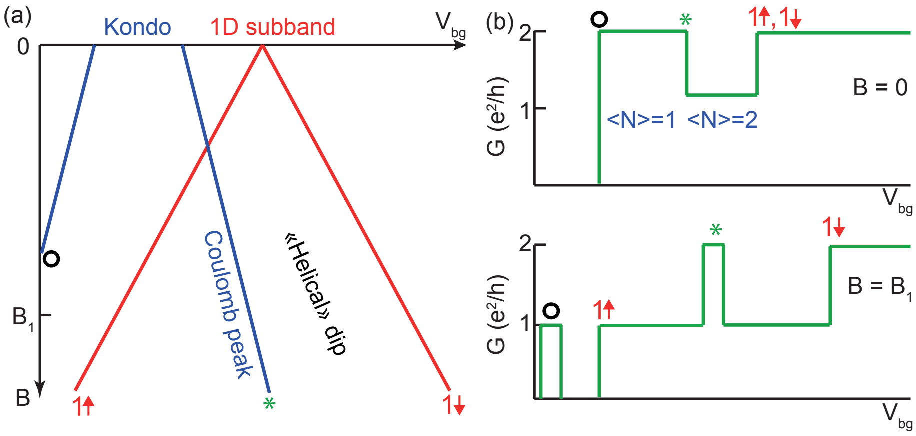

Figure 3.9: **a** Schematic magnetic field evolution of the Coulomb peaks (blue lines) of a Kondo resonance from a quantum dot and of a subband (red lines) from a 1D channel conducting in parallel. The scheme is similar to the experimental data from Figure 4.10**a**; however, for simplification, the orbital effect of the field has been omitted. The Coulomb peaks have been labeled by a circle and an asterisk as for the data, whereas the spin-resolved subband is labeled in red. **b** Qualitative differential conductance cut-lines from **a**, at B = 0 and at a large field B = B_1. At B = 0 (top panel), the $< N > = 1$ Kondo resonance can reach $2e^2/h$, and the $< N > = 2$ Coulomb valley that follows may imitate the conductance dip expected from a helical gap opened by interactions [66]. At B = B_1 (bottom panel), the Kondo resonance splits into two Coulomb peaks corresponding to the charge degeneracies 0⟶1 (circle) and 1⟶2 (asterisk). The 1⟶2 peak lays on top of the spin-resolved 1↑ subband, resembling a conductance dip from a helical gap opened by the Zeeman interaction [33].

False positives of helical states

A quantum dot conducting in parallel with a 1D channel may give false positives of helical states at zero and finite magnetic field. The feature indicated by a green asterisk in Figure 4.10, which is a Coulomb peak on top of a $1e^2/h$ plateau, resembles a Zeeman-induced helical conductance dip appearing in a $2e^2/h$ plateau above B = 4 T [33]. However, the magnetic field is oriented perpendicular -and in-plane- to the axis of the nanowire, which rules out a Rashba helical gap in this device. At B = 0, the Coulomb valley coming after the unitary-limit Kondo resonance may resemble a conductance dip coming from a helical gap produced by interactions [66]. These two possibilities are explored in the schemes of Figure 3.9.

Overall, the measurements in this section indicate that it was possible to obtain a 1D system in an InSb nanowire with our method of microfabrication. Nevertheless, the presented experiment tells us that, even in the ballistic regime, with clear evidence of conductance quantization, the possibility of coexisting quantum dot behavior remains, leaving room for possible misinterpretations of the observed transport signatures.

3.3 Two quantum wires in parallel

The device presented in the previous section was gated with a global gate. This is sufficient to form a quantum point contact (QPC) in the nanowire, but ultimately, it would be desirable to study the 1D character of the nanowire under multiple gates. The presence of multiple gates can be used to tune locally the edge of the conduction band, allowing one to form a QPC at demand at any section of the nanowire. In such a scenario one could study, for instance, the effect of the hybridization of the metal reservoirs on the properties of the nanowire subbands, by forming a QPC near one of the reservoirs and far away. One could also use one gate to form a QPC and the others to tune the size and transverse confinement of the QPC, affecting quantities like subband energy spacing and g-factor. If one additionally changes the shape of the QPC through gate manipulation, one could also hope to improve the visibility of the conductance plateaus by making the spatial change of the edge of the conduction band smoother [32].

Moreover, multiple gates may help tuning the strength of the Rashba spin-orbit interaction and the visibility of the spin-orbit gap. Looking further into the future, these studies are also a necessary background for Majorana bound states generation and manipulation, since the great majority of schemes to do this in nanowires rely on the use of local gates [3]. These questions were in my head during the last year of my PhD, and I decided to address them by measuring a nanowire with multiple gates, in which some of these basic properties could be probed.

In this section, I will present measurements performed in a device with three local bottom gates in good capacitive coupling to a relatively large InSb nanowire -of 160 nm of diameter as compared to the more typical 100 nm. These measurements were done in a Helium 3 refrigerator equipped with a one-axis superconducting coil, with a base temperature of 260 mK. A SEM image of the device is shown in Figure 3.10**a**, and a scheme in Figure 3.10**b**. In both image and scheme, the central gate of the device is labeled C, while the left and right gates are labeled L and R, respectively. The InSb nanowire was deposited with a micromanipulator on top of 10 nm of hafnium oxide. It was later contacted by 120 nm-thick Al contacts through e-beam lithography followed by metal evaporation and lift-off. For more details, see the full typical process described in Appendix A.

The lateral gates were typically swept together. In Figure 3.10**c**, for instance, V_G is the voltage of V_L, while V_R was simultaneously swept with the following linear dependence on V_L: $V_R = \alpha_{R/L}(V_L - V_{L0})$, where $V_{L0} = 0.74$ V is the value of V_L when $V_R = 0$, and $\alpha_{R/L} = 0.875$ is a sort of lever-arm between both gates. In this sense, V_G is a detuning voltage. If high enough voltages are applied in the lateral gates, a quantum point contact is formed above gate C.

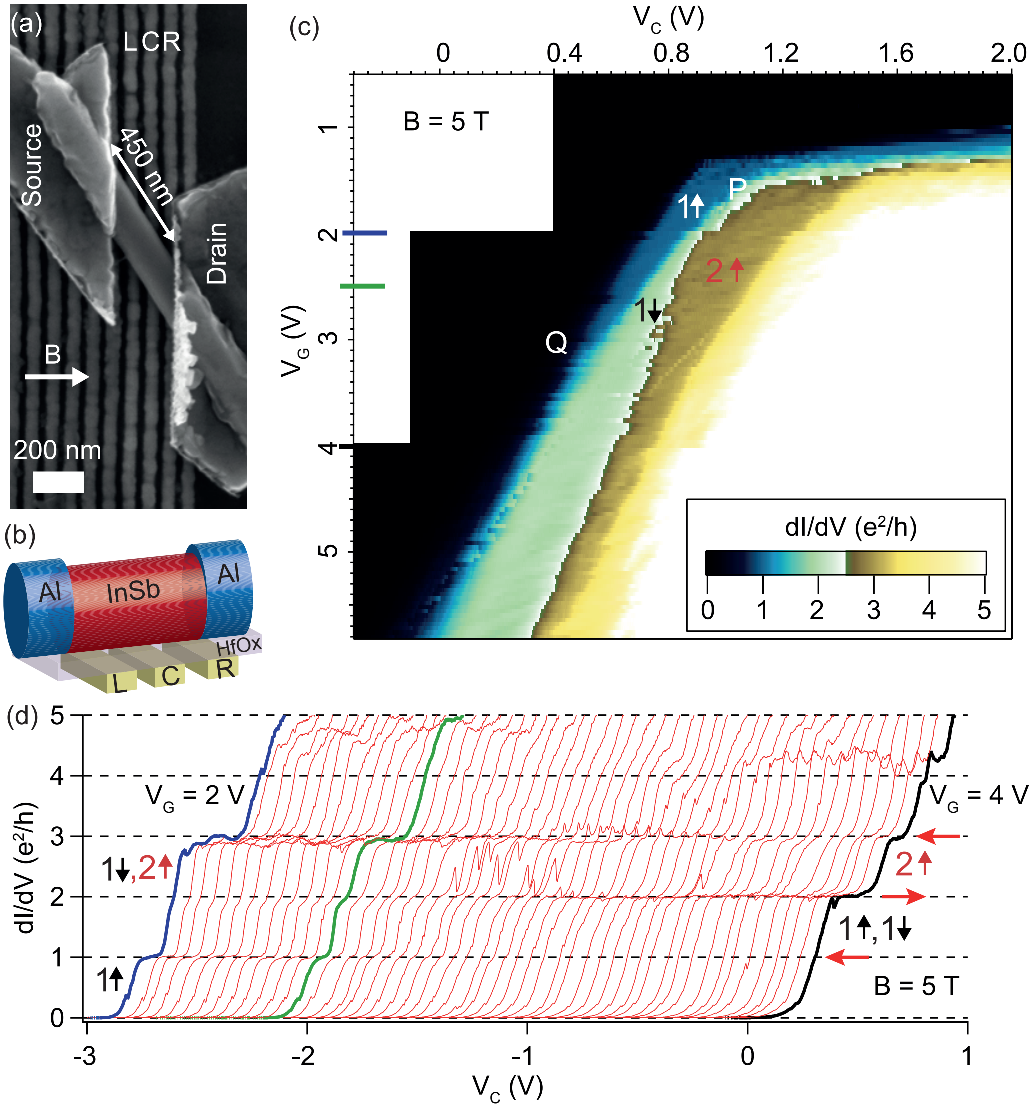

Figure 3.10: (a) SEM image of the device, taken after the measurements. The field orientation was in-plane and as indicated in the image (58 ° with respect to the axis of the nanowire). **(b)** Scheme of the device. **(c)** Conductance map as a function of the central gate and the two lateral gates -simultaneously swept-, taken at T = 260 mK. The plateaus corresponding to each subband are labeled by their orbital number *n* and their spin species -↑ or ↓. Detuning voltages P and Q denote subband degeneracy points. **(d)** Conductance cuts taken from **(c)**, for V_G between 2 V and 4 V. The blue, green, and black curves correspond to V_G = 2, 2.5 and 4 V, respectively, and show a subband degeneracy resulting in the absence of the 2 e^2/h plateau (blue); no subband degeneracy (green); and a degeneracy resulting in the absence of the 1 e^2/h plateau. Horizontal red arrows indicate the trend of expansion of the width of the plateaus. In all the measurements, a contact resistance of 1.2 kΩ was subtracted so that the conductance value of the three first plateaus stayed, respectively, at 1 e^2/h, 2 e^2/h and 3 e^2/h.

Conductance plateaus at fixed field

Figure 3.10**c** shows a conductance map obtained by sweeping the central gate C of the device while stepping simultaneously the two lateral gates L and R (as explained later). In this plot, which was taken at a magnetic field B = 5 T, we see a series of color bands -blue, green and brown- which correspond to conductance plateaus of, respectively, 1 e^2/h, 2 e^2/h and 3 e^2/h. In the region in yellow and white, the conductance goes above 3 e^2/h, while in the region in black the conductance is zero.

These plateaus behave in a curious way as the detuning voltage V_G is stepped. At the point in the conductance map labeled by the letter P, the plateau 2 e^2/h has vanished. The conductance jumps directly from 1 e^2/h to 3 e^2/h. In a similarly striking way, at point Q -at larger V_G-, the plateau 1 e^2/h has entirely disappeared, engulfed by the 2 e^2/h plateau. For a V_G more positive than point Q, the conductance jumps from zero directly to 2 e^2/h, and the 3 e^2/h plateau becomes less and less visible. Finally, for a V_G in between points P and Q, the three plateaus 1 e^2/h, 2 e^2/h and 3 e^2/h are visible.

The above described behavior of the plateaus can also be seen in the horizontal cuts shown in Figure 3.10**d**, which were taken from the map of Figure 3.10**c** at voltages V_G = 2 V to V_G = 4 V. In particular, the blue curve, taken at V_G =2 V, which is a slightly larger detuning voltage than point P, has a nearly-absent 2 e^2/h plateau. In the green curve, taken at V_G = 2.5 V, which is a detuning voltage situated between points P and Q, the 2 e^2/h plateau has developed and the three first spin-resolved plateaus are therefore visible. Finally, the black curve, taken at V_G = 4 V, which is a detuning voltage larger than point Q, has an absent 1 e^2/h plateau. The conductance progresses smoothly between these three cases (red curves).

This intriguing data brings a few questions to the table. In particular, how is it possible that at B = 5 T the 1 e^2/h plateau can be tuned out-of-existence by just applying voltages on lateral gates? In nanowires with a g-factor of the order of 50, this observation is particularly puzzling, since the associated Zeeman energy would be ~14.5 meV, which would be equivalent to 0.36 V in gate voltage V_C (when using the lever-arm of this gate). Somehow, it appears that lateral gate voltages above point Q suppressed the Zeeman-splitting of the first subband. Does this involve the subbands of *one* or the subbands of two or *more* conduction paths? Are the subband energy spacing, g-factor or orbital effect changing with the detuning voltage?

In Figure 3.10**c**, I put a label in each of the plateaus according to the orbital number *n* of the corresponding subband and its spin projection on the magnetic field axis, which is either ↑ or ↓. This helps to keep track of how the subbands become degenerate, if it is possible to interpret the data as the result of transport through a *single* 1D channel. For instance, the plateau 1 e^2/h is labeled by 1 ↑, indicating that the edge of the first spin-split subband is within the chemical potential of the leads. This labeling is based on the field dependence of the plateaus, which will

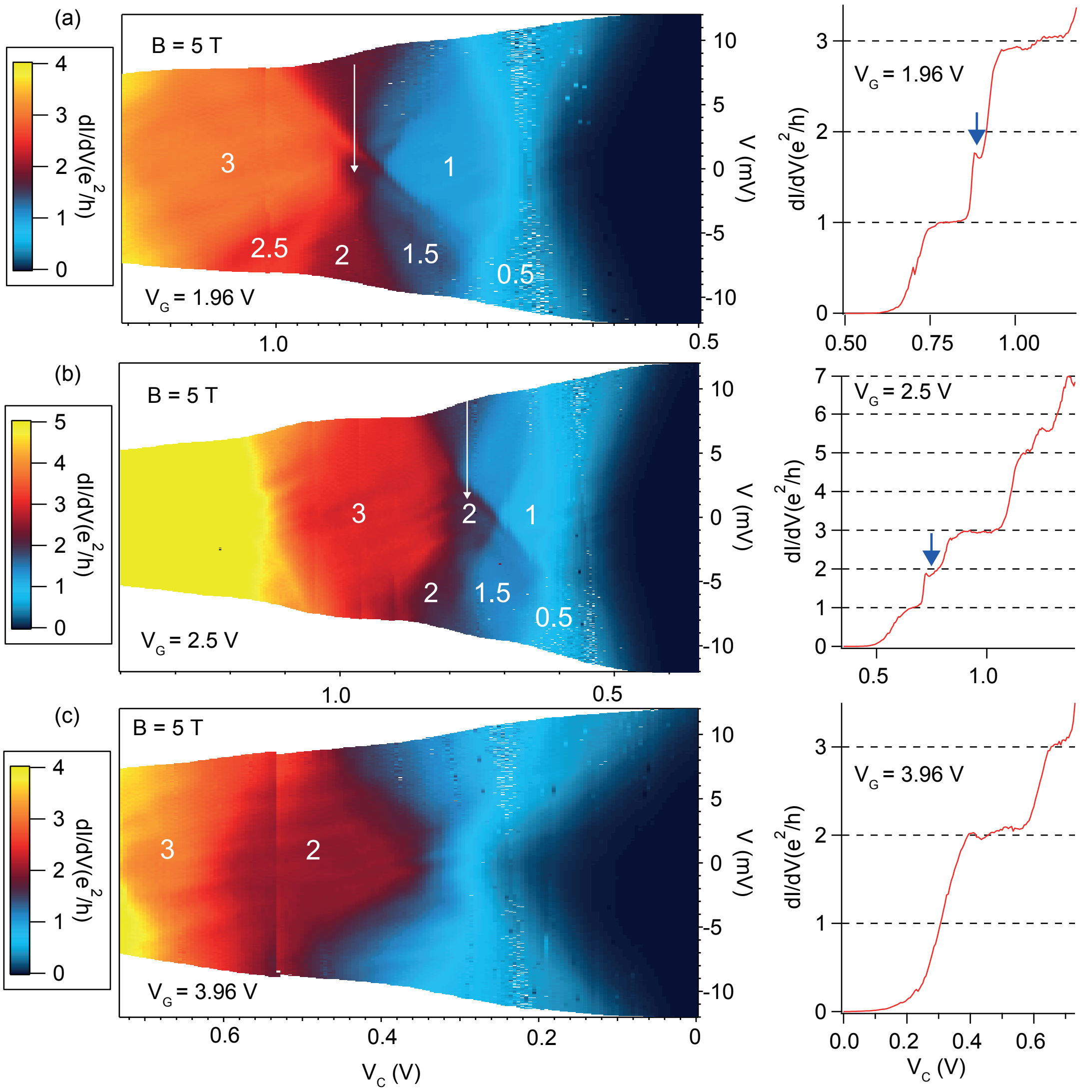

Figure 3.11: Non-linear conductance maps (left panels) at B = 5 T, as function of bias voltage and central gate voltage V_C for three representative values of V_G: **(a)** 1.96 V, **(b)** 2.5 V and **(c)** 3.96 V, accompanied by zero-bias cuts (right pannels). Plateaus -at zero bias- and half-plateaus -at high bias- are identified by their conductance in multiples or fractions of 1 e^2/h. As elsewhere in this section, a contact resistance of 1.2 kΩ was subtracted from the measured conductance.

be shown later.

The 1D character of the subbands of Figure 3.10**c** can be verified through the measurement of their non-linear differential conductance. Figure 3.11 contains maps of conductance (left panels) at B = 5 T as a function of bias voltage V and the central gate voltage V_C, for three representative values of V_G: 1.96 V, 2.5 V and 3.96 V, which correspond roughly to the blue, green, and black curves in Figure 3.10**d**. This Figure also shows zero-bias cuts through these maps in the right

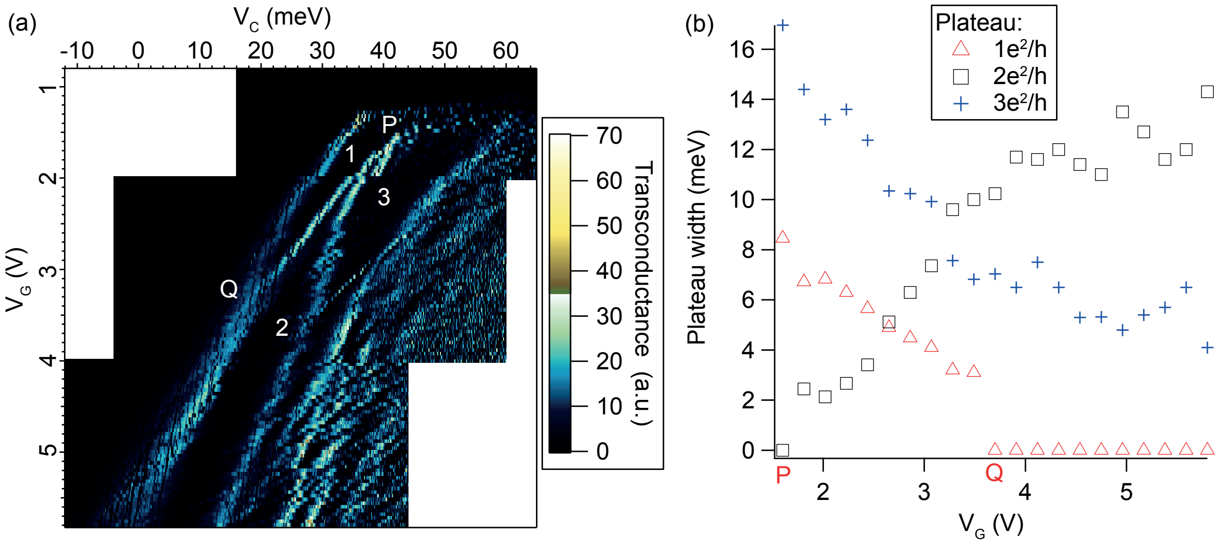

Figure 3.12: **(a)** Transconductance map vs. central gate energy V_C and detuning voltage V_G. The transconductance was obtained by the deriving the dI/dV data of the map in Figure 3.10**c** with respect to V_C. The V_C voltage was converted to energy by using the lever-arm of this gate, α_C=0.04. **(b)** Energy width of the first three plateaus as a function of V_G, from V_G = 1.6 V (~ P point) to 5.8 V. The P and Q points are marked in both plots. The width of a plateau is considered zero when the two transconductance peaks that define it cannot be individually resolved.

panels.

The expected diamond-shaped signature with a quantized conductance in multiples of 1 e^2/h inside of each diamond is observed in all the three cases. However, some plateaus are missing. In Figure 3.11**a**, when V_G = 1.96 V, the diamond corresponding to the 2 e^2/h plateau has almost vanished. Moreover, instead of a flat 2 e^2/h, there is *dip* (white arrow on the left pannel, blue arrow on the right one) at zero-bias that decreases the conductance from the quantized value. However, the expected half plateaus 1.5 e^2/h, 2 e^2/h and 2.5 e^2/h at high-bias are all seen, which means that the subband that generates the 2 e^2/h plateau is non-fully degenerate with another subband. The degeneracy point is at a lower V_G, when V_G = P and the 2 e^2/h plateau fully vanishes.

This is to be contrasted with the V_G = 2.5 V case (Figure 3.11**b**, where the diamond corresponding to the 2 e^2/h plateau (1 ↓) is clearly developed. Half-plateaus at 1.5 e^2/h and 2 e^2/h are also seen. There is still, however, a small dip in the zero-bias conductance of this plateau, which is pointed by a blue arrow in the cut shown in the right pannel. The origin of this kind of dip, which occurs at the onset of the 2 e^2/h plateau at a large enough magnetic field, will be discussed further below.

The other extreme occurs at V_G = 3.96V (Figure 3.11**c**), where the diamond corresponding to the 1 e^2/h plateau has vanished, indicating a degeneracy of both spin species of the first spin-split subband -within a single 1D channel picture. The first plateau is instead 2 e^2/h, which is unexpected at B = 5 T. At large bias, only the 1.0 e^2/h plateau is seen, which is a half-plateau corresponding to the 2 e^2/h plateau at zero bias. The absence of clear 0.5 e^2/h and 1.5 e^2/h plateaus at large bias is consistent with the absence of the 1.0 e^2/h plateau at zero bias.

From the maps in 3.11 we can also extract the lever arm of the gate V_C, which is α_C=0.04 in the three cases. This allows converting the gate voltage V_C into energy and extract the width of the plateaus, providing a measurement of the subband spacing. To obtain these values, I numerically derived the dI/dV data from Figure 3.10**c** with respect to V_C and obtained the transconductance map of Figure 3.12**a**. The x-axis of this map is the central gate voltage V_C converted into energy. In this plot, the plateaus are indicated by their conductance in multiples of 1 e^2/h. P and Q are also marked. Every time the conductance raises to reach a new plateau there will be a corresponding peak in transconductance, which gives a direct measurement of the width of the plateaus.

The width of the plateaus as a function of the detuning voltage V_G is given in Figure 3.12**b**. The width of the 1 e^2/h and 3 e^2/h plateaus decreases with increasing V_G, while the opposite happens to the 2 e^2/h plateau. In the points P and Q, the width of the 2 e^2/h and 3 e^2/h plateaus is, respectively, zero. This occurs because I took the convention to attribute a zero value to the width of the plateau whenever the two peaks of transconductance that define it cannot longer be individually resolved. This is good enough for point P as the merged transconductance peak -from the disappearance of the the 2 e^2/h plateau- is small; however, for $V_G >$ Q the width of the merged peak is large. Part of the broadening comes from charge switches in the hafnium oxide or in the nanowire native oxide. The width of the 1 e^2/h may thus not be strictly zero beyond the Q point, but it is certainly below 4 meV (which is much lower than the Zeeman splitting of 14.5 meV expected if $|g| = 50$).

This data shows that an enormous degree of tuning of the subband spacings can be obtained by varying the detuning voltage V_G at B = 5 T. In a single-subband picture, if we attribute to each of the first three plateaus the quantum numbers $1\uparrow$, $1\downarrow$ and $2\uparrow$, as it was done before, then it is possible to identify the width of the 1 e^2/h plateau with the Zeeman splitting of the first subband (E_{z1}), and the width of the 3 e^2/h plateau with the Zeeman splitting of the second subband (E_{z2}). The g-factor of the first subband would be $|g_1| = 28$ at point P, and it would decrease down to $|g_1| < 13$ near point Q. Similarly, at point P, the g-factor of the second subband would be $|g_2| = 56$, and it would reduce down to $|g_2| < 14$ at $V_G = 5.8$ V. There is no precedent for such a giant g-factor tunability of nanowire subbands; however, there is in nanowire quantum dots. In an InSb nanowire quantum dot, *level-to-level* variations of 20 to 70 were observed [63]. In an InAs nanowire quantum dot, gate-tuning could increase the g-factor by a factor of 2 in the *same* state [62].

In fact, the g-factor of the second subband should be slightly smaller than the first one according to previous simulations [22]. In our case, it is twice as big. The single 1D channel interpretation is thus making little sense so far.

Magnetic evolution of the plateaus

The last piece of the puzzle lays in the magnetic field dependence of the conductance plateaus. The measurement can be displayed in two complementary ways. One way is to take conductance maps as a function of V_C and V_G such as the one in Figure 3.10**c**, but for B ≠ 5 T. The other is to show the magnetic field dependence of the linear conductance as a function of V_C at fixed V_G.

The first type of measurement is shown in Figure 3.13, at four different magnetic fields. In these plots (left panels), the degeneracy point Q moves smoothly towards higher V_G as the degeneracy of the first subband is lifted at an ever larger field for an ever higher V_G (compare the maps at B = 3 T, 5 T and 6.5 T). At B = 8 T, the 1 e^2/h plateau is visible in the whole conductance map of Figure 3.13**c**, as a result of the lifting of the degeneracy of the first subband over all the V_G range shown. In Figures 3.13**e,f,g**, cut-lines before (blue curves) and after (green curves) point Q are shown. Note the absence of the 1 e^2/h plateau in all the green curves when B = 3.5 T → 6.5 T.

The second type of measurement is shown in Figure 3.14 for the three fixed values of V_G that were also used in Figure 3.11: V_G = 1.96 V, 2.5 V and 3.96 V. These plots tell us three important things.

First, that there is a radical change in the extended degeneracy of the subbands as a function of V_G. At V_G = 1.96 V, the first and second subbands Zeeman-split at low field. At V_G = 2.5 V, the Zeeman splitting of the first subband starts to be observable at B = 2 T (point Q), while the second subband splits at low field. Finally, at V_G = 3.96 V the first subband stays degenerate up to 6 T (the point Q has shifted to a larger field for a larger V_G), while the second subband just Zeeman-splits at 2 T.

Second, that at B = 0.1 T (which is a field high enough to suppress the superconductivity of the Al contacts) the plateaus are plagued by resonances, making them difficult to identify. These resonances vanish at large field, which points to a backscattering origin [20] washed out by edge states emerging with the field. Because of this issue, the subband spacing ΔE near zero field cannot be calculated from the width of the plateaus. Instead, it can be extracted by taking the energy difference between the green-dashed lines in Figure 3.14 (upper pannels) at B = 0.1 T, by recognizing that only plateaus and not the resonances Zeeman-split. Using this method, ΔE = 6.4 meV at V_G = 1.96 V, ΔE = 8.4 meV at V_G = 2.5 V and ΔE = 6.4 meV at V_G = 3.96 V.

The third observation is that the orbital effect of the magnetic field is rather large and changes dramatically with V_G. Furthermore, it appears to depend not only on the subband n but also on the spin species. It could be postulated that the different V_C voltages at which each subband is seen contribute in deforming differently their wavefunctions, but this explanation falls down when we are dealing with spin-degenerate subbands, which are affected by the same V_C. Even in this case, it could be speculated that V_C acts differently on wavefunctions of different spin belonging to the same subband, but there is no elemental reason to support this.

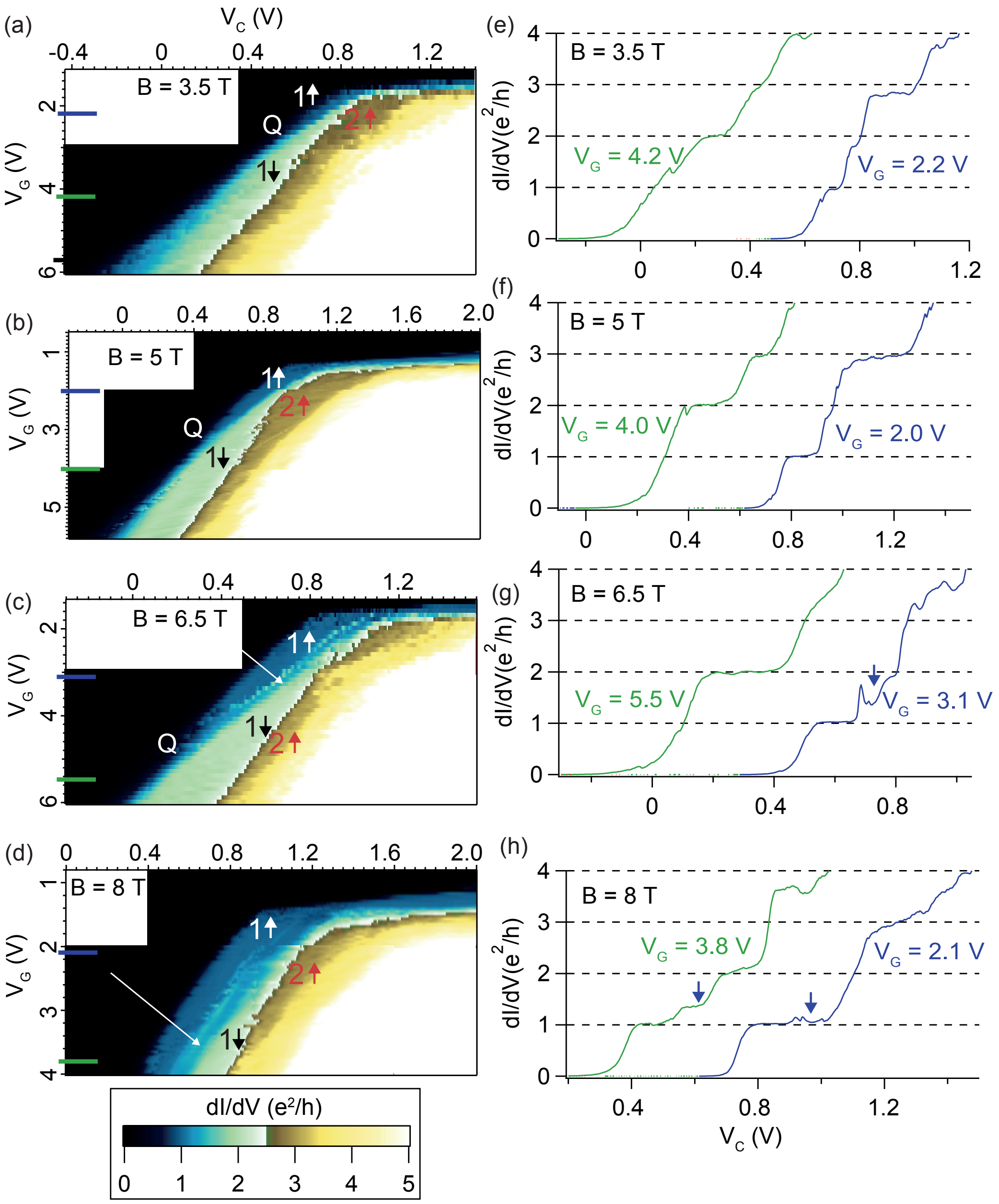

Figure 3.13: Linear conductance maps as a function of the central gate voltage V_C and the detuning voltage V_G similar to Figure 3.10**c**, taken at B = **(a)** 3.5 T, **(b)** 5 T (same as Figure 3.10**c**), **(c)** 6.5 T and **(d)** 8 T, sided with corresponding cuts at V_G < Q (blue curves) and V_G > Q (green curves) **(e-h)**. The first three plateaus were attributed the same quantum numbers 1 ↑, 1 ↓ and 2 ↑ as before. Notice that the gate range V_G is smaller in panel **(d)**. In the maps (left panels), point Q has the same meaning as in Figure 3.10**c**: it is the gate voltage V_G at which the 1 e^2/h plateau vanishes. Point Q shifts towards larger V_G as the field is increased.

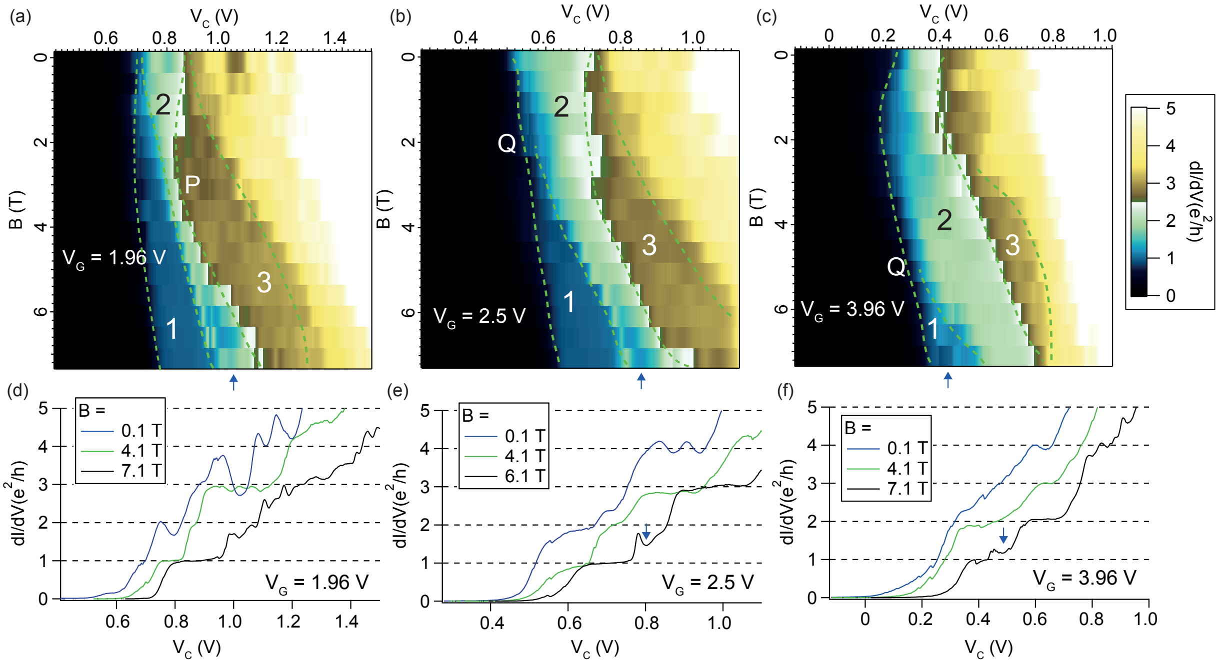

Figure 3.14: Maps of magnetic field dependence of the linear differential conductance as a function of V_C for three values of V_G: **(a)** 1.96 V, **(b)** 2.5 V and **(c)** 3.96 V and corresponding cut-lines at selected values of field **(d-f)**. Plateaus corresponding to each subband are labeled by their conductance in units of 1 e^2/h. A green-dashed line was added as a guide to the eye to follow their field dependence. In the maps, point P denotes the field at which a crossing of two spin-resolved subbands with a different orbital number suppresses the 2 e^2/h plateau. Point Q denotes the field *below* which the first subband retains its spin-degeneracy, resulting in the suppression of the 1 e^2/h plateau. These points give raise to the gate voltage points P and Q in Figure 3.10**c**.

On a side note, the orbital effect of the field pushes the subbands towards higher energy, as predicted by the simulations of Ref. [22]. The orbital effect could be responsible for bringing the $1\downarrow$ and $2\uparrow$ subbands together at the degeneracy point P, but it cannot explain by itself the spin degeneracy of the first subband in a single 1D channel interpretation.

Figure 3.15 summarizes the mechanisms leading to the subband degeneracies observed, in a single channel interpretation. This Figure shows schemes of the bottom edge of the subbands drawn from the magnetic evolution of the plateaus in Figure 3.14 (upper panels), or extrapolated from the data at B = 3.5 T, 5 T, 6.5 T and 8 T on the maps of Figure 3.13 (left panels). The P degeneracy occurs when the subbands $1\downarrow$ and $2\uparrow$ overlap at low V_G (panel 3.15**a**), erasing the 2 e^2/h plateau from the conductance. This degeneracy is lifted at larger V_G (panels 3.15**b-e**) due to a larger subband spacing ΔE and/or the orbital effect of the field on the subbands. As the degeneracy is lifted by raising V_G, the 2 e^2/h plateau appears and widens in the conductance data, and the 1 e^2/h and 3 e^2/h plateaus shrink. This is shown in the conductance maps of Figures 3.10**c** and 3.13. In panels 3.15**d,e**, the crossing of the $2\downarrow$ and the $3\uparrow$ subbands is used to explain

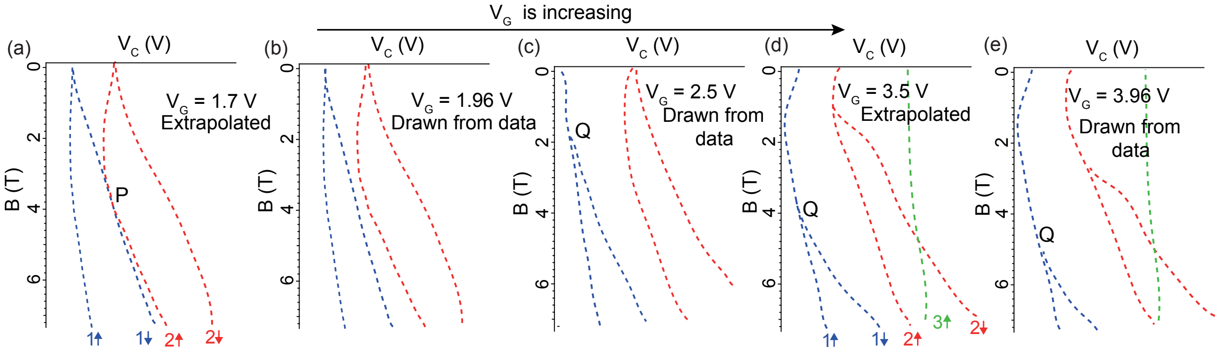

Figure 3.15: Evolution of the magnetic field dependence of the bottom edge of the subbands (colored dashed lines) with the lateral gate voltage V_G. The first subband is in blue, the second in red and the third in green; arrows denote the spin projection. The subbands in **(b)**, **(c)** and **(e)** were directly drawn from the data in Figure 3.14 (upper panels). The subbands in **(a)** and **(d)** were extrapolated from the data at B = 3.5 T, 5 T, 6.5 T and 8 T on the maps of Figure 3.13 (left panels) and 3.10**c**.

the strange kink seen in the field evolution of the 3 e^2/h plateau in Figure 3.14**c** (upper panel) at B > 4 T.

The Q degeneracy, on the other hand, may arise from a reduction of the g-factor of the first subband by magnetic confinement. In Ref. [100], it was theoretically discussed that a reduction of the size of InAs quantum dots below the magnetic length ($L_m = \sqrt{\hbar/eB}$) would quench the orbital angular momentum, leading to a strong decrease of the g-factor. The g-factor dropped from the bulk value of -15 for very large dots to zero for intermediate-sized dots, and tended towards 2 when the size of the dot was very small. In the present case of an InSb nanowire QPC, it can be speculated that the g-factor changes with the size of the constriction in the direction out of the plane of the substrate -which can be tuned by V_G-, given that the field has a component perpendicular to the nanowire and in the plane of the substrate which can lead to cyclotron motion in the plane perpendicular to the substrate.

Within this picture, we can think of the QPC constraining a 1D gas of electrons of size L at the top of the nanowire. When V_G is large (above point Q) then L < L_m, which quenches the g-factor of the first 1D subband to a value effectively close to zero, and prevents the observation of a 1 e^2/h plateau. This concept is illustrated in Figure 3.16. At large magnetic field, L_m becomes smaller than L and the g-factor attains a larger value, leading to the emergence of the 1 e^2/h plateau. The panels 3.15**c-e** show how point Q can be pushed towards a larger magnetic field by increasing the gate voltage V_G. In fact, point Q can be tuned from B = 0 T (at V_G < 2 V) to B = 6.5 T (at V_G = 5.2 V). The larger g-factor of the second subband is explained by the smaller confinement of this subband, which ensures L > L_m up to a larger V_G than the first subband.

There is no precedent for gate tuning of the magnetic field at which the extended degeneracy is broken (i.e., point Q). However, extended degeneracy has been observed before in InSb nanowires

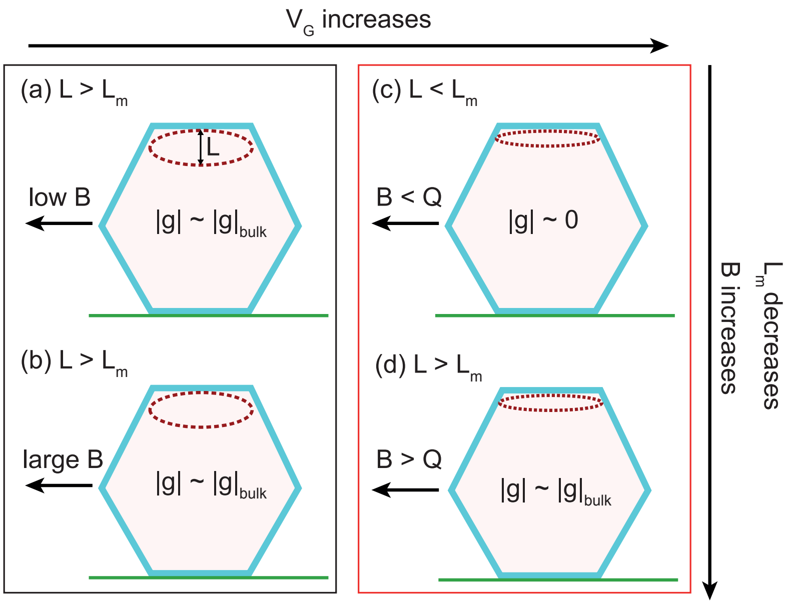

Figure 3.16: Sectional schematic views of the InSb nanowire, explaining the quenching of the g-factor at large V_G. The 1D electron gas is drawn in the top part as a red-dashed ellipse, with its size L indicated in panel **(a)**. The magnetic field direction is indicated by a black arrow in each of the four panels. **(a,b)** At low V_G, L > L_m independently of the magnitude of the field, and the g-factor tends to the bulk value. **(c,d)** At large V_G, the g-factor is negligible when **(c)** L < L_m at low field -i.e., at a field below point Q-, but tends to the bulk value at large field, when **(d)** L > L_m.

from the same growers up to large magnetic fields [19]. In that work, the first subband showed an extended degeneracy up to B = 0.6 - 0.7 T for a magnetic field applied parallel or perpendicular to the nanowire. The second subband, on the other hand, was degenerate with the third one at zero field. At finite field, they observed an extended degeneracy of the spin-resolved 2 ↑ and 3 ↑ subbands that was lifted at B = 3 T for a field oriented perpendicular to the nanowire and in the substrate plane. However, the 2 ↓ and 3 ↓ subbands kept their degeneracy until the largest field that they measured (B = 4 T). Interestingly, their simulations of the band dispersion of bare InSb nanowires (100 nm diameter) did not predict any of these degeneracies either at zero field or in parallel or perpendicular field [19].

Other simulations of bare InSb nanowires (100 nm diameter) managed to reproduce the degeneracy between the second and third subbands at zero field. These simulations, however, did not predict an extended degeneracy of the first subband or of the 2 ↓, 3 ↓ and of the 2 ↑, 3 ↑ subbands. Therefore, it seems that bare nanowire simulations may not be enough to grasp all the physics involving the orbital effect in real InSb nanowire devices. The discrepancy could be further aggravated in many-gate devices such as the one discussed in this section. In these devices, the electric fields produced by the gates may distort the transverse wavefunction along the axis of the nanowire, complicating the agreement with calculations that do not take this effect into account.

If this interpretation is correct, the implications for experiments targeting the observation of Majorana bound states will be profound. In these experiments, a zero-bias peak emerging with magnetic field within the superconducting gap is taken as the main evidence of their existence [1]. The absence of splitting of the zero-bias peak is used to rule out [2][83] a more trivial explanation based on a quantum phase transition experienced by quantum dot-related Andreev bound states [12]. The quenching of the g-factor at low fields proposed here may explain this absence of splitting.

Alternative explanation for subband degeneracy: Conductance through two parallel 1D channels

There is another way of explaining the subband degeneracy seen in the data presented before. This new interpretation can easily explain the remarkable absence of a 1 e^2/h plateau at Zeeman energies as enormous as $\sim$ 19 meV (for B = 6.5 T and $|g| = 50$). This alternative hypothesis does not rely on a size-dependent g-factor to explain the absence of Zeeman-splitting in the first subband of a single 1D channel -as the previous hypothesis did. Instead, conduction through two *parallel* 1D channels is assumed (depicted artistically in Figures 3.17**b,c**), along a similar reasoning as for the previous section.

Figure 3.17**a** shows the 2D map at B = 5 T previously shown in Figure 3.10**c**, under this new interpretation. The orange (purple) dashed lines indicate the limits of the first spin-resolved subband (i.e. the 1 e^2/h plateau) of the first (second) 1D channel. The g-factors (|g|) of the first subband corresponding to the first 1D channel (which is gate-dependent and increasing according to the orange arrow) and the second 1D channel (which is nearly constant) are also indicated, with a superscript (1) or (2) to identify the channel to which they belong to. In the case of the first subband of channel 1, $|g^{(1)}|$ goes from 29 (at $V_G = 2$ V) to 45 (at $V_G = 4$ V) in a smooth way. In the case of channel 2, $|g^{(2)}| = 55$ from $V_G = 2$ V to 3.2 V, but it increases slightly to $|g^{(2)}| = 57$ at $V_G = 4$ V.

The subbands are brought together at point P ($V_G \sim 2$ V) and beyond point Q ($V_G > 3$ V), and do not move apart at lower or larger Zeeman energy (from 3.5 T to at least 6.5 T; see the maps in Figure 3.13) thanks to a level-locking mechanism [101]. This mechanism, shown schematically in Figure 3.10**d**, locks together the subbands of the two different channels when they approach in energy. The subbands may approach because of their different g-factors, different orbital effects and different subband spacing, with the first two factors being magnetic field-dependent. Under this mechanism, the 1 e^2/h plateau appears at large magnetic field whenever the subband spacing between the 1↑ subbands of the two channels is larger than the Coulomb potential that generates from the charge imbalance in their respective Van-Hove singularities.

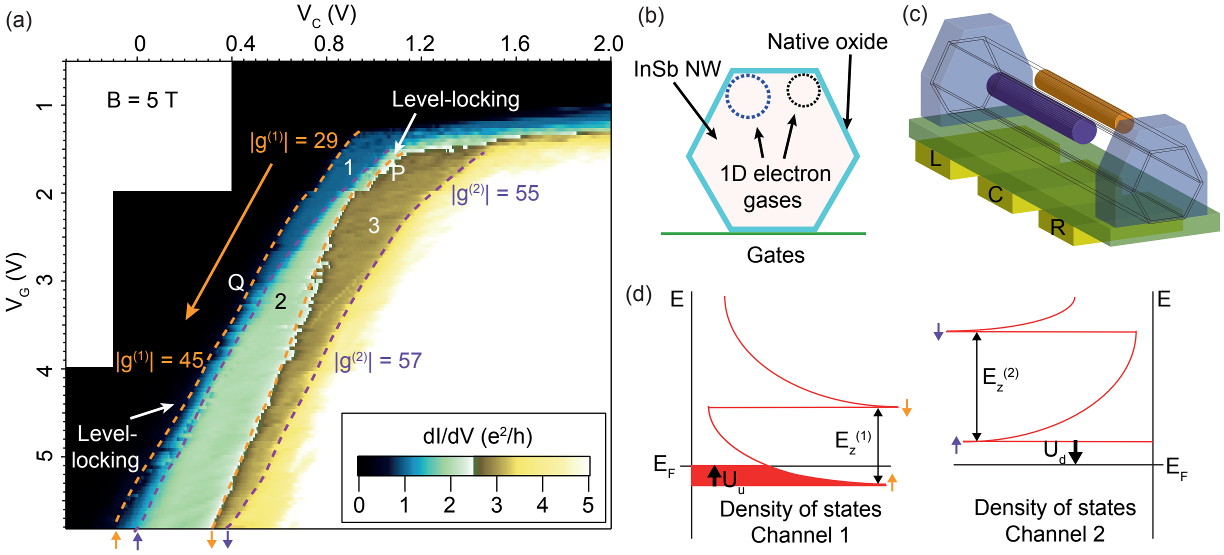

Figure 3.17: **(a)** Variation of Figure 3.10**c** under a two-parallel channel interpretation. The conductance of each plateau is indicated in units of 1 e^2/h. The orange and purple dashed-lines delimit the 1 e^2/h plateau of each of the 1D channels conducting in parallel. Channel 2 has a significantly larger g-factor than channel 1, but its nearly V_G independent, in contrast to the g-factor of channel 1 which varies significantly with V_G. Spin-projections of the first spin-resolved subband of each channel are indicated by ↑ or ↓ in orange or purple. When the subbands of the different channels approach, they stay level-locked, as indicated by a white arrow (see Ref. [101]). **(b)** Schematic sectional view of the InSb nanowire hosting two 1D channels of similar transverse confinement. The transverse size of the 1D channels, extracted from the subband spacing and assuming the potential energy of an harmonic quantum oscillator is $2x_0 \sim 25$ nm. The validity of this model is being investigated through theoretical simulations. **(c)** 3D artistic impression of the two 1D electron gases in the channel of the device. **(d)** Mechanism of level-locking. A charge imbalance produced when the Van-Hove singularity in the density of states of channel 1 begins to fill generates an electric potential U_u that pushes the spin ↑ subband up, while a similar potential U_d pushes the spin ↑ subband of channel 2 down. This reduces the energy spacing between the subbands of the two different channels by a large factor, and even can lock them together [101].

Figure 3.18 shows cut-lines taken from the map in Figure 3.17**a** at four different V_G voltages (red curves): V_G = **(a)** 2 V, **(b)** 2.5 V, **(c)** 3.2 V and **(d)** 3.96 V. These curves were fitted with the saddle point model (using the equations from ref. [99] at V = 0) to deconvolute the conductance of channel 1 (orange curves) from channel 2 (purple curves). This was done in order to evaluate the parameters of the subbands of each of the two channels independently. The parameters extracted in this way are shown in the Figure 3.18 and its caption.

Under this interpretation, the zero-field level spacing that we found previously in Section 3.3 (ΔE = 6.4 meV at V_G = 1.96 V, ΔE = 8.4 meV at V_G = 2.5 V and ΔE = 6.4 meV at V_G = 3.96 V) is re-interpreted as the difference in threshold voltage between the two QPCs: $V_{th}^{(1)}$ - $V_{th}^{(2)}$. At large magnetic field, this value is altered by the different orbital effect that acts on each 1D channel,

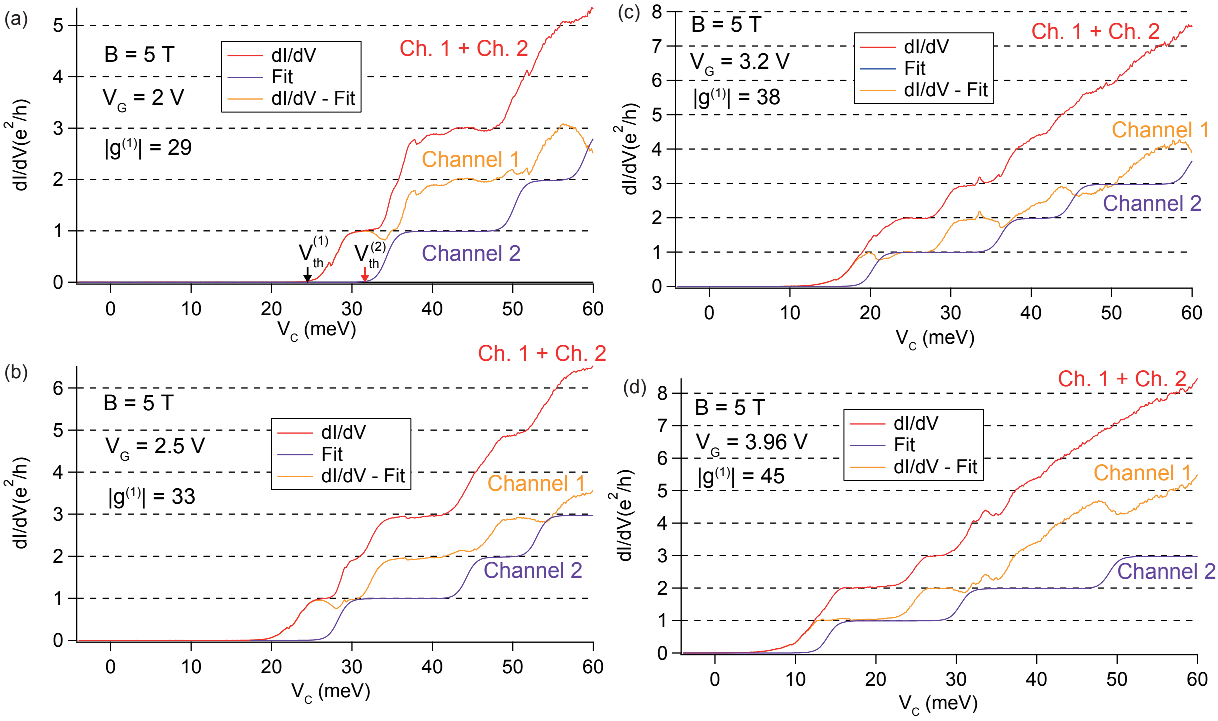

Figure 3.18: Experimental dI/dV data at B = 5 T (red curves) fitted by the saddle point model (purple curves), and subtraction of the first minus the second (orange curves), at V_G = **(a)** 2 V, **(b)** 2.5 V, **(c)** 3.2 V and **(d)** 3.96 V. Under a two-channel interpretation, the black curves correspond to channel 1 and the blue curves to channel 2. The fit was chosen to obtain the best first and second plateaus in the black curves. In all fitted curves, ω_x = 4, ω_y = 0.5, $|g^{(2)}|$ = 55 (of the first subband, except for V_G = 3.96 where it is 57), $|g^{(2)}|$ = 50 (of the second subband), and the spacing between the first and second subbands is $\Delta E^{(2)}$ = 24 meV (which is altered from the zero-field value by the orbital effect). The g-factor of the first subband of channel 1 ($|g^{(1)}|$) is indicated in the plots. The subband spacing between the first and the second subbands of channel 1, also altered by the orbital effect with respect to the zero-field value, is $\Delta E^{(1)} \sim$ 22 meV. This latter value was estimated from a fit to the saddle point model to the channel 1 curve shown in Figure 3.18**(c)**, with ω_x = 6 and ω_y = 0.5. The g-factors thus obtained were $|g^{(1)}|$ = 33 for the first subband and $|g^{(1)}|$ = 30 for the second subband. The difference between the threshold voltages of both subbands ($V_{th}^{(1)}$ - $V_{th}^{(2)}$) is tuned from ~ 7 meV at V_G = 2 V to ~ 4 - 5 meV at V_G = 3.96 V. Notice that the gate scale is the same in the four plots and that it has been transformed into energy by using the lever-arm α_C.

depending on the details of their wavefunctions. At B = 5 T, $V_{th}^{(1)}$ - $V_{th}^{(2)}$ was tuned from ~ 7 meV at V_G = 2 V to ~ 4 - 5 meV at V_G = 3.96 V. These values have slightly changed with respect to the zero-field value, indicating that the orbital effect of the field is not the same in both channels. Level-locking could also be responsible for this.

The transverse size of the two 1D channels can be extracted from the subband spacing ΔE of each subband, which is $\Delta E^{(1)} \sim$ 22 meV for channel 1 and $\Delta E^{(2)}$ = 24 meV for channel 2 at B = 5 T, provided that the orbital effect of the field acting on the subbands 1 and 2 of each channel is

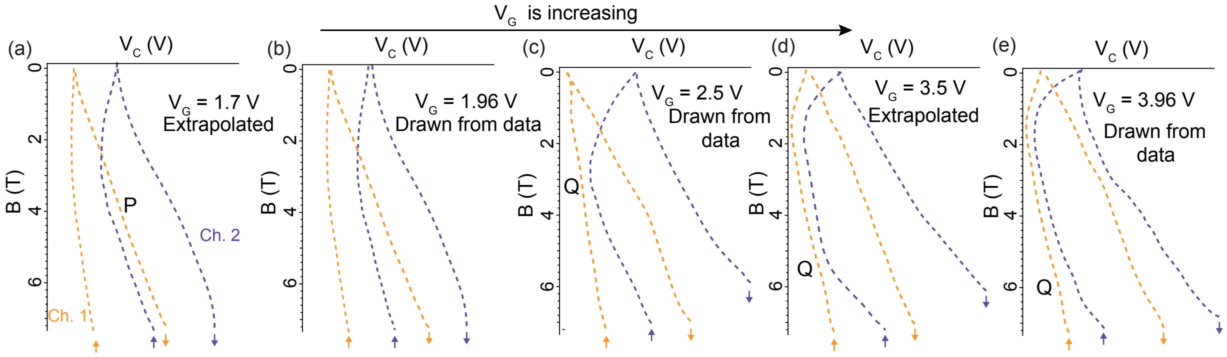

Figure 3.19: Variation of Figure 3.15 under the two-channel interpretation. The first spin-resolved subband of each of the 1D parallel channels (orange dashed-line for channel 1, purple-dashed line for channel 2) has been drawn from the data of Figure 3.14 or extrapolated from the data of Figures 3.10**c** and 3.13, as indicated in each panel. The extended degeneracy that was observed (broken for a field above point Q), which resulted in an absent plateau 1 e^2/h, is explained under this new optics as a result the level-locking of the threshold voltages $V_{th}^{(1)}$ and $V_{th}^{(2)}$ of the spin ↑ subband of each channel. The degeneracy at point P, on the other hand, which resulted in an absent 2 e^2/h plateau, is explained as a result of the level-locking of the spin ↓ subband of channel 1 and the spin ↑ subband of channel 2. Notice that the g-factor stays constant at all fields; the level-locking only adjusts the threshold voltages of the spin-resolved subbands but does not alter their Zeeman splitting.

the same. It is noted that $\Delta E^{(2)}$ does not change at different values of V_G in the four fits of Figure 3.18. If the potential of a quantum harmonic oscillator is assumed for the transverse confinement, then the size of each of the 1D channels is $2x_0 = \hbar/\sqrt{m^*E} \sim 25$ nm. This is significantly below the diameter of the nanowire (160 nm) and the size of a facet (80 nm). The spacing between the two 1D gases would be of the order of 60 nm even if they laid on the corners of the same facet, which is significant to establish an opaque tunnel barrier between both gases if the nanowire is depleted in between. A requirement for the level-locking mechanism is the absence of tunneling between the two 1D gases [101]. However, the orbital effect is not expected to be identical in the two subbands. It could significantly distort the subband spacing with respect to the zero magnetic field value if it is not.

A more accurate way to determine the subband spacing would be to measure the plateaus at zero field. Unfortunately, the linear conductance characteristic at zero magnetic field had too many resonances to accurately distinguish between those of channel 1 and those of channel 2, as discussed before. These resonances vanished when the magnetic length fell behind the size of each channel at roughly $B \gtrsim 3$ T. Due to this issue, the subband spacing of each of the two channels could not be measured at zero field.

It is expected that the g-factors slightly decrease as the subband number increases [22]. This trend is seen in the data. For example, at $V_G = 2.5$ V, the g-factors obtained for channel 1 were $|g^{(1)}| = 33$ for the first subband and $|g^{(1)}| = 30$ for the second subband. They were in turn $|g^{(2)}| =$

55 for the first subband and $|g^{(2)}| = 50$ for the second subband of channel 2. These values are of the right order of magnitude for InSb nanowires.

The magnetic field evolution of the plateaus shown in Figures 3.14 can be readily interpreted in terms of the two parallel channels. Figure 3.19 is a variation of Figure 3.15 following the two-channel hypothesis. The absence of the 1 e^2/h plateau over large spans of magnetic field (see, for instance, Figure 3.14**c**) at large V_G is conveniently explained by the level-locking of the first spin-up subbands of both parallel channels. Similarly, the absence of the 2 e^2/h plateau at $V_G \sim 2$ V is explained by the level-locking of the spin ↓ subband of channel 1 and the spin ↑ subband of channel 2. The subbands avoid crossing because the Zeeman effect pushes the spin ↑ subbands towards lower energy, whereas the orbital effect of the magnetic field pushes them in the opposite direction. This balance is ensured by the level-locking of the subbands.

A way of discerning the relevance of this explanation is being investigated. It will involve simulations of the feasibility of generating two 1D channels in a single InSb nanowire -not yet completed-, and then an evaluation of the level-locking effect in these two 1D channels. If this is the correct interpretation, then it would also help explaining why subband degeneracies were observed in Ref. [19] at zero and large magnetic field. The possible observation of two quantum wires in the same nanowire means that these systems can be used to search for fractional helical liquids and Majorana bound states, provided that a tunnel coupling between the two wires can be established [13].

Signatures of the helical spin-orbit gap

The device had conductance signatures that resembled the spin-orbit gap expected from helical states. These signatures appeared at some detuning voltages and over some magnetic field ranges. They are pointed by blue or white arrows in the maps and traces previously shown (Figures 3.11, 3.14 and 3.13)

Figure 3.20 shows an example of the helical dip feature (blue arrow) to which I am referring to. The size of the dip, which can be roughly related to the spin-orbit gap (see Figure 2.2**d**), is $\Delta_{SO} = 5.2$ meV, transformed into energy with the lever-arm of the central gate ($\alpha_C = 0.04$). This zero-bias conductance trace as a function of the central gate V_C was taken at a magnetic field of 7.8 T and at lateral gate voltages $V_L = 2.92$ V and $V_R = 2.55$ V. The dip always appears at the onset of the 2 e^2/h plateau, and it may be preceded by either a 1 e^2/h plateau -like in this case-, or by zero conductance. Therefore, it is perhaps more suitable to refer to this feature as a peak in the 1 e^2/h plateau.

Simulations (with the value of $E_{SO} = 6.5$ meV as a given) have shown that the visibility of the spin-orbit gap depends on the contact spacing, the spin-orbit strength and the angle between the spin-orbit effective field and the direction of the external magnetic field applied [33]. A larger

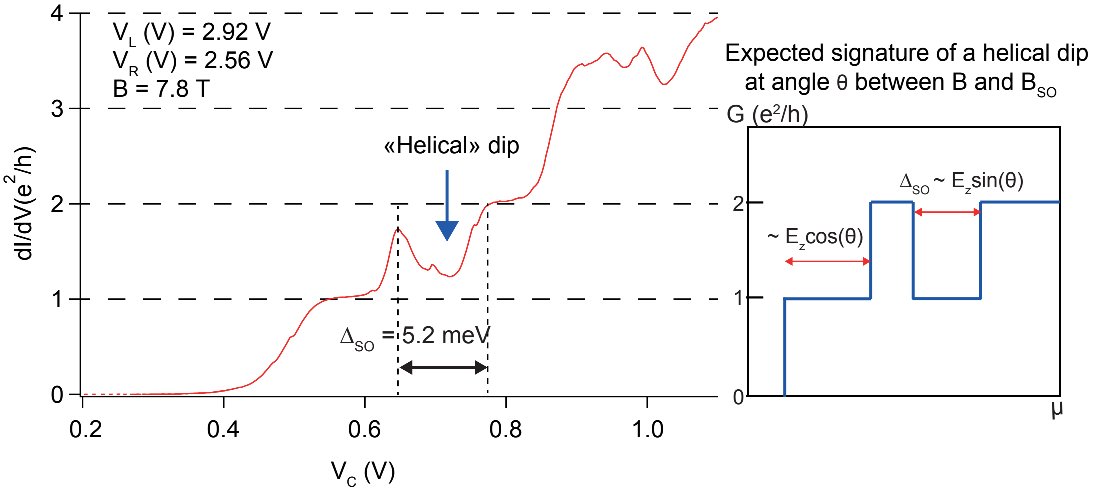

Figure 3.20: Left: Example of a "helical" dip in a linear conductance trace at high magnetic field. **Right**: expected signature of the "helical dip" in this magnetic field orientation.

contact spacing, stronger spin-orbit coupling or an angle closer to 90° -i.e., closer to a direction parallel to the nanowire- contribute in increasing the visibility of the spin-orbit gap.

The large contact spacing of my the device (450 nm) situates it in the optimum to observe the spin-orbit gap, according to ref. [33]. Moreover, the large size of the InSb nanowire (diameter = 160 nm) used to make this device should also contribute in increasing the spin-orbit interaction. However, the angle between the external magnetic field and the axis of the nanowire (58°) puts the angle between the external magnetic field and the expected effective field from the Rashba spin-orbit interaction at 32°. This is a bit far from the optimum 90°. Nonetheless, the simulations show that for a strong spin-orbit interaction, the helical dip should be visible for angles as small as 17° [33].

Yet, tight-binding atomistic non-self consistent simulations show that the spin orbit interaction for a 100 nm bare InSb nanowire subject to an out-of-plane electric field of 2 meV/nm should be very small (E_{SO} less than 100 μV). Similar calculations in a 100 nm bare InSb nanowire under a larger electric field of 10 meV/nm, this time with the field screened over a length of 15 and 20 nm, still result in a tiny E_{SO} of less than 100 μV [2]. Therefore, at high magnetic field no signature of the spin-orbit gap should remain, as the Zeeman energy polarizes the spin of the electrons along the field axis and any mixing by the spin-orbit interaction can be considered absent.

In the same InSb nanowire device presented here, but in a different gate configuration, I confined a quantum dot and performed a spectroscopy of the singlet-triplet anti-crossing of its excited-state levels. I found Δ_{SO} values of 0.36 mV at 1.3 T and 0.40 mV at 1.85 T in two of these crossings, which are significantly below the 5 meV found above.

---

[2] All calculations done by Zaiping Zeng from CEA/Grenoble.

If the spin-orbit energy is of the order of 6.5 meV, which is the case of the InSb nanowire device of Ref. [33] for which the simulations mentioned two paragraphs above were made, then a helical dip could in principle be observed in my device, given the quality of the plateaus at large magnetic field and the points discussed above. In what follows, however, I will propose the hypothesis that the dip that I observed could be due to a quantum dot that presented a *parallel* conduction path to the one-dimensional channel, such as in the case of the device of Section 3.2. And therefore, it may have nothing to do with helical states.

The clues to verify this hypothesis come from a measurement at a slightly different detuning of the lateral gates. I name this new detuning V_{Gw} -where w stands for white. To obtain this gate detuning, V_L and V_R were simultaneously stepped using the relation $V_R = \alpha_{R/L}(V_L - V_{L0})$, where $\alpha_{R/L} = 0.875$ as before and $V_{L0} = 0$ V. Using this new detuning, the three conductance maps shown in Figure 3.21 (left panels) were taken. As evidenced by these measurements, the magnetic evolution of the plateaus for detuning V_{Gw} is alike detuning V_G.

Figure 3.22 shows a zoom (top left panel) of the top of the conductance map of 3.21**c**, and cuts at three different V_{Gw} voltages (top right panel). A QPC and a quantum dot regime could be achieved by creating barriers with the detuning voltage V_{Gw}.

A Coulomb peak, pointed by a green arrow in the black curve of panel 3.22**b**, appears at the onset of the first spin-resolved subband of channel 1 when the lateral gates set a camel-shape bottom of the conduction band at low charge density, as indicated in the scheme in panel 3.22**c**. After the peak, a plateau at 1 e^2/h (red arrow) is seen -when the camel-shape band edge is gone and the charge density increases (panel 3.22**d**). The plateau is resonant-free, which indicates nearly zero backscattering at that gate region.

In strike contrast, the blue curve of panel 3.22**b** does *not* display a Coulomb peak before the 1 e^2/h plateau. Instead, a resonance appears on top of the perfectly quantized 1 e^2/h plateau (blue arrow). This peak is indicated by a white arrow in the conductance map of panel 3.22**a**.

The peak is strongly gate-dependent, both in height and in width, as shown in Figures 3.22**a** and 3.21**c** (white arrow). This should be the case if the spin-orbit interaction were sensitive to the electric field -as expected for a Rashba interaction. Moreover, the peak always stays *parallel* to the 2 e^2/h plateau; i.e., its position does not change significantly with respect to this plateau at a fixed magnetic field (see, for instance, Figures 3.13**b,c**). Its position may vary, though, if the magnetic field is cranked up (see Figure 3.14), as it is expected if the spin-orbit gap increased with magnetic field.

However, the observation made above allows to propose an alternative mechanism. Simply put, the Coulomb peak that appears on top of the 1 e^2/h plateau (blue curve of Figure 3.22**b**) belongs to the onset of conduction in channel 2, in analogy to what is seen in channel 1 (black curve of Figure 3.22**b**). This feature naturally mimics the re-entrant signature of helical states. Under this

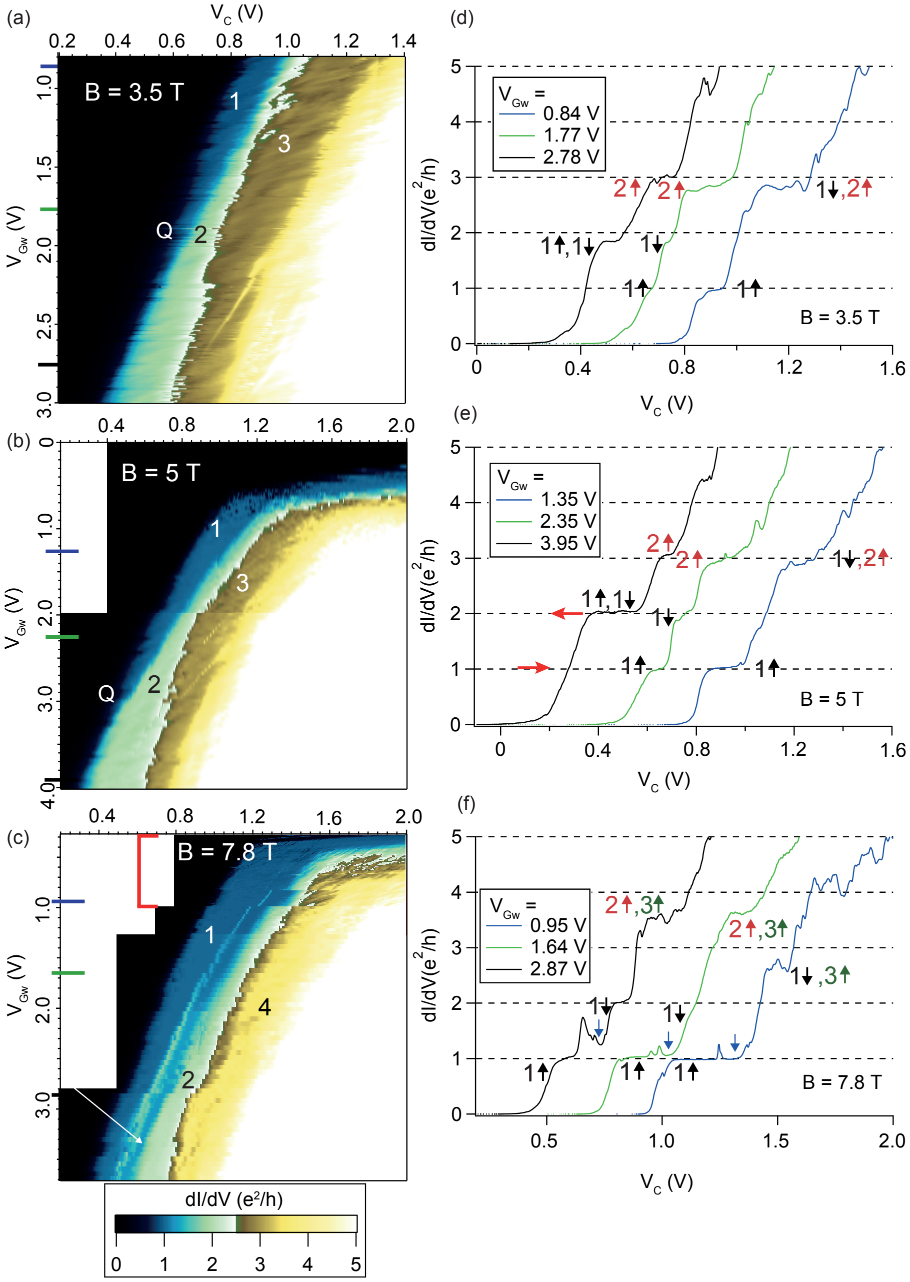

Figure 3.21: Linear conductance maps as a function of the central gate V_C and the gate V_{Gw} for B = **(a)** 3.5 T, **(b)** 5 T and **(c)** 8 T, sided with corresponding cuts at specific V_{Gw} **(d-f)**. Horizontal red arrows indicate the V_{Gw} direction in which plateaus widen. Unlike 3.10**c**, in this case the lateral gates were swept following the detuning voltage V_{Gw}. In these maps, point Q has the same meaning as in Figure 3.10**c**: it is the detuning voltage V_{Gw} at which the 1 e^2/h vanishes.

picture, the detuning voltage acts on the tunnel coupling to the leads of the quantum dot level that produces this resonance, and therefore tunes its broadening and its intensity. The magnetic field

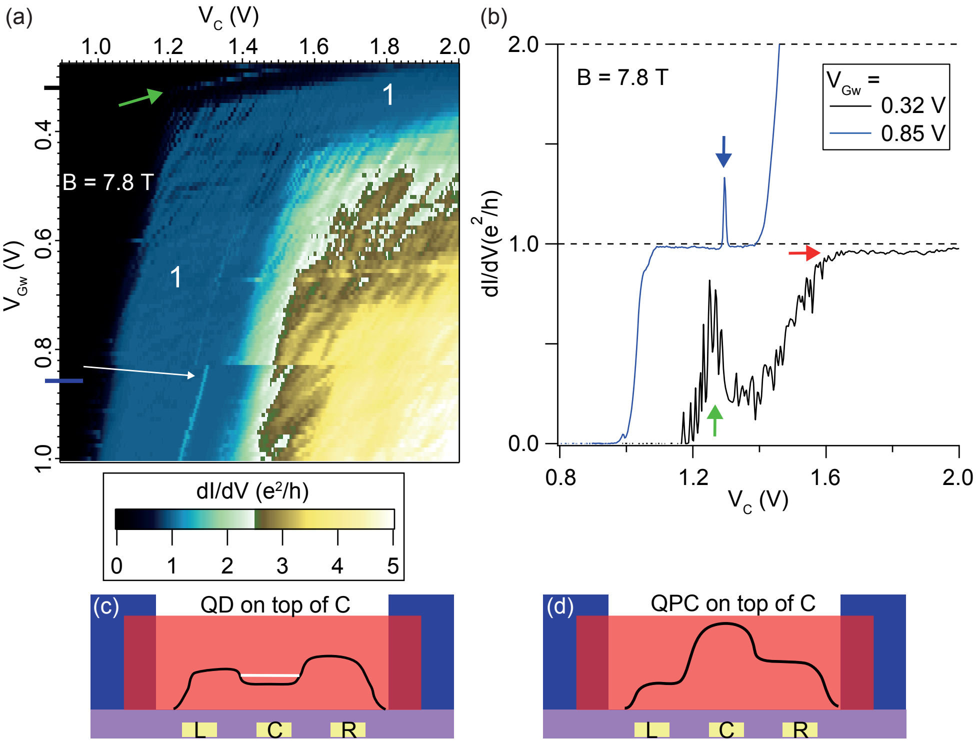

Figure 3.22: Formation of a QPC with detuning V_{Gw}. **(a)** Zoom on the red-marked zone of the conductance map in Figure 3.21**c** (left pannel). The 1 e^2/h plateau is indicated. A Coulomb resonance is also indicated by a green arrow. **(b)** Cuts at two different V_{Gw} detuning voltages through the map in **(a)**. **(c,d)** Schemes of the the profile of the conduction band edge, at the gate points indicated by a **(c)** green and **(d)** red arrows in the black curve of plot **(b)**. A positive (negative) voltage accumulates (depletes) electrons in the channel. **(c)**. A quantum dot is formed on top of gate C. **(d)**. A QPC is formed on top of gate C.

may also shift it, resembling a Zeeman-enhanced spin-orbit gap. In ideal conditions, the intensity of the peak can reach 1 e^2/h, which on top of a 1 e^2/h plateau would appear as a 2 e^2/h peak[3].

The peak appears generally when the spin-degeneracy of the first spin-split subband is broken (see the maps in Figure 3.14) -and this is gate-dependent, as we established before. This is not always the case, though. Figure 3.23 shows the magnetic field evolution of the plateaus at V_{Gw} = 0.946 V. In this plot, the peak emerges at B = 5.68 T in the middle of an already developed 1 e^2/h plateau, without any relationship to the 2 e^2/h plateau [4]. This is suspicious for a peak related to

---

[3] A third explanation is possible, in the context of tunnel-coupled double quantum wires under a magnetic field applied in the direction out of the plane of the wires, and thus perpendicular to their the tunnel coupling [102][103]. This mechanism produces a pseudogap similar to the one shown in Figure 2.2**c** (central panel), when two subbands of the wires are degenerate. The tunnel coupling shifts the bottom of the subbands in proportion to the field applied. The absence of clear anti-crossings in our data, which should be observed in tunnel-coupled double wires [104][105], the inconsistency between a finite tunnel coupling and level-locking, and the fact that the field was applied in the plane of the two wires, put this explanation in an untenable position.

[4] It is important to stress that this cannot be explained by a charge switch of a resonance at larger energy, since the

helical states. The feature should appear as part of the 2 e^2/h plateau, and not in this disconnected way. As elsewhere, the peak appears parallel to the spin ↑ subband of channel 2. As the field is increased, its conductance rises until it reaches its maximum at B = 6.52 T and then decreases again. Notice that the conductance of the two peaks at larger gate voltage (green arrows) also increases with the magnetic field.

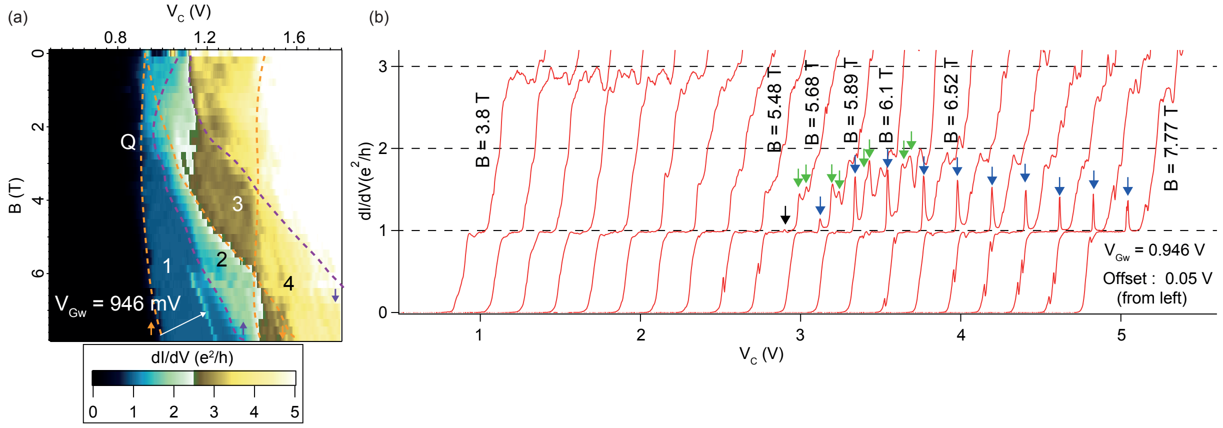

Figure 3.23: **(a)** Linear conductance map at V_{Gw} = 0.946 V as a function of the central gate voltage V_C and the magnetic field B. The conductance of the plateaus is indicated in units of 1 e^2/h. The two left-most orange and purple dashed-lines delimit the 1 e^2/h plateau of each of the 1D channels conducting in parallel. Point Q has the same meaning as before. **(b)** Cut-lines from **(a)** taken every 208 mT from 3.8 T to 7.77 T, showing the magnetic field evolution of the Coulomb peak (indicated by blue arrows). At the first field at which it appears (B = 5.68 T) the peak is indicated by a black arrow. Peaks at larger energy are identified by green arrows. The curves have been offset for better visibility.

This observation could be explained if the tunnel coupling of the state to the leads depends on the magnetic field applied. A reason for the change of tunnel coupling could be in the details of the magnetic confinement of the wavefunction of the state. I also observed a tunnel coupling increasing with magnetic field in InAs nanowires (see Chapter 5 and Figure 6.19 of Chapter 6).

The findings of this section can be summarized as follows. The main experimental observation made was that the width plateaus and their degeneracy could be tuned by the voltage of two lateral gates simultaneously swept. In particular, when the voltage was large, the 1 e^2/h plateau did not show up to very large magnetic field. This observation was interpreted in two ways. The first interpretation involved a quenching of the g-factor by magnetic confinement. The second one was based on the assumption of the coexistence of two 1D channels in the same nanowire. The additional observation of a Coulomb peak at the onset of the 2 e^2/h plateau could be best interpreted by assuming the formation of a quantum dot at the onset of one of the 1D channels, adding support behind the two-1D channels hypothesis.

---

other features do not switch.

3.4 Conclusions

Remarkable signatures of parallel transport were found in two single InSb nanowire devices. In the first device presented, clear signatures of a quantum dot conducting in parallel with a 1D conductor were found in an InSb nanowire. Coulomb peaks and Kondo resonances of the dot were observed on top of plateaus of quantized conductance of the 1D channel. The deconvolution of the two transport characteristics allowed to find the g-factor of the dot states and the g-factor of the first subband of the 1D path. The observation of a 1D channel of conduction in parallel with a 0D channel has no precedent in transport through nanowire devices.

The observation of ballistic and zero-dimensional signatures on the same nanowire may have serious implications in the search for Majorana bound states in these nanowires [1]. In the next chapter, superconducting-state measurements done in the same device will be discussed, showing that the dot in parallel can produce a zero-bias peak emerging with a magnetic field aligned parallel to the nanowire. This is the Holy-Grail signature of Majorana bound states, trivially reproduced by a quantum dot in a system thought to be one-dimensional [83][19].

The second device showed plateaus of quantized conductance with intriguing magneto-transport characteristics. At high magnetic field (at Zeeman energies as large as 19 meV for a g-factor of 50 and a field of 6.5 T) the expected 1 e^2/h was incredibly absent. This baffling occurrence was gate-dependent, meaning that the 1 e^2/h could re-appear at a fixed magnetic field by properly tuning the gate voltages. Moreover, at some gate voltages, the 2 e^2/h plateau vanished, without re-emerging for a large range of field.

These observations were best interpreted as the result of two quantum wires that were conducting in parallel on the same nanowire. These 1D paths had a different g-factor and a different orbital effect. The observed degeneracies at high magnetic field were then naturally explained by the overlapping of the spin-resolved plateaus and a level-locking effect [101]. In particular, the degenerate 2 e^2/h plateau emerged as a superposition of the 1 e^2/h plateaus of the two channels. The gate voltage dependence of the plateaus and their degeneracies at fixed magnetic field was also naturally explained as a shift of the energies of the subbands of each 1D path. Calculations to check the conditions at which these parallel paths of transport emerge in a single InSb nanowire are under progress.

It was also shown that the conductance signatures expected in the helical regime could be replicated by a dot conducting in parallel to a 1D channel. This is a possibility that should also be considered in the new field of helical states in III-V nanowires [33][66].

Chapter 4

Superconducting proximity effect in 1D nanowires exhibiting localization

4.1 Introduction

Superconducting transport through one-dimensional (1D) semiconductor nanowires is interesting because of the possibility to generate Majorana bound states (MBS) in these nanowires [4]. In my thesis, I investigated the basic requirements for this to happen. These include 1D transport, helical states, and the coupling of superconductors to 1D nanowires. The need to understand the coupling between a 1D nanowire and a superconductor, even in short junctions, is basic in the context of MBS physics. Additionally, the induced gap should be hard -i.e., devoid of states-, to clarify the interpretation [11].

In this chapter, I will present measurements of the superconducting gap and/or the Josephson current in some of the 1D nanowire devices of Chapter 3, and in additional devices not discussed there. I find these measurements complementary, since in the former case the low-charge density regime prone to strong Coulomb interactions is probed, while in the latter the large-charge density, interaction-free regime is tested. Instances of the correlation of conductance quantization and supercurrent will be explored, as well as the spectroscopy of the induced gap through localized states at the onset of 1D conductance.

When a dot is conducting in parallel to a 1D channel, it will be shown that a zero-bias peak related to the dot can emerge in the gap when a magnetic field is applied. This alerts us of a novel way in which a seemingly 1D nanowire can show MBS-related features, without necessarily being topological.

This chapter may also bring useful insights in the road to search for the superconducting materials that produce the best possible contact to InAs and InSb nanowires, with the hardest superconducting gap, the largest possible Josephson current, and the cleanest 1D transport characteristic. I grouped the results by superconductor used and from a device perspective; however, at the end of the chapter I show a comparison of Δ, B_c, and the hardness of the induced gap in all the superconductor / nanowire possibilities explored.

4.2 Optimization of the contact between superconductors and nanowires

Before switching to the experimental data, I will discuss a few points about the optimization process that I used to obtain a good contact between the superconducting leads and the nanowires.

A good contact, hard gap, large Josephson current and clean 1D transport are not granted to simultaneously occur in a given device. However, the removal of the native oxide in a mild way is key to maximize the chances for this to happen. The way that I chose was to do this was by using in-situ Ar^+ etching [1]. This technique is not really mild (see Figure A.13 of Appendix A); however, if the time of etching is optimized then the outcome can be positive.

After optimizing the Ar^+ etching time for one superconductor/nanowire combination, I used the same etching time for other superconductors deposited on top of the same type of nanowire. I did this with Vanadium on InSb nanowires and Aluminum on InAs nanowires, and found that 45 seconds at 250 V of Ar^+ bombardment, before metal deposition, was the optimal for both cases. This became my standard etching time and I did little variations around this number during the rest of my thesis. I hypothesized then that this time should not depend on the metal used. So I did not optimize all over again the etching time for other materials like Tantalum.

This optimization procedure started by fabricating two-terminal devices with one local backgate and measuring their resistance at room temperature post-fabrication. This was an indication of the quality of the contact between the superconductor and the nanowire. Resistances of less than 10 kΩ were preferred. This method was good enough for InAs nanowires, since their room temperature resistance was highly sensitive to the amount of etching -it would diverge if the etching time was 30 seconds shorter or longer.

However, in InSb nanowires, there was virtually no difference in the room temperature resistance when the etching time was 45 seconds or 150 seconds. When the devices worked, their resistance was most of the time below 100 kΩ anyways. Therefore, InSb nanowires needed to be cooled-down to find out which etching time was better. I found that 150 seconds produced preferably quantum dots and very soft and small gaps in the initial Vanadium/InSb nanowire optimization [2].

---

[1] Sulfur passivation of InAs nanowires was also tested, but did not lead reproducibly to low nanowire resistance or a high yield of working devices, and thus it was abandoned.

[2] The ratio of the normal ($V > 2\Delta$) to the superconducting conductance (zero-bias) was $G_N/G_S = 1.5$, while Δ

Additionally, I found out that InAs nanowires with Aluminum and Vanadium contacts were sensitive to the dielectric on top of which they were deposited [3]. A silicon-nitride sputtered dielectric systematically resulted in InAs nanowires with naturally-occurring quantum dots and room temperature resistances in the MΩ range. In strike contrast, a hafnium-oxide dielectric deposited by atomic layer deposition yielded devices with room temperature resistances in the kΩ range, showing in a few cases signs of conductance quantization. Hafnium oxide was then preferable as dielectric [4].

4.3 Aluminum

Aluminum (Al) has been widely used for contacting InAs nanowires in the past. In most cases, the native oxide of these nanowires was removed by either in-situ Ar^+ etching [89][11] or by sulfur passivation [106][107] before depositing it by electron-gun evaporation. A Δ of $\sim$ 150 μeV was almost universally reported, but most works did not pay close attention to the hardness of the gap. Although metal evaporation has been the most common route followed for depositing this superconductor on top of InAs nanowires, recently, epitaxial Al was grown directly on top of InAs nanowires inside of a MBE chamber. Ultra-hard gaps ($G_N/G_S \sim 100$) and a Δ of 190 μeV were obtained in this way. The same group reported a gap hardness of $G_N/G_S \sim 5$ for a control Al-evaporated InAs nanowire device.

There also have been some recent works that used Al for contacting InSb nanowires. Sulfur passivation was shown to provide hard gaps and a Δ of $\sim$ 150 μeV [84], similar to what had been achieved in InAs nanowires. Other works have reported a softer and smaller gap by this method [108]. The Josephson effect, on the other hand, was demonstrated in a more coupled device, also passivated by sulfur [109]. An $I_c R_n$ product between 4 and 34 μV, substantially lower than $\Delta \sim 150$ was found in this latter case. There are no published studies of superconductivity in Al-contacted InSb nanowires in which the native oxide was removed with Ar^+ etching.

In my thesis, I achieved transparent contacts, conductance quantization, moderately-hard gaps and large Josephson currents in both InAs and InSb nanowires using this superconductor and removing the native oxide by in-situ Ar^+ etching.

---

itself was half of the expected value. On a site note, at least one InSb nanowire device etched during 150 seconds yielded conductance plateaus at high magnetic field. This implies that the hardness of the gap and the observation of ballistic transport are two separate issues. The first one relies heavily on the S/NW interface, while the second one depends on a good contact and a pristine nanowire channel

[3] This could also be true for other superconducting materials, like Tantalum, but I only tested it with Aluminum and Vanadium-contacted InAs nanowires, so I cannot really tell if this also holds for these other materials.

[4] Nevertheless, both types of devices showed a hard superconducting gap, implying, once again, that what happens at the S/NW interface dictates the hardness of the gap, and what happens in the NW channel dictates mostly if the transport is ballistic or localized.

Devices made of Al, using either InAs and InSb nanowires, displayed remarkably low room-temperature two-terminal resistances. These were of less than 10 kΩ in more than 80 % of the working devices. The yield of working devices, defined as the ratio of devices with a finite resistance to the number of total fabricated devices in a chip, was also high, of the order of 80 %. These two characteristics gave me the option to choose among a large pool of devices the less resistive ones, using resistance as a predictor of the chances of getting 1D transport at low temperature. Unfortunately, this also made these devices more sensitive to electric discharges during bonding, plugging of the chip carrier on the cryostat, and any other manipulation without grounding. Therefore, the final yield of working devices on the refrigerator, compared to the total number of devices cooled, was of the order of 20 to 60 %.

In this section, I will show bias spectroscopy measurements in two-terminal InSb and InAs nanowire-based devices with Al contacts. Moreover, a bit of background about each device will be provided, if it has not already been done in other chapters of this thesis. Although the main goal of this chapter is to contrast and compare the superconducting gap/Josephson current of devices made out of several combinations of nanowire and superconductor materials, I also would like to relate some of these findings to the physics of the system itself -whenever it is possible-, and not only to the materials used.

QPC in an InSb nanowire with a localized state at the onset of conductance

The first device that I want to discuss is the two-terminal InSb nanowire device in which the study of electrical control of the subband degeneracy was performed in Section 3.3 of Chapter 3. As a reminder, this device had three local bottom gates (V_L, V_C and V_R) which could be used to obtain a quantum point contact (see Figure 3.10 of Chapter 3). At low field, it displayed two plateaus of quantized conductance, while at large field these plateaus could be split into four well-defined plateaus. From these observations, the 450 nm - long nanowire channel could be considered in a ballistic regime. Moreover, the nanowire seemed to have two quantum wires in parallel. However, the measurements presented here were taken in a different gate configuration, where the QPC was defined by the lateral gate V_L instead of V_C.

Figure 4.1**a** shows a map of the conductance of the device as a function of the right gate V_R and the bias V in the superconducting state, at T = 250 mK and B = 0 T, with the left gate fixed at V_L = 2 V and the central gate fixed at V_C = 1.28 V. To obtain this plot, the raw conductance and bias were corrected by subtracting the series resistance R_s = 4.4 kΩ of the measuring circuitry and the RC filters, plus a contact resistance R_c = 1.2 kΩ that was used to make the spin-resolved plateaus reach 1 e^2/h, 2 e^2/h and 3 e^2/h. The symmetric feature around zero-bias in this plot is the result of the superconducting gap of the two contacts. As the conductance of the device increases, the subgap conductance increases steadily until a zero-bias peak of supercurrent develops. The conductance of the first two spin-degenerate plateaus (2 e^2/h and 4 e^2/h) is also indicated in the plot.

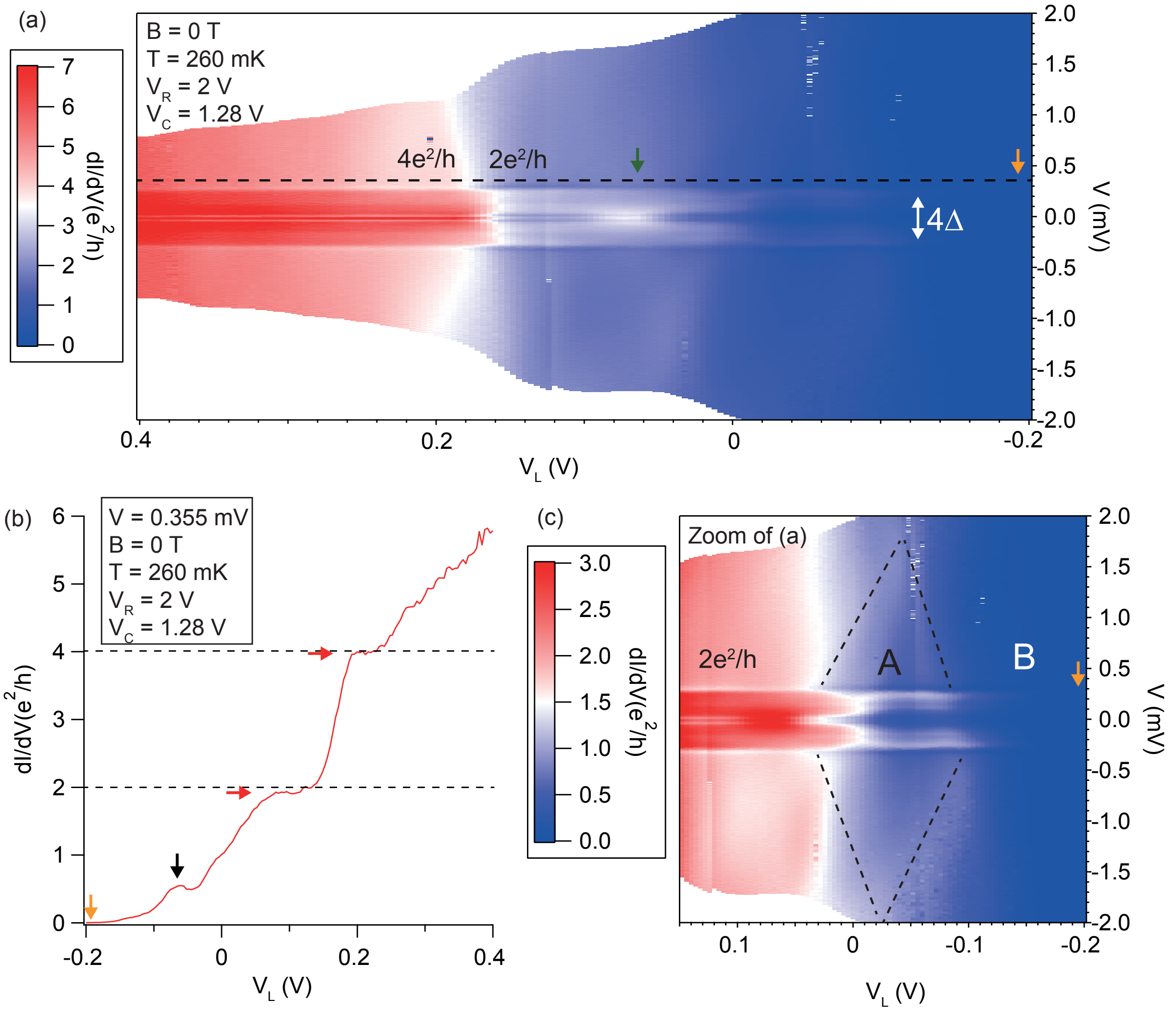

Figure 4.1: **(a)** Map of conductance of the Al/InSb NW/Al QPC device as a function of the left gate and the bias voltages. The conductance of the first two plateaus is indicated, as well as the extension of the gap. A ZBP belonging to supercurrent is seen at large conductance, towards the left of the plot. **(b)** Cut at $V > 2\Delta$, through the black dashed line of **(a)**. The first two plateaus are indicated by red arrows. A resonance at the onset of the QPC is also pointed (black arrow). **(c)** Zoom of the map in **(a)**. A Coulomb diamond belonging to the resonance has been drawn in dashed-black.

A cut through this map at a finite bias above the gap (shown in Figure 4.1**b**) reveals the presence of the first two plateaus (blue arrows), but also of a broad peak preceeding the opening of the 1D channel (denoted by a black arrow). A Coulomb diamond of this last feature is seen in a zoom of the map of Figure 4.1**a**, shown in Figure 4.1**c**. In this zoomed map, the diamond is indicated by a letter A and highlighted by a black-dashed line. The existence of this diamond implies that the broad peak mentioned before is coming from the spatial localization of electrons. The associated charging energy U is of around 2 meV.

Figure 4.2**a** shows a V - dI/dV curve taken at the gate point indicated by an orange arrow in Figures 4.1 and 4.2**c** (at V_L = -0.195 V), in the region named B. The more prominent features of the measurement are two large conductance peaks symmetric with respect to zero bias (indicated by blue arrows), separated from each other by 0.56 mV. Flanking the two peaks, the are two symmetrically-positioned *dips* of conductance (green arrows), separated by 0.68 mV. And in between the two peaks, there are two small shoulders, separated by 0.32 mV.

This measurement also serves to evaluate the *hardness* of the gap, G_N/G_S. In Figure 4.2**a**, G_N was evaluated by taking the average of the conductance at V = ±1 mV, while G_S was evaluated at zero bias. I find G_N/G_S = 10, which is a rather respectable value for these nanowires [84][108].

A similar cut-line was taken inside the diamond A at V_L = - 0.041 V (gray arrow in Figure 4.2**c**). This cut-line is shown in Figure 4.2**b**. Aside from the comparatively larger subgap and normal state conductance, this curve is qualitatively similar to the one in the more closed regime of Figure 4.2**a**. However, the larger outer peaks have slightly shifted (their voltage spacing is now 0.50 mV instead of 0.56 mV), as well as the inner peaks (their voltage spacing is now 0.26 mV instead of 0.32 mV).

In the light of a quantum dot interpretation in an asymmetric tunnel coupling regime, the large peaks appearing in Figures 4.2**a,b** are explained as the probing of ABS in the strongly coupled lead by the BCS peaks of the gap of the weakly coupled lead. Therefore, they are separated by a bias $2(\Delta + E_b)$ [92][91]. Since the plots do not show NDC but instead a dip of conductance (pointed by green arrows in Figure 4.2**a**) that does not reach negative values, the asymmetry in the tunnel couplings has to be small [91]. The shoulders appearing between the large peaks, however, cannot be consistently interpreted as the peaks expected at $2(\Delta - E_b)$ [91]. Nor can they be interpreted as the peaks expected for a soft gap, at $\pm E_b$ [11] or $\pm\Delta$.

Figure 4.2**c**, which is a zoom at low-bias of Figure 4.1**c**, shows in white-dashed lines the motion with the gate voltage of the bottom inner shoulders (black arrow) and outer peaks (blue arrow). Each of these two features seems to obey a different gate dependence, as if the two were related to different ABS. This explains why the shoulders do not have the energies expected if they would belong to the same ABS as the outer peaks. In contrast, the two dips that flank the two outer peaks (green-dashed lines) stay at fixed bias as the gate voltage is swept. The behavior of the dips is expected if ABS very close to the continuum of quasiparticles are being probed by the BCS peaks of the weakly-coupled lead.

Taking $\Delta + E_b$ and the dip spacing as the lower and upper bounds for 2Δ, I found $140\ \mu\text{V} < \Delta < 170\ \mu\text{V}$. This value for Δ is in line with previously reported values in these nanowires [84][108]. The critical field of these features ($B_c \sim 60$ mT) also agrees with previously found values for InAs nanowires contacted by Al films of similar thickness [11].

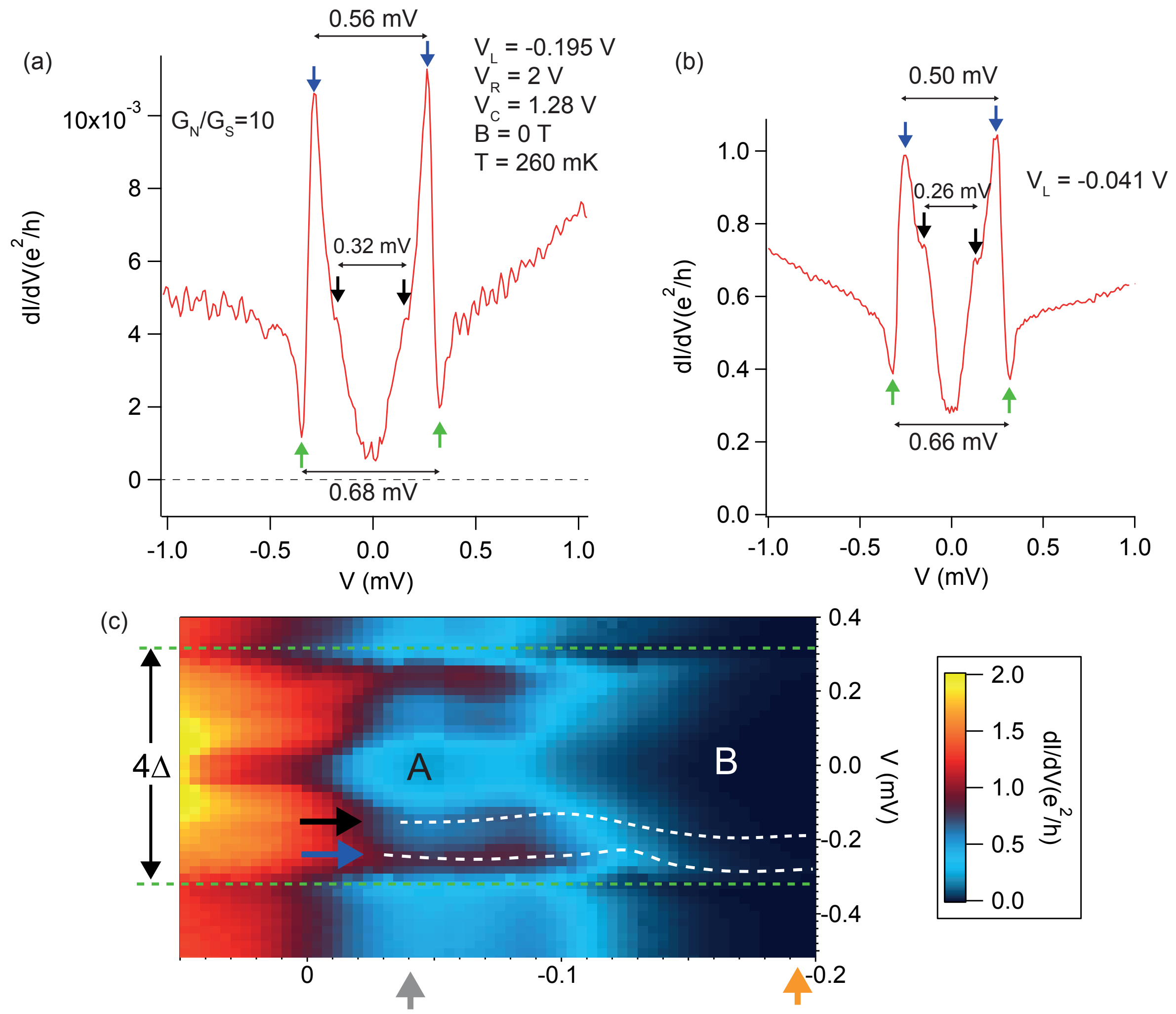

Figure 4.2: Cut-lines at the gate voltages indicated by the **(a)** orange and **(b)** gray arrows from the conductance map in **(c)**. This map is a zoom at low-bias in the gate region of diamond A from the map in Figure 4.1**a**.

Supercurrent correlated to conductance plateaus

The critical current of the nanowire was roughly estimated from the data in the map of Figure 4.1**a**, and from a similar current (I) map simultaneously recorded. With this information, the data was numerically converted into an I - dV/dI map, which is shown in Figure 4.3**a**. In this type of map, a supercurrent appears as a dip in resistance, surrounded by two peaks at which a switch to the dissipative state happens. To estimate the supercurrent, I extracted the current at which the right peak appeared, indicated by a white arrow in the map 4.3**a**, and plotted it in Figure 4.3**b** (black circles joined by a red line). I named this quantity I_m, since it is not really a switching current [5]

---

[5] At T = 260 mK, the thermal fluctuations effectively smear out any signature of a switching current.

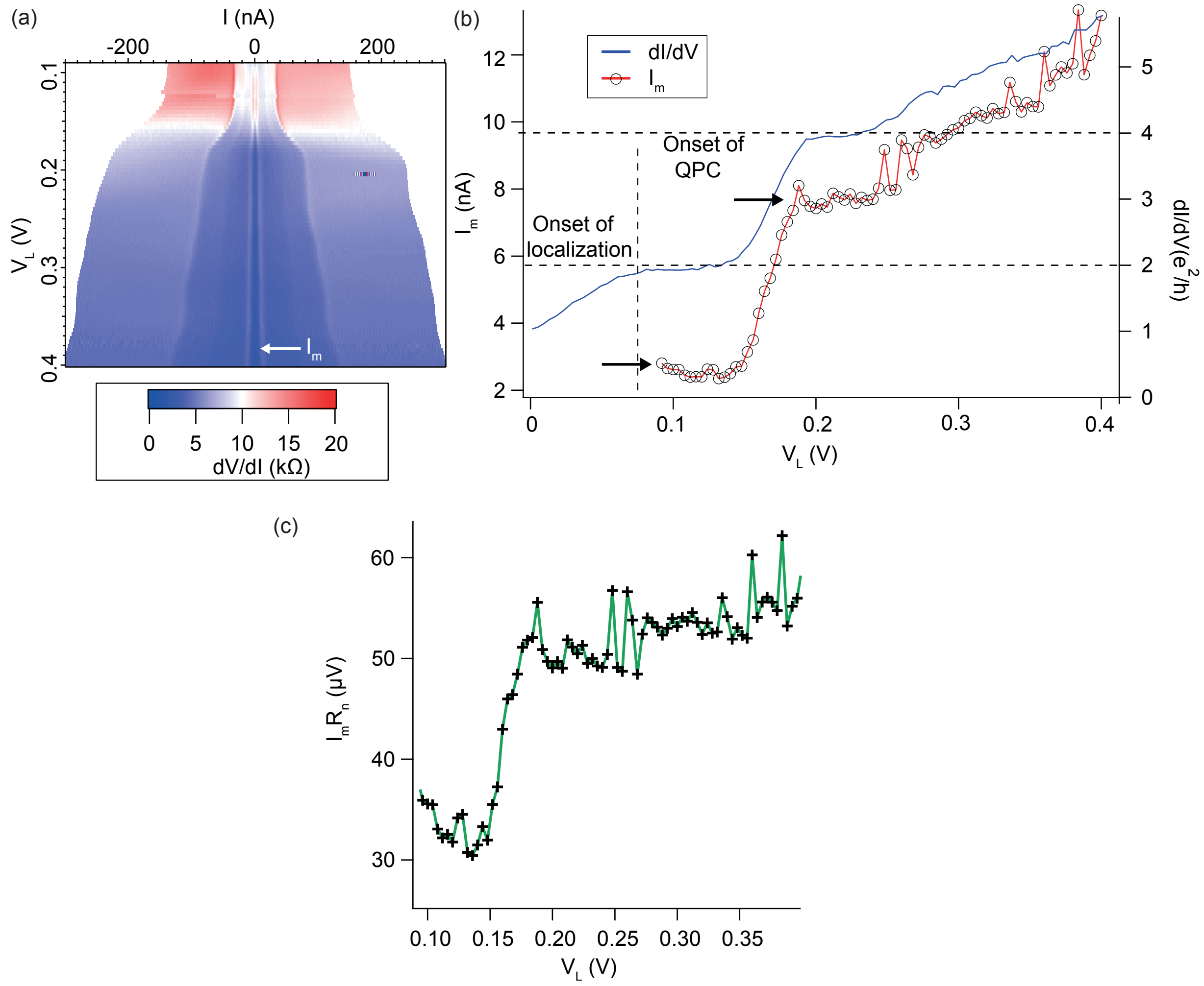

Figure 4.3: **(a)** Differential resistance map (dV/dI) as a function of the current (I) and the gate voltage V_L, numerically converted from the dI/dV map in Figure 4.1**a** and simultaneously recorder I map. The current I_m at which there is a peak in dV/dI, is indicated. This peak occurs when the sample changes resistance from the dissipative to the Josephson regimes. **(b)** I_m is plotted as a function of the gate voltage (black circles) together with the normal-state conductance dI/dV (blue line) taken at V = 0.355 mV. Two steps of supercurrent are indicated by black arrows. At lower gate voltage than ~ 0.1 V, the dV/dI peaks at $\pm I_m$ merge together and I_m cannot be extracted (green arrow in Figure 4.1**a**). The vertical dashed-line points to the onset of localization, where one of the Coulomb peaks of diamond A was observed. **(c)** I_mR_n product extracted by multiplying I_m with 1/(dI/dV) in the normal state.

[110].

Purposely, I also plotted the normal conductance of the sample taken at V = 0.355 mV on the same gate scale (blue line). Intriguingly, the I_m quantity has two steps (black arrows) that *coincide* with the first two normal conductance plateaus of the sample. This is a signature of *supercurrent quantization* [97][21], and therefore, of the ballistic character of transport in this device. Indeed, the critical current is sensitive to the square of the transmission, unlike the conductance, which only depends linearly on this quantity [111]. Because of this, a plateau of supercurrent is much harder to obtain than a plateau of conductance.

Equation 2.3 sets a maximum I_c of 36 nA for the 2 e^2/h plateau and 72 nA for the 4 e^2/h plateau. My measurements show that I_m is ~ 2 - 3 nA in the 2 e^2/h plateau, and 8 nA in the 4 e^2/h plateau. Even if weaker than the ideal case by 9 to 18 times, the magnitude of I_m shown here is two to four times larger than the only report of the correlation between supercurrent and conductance quantization in a III-V nanowire up to this date, measured in an InAs nanowire with Al contacts and a junction channel three times shorter than the device presented here [21]. A much stronger supercurrent was measured in GeSi nanowires; however the conductance plateaus were not as resolved as in InSb nanowires [112]. In both cases, the temperature of the measurement was lower than what is presented here, which improves the size of the switching current.

To further compare equation 2.3 with my measurements, I plotted in Figure 4.3**c** the $I_m R_n$ product, where R_n is the inverse of the normal state conductance shown in the plot 4.3**b**. In the ideal case, the product $I_c R_n = \pi\Delta/e$ should be equal to 0.47 meV, a constant quantity. The plot 4.3**c** shows that 1) $I_m R_n$ is not a constant and 2) it is lower by a factor of 9 to 13.

These differences between the ideal case and my experiment can be the result of 1) the finite contact resistance of the Al leads to the nanowire, found to be 1.2 kΩ; 2) the way I_m was estimated, which might underestimate it due to thermal fluctuations [6]; and 3) the possibility that the 450 nm long junction does not belong to the short junction regime.

The coherence length ξ_N in the nanowire can be estimated as $\xi_N = \hbar v_F/\pi\Delta$, in the limit when ξ_N is larger than the mean free path. At the middle of 2 e^2/h plateau, one can estimate a Fermi energy of 4.8 meV by transforming the gate voltage difference (~ 0.3 V) from pinch-off to energy (with a lever-arm of 0.016), and extract $v_F = 3.4 \times 10^5$ m/s (using the effective mass of electrons in InSb, $m^* = 0.014$). This gives $\xi_N = 400$ nm, which means that the coherence length is slightly shorter than the length of the channel of the junction (450 nm) in the first plateau.

These measurements also indicate that, in the limit of large charge density, the Josephson effect can be a good alternative to study the interplay between superconductivity and one-dimensionality in a nanowire. At large charge density, one can avoid more easily the spatial localization of electrons. In this regime, I demonstrated that supercurrent plateaus can be correlated to a quantized conductance in the nanowire.

---

[6] At this point, a distinction between the switching current I_s, the experimental critical current, and the theoretical critical current is necessary. The first one is affected by thermal fluctuations and phase slips owing to the coupling of the junction to an electromagnetic environment. It is measured by taking a single I - V trace, and will change from trace to trace. The second one will be larger, as it comes out of the distribution of I_s measured out of many I - V traces. The third one is calculated through a model of the junction. Throughout my thesis, I measured I_s (or I_m in the over-damped regime).

On the other hand, these first measurements show that Aluminum is a good alternative for obtaining a moderately hard superconducting gap in an InSb nanowire, as well as a moderate supercurrent.

Quantum dot in an InSb nanowire

The *same* device presented in the previous section could be transformed into a high-impedance quantum dot, by lowering the voltage of the lateral gates V_L and V_R and using the central gate V_C as a plunger gate. Figure 4.4**a** shows a map of the conductance through the dot as a function of V_C and the bias V, taken at V_L = 0.03 V and V_R = -2.931 V.

This charge stability diagram shows a series of well-defined Coulomb diamonds. Around zero-bias, a symmetric feature crosses all diamonds. This feature is related to the superconducting gap of one of the leads probing the other through the dot. It is indicated by 4Δ in between the two black lines of the map 4.4**a**.

Far from the charge degeneracy crossings and near zero-bias, the conductance is very weak due to the low coupling of the dot to the leads. Deep within the diamond, a low coupling means that cotunneling is nearly nonexistent, which severely lowers the visibility of any gap features. In these conditions, the current reveals more information than the conductance.

In Figure 4.4**b** I show a V-I trace in the middle of the diamond marked by the letter C in the map 4.4**a**, along the blue dashed line. This diamond has a charging energy of 5 meV -way larger than the expected gap-, an even mean-occupation and an asymmetric tunnel coupling to the leads. The main features of this trace have been indicated by colorful arrows. The blue arrows indicate inflexion points where peaks would appear in conductance, while the green arrows point dips or NDC features. This type of V-I trace would result in a V-dI/dV trace similar to the one of Figure 4.1**a** -i.e., two conductance peaks flanked by two dips-, except for the two inner peaks indicated by black arrows in that former plot.

The dips (green arrows) are separated by 0.64 mV, similarly to what was found in Figure 4.1**a**. To find the separation between the peaks, I numerically differentiated the V-I curve of Figure 4.4**b**. The resulting V-dI/dV trace is shown in Figure 4.4**c**. The peak-to-peak distance (blue arrows) turns to be 0.54 mV, which is also comparable to what was found in Figure 4.1**a**. The bounds for Δ are then the same as when the device was tuned to a QPC regime with a QD at its onset.

I also evaluated the hardness of the gap. Given by the ratio of the slopes of the curve 4.4**b** at V = -1 mV and V = 0 mV, I found it to be $G_N/G_S = 6$. This is roughly half of the estimation done in the same device in the gate configuration of the previous subsection.

These measurements show that it is possible in principle to tune the same device from a QPC to a QD regime, and compare the superconducting properties in both the very-open and very-closed cases.

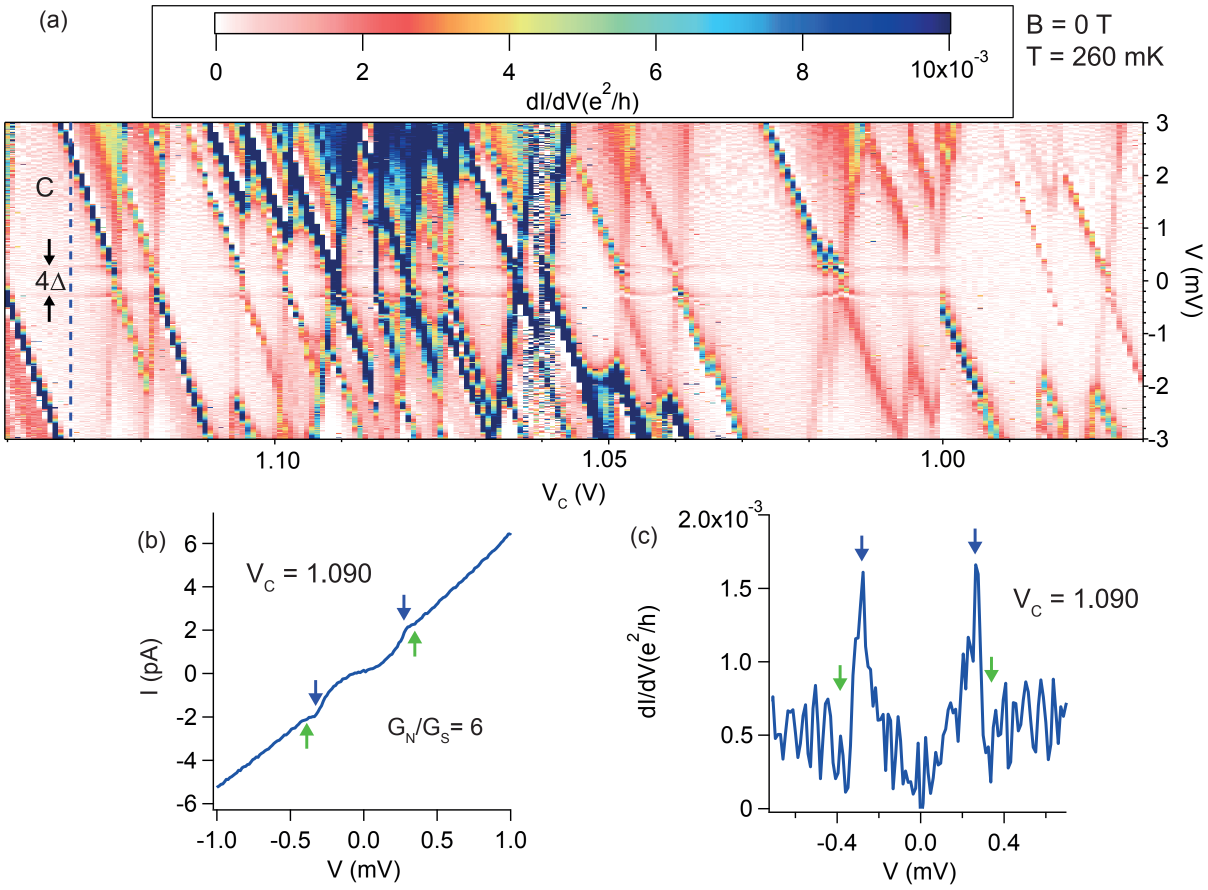

Figure 4.4: **(a)** Quantum dot regime obtained by tuning the gate voltages in the same Al-InSb NW-Al device as the previous section. This stability charge diagram is a map of conductance as a function of gate and bias voltages. The gaped band 4Δ, determined by the gaps of the two Al leads, is indicated in the map. **(b)** This I - V curve was taken from a simultaneously recorded I map, at the gate point indicated by the blue dashed line, in diamond C of **(a)**. **(c)** Numerically derived dI/dV - V trace (from the I - V curve in **(b)**) Peaks and dips in dI/dV are indicated by blue and green arrows, respectively.

QPC in an InAs nanowire with Fabry-Pérot oscillations

InAs nanowires contacted by Al also showed quantized conductance, in spite of having a few stacking faults, inherent from a growth that results in a wurzite structure (TEM images depicting this issue are shown in Figure A.9 of Appendix A). Here, I discuss one of these devices.

The device was made of a 60 nm diameter InAs nanowire placed on top of one large metal gate with a 30 nm hafnium oxide (HfOx) dielectric (for a SEM image of the device and a scheme, refer to Figures 4.5**a,b**, respectively).

Figure 4.5**c** shows the magnetic field evolution of the conductance as a function of the backgate voltage V_{bg}. In this plot, all traces measured at T = 250 mK and at zero bias, except for the one at

B = 0 T, which had to be measured at a bias higher than the Al gap of the two contacts (V > 2Δ). The B = 0 T and the B = 8.5 T traces were labeled by the orbital number *n* and the spin species ↑ or ↓ of the corresponding subbands. At B = 0 T, two plateaus can be seen (blue curve), each with transparency lower than 1 and a few resonances super-imposed on them. These two plateaus are labeled, respectively, with the indexes 1 ↑, 1 ↓ and 2 ↑, 2 ↓, for each of them are spin degenerate. At B = 8.4 T, plateaus at 1 e^2/h, 2 e^2/h, 3 e^2/h and 4 e^2/h appear. These correspond in turn to the spin-split subbands 1 ↑, 1 ↓, 2 ↑ and 2 ↓, respectively. At intermediate fields, the resonances make it complicate to follow the evolution of each plateau with magnetic field; however, at this resolution, the first subband can be seen splitting starting from B = 3 T, while the second subband starts to split from B = 5 T.

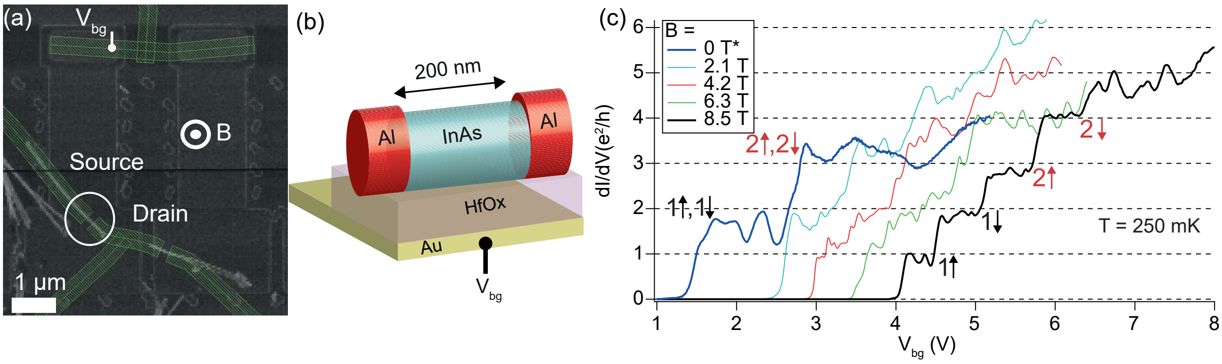

Figure 4.5: **(a)** SEM image of the Al-InAs NW-Al nanowire device (encircled in white) before metal deposition. The lithography design of the contact pads is shown in green. The magnetic field was oriented out of plane. **(b)** Scheme of the device. **(c)** Magnetic field evolution of the conductance as a function of the backgate voltage V_{bg}. The trace at B = 0 T was taken at V = 0.35 mV -through the dashed black line in Figure 4.6**a**-, above the superconducting gap of Al. All the other traces were measured at zero bias, and were offset for better visibility. The subbands are labeled by their orbital number *n* and their spin species ↑ or ↓. At B = 8.5 T, four clear plateaus appear. A contact resistance of 2.3 kΩ was subtracted to make the four plateaus reach 1 e^2/h to 4 e^2/h.

To study more in detail the origin of these resonances, I measured the non-linear conductance of the sample, producing the map in Figure 4.6**a**. This map is a measurement of the conductance as a function of bias voltage *V* and backgate voltage V_{bg} at B = 0 T and T = 250 mK. The resonances appear at irregular but nearly-valued intervals of roughly 0.5 V of V_{bg}, which hints that they may be Fabry-Pérot (FP) resonances. Taking into account the lever arm of the first resonance (α = 0.006), this interval corresponds in energy to 3 meV. A zoom of this map, shown in Figure 4.6**b** shows better that this is indeed the case. Diamonds were drawn to highlight the first three FP resonances.

If we take the length of the resonance cavity as $L_c = \hbar\pi/2m^*\Delta E$, where ΔE is the smallest energy interval between two Fabry-Pérot resonances for parabolic subbands and $m^* = 0.023m$ is the effective mass of InAs, we find that $L_c = 70nm$. Interestingly, this length of cavity does not correspond to the channel length, which the lithography design sets to be at 200 nm. An

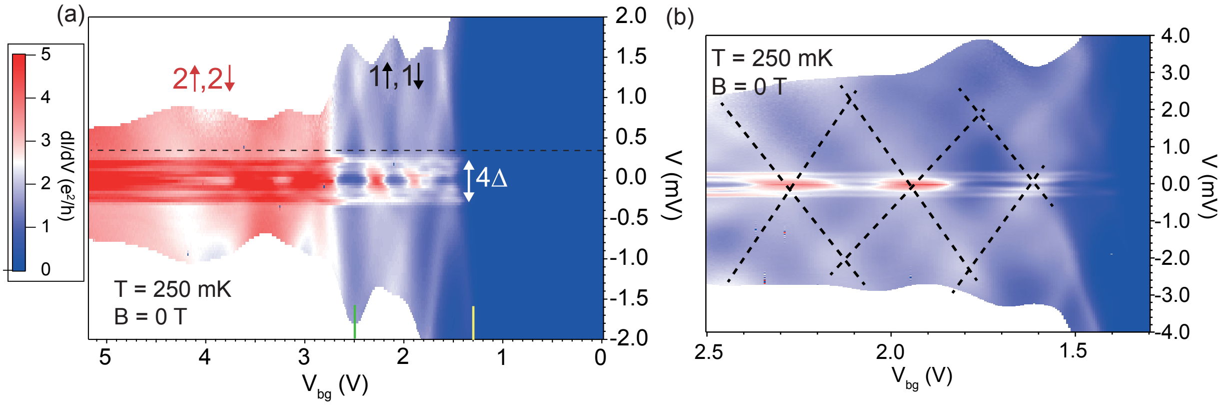

Figure 4.6: **(a)** Non-linear conductance map of the Al-InAs NW-Al device at B = 0 T and T = 250 mK, in which the first two spin-degenerate subbands are indicated. Fabry-Pérot oscillations modulate the conductance of the plateaus. **(b)** Zoom of the non-linear conductance in the 2 e^2/h plateau, between the gate points indicated by a green and a yellow line. Diamonds were drawn to highlight the first three Fabry-Pérot resonances. Notice the different bias scale.

overdose in the lithography may have resulted in a smaller channel length, and this may explain the smaller cavity length obtained through this calculation. Such a large error was however unheard off. A more probable explanation is that the cavity was set by stacking faults within the nanowire. Transmission electron microscopy images of nanowires belonging to the same growth substrate (see Figure A.9 of Appendix A) show a few of these defects randomly spaced, implying the possibility that by chance the channel of the nanowire had two of these spaced by $\sim$ 70 nm.

Figure 4.7**a** shows a dI/dV map as a function of the backgate voltage V_bg and the bias V, taken at B = 0 T and T = 260 mK. This map was obtained at the onset of the conduction of the QPC, indicated by a yellow line in Figure 4.6**a**. As the gate is swept towards more positive voltage, the gap quickly populates with states and a zero-bias peak of supercurrent appears. This is better seen in the cuts of this map plotted in Figure 4.7**b**, between V_bg = 1.32 V and 1.37 V. The appearance of these states limits quite drastically the gate region where a gap spectroscopy can be performed.

Figure 4.7**c** shows a V - dI/dV cut-line taken through the orange-dashed line in the map 4.7**a**, at V_bg = 1.325 V. This cut is a tunnel spectroscopy of the gap, in which presumably the QPC constriction is acting as a tunnel barrier between the two Al contacts. This plot has an appearance similar to the one in Figure 4.2**a**. Moreover, the voltage separation of the peaks (blue arrows) and flanking dips (green arrows) are nearly the same in both cases. What this indicates is that the gap features seen are probably those of the Al contacts, and not those of an induced gap in the InAs and InSb nanowires. However, this curve has a peak at negative bias (black arrow) that does not find a counterpart at positive bias. This feature was more symmetrical in the case of the InSb nanowire. When the gate voltage is swept towards more positive values than V_bg = 1.325 V, the two peaks at negative bias merge (white-dashed line in Figure 4.7**a**).

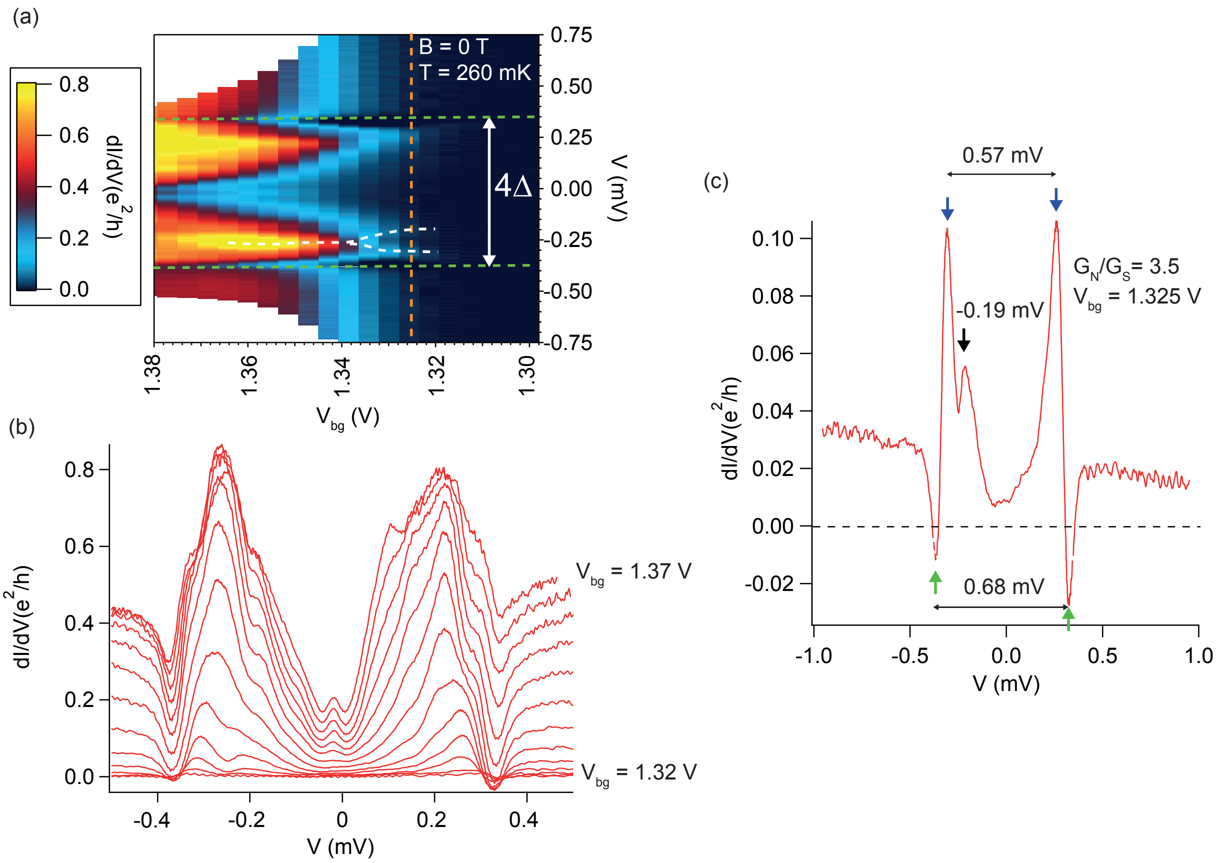

Figure 4.7: **(a)** Conductance map of the Al-InAs NW-Al device as a function of gate and bias voltage, focusing in the low-energy region where the gap is visible. The forbidden band 4Δ is indicated between two green-dashed lines. A white-dashed line shows the splitting of a conductance peak inside of the gap as the gate is swept. **(b)** Cut-lines belonging to **(a)**, showing the rapid raise of the conductance as the gate is swept. A ZBP related to supercurrent develops at large conductance. **(c)** Spectroscopy of ABS (blue arrows), showing NDC dips (green arrows). The left inner peak (black arrow) has an unknown origin.

The hardness of the gap is nevertheless different for both nanowires. In this InAs nanowire QPC, the ratio G_N/G_S is 3.5, while it was at least twice this value in the InSb nanowire device of the previous section.

Supercurrent correlated to the Fabry-Pérot oscillations on the plateaus

Figure 4.8 shows a dV/dI (vs. current and gate) map at B = 0 T and T = 250 mK numerically converted from the map of Figure 4.6**a**, and from a simultaneously recorded map of the current I. In this map, I_m (black arrow) corresponds to a peak in dV/dI at positive current, with the same interpretation as before. The normal conductance (black line), taken at V = 0.35 mV, has been super-imposed in the map. In this curve, the ideal conductance of the first two plateaus has been indicated (2 e^2/h and 4 e^2/h).

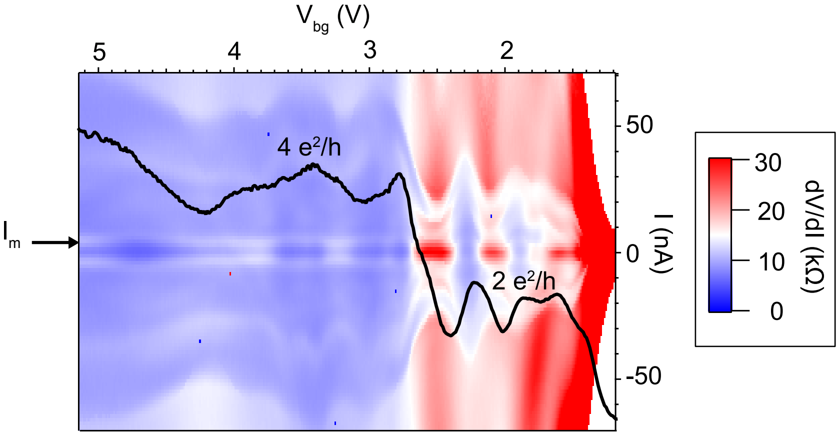

Figure 4.8: Differential resistance map as a function of current and gate voltage, obtained numerically from the dI/dV map of Figure 4.6**a** and simultaneously recorded map of the current I. The map gives a rough estimation of the critical current, by means of the proportional quantity I_m, which is a peak of dV/dI when the sample changes resistance in the Josephson regime. On top of this map, the normal-state conductance of the sample is plotted in black. The ideal conductance of each of the first two plateaus has been indicated (2 e^2/h and 4 e^2/h).

In contrast to the InSb nanowire QPC presented before, the InAs nanowire QPC shows a Josephson effect that is heavily modulated by FP resonances. This ballistic and coherent regime has been studied before [113], but never in correlation to FP oscillations in clearly quantized plateaus. The coherence length ξ_N in the nanowire can be estimated as $\xi_N = \hbar v_F/\pi\Delta$, in the limit when ξ_N is larger than the mean free path. From the subband spacing ΔE ~ 14 meV, estimated from the linear conductance characteristic in Figure 4.5**c** at B = 0 T and assuming the validity of the lever arm α = 0.006, one can estimate a similar Fermi energy in the onset of the second subband and extract $v_F = 4.6\times10^5$ m/s. This gives ξ_N = 600 nm, which means that the coherence length is larger than the length of the channel of the junction, which is 200 nm.

The maximum I_m current in the 2 e^2/h is ~ 4.5 nA, and it is ~ 6 nA in the 4 e^2/h plateau. Equation 2.3 sets a maximum I_c of 36 nA for the 2 e^2/h plateau and 72 nA for the 4 e^2/h plateau (assuming the same Δ = 150 μV). The maximum I_m values in each plateau are 8 - 13% of the ideal I_c value (bear in mind that we are not measuring here the experimental I_c value, which is larger than I_m as explained before). This difference can be attributed mainly to the decrease of normal conductance set by FP resonances, to the contact resistance of 2.3 kΩ, and to thermal fluctuations that reduce the switching current in the Josephson junction. I_m can drop significantly out-of-resonance -i.e., when a FP resonance does not enhance it.

These measurements highlight the differences in I_m between a QPC without FP resonances, as in the InSb nanowire of the previous section, and a QPC plagued with them. Surprisingly, Al contacts can produce high-transparency contacts, moderately hard gaps and a strong supercurrent correlated to the ballistic regime in both InAs and InSb nanowires. Through this we learn that the surface treatment chosen to remove the native oxide of the nanowire (Argon etching) before depositing Al is mild enough for superconducting and ballistic properties of both types of devices.

The evidence of 1D transport in this device was promising and motivated me to fabricate other devices with higher critical field superconductors, towards understanding superconducting 1D transport under high magnetic field.

4.4 Vanadium

Vanadium is a superconductor that has been rarely used to contact low-doping InAs or InSb nanowires. However, it has quasi-ideal properties for making high critical field hybrid devices. In Ref. [12], an InAs nanowire contacted by Vanadium was found to have a critical field of $B_c = 2$ T, and a gap size of $\Delta = 0.55$ mV.

In my work, and in strike contrast to the case of Al, devices made of InAs or InSb nanowires did show the same superconducting properties when contacted by V. In the next section I will show, however, that adding a 20 nm under-layer of Al before V deposition could improve the hardness of the gap in the case of InAs nanowires.

V contacts on InAs nanowires produced either devices with naturally-occurring quantum dots or devices plagued by FP resonances at low temperature. These contacts increased considerably the room-temperature two-terminal resistance of the devices -in the order of 1 MΩ. The yield of working devices was also low, of the order of 20 %. At low temperature, however, it was possible to obtain much lower resistances -as low as 5 kΩ. Al/V contacts, on the other hand, yielded only quantum dots at low temperature, and similar yields and room-temperature resistances.

Devices made out of InSb nanowires with pure V contacts, without the Al under-layer, had in general deteriorated transport characteristics. The room-temperature resistance of these devices was of the order of 30 to 100 kΩ, but with a low yield of around 20 to 40 %. They displayed noise and recurrent charge switches. Some of these devices were "quantum dot-ish", but most did not show definite signs of Coulomb blockade. In general, the lack of a clear system complicates the interpretation of the origin of soft gaps, since they can be the result of ill-defined barriers with considerable Andreev transport, and not necessarily reflect the quality of the interface. However, at least one of these devices showed a conductance plateau at zero magnetic field, which highlights the variability found in these devices.

InSb nanowires

I investigated Vanadium contacts on InSb nanowires during the first year of my thesis. In contrast to most of the devices presented in this document, these first-generation devices were fabricated on top of a silicon highly-doped substrate with a 300 nm-silicon oxide thermally-grown dielectric. This type of substrate could be used as a global backgate.

The Vanadium (V) contacts consisted on a tri-layer of Ti (2.5 nm), V (120 nm) and A (5 nm). Ti (Titanium) acted as a sticking layer for V, while Al was used as a capping layer to prevent the oxidation of V [114]. As we will see, these films yielded a decent-sized gap, with moderate hardness and moderate critical field when they were used to contact InSb nanowires.

The devices were cooled-down to 260 mK to find signatures of superconductivity. Unfortunately, their transport characteristics were found to be unstable and noisy. Some of the devices showed signs of Coulomb blockade, but their gate and bias instability did not allow to measure properly the corresponding charge stability diagrams. However, one of the devices displayed a conductance plateau at zero field, indicating that at least one of the nanowires maintained one-dimensional properties.

Figure 4.9**a** shows a linear conductance trace of this device -named here device A- as a function of the backgate taken at B = 0 T and T = 7 K. This trace has a clear plateau at 2 e^2/h (blue arrow) -no contact resistance was subtracted. At the onset of the plateau, the conductance is decreased from 2 e^2/h to 1.2 e^2/h (green arrow). This is reminiscent of the decrease in conductance at the onset of the 2 e^2/h in quantum point contacts in 2DEGs, termed the 0.7 anomaly [25]. Unfortunately, the gate instability and noise in this device did not allow to investigate this further.

Superconductivity, on the other hand, was present in all the devices. Figure 4.9**b** shows an example of a measurement of the gap in device A. This V - dI/dV curve was taken at B = 0 T and T = 260 mK. Symmetric peaks coming in pairs are observed, flanked by NDC. Their origin could be in ABS similar to those measured in the the case of devices with pure Al contacts (compare, for example, with Figure 4.2**a**); however, the features are broadened. This can be a consequence of a deteriorated interface, an ill-defined tunnel barrier or a large tunnel coupling. The peak-to-peak spacing (blue arrows) falls within the expected $4\Delta = 2.2$ meV of Vanadium.

Figure 4.9**c** shows the magnetic field dependence of the gap of device B. It closes at $B_c \sim 1.4$ T, which is below the expected critical field of 2 T reported in Ref. [12]. A lower bound of $\Delta \sim 0.38$ mV can be estimated (from the peak spacing of Device B). The hardness of the gap, in turn, can be evaluated at $G_N/G_S = 4$.

When the gate voltage pushed the devices to a more conductive regime, all of them displayed a Josephson supercurrent. In device B, for example, a Josephson switching current of 8 nA was measured at a normal resistance of 8 kΩ, giving an $I_m R_n$ product of 64 μV, which is one order of magnitude below Δ.

In summary, the gap was smaller than what Lee et al. achieved, and the critical field was also lower [12]. Additionally, the measured Josephson current was significantly below the expected value.

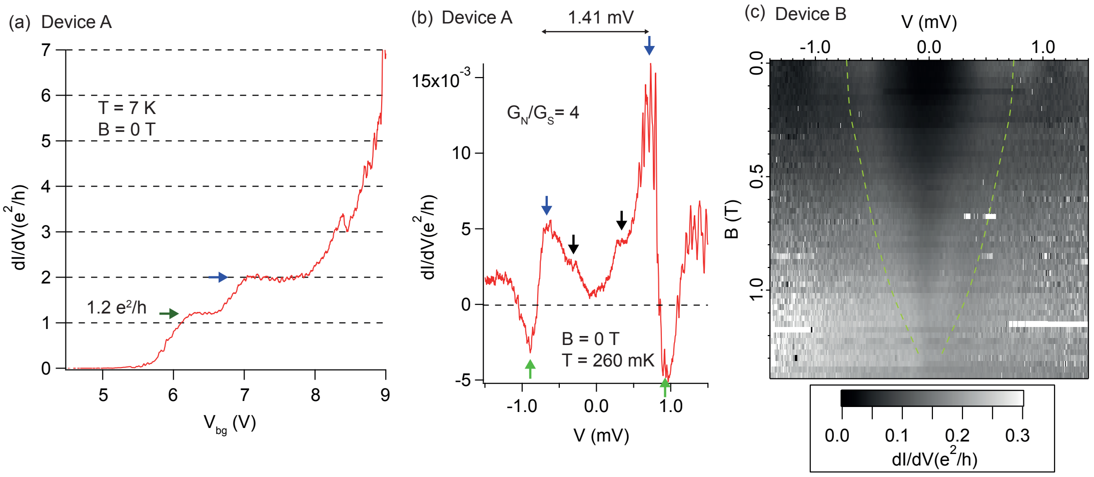

Figure 4.9: **(a)** Linear conductance of the V-InSb NW-V Device A at B = 0 T and T = 7 K. A blue arrow points to a plateau at 2 e^2/h, and a green arrow to a shoulder of reduced conductance (1.2 e^2/h) at the onset of the plateau. **(b)** V - dI/dV curves of device A, measured at B = 0 T and T = 260 mK. The subgap features come in pairs and are indicated by arrows of different colors. NDC points to the relationship of these features to ABS. **(c)** Field evolution of the gap in Device B. The gap features vanish at a critical field of ~ 1.4 T.

Irrespective of these superconducting properties, the noise and gate instabilities observed in these devices had to be improved if this nanowire / superconductor combination was to be used for studying 1D nanowires coupled to superconductors. In a second test, the substrate on which the device was made was changed. This time, on top of the 300 nm of thermally oxidized silicon with doped silicon as backgate, a set of local gates were fabricated, using hafnium oxide as the dielectric. The nanowires were deposited on top of hafnium oxide and then contacted as usual with the Vanadium tri-layer described above. The reasoning behind this was that changing the dielectric in contact with the nanowire would give cleaner transport characteristics.

Unfortunately, the new set of devices also had noise and gate instabilities. Analyzing this in retrospective, one can postulate the possibility that the highly-doped silicon substrate with the thermally oxidized silicon, which was used as a backgate in both cases, was probably the culprit. Two noise-free cases in which this substrate was not used support this claim. The first corresponds to the InSb-nanowire device with Al contacts described in Sections 4.3 and 3.3. This device was made on top of local fine gates with a hafnium oxide, on the surface of a non-doped silicon substrate without thermal oxide. The second corresponds to the InSb nanowire device with Al/V contacts mentioned in Section 3.2. This device was made on top of large local gates with a silicon nitride dielectric, which were in turn laying on the surface of a non-doped silicon substrate without thermal oxide.

InAs nanowires

A first test of InAs nanowires with pure Vanadium contacts was done on devices with local bottom gates separated from the nanowire by a 60 nm layer of silicon nitride. The "pure" Vanadium contacts were in reality -as for InSb nanowires- a tri-layer film of Titanium (2.5 nm), Vanadium (100 nm) and Aluminum (7.5 nm). This test was done at 330 mK.

Unfortunately, the yield of working devices was very low (< 10 %). The only working device at low temperature had no recognizable features of the gap, except for some low-energy peaks followed by NDC dips, non-symmetrically positioned with respect to zero-bias -and with non-symmetrical magnitude. These peaks fell at a voltage within $2\Delta = 1.1$ meV of Vanadium.

A second test of InAs nanowires devices contacted by this trilayer film was done at 4.2 K in a dipstick. This time, the devices were fabricated on top of local backgates with a 30 nm-thick hafnium oxide dielectric (instead of silicon nitride). Three out of four devices measured showed a Fabry-Pérot pattern. Surprisingly, the three devices had the same energy spacing of 5.0 ± 0.5 meV, which resulted in a cavity length L_c of around 40 nm. This cavity length could in principle have been set by two stacking faults in the InAs nanowires (the channel length was 200 nm). In contrast to the Al-NW-Al QPC device of the previous section, these Fabry-Pérot patterns were not modulating the conductance of quantized plateaus. Instead, the modulation occurred over a monotonically-growing background of conductance.

4.5 Aluminum/Vanadium bilayer

InSb nanowire QPC with a zero-bias anomaly from a quantum dot in parallel

In this part, I will present superconductivity measurements performed on the InSb nananowire device described in Section 3.2 of Chapter 3, at T = 15 mK in a dilution refrigerator equipped with a two-axis vector magnet. The contacts of this device were made of an evaporated tetra-layer thin film with the following composing materials: Ti (2.5 nm), Al (10 nm), V (100 nm) and Al (10 nm).

As a reminder, this device behaved as a QPC in *in parallel* with a quantum dot. Figure 4.10**a** shows the deconvoluted quantum dot conductance (black line) that was obtained by subtracting from the measured conductance (red line, at B = 0 T and T = 4 K) the QPC conductance obtained from the saddle point model (blue line). Two large Kondo resonances in the deconvoluted trace had been identified before, and are indicated in Figure 4.10**a** by a black circle/green asterisk and by a blue square/red triangle (i.e., the same symbols as in Section 3.2). The bias spectroscopy measurements of the superconducting gap shown in the first part of this section refer to the gate region indicated by the letter Q in this plot. It is worth noting that the QPC in parallel with the quantum dot is closed at this point (see the central inset of Figure 4.10).

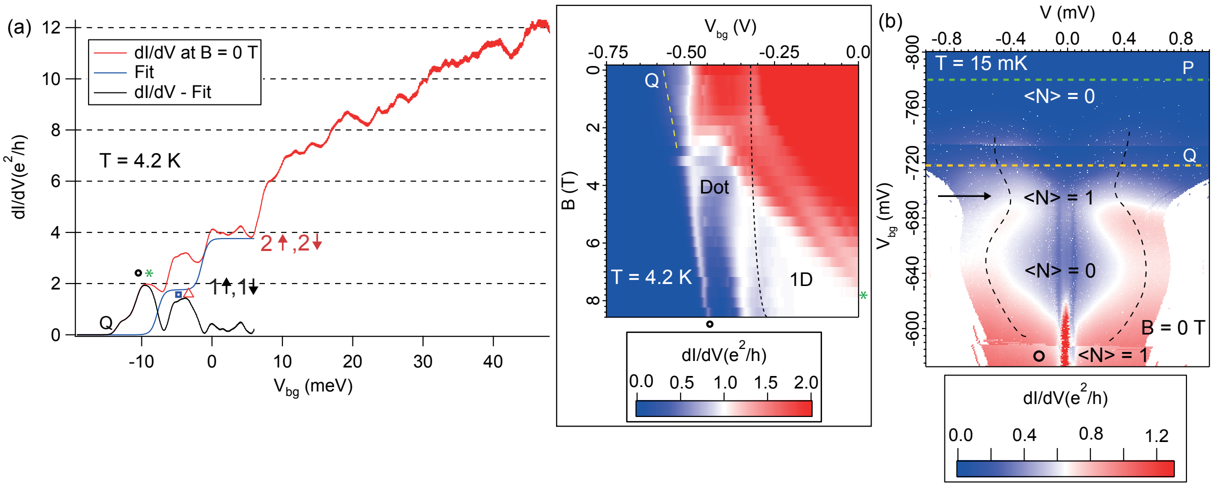

Figure 4.10: (a) Linear conductance at B = 0 T and T = 4.2 K (red line) measured in the Al/V-InSb NW-Al/V device presented in Section 3.2 of Chapter 3, plotted together with a fit to the saddle point model (blue line) and a subtraction of the first minus the second (black line). In addition to the features identified in Section 3.2, a letter Q has been added to indicate an additional resonance coming at the onset of conduction of the parallel quantum dot. Notice that the gate voltage has been converted to energy by using the lever-arm of the device. **Central inset**. Variation of Figure **a** at different colorscale, showing the field evolution of the resonance Q, whose right flank has been indicated by a yellow-dashed line. A black-dashed line divides dot conduction from dot conduction in parallel with 1D conduction. **(b)** Conductance map as a function of gate and bias voltages, taken at B = 0 T and T = 15 mK. Black-dashed lines follow the gate voltage dependence of ABS. The mean level occupation $< N >$ of all the Coulomb diamonds involved here -obtained from Coulomb peaks, Kondo resonances at T = 4.2 K and ABS behavior- is indicated as an aid to give sense to the motion with gate of the ABS. The absence of additional ABS indicate that the parallel 1D channel is closed in this map.

Figure 4.10**b** shows a map of the conductance at T = 15 mK as a function of the bias and the backgate voltages, taken at low bias and to the *left* of the black circle of Figure 4.10**a**. In this map, the black circle in the bottom corresponds to the same gate voltage at which the large Kondo resonance appears in Figure 4.10**b** (also indicated by a black circle). The mean occupation of the energy level of the dot within the bias window is $< N > = 1$ at this point. Exactly at the black circle there is a supercurrent zero-bias peak, which vanishes as the gate is swept towards more negative voltage and the tunnel asymmetry increases. When the asymmetry between the couplings of the dot to the leads is large enough, ABS appear in the $< N > = 0$ diamond right after the black circle. The gate-dependence of the ABS helps to identify the next diamond as $< N > = 1$. This mean occupation is confirmed by the existence of a Kondo resonance at this gate voltage, as it will be discussed later.

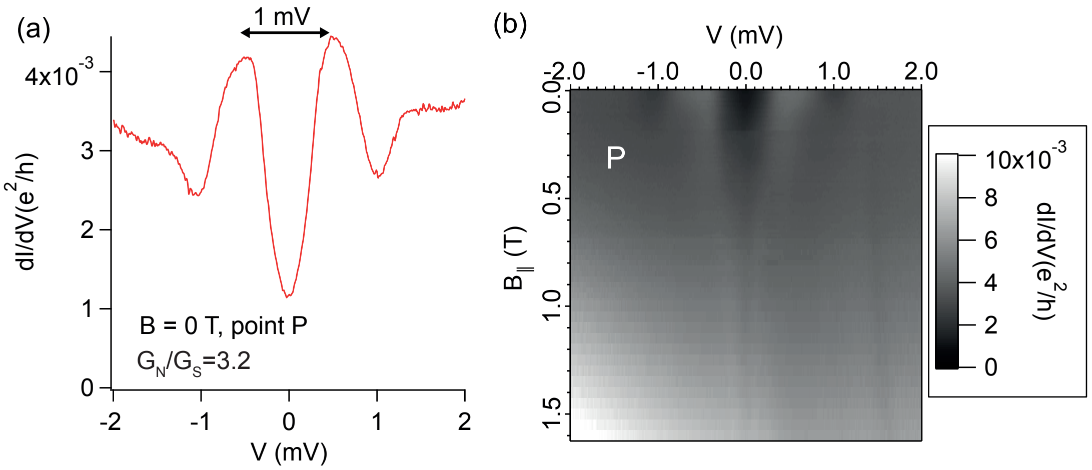

Figure 4.11: **(a)** V - dI/dV cut-line at gate point P (green-dashed line) of Figure 4.10**b**. The two peaks can be identified as ABS. The hardness of the gap is indicated. **(b)** Field dependence of the gap feature in **(a)**.

A zero-field V - dI/dV measurement of the superconducting gap through the green-dashed line (gate point P) in Figure 4.10**b** is shown in Figure 4.11**a**. The ABS features in this curve have a peak-to-peak separation of 1 mV and the G_S/G_N ratio is 3.2. The large peak-to-peak separation confirms that Vanadium is responsible for the superconductivity observed.

Figure 4.11**b** portrays the magnetic field evolution of these features. The ABS peaks close and decrease in visibility as the field increases, up to 0.8 T. At this field, they become two small peaks that close slowly with the magnetic field, and do not disappear in all the range of this measurement (up to 1.6 T).

Zero-bias anomaly under magnetic field

The magnetic field dependence at point Q, in the edge between $< N > = 0$ and $< N > = 1$, is startlingly different. Figures 4.12**a,b** show the magnetic field evolution of the V - dI/dV characteristic when the field is oriented *parallel* ($B_{||}$) to the nanowire. At around $B_{||}$ = 0.1 T, a zero bias peak emerges between the ABS features. As the field is further increased, the maximum of this zero-bias anomaly (ZBA) traces a slight arch that brings it back to zero bias at $B_{||}$ = 0.5 T (black dashed line in the traces of Figure 4.12**b**). Figure 4.12**c** shows the trace at $B_{||}$ = 0.5 T alone, to indicate that the peak is broad.

The bottom panels of Figure 4.12 correspond to a measurement such as the upper panels, but for a magnetic field oriented perpendicular to the nanowire ($B_\perp$. A ZBA is also observed for this magnetic field orientation (Figures 4.12**d,e**). Even though it decreases in magnitude, it does not fully vanish up to $B_\perp$ = 1 T, which was the maximum range of this measurement. In Figure 4.12**f**, one trace at $B_\perp$ = 1 T has been isolated, to show that this ZBA is much sharper and weaker than the one that appears in parallel field.

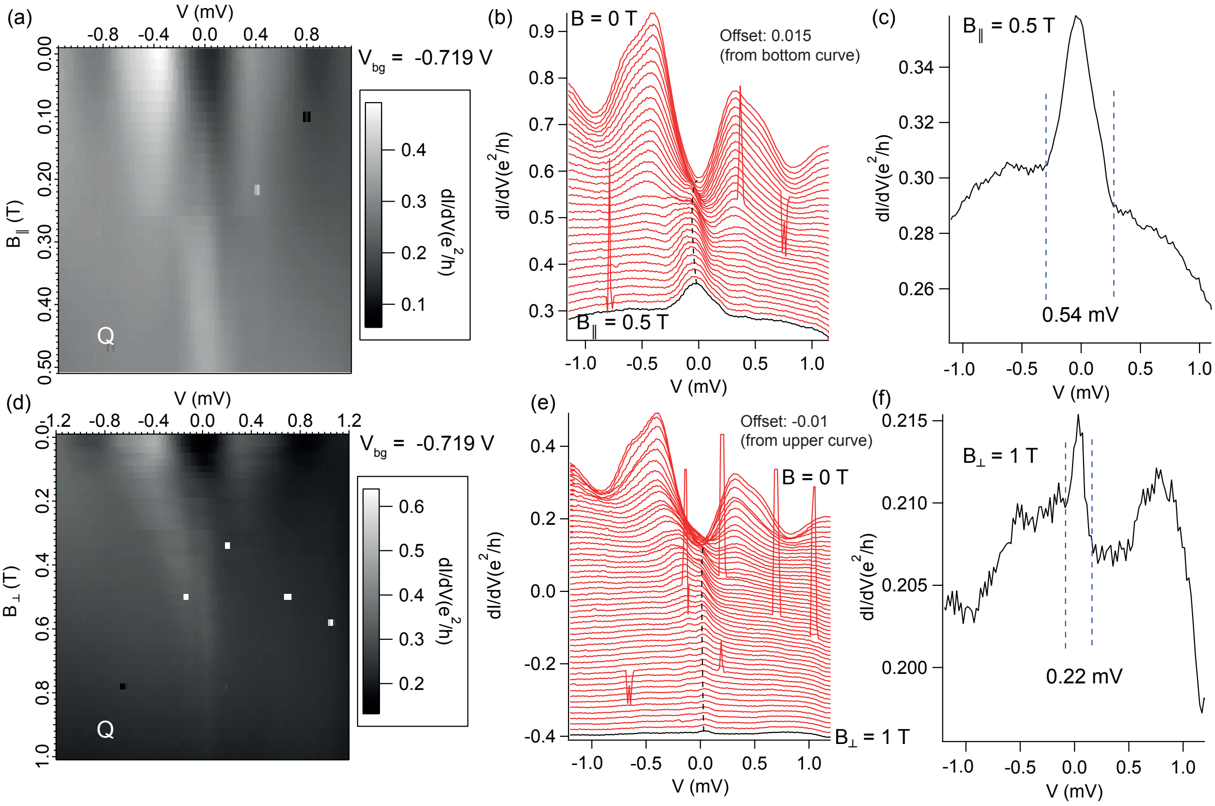

Figure 4.12: Magnetic field evolution of the low-bias V - dI/dV characteristic at the cut-line in point Q (yellow-dashed line) of Figure 4.10**b**, for **(a,b,c)** parallel and **(d,e,f)** perpendicular field orientation with respect to the axis of the nanowire. In both cases, a ZBP of different width emerges with magnetic field. (a,d) dI/dV maps as a function of bias and magnetic field B. (b,e) Cut-lines taken respectively from the maps (a,d), shown with an offset with respect to each other indicated in each plot. The curves at the largest field are indicated in black. (c,f) Curves at the largest field for each field orientation. The peak is broader when the orientation is **(c)** parallel than when it is **(f)** perpendicular.

This weaker ZBA is probably related to reflection-less tunneling from a disordered NS interface [115]. It has been observed before in N-NW-S devices [106]. In the case of our S-NW-S device, reflection-less tunneling gains importance when the gap populates with states as the field is boosted and turns effectively into an N-NW-S junction. As expected for reflection-less tunneling, the conductance of the ZBA under perpendicular field decreases steadily when the field is raised (from 0.3 T to 1.0 T). In contrast, in parallel field the ZBA increases its conductance as the field is raised, saturating at its maximum at around 0.5 T.

It was possible to learn more about the ZBA in parallel field by observing its gate dependence at various magnetic fields. Figure 4.13**a** shows a map of the conductance as a function of the bias and the backgate voltages, taken at $B_{||}$ = 0.3 T. In this map, the ZBA emerges from the crossing of two peaks (yellow dashed lines) that appear between the ABS at $B_{||} \sim 0.2$ T -they were absent at B

= 0 T and $B_{||}$ = 0.1 T. These peaks can be seen in the cuts taken from this map shown in Figure 4.13**b**. Each cut was taken through the dashed lines of the same color as each curve. ABS are indicated by green arrows, the satellite emerging inner peaks by black arrows, and the ZBA by red arrows. After the inner peaks cross, the ZBA tends to move to the right.

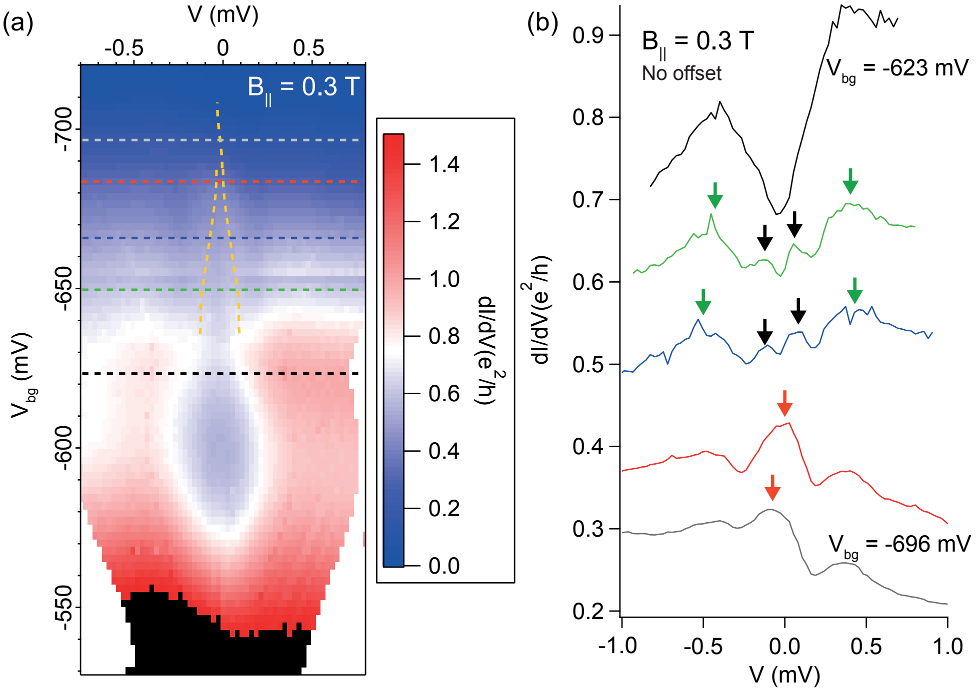

Figure 4.13: **(a)** Map of the gate evolution of the V - dI/dV characteristic at B = 0.3 T. A yellow dashed line indicates the motion with the gate voltage of the inner spin-split ABS. **(b)** Cut-lines taken from **(a)** at the gate point indicated by dashed lines of the same color as each curve. Green and black arrows point to the pairs of Zeeman-split ABS (green and black curves). The inner pairs merge and produce a ZBA (red arrow) in the red curve. The ZBA moves away from zero-bias when the ABS traverse the quantum phase transition (QPT).

The ZBA anomaly is visible at larger fields, all the way up to $B_{||}$ = 1.0 T. At $B_{||}$ = 0.5 T (Figures 4.14**a,b**), as the gate is swept towards negative voltages -from the upper traces to the bottom ones-, a positive bias peak emerges (green curve) and crosses zero-bias to turn into the ZBA anomaly (orange and blue curves), and then becomes a negative-bias peak (gray curve). In the conductance map of Figure 4.14**a**, the peak is indicated by a yellow dashed line. At this field and within the $< N > = 1$, the ZBA is the only subgap structure visible -the ABS side peaks have vanished.

Traces belonging to the $B_{||}$ = 1 T case are displayed in Figure 4.14**c**. When the peak is the furthest away from zero-bias, it is always below ± 0.1 mV, as measured at $B_{||}$ = 0.5 T, 0.6 T, 0.7 T, 0.8 T, 0.9 T and 1.0 T. At $B_{||}$ = 1.5 T, all signs of the ZBA have vanished, as seen in the traces of Figure 4.14**d**.

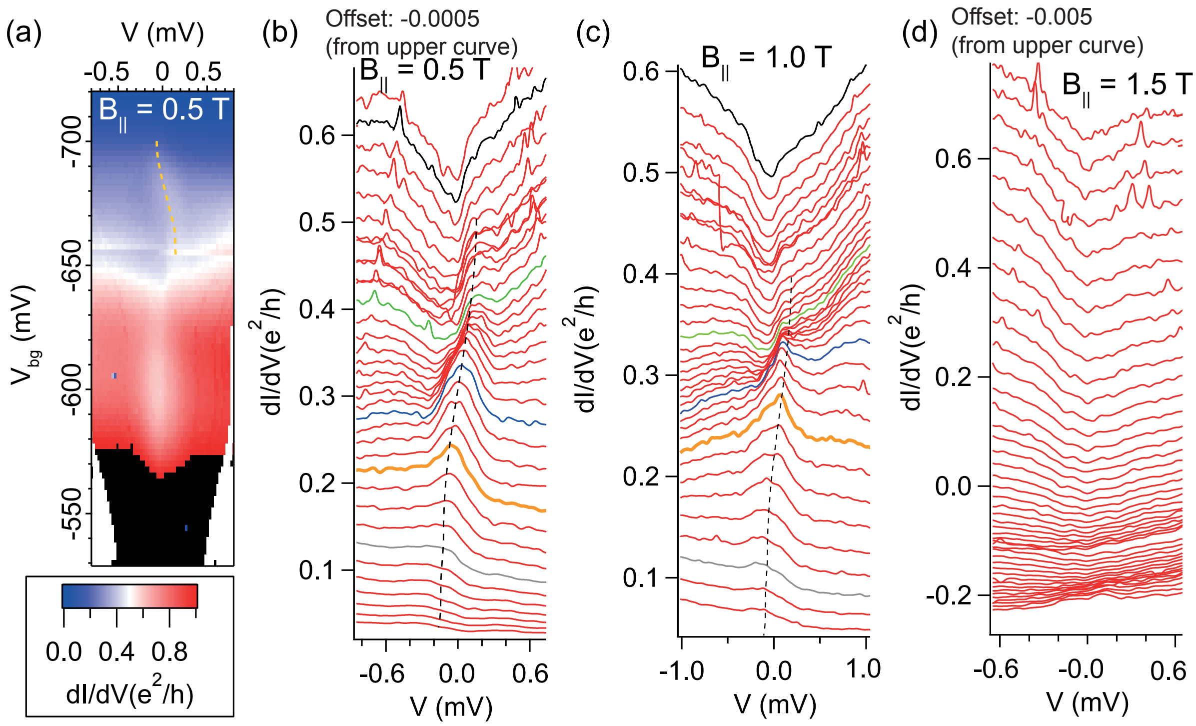

Figure 4.14: Gate evolution of the V - dI/dV characteristic at **(a,b)** $B_{||}$ = 0.5 T, **(c)** $B_{||}$ = 1 T and **(d)** $B_{||}$ = 1.5 T. In the map of **(a)**, a yellow-dashed line indicates the motion of the ZBA with the gate voltage. The curves of **(b,c,d)** are cut-lines taken from V_{bg} -0.58 V (upper curve) to V_{bg} -0.72 V (bottom curve). The curves in **(b,c)** were offset in a similar way we respect to each other, for visibility; the curves in **(d)** have a different offset. Some of the curves in **(b,c)** were colored differently, to illustrate the motion of the ZBA with gate voltage. With the same purpose, a black-dashed line was added on top of these curves.

A high-bias measurement in the gate range where the ZBA appears can also give us clues of its origin. Figure 4.15 shows V - dI/dV curves taken over a large bias window, at four different magnetic fields. At $B_{||}$ = 0.5 T, the ZBA anomaly is seen on top of a broader zero-bias peak, which belongs to a Kondo resonance. From the width of the resonance, which is broadened by the Zeeman energy, a Kondo temperature of ~ 9 K (~ 0.8 meV) is extracted. At B = 1.0 T, a weaker and broadened Kondo resonance is still observable (blue curve). At larger field (green and red curves), it splits with a g-factor $|g|$ ~ 25, which is comparable to what was measured for the other two Kondo resonances that appear after (black circle/green asterisk and blue square/red triangle of Figure 4.12**a**, see also Section 3.2). The existence of a Kondo resonance confirms that the ZBA occurs in a $< N > = 1$ dot level. The reason why this resonance coexists with superconductivity at large field may be in the finite density of states in the gap [11].

In a Josephson junction like this one, with a quantum dot bridging two superconducting leads, a supercurrent-related zero-bias peak (ZBP) is expected when the conductance is large. Here, the normal conductance is below 0.25 e^2/h, and there is no ZBP at zero field. Nevertheless, it is

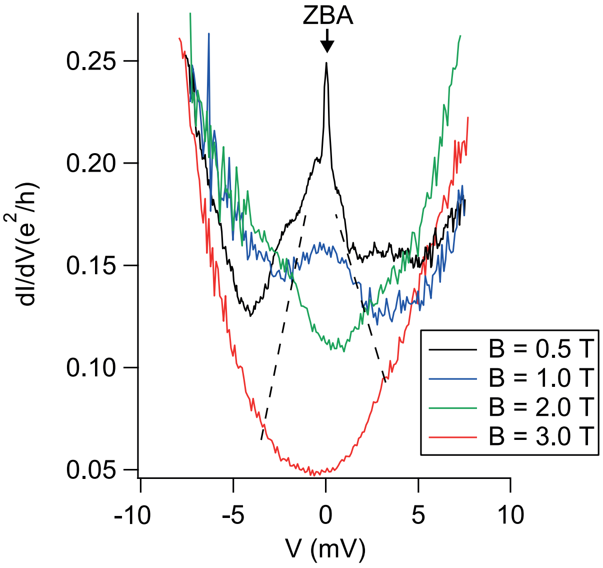

Figure 4.15: V - dI/dV traces at four different magnetic fields parallel to the nanowire: $B_{||}$ = 0.5 T (black curve), 1.0 T (blue curve), 2.0 T (green curve), 3.0 T (red curve) and 3.0 T. There is no offset in these curves. Black-dashed lines guide the eye to follow the Zeeman-splitting of the Kondo resonance seen in the black curve.

possible to see an emergent supercurrent ZBP with magnetic field when the mean-occupation is $< N > = 1$. The physics behind this is thoroughly explained in Chapters 5 and 6. The emergent zero-bias peak in this interpretation is a supercurrent associated with a π-junction. However, the ZBP arising from this transition should not move away from zero bias. The ZBA that is observed in this device slightly moves away from zero bias with both the magnetic field and the gate voltage, ruling out this interpretation.

The ZBA, instead, seems to appear from the Zeeman-splitting of ABS states belonging to the $< N > = 1$ Kondo-singlet ($|s\rangle$) diamond, exactly when the lowest spin-split $|d\rangle$ reaches the quantum phase transition (QPT) point [12]. The mechanism is summarized in the scheme of Figure 4.16. The peak-to-peak separation between the split-peak features in Figure 4.13**b**, corresponding to the green and black arrows in the green and blue curves, is ~ 0.4 mV. This is nearly the same as the Zeeman-splitting $E_z = |g|\mu_B B = 0.43$ mV expected at B = 0.3 T for $|g| = 25$. In the center of the $< N > = 1$ diamond, the ABS peaks are closer (black arrow of Figure 4.13**b**), and therefore by splitting with the magnetic field they will give raise to a zero-bias peak (ZBP). After the ZBP is established, increasing the magnetic field should make the peaks split again ($|d\rangle \rightarrow |s\rangle$ transition after the QPT), which is seen in our case as a slight deviation from zero-bias of the ZBA (Figures 4.12 and 4.14). The deviation is not as large as it should be (it should be as large as the Zeeman energy) because the closure of the gap pushes the ABS split-peaks to zero bias. For this picture to work, one needs to assume that there is a finite D.O.S. at the Fermi level in the gap that is probing

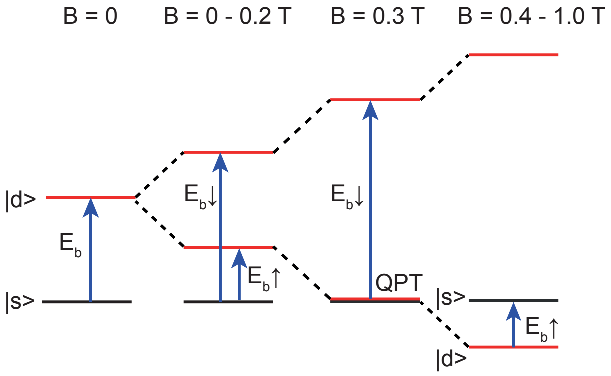

Figure 4.16: Zeeman-splitting of ABS induces changes in the ground state (Figure adapted from Ref. [12]). On top, the relevant magnetic fields for the Al/V-InSb NW-Al/V device are indicated. At zero field, the presence of a Kondo resonance in the device indicates that the occupation is zero and the ground state is a Kondo singlet $|s\rangle$. Only the transition $E_{b\uparrow}$ is seen in the data. At finite field, the $|d\rangle$ excited state Zeeman-splits, leading to two possible transitions which appear as a split-peak in the data. At a larger field ($B_{||}$ = 0.3 T), the lowest spin-resolved doublet crosses zero-energy and a QPT is occurs. The crossing appears as a ZBA in the data, with two satellite peaks that represent the $E_{b\downarrow}$ transition. These satellite peaks disappear at larger magnetic field, as the transition $E_{b\downarrow}$ becomes forbidden with the change of ground-state. The ZBA, on the other hand, shifts away from zero-bias when $E_{b\uparrow}$ increases. However, the field also reduces the gap, pushing E_b towards lower energy.

the ABS, which is expected for a soft gap as the one displayed by this device [11].

Let us not forget that these observations were made in an InSb nanowire that hosted a *quantum dot in parallel with a quantum point contact*. This system displayed clear plateaus of quantized conductance at large magnetic field (see Section 3.2). However, at low field, what may seem as the first 2 e^2/h plateau was in reality a Kondo resonance in the unitary limit from the quantum dot in parallel, which became the only conducting channel as the 1D parallel channel was closed at this point. It is at the onset of the 2 e^2/h "plateau" that the ZBA was found. This ZBA was not related to a Majorana bound state (MBS), but rather to trivial quantum dot - ABS. This observation is an example in which localization "hidden" in a seemingly 1D device can lead to a false signature of MBS.

Josephson effect through a QPC in parallel with a quantum dot

Figure 4.17**b** shows a current-biased map of the voltage drop through the sample as a function of the backgate voltage. To obtain the voltage drop through the sample, a series resistance of about 40 kΩ coming from the RC filters and the measuring circuitry was subtracted. The map was taken at B = 0 T and T = 15 mK. An I-V trace taken from the map is superposed in the plot, with the switching (I_s) and re-trapping (I_r) current identified. This map shows that I_s and I_r are modulated by the backgate voltage.

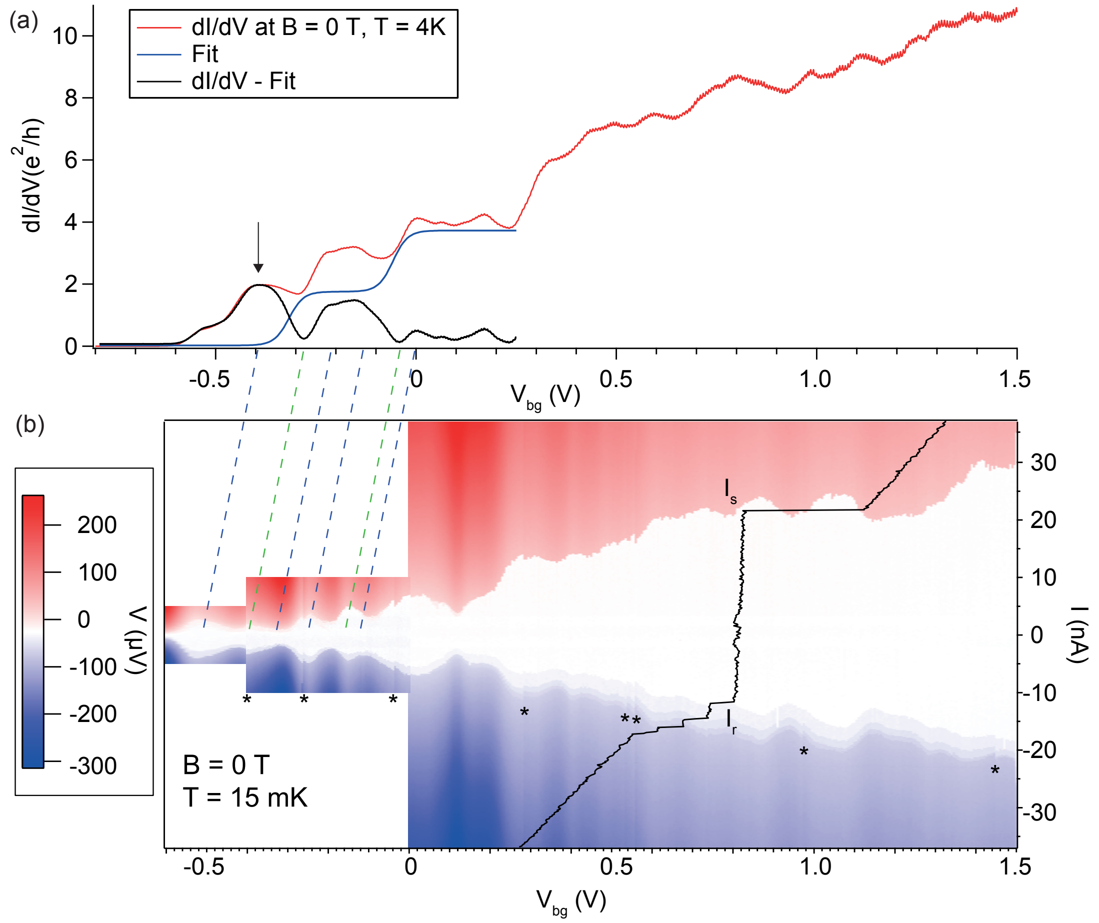

Figure 4.17: **(a)** Linear conductance at B = 0 T and T = 4 K (red line) measured in the Al/V-InSb NW-Al/V device presented in Section 3.2 of Chapter 3, plotted together with a fit to the saddle point model (blue line) and a subtraction of the first minus the second (black line). **(b)**. Map of the voltage drop across the sample as a function of the current applied. In white is a zero-voltage region indicating that a Josephson supercurrent is passing through the sample. The upper and lower borders of this region indicate the I_s and I_r currents. A cut-line that also indicates these two quantities has been superposed to the map. Black asterisks denote charge switches. The normal-state conductance in **(a)** has been correlated to the supercurrent in **(b)** through dashed lines. Blue (green) dashed lines are for in(out of)-resonance dot states, which can be either Kondo resonant [116][117] or level-resonant [94].

Figure 4.17**a** shows a plot of the linear conductance of the sample at B = 0 T and T = 4 K (red curve), together with a fit done using the saddle-point model (QPC characteristic, blue curve) and the deconvoluted quantum dot characteristic (black curve). By comparing the map and this plot, it can be seen that the modulation of the switching current comes from the modulation of the linear conductance [7]. Blue dashed lines were added to aid following some of the quantum dot resonances

---

[7] The supercurrent map has a few voltage offsets indicated by black asterisks, which complicate a one-to-one comparison between the linear conductance and the switching current.

in the conductance and compare them with supercurrent hills. The blue-dashed lines are tilted because there was a gate offset when the sample was grounded to go from a voltage-biased to a current-biased measurement. Interestingly, most of the supercurrent modulations are explained by the quantum dot characteristic (black curve).

In the open regime (V_{bg} = 1.5 V), an I_sR_n product of 39 μV is found, which is significantly lower than Δ of Vanadium (550 μV). In the unitary Kondo resonance (black arrow in 4.17**a**) -with charge switches taken into account-, the I_sR_n product is 65 μV. At this point, the QPC is closed, so the supercurrent is passing *only* through the QD. It is to be noted that the Kondo effect can enhance a supercurrent by developing a resonant path at zero energy [116][117], which explains the different I_sR_n product in both regimes.

InAs nanowires

A 20 nm Al under-layer deposited before Vanadium drastically improved the hardness of the measured superconducting gap in InAs nanowires. However, a 10 nm Al-underlayer was not enough to change the hardness appreciably.

10 nm Aluminum under-layer

InAs nanowires contacted by a tetra-layer thin film of Ti (2.5 nm), Al (10 nm), V (100 nm) and Al (10 nm) showed a quantum dot characteristic and soft gaps. The devices were two-terminal and had one local backgate, which was separated from the nanowires by 30 nm of hafnium oxide.

The magnetic field dependence of the gap is shown in the conductance map of Figure 4.18**a** and in the traces of Figure 4.18**b**. In the map, measured at 260 mK, the black-dashed lines serve as a guide to follow the field dependence of two peaks related to the gap. The gap closed at a critical field of B_c = 2.1 T, significantly larger to what was found without the Al under-layer.

The gap is clearly soft, having a G_N/G_S ratio of ~2.5 (this value was confirmed by measuring three other devices).

Since both the gap size and its critical field are much larger than anything that can be attributed to Al, it is reasonable to say that the 10 nm of Al did not affect much the superconducting properties of V. However, they certainly did not contribute to see transparent regimes in these nanowires (no supercurrent was observed), nor to obtain a harder gap.

20 nm Aluminum under-layer

A 20 nm aluminum under-layer could significantly improve the hardness of the gap. Unfortunately, I could not obtain QPCs in any of the devices that I measured -a quantum dot behavior was the rule. The devices presented in this part were two-terminal and had one local backgate, which was

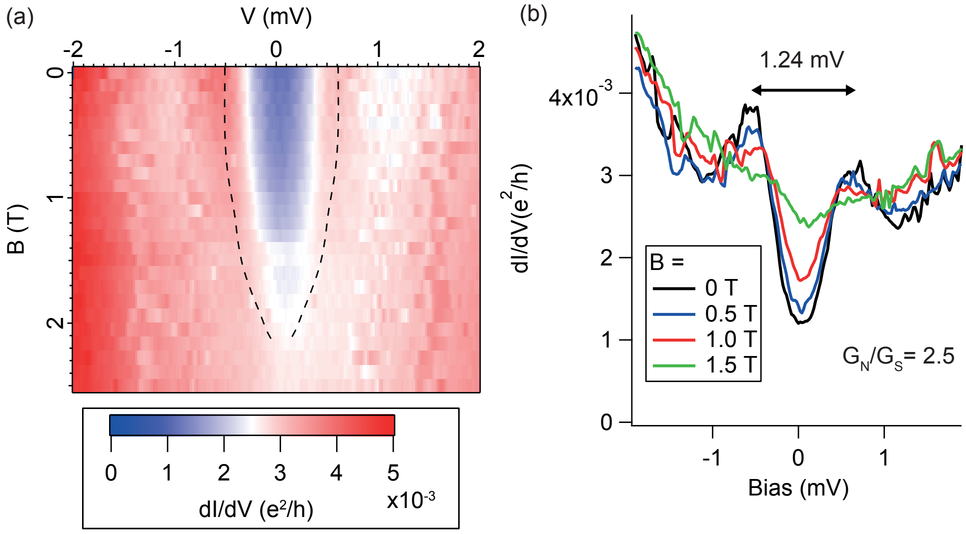

Figure 4.18: **(a)** Map of the magnetic field evolution of the low-bias V - dI/dV characteristic of an Al/V-InAs NW-Al/V device with a 10 nm Al under-layer. The critical field (B_c = 2.1 T) is the one expected for a V film contacting a nanowire without an Al under-layer [12]. **(b)** Cut-lines from **(a)**.

separated from the nanowire by a 30 nm film of hafnium oxide. They were all measured in the same cool-down, at 330 mK.

Figure 4.19**a** shows a typical conductance map of one of the devices, measured at low-bias and at zero field, as a function of the backgate. Some pairs of subgap ABS (pointed by green arrows), symmetric around zero bias, are seen going through different consecutive charge states. A vertical trace of a pair of these subgap states taken at the black dashed line of this map is shown in Figure 4.19**b**.

The curve is reminiscent of the gap spectroscopy measurement in devices with pure Al contacts, described in the previous section. The peak-to-peak separation measured is 1.48 mV, which is much larger than anything that can be attributed to Al. In fact, this peak-to-peak spacing is 150 % larger than what was observed with a 10 nm Al under-layer. This implies that vanadium is playing an important role in defining the size of the gap, thanks to the thicker Al under-layer. The energy spacing between the peaks, on the other hand, was gate and device-dependent, as expected for ABS.

I measured the hardness of the gap from the data in Figure 4.19**b**, by taking the average of G_N at V = ±2 mV and dividing it by the zero-bias conductance. I found a G_N/G_S **ratio of 29**, which is comparatively larger than the one obtained in all Al or V-contacted nanowire devices shown in the previous section. In fact, the hardness of the gap in this device is comparable to the best results reported in the literature for hybrid nanowire devices [84][85]. The hardness of the gap was confirmed by measurements in three other devices, which gave ratios G_N/G_S of the order of 20 to

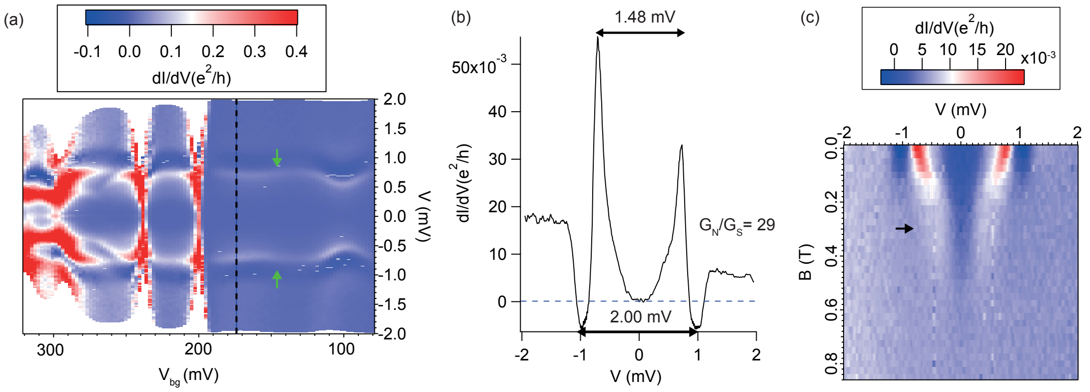

Figure 4.19: (a) Low-bias conductance map of an Al/V-InAs NW-Al/V device (20 nm Al under-layer) as a function of the gate and bias voltages. Symmetric signatures of ABS are indicated by a green arrows. **(b)** V - dI/dV cut-line taken at the black-dashed line in **(a)**. The hardness of the gap is $G_N/G_S = 29$, an astonishing value in pair with the best results achieved in hybrid nanowire devices so far [84][85]. **(c)** Magnetic field evolution of the V - dI/dV characteristic at low-bias. The black arrow points to a change in the pace of the closing of the ABS features, probably due to the inverse proximity effect of the 20 nm Al under-layer.

30. These values were obtained through gap spectroscopy in the middle of low-coupling Coulomb diamonds, such as the one of Figure 4.19**a**. Adding a 20 nm Al under-layer allows obtaining a gap which is at least one order of magnitude *harder* than the gap obtained with a 10 nm Al under-layer.

I also measured the magnetic field dependence of the gap, at a gate voltage point inside of the rightmost diamond of Figure 4.19**a**. This measurement, which consists in taking V - dI/dV curves at various magnetic fields, is shown in Figure 4.19**c**. Interestingly, as the field is raised, the gap starts to close initially with a rather fast pace. Then at B ∼ 0.3 T (black arrow) it continues to close but with a slower pace. This trend continues until the gap fully vanishes at $B_c = 0.54$ T. This critical field is much lower than the case with a 10 nm Al under-layer. These two observations -a lower B_c and a two different paces for the closure of the gap- probably come from the inverse proximity effect by the thicker 20 nm Al under-layer. This is not good news if this combination is to be used for high critical field hybrid nanowire devices.

It was also possible to see a Josephson current in a device that could be gated to a more open regime. For obtaining the Josephson current, I recorded the voltage drop through the junction in a two-terminal current-biased configuration. Figure 4.20**a** shows a map of the voltage -from which I subtracted a resistance of around 50 kΩ from the RC filters and the measuring circuitry- as a function of the current and the backgate voltage, taken at B = 0 T. In this map, the zero-resistance state appears in white. The two green arrows in the map point to the current at which the junction becomes dissipative. On top of this map, I superposed one I - V trace (black curve), in which I indicated the switching (I_s) and re-trapping (I_r) currents. From the map, it is clearly seen that the switching current depends on the gate, as it is the case in these type of nanowire Josephson junctions measured in other works [109].

Unfortunately, I found that the $I_c R_n$ product of this junction was very low, of just 100 μV. This is 30 times less than that of a tunnel Josephson junction with vanadium leads, assuming Δ = 550 μV.

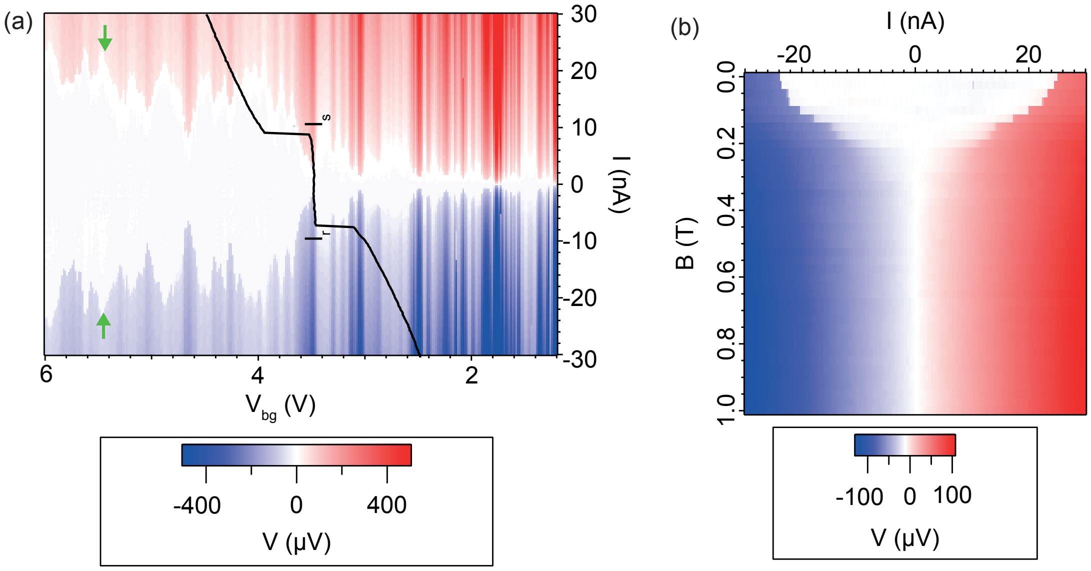

Figure 4.20: **(a)** Map of the voltage drop through the current-biased Al/V-InAs NW-Al/V (20 nm Al under-layer) sample, as a function of the gate voltage. The white-colored region indicated a zero voltage state, where supercurrent flows. A cut-line (black curve) has added on top of the map to identify the switching (I_s) and re-trapping (I_r) currents. **(b)** Evolution of the supercurrent with magnetic field.

I also measured the magnetic field dependence of the Josephson current. This measurement is displayed in Figure 4.20**b**, which is a map of the voltage drop trough the junction as a function of the current and the magnetic field. The supercurrent vanishes at a critical field of approximately 0.3 T. Curiously, this agrees with the field at which the closure of the gap with the field changed pace in Figure 4.19**c**.

These results show that a 20 nm Al layer deposited before V can improve significantly the size and hardness of the superconducting gap, and make possible the passage of a supercurrent through the junction, as compared to cases without the under-layer or with just 10 nm of under-layer. However, for the purpose of studying superconductivity through a one-dimensional channel, this was not enough, since these devices did not produce QPCs. Moreover, the Al under-layer diminished the critical field of V from 2.2 T (for a 10 nm Al under-layer) to 0.54 T.

4.6 Niobium/Tantalum bilayers

Tantalum on InAs nanowires

Pure Tantalum (Ta) films could produce good contacts with InAs nanowires [8] and sometimes ballistic transport at low temperature. The best example of the latter is the Ta/InAs nanowire device of Chapter 5, which hosted a QPC or a QD depending on the configuration of the gates. The critical field of the contacts was typically around 1.6 T - 1.8 T, and the Josephson effect could be measured at fields as large as 1.4 T at 15 mK.

Ta has the disadvantage that its critical temperature is low -around 0.7 K-, which is probably due to a crystallization of the beta phase, instead of the high T_c (4.3 K) alpha bcc-phase [118]. This was no surprise, since Ta sputtered on silicon was expected to crystallize in the low T_c beta phase, as shown in Ref. [119]. The Ta films that I evaporated had a room temperature resistivity of the order of 120 ± 25 $\mu\Omega$.cm, which is of the same order as the resistivity measured in beta-phase Ta films *sputtered* on silicon [119]. The low T_c resulted in a small superconductor gap in Ta/InAs nanowire devices, of the order of 70 to 80 μV.

Ta contacts present an additional difficulty. Evaporated Ta films are hard to lift using the traditional lift-off procedure described in the Chapter A. This resulted in a low yield of working InAs nanowire devices, of around 15 %. Three different resists were used to try improving this: PMMA bilayers, MMA/PMMA bilayers and ZEP, without significant differences. The probable cause of this lift-off issue is the baking of the resist by the hot Ta in the evaporation chamber.

Niobium/Tantalum on InAs nanowires

Previous work on Ta films sputtered on silicon substrates had shown that a 10 nm Niobium (Nb) under-layer sputtered before sputtering Ta resulted in an increase of the alpha-phase, and consequently a large T_c (of 4.3 K) [119]. Inspired by this work, I set to investigate if the same could be achieved by *evaporating* Nb before Ta.

I evaporated -by electron beam- thin films of Nb/Ta at 1×10^{-7} mbar, at rates of deposition of 0.75 nm/s for Nb and 0.5 nm/s for Ta. Given that it was not certain that the Nb under-layer would increase the T_c of Ta by *evaporation*, I first varied the thickness of the Nb under-layer, while keeping constant the thickness of Ta at 80 nm. Table 4.1 summarizes the results of this first test. On one hand, an increase of the T_c was observed for a Nb underlayer thickness of 5 nm and 10 nm. On the other hand, there appears to be no correlation between the room temperature resistivity and T_c.

---

[8] The contact with InSb nanowires was not tested.

Nb/Ta thickness (nm)	ρ at 300 K ($\mu\Omega$.cm)	T_c
0 / 80	120 ± 5	0.7
2.5 / 80	34 ± 7	0.92
5 / 80	17 ± 5	1.915
10 / 80	74 ± 9	1.9
20 / 80	140 ± 9	0.98

Table 4.1: Thickness influence on the room temperature resistivity (ρ) and critical temperature (T_c) of evaporated Nb/Ta bilayers.

Additionally, a characterization of the critical field of the supercurrent through the 5 nm/ 80 nm Nb/Ta at T = 300 mK was made. In the in-plane direction, I found $B_{c||}$ = 2 T, while in the out-of plane direction, $B_{c\perp}$ = 1.62 T.

After this test, I proceeded to make devices consisting on InAs nanowires with evaporated 5 nm/ 80 nm Nb/Ta contacts. I privileged this thickness because of the large T_c obtained in thin films without lift-off, and because of the low thickness of Nb needed to produce this T_c.

Through bias spectroscopy, I obtained signs that the gap was doubled with respect to the 70 - 80 μV gap measured in InAs nanowire devices without the Nb underlayer. Figure 4.21**a** shows the gap obtained in one these devices -named Device 1. The device was a S-NW-S junction equipped with a local backgate isolated from the junction by 10 nm of hafnium oxide dielectric. Δ was found to be 155 μeV, and the hardness of the gap was evaluated at G_N/G_S = 6.9.

It was also relevant to find out if the large critical field observed in thin films was preserved in these devices. Figure 4.21**b** shows the magnetic field evolution of the gap. A faint signature of the gap still remains up to 2 T, showing that it is indeed the case.

All the InAs nanowire devices had naturally-occurring quantum dots. Figure 4.21**b** shows a fine example of a conductance map (vs. bias and backgate voltage) of a second device exhibiting Coulomb diamonds (Device 2).

The devices also exhibited the Josephson effect at large coupling, surviving up to large magnetic field, which presented me with the opportunity of performing an experiment similar to the one in Chapter 6 in a system with twice the gap, and thus a larger Josephson current [9]. Unfortunately, I could not find in these devices a regime with the adequate Γ/U ratio [10]; i.e., close enough to the 0 → π phase transition at zero-field. I found instead two limiting cases. Either 1) the Josephson junction was already a π-junction, in which case the ground-state was a doublet and increasing the magnetic field would not change that ground-state or 2) at zero field it was a 0-junction so

---

[9] It is recommended to read Chapters 5 and 6 before continuing with the discussion that follows.

[10] A larger superconducting gap pushes the 0 → π phase transition point to a value Γ/U that is consequently larger [120]. This happens because the doublet-ground state region of the phase diagram of Figure 6.1 (Chapter 6) enlarges. Thus, Nb/Ta and Ta quantum dot devices will have different phase diagrams for the same charging energy.

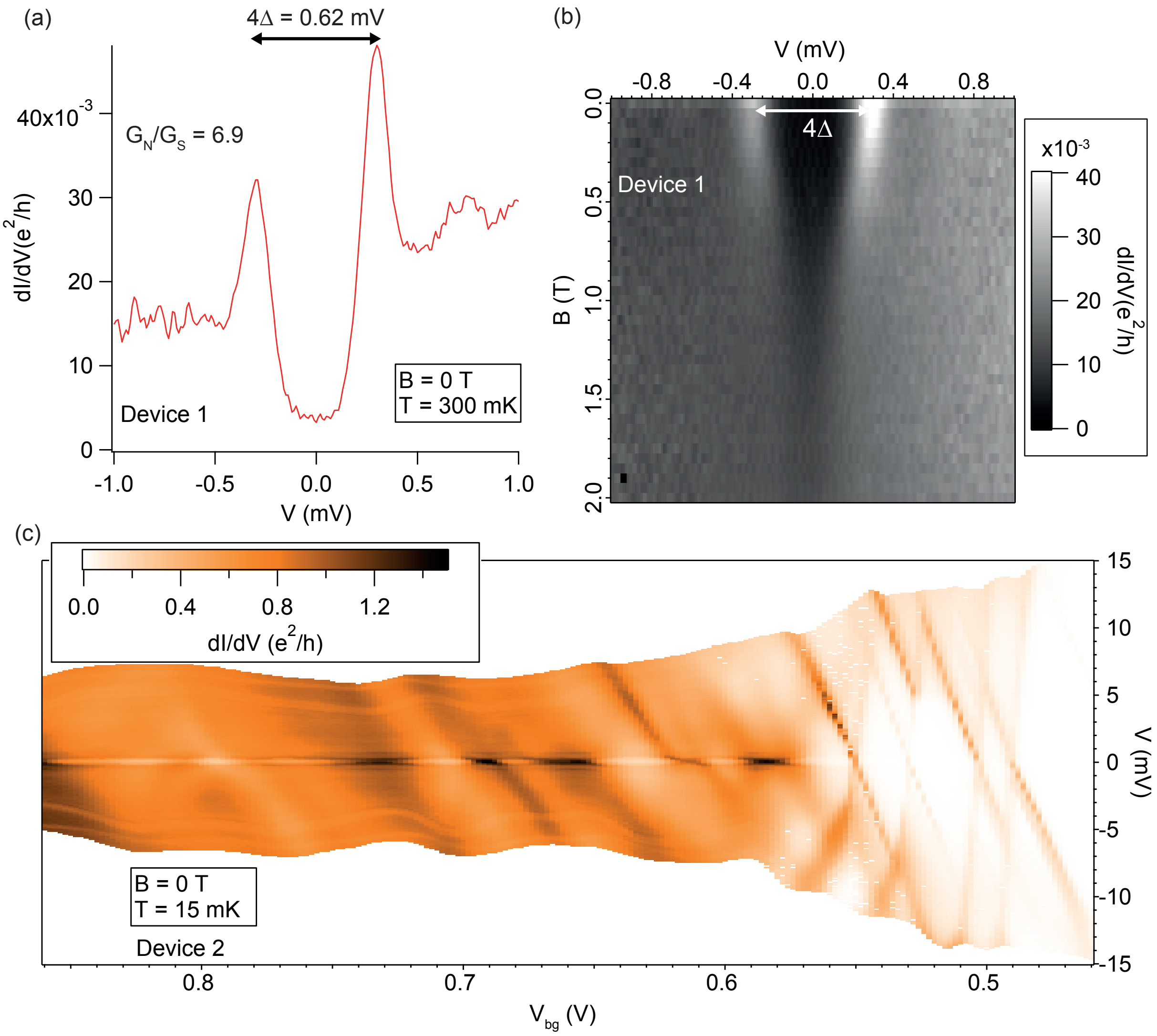

Figure 4.21: (a) Low-bias V - dI/dV trace at zero field, showing a spectroscopy of the gap in a Nb/Ta-InAs NW-Nb/Ta device (Device 1), measured at T = 300 mK. **(b)** Magnetic field evolution of the V - dI/dV characteristic. The gap did not close up to B = 2 T, implying a B_c > 2 T. **(c)** Conductance map as a function of gate and bias voltage in another Nb/Ta-InAs NW-Nb/Ta device (Device 2), measured at T = 15 mK and B = 0 T. According to this map, the device behaves as a quantum dot.

well-coupled that at a magnetic field of B = 1.2 T -i.e., near the field where supercurrent could not be observed anymore at any gate voltage- the $0 \longrightarrow \pi$ transition was not yet reached.

Figure 4.22 shows raw-data conductance maps as a function of gate and bias voltage, illustrating these two limiting cases. In these maps, as explained in Section 5.5 of Chapter 5, the voltage at which the conductance of the sample switches from $1/R_s$ -where R_s is the series resistance given by the RC filters and the current amplifier- to a smaller value indicates a transition from a zero

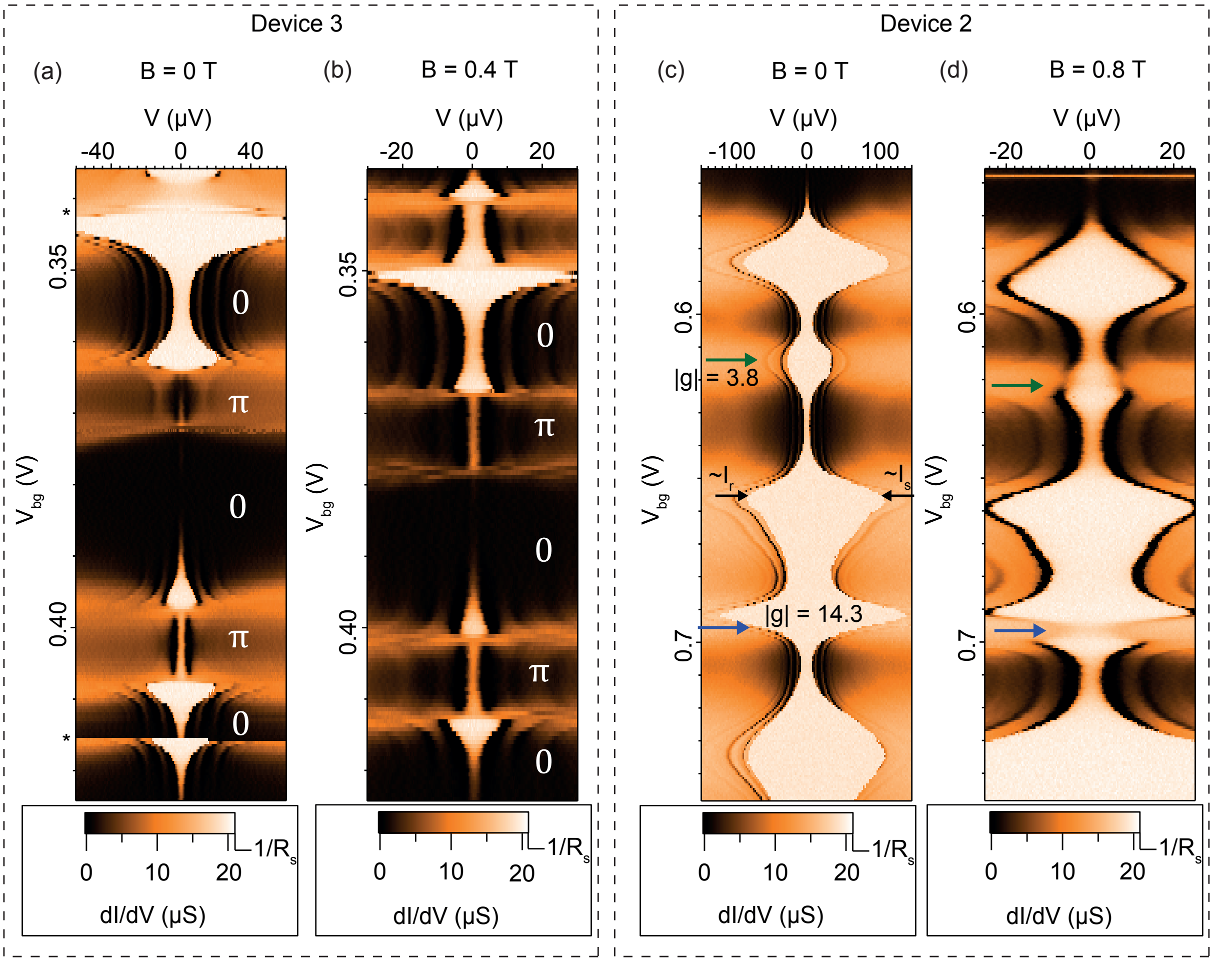

Figure 4.22: Conductance maps as a function of bias a gate voltages from two different devices (**(a,b)** Device 3 and **(c,d)** Device 2), measured at T = 15 mK and different magnetic field: B = **(a)** 0 T, **(b)** 0.4 T, **(c)** 0 T, **(d)** 0.8 T. In the case of Device 3, all the singly-occupied levels have a doublet ground-state at zero field **(a)**, and applying a magnetic field does not change this ground state **(b)**. In the case of Device 2, the singly-occupied levels have a Kondo singlet ground-state at zero field **(c)**. Applying a magnetic field can in principle change this ground state to a doublet. However, **(d)** this is not seen because the g-factor is not large enough or because Γ is not low enough to see the $|s\rangle \rightarrow |d\rangle$ QPT before killing superconductivity with a large field. The g-factors of the diamonds that show a decrease of supercurrent with magnetic field but not a QPT are indicated in **(c)**, as well as the voltages proportional to I_s and I_r.

resistance state (caused by supercurrent) to a dissipative state. In turn, this voltage, by virtue of R_s, which turns the voltage-biased junction into an effectively current-biased junction, is proportional to the switching current. As an example, the voltages proportional to the switching (I_s) and the re-trapping (I_r) currents are indicated in Figure 4.22**c** by black arrows for one gate point. When the color in the map is white, the junction is in the supercurrent branch. This branch is positioned around zero-bias in all the maps.

The first limiting case, when Γ/U is so small that the supercurrent in the $< N > = 1$ diamonds is always π independently of the field, is shown in Figures 4.22**a,b** for B = 0 T and B = 0.4 T -corresponding to a third device, named Device 3. The magnetic dependence of the Coulomb peaks, not shown here, allowed to identify the singlet and doublet diamonds. In the maps, the diamonds are identified according to the phase of the supercurrent, either 0 or π. There is a sharp decrease of the supercurrent in the phase boundaries, which also helps to identify the phase of the supercurrent. At B = 0 T and B = 0.4 T -and all the way to B = 1.2 T, not shown here- the supercurrent does not transit, because the π phase has already been attained at zero field.

The second limiting case, when Γ/U is so large that the supercurrent in the $< N > = 1$ diamonds does not experience a $0 \rightarrow \pi$ phase transition before the supercurrent over all the gate range vanishes, is shown in Figures 4.22**c,d** -corresponding to Device 2, whose Coulomb diamonds were shown in Figure 4.21**b**. This case is pointed by a blue arrow. The supercurrent in the "middle" of the diamond has still not transited at B = 0.8 T, and it does not transit up to B = 1.2 T -not shown here.

A third limiting case, not discussed above, can exist. Γ/U can be small enough to produce a low starting critical current close the phase transition, but if the Zeeman energy is not large enough compared with the charging energy U, then no transition will be observed. This can happen when the g-factor of the diamond is not large enough, in which case the doublet region does not grow fast enough for a phase transition to be observed before the critical field is reached. This particular case is pointed by a green arrow in Figures 4.22**c,d**. Even though the starting supercurrent is smaller than in the blue arrow case, the transition is not yet observed at B = 0.8 T. This happens because the g-factor of this diamond is 3.8 times smaller than the g-factor of the diamond pointed by the blue arrow.

These results point to the interesting physics at high magnetic field that can be accessed in the supercurrent regime when a nanowire can be contacted by a high critical field superconductor. Two striking examples of this will be shown in Chapters 5 and 6. Additionally, it was demonstrated that it is possible to raise the Δ of β-phase Ta from 80 μV (see 5) to 155 μV by adding a 5nm Nb under-layer, while keeping a comparably high critical field.

4.7 Comparison of superconductor/nanowire combinations

Tables 4.2 and 4.3 summarize the superconducting and transport properties of InAs and InSb nanowires -respectively- contacted by various superconductors. Promising routes of exploration for high-critical field, hard-gap superconductivity and sizable supercurrent are highlighted in blue. Promising routes of exploration of 1D physics in combination with low-critical field superconductivity are, in turn, highlighted in orange.

Superconductor	Δ (**μV**)	G_N/G_S	B_c **(T)**	**System**
Al	140 - 170	3.5	-	QPC w/FP
V	-	-	-	FP or disordered QD
10 nm Al / V	310	2.5	2.1 T	QD
20 nm Al / V	370 - 500	29	0.54 T	QD
Ta	80	5	1.8 T	QPC or QD
Nb / Ta	155	6.9	>2 T	QD

Table 4.2: Summary of superconducting and transport properties of InAs nanowires when contacted by different superconducting thin films. QD, FP and QPC stand, respectively, for quantum dot, Fabry-Pérot and quantum point contact. The data for Ta is presented in Chapter 5.

Superconductor	Δ (**μV**)	G_N/G_S	B_c **(T)**	**System**
Al	140 - 170	10	0.06	QPC or QD
V	380	4	1.4	noisy QPC or QD
10 nm Al / V	250	3.2	>1.5 T	QPC in || w/ QD

Table 4.3: Summary of superconducting and transport properties of InSb nanowires when contacted by different superconducting thin films.

In the case of InAs nanowires, QPCs could only be obtained with Al and Ta contacts. The reason for this may be in principle luck, as these nanowires were shown to have random stacking faults in TEM images, which could increase the possibility of localization.

Al/V (20 nm under-layer of Al) and Nb/Ta contacts yielded the best combination of gap hardness, Josephson current and critical field of all superconductors studied in coupling to InAs nanowires. Al/V could certainly be useful to pursue experiments such as those shown in 6. If the lift-off issues with Nb/Ta or Ta films are resolved, they could become excellent alternatives, which should also be tried with InSb nanowires.

In the case of InSb nanowires, all superconductors studied could yield QPCs. Some of the issues encountered may be solved in rather simple ways. The noise issue found in V/InSb NW devices should be improved if the substrate used does not contain a thermal oxide that could trap oxides. The soft-gap issue of V and Al/V with a 10 nm Al under-layer InSb nanowire devices could in principle be resolved like in the case of InAs nanowires; i.e., by using a thicker Al under-layer of 20 nm. These are perspectives worth researching.

One reason for the need of a 20 nm - thick Al under-layer before depositing V for improving the hardness of the gap in InAs nanowires could be in the large thickness of the V films used. In Ref. [12], V did not need an Al-underlayer to provide hard gaps. However, the InAs nanowires used there were thinner and thus a thinner V layer of 45 nm could be used. In the InAs and InSb nanowire devices presented in this chapter, 100 nm - thick V films were used. A thicker film could pose larger strain on the nanowire, and the Al under-layer may help to release this strain. In Ref.

[121], 90 nm - diameter InAs nanowires were contacted with a 120 nm - thick V film. A good Josephson coupling was obtained; however, it is to be noted that the nanowires were doped with Se in that work. Interestingly, the 120 nm - thick V film had a 15 nm - thick Ti under-layer, pointing again towards the need of an under-layer when using thick V films on semiconductor nanowires.

4.8 Conclusions

- A 1D InSb nanowire can host a quantum dot in parallel which can exhibit a zero-bias anomaly (ZBA) in conductance emerging in the superconducting gap when an external magnetic field is applied. The origin of this ZBA was linked to spin-resolved Andreev bound states crossing the Fermi level.
- A supercurrent linked to a quantized conductance was measured in an InSb nanowire with Al contacts. The values of the current were two to four times larger than the state-of-the-art in III-V nanowire QPCs. However, the current was reduced with respect to the data for Ge/Si nanowires.
- A Fabry-Pérot modulated supercurrent was obtained in an InAs nanowire QPC with Al contacts.
- Pure vanadium contacts led to soft gaps in both InAs and InSb nanowires. Depositing a 10 nm under-layer of Al was not enough to improve the hardness of the gap in either case. However, a 20 nm Al under-layer before depositing V could produce a hard gap in InAs nanowires. A conductance suppression inside of the gap of 29 was measured, which is a value comparable to the state of the art in gap hardness. It was suggested that Al could relax strain on the nanowire induced by the 100 nm - thick V film, improving in this way the nanowire / superconductor interface and the corresponding gap hardness. The question that remains open is if a 20 nm Al under-layer could also improve the hardness of the gap in V-contacted InSb nanowires.
- Establishing a 1D ballistic channel in the nanowire is independent of obtaining a hard gap. V contacts on InSb nanowires led to one-dimensional transport, but the gap measured was soft. Al contacts on these nanowires also led to 1D transport; however, in contrast with V, the gap measured in this case was hard. This indicates that the former is related to the quality of the nanowire channel, while the latter rests on the quality of the nanowire / superconductor interface.
- A 5 nm Nb under-layer deposited before Ta could improve the size of the gap in InAs nanowires, from 80 μeV to 155 μeV, while keeping a similar high critical field. Ta and Nb/Ta remain to be tested in InSb nanowires.

- A Josephson current was measured in InAs nanowire devices with Nb/Ta contacts in the quantum dot regime. It was shown that a large Γ/U ratio or a small g-factor may prevent the observation of a magnetic-field induced quantum phase transition in the supercurrent, setting a prelude for the measurements of Chapter 6.

Chapter 5

Josephson effect through a spin-split 0.7 anomaly in an InAs nanowire

5.1 Introduction

The coupling of superconductors of high critical field to a III-V nanowire of large g-factor can allow studying the effect of spin-polarized electrons on the transport of Cooper pairs, before destroying superconductivity by the effect of a strong magnetic field. In the 1D regime, the strong spin-orbit interaction in the nanowire opens the additional possibility of obtaining triplet Cooper pairs through spin mixing.

In this chapter, a seemingly 1D InAs nanowire Josephson junction showing some puzzling supercurrent suppression and re-emergence under an external magnetic field is presented. It is revealed that the 1D signatures were being copied by a spin-split localized state, whose ground-state transitions were responsible for the strange supercurrent behavior observed[1].

5.2 The device

The two-terminal device used to obtain the results presented in this chapter was made of an InAs nanowire (diameter= 65 nm) contacted by a bilayer of Tantalum (Ta) and Aluminum (Al), of thicknesses of 60 nm and 15 nm, respectively. It thus constituted a Josephson junction below the critical temperature of Ta (T_c). The T_c of similarly evaporated Ta films was determined to be around 0.8 K, which is expected for β-phase Ta (T_c = 0.67-0.9 K [118]), as discussed before in chapter 4. The channel length of the nanowire was 280 nm. As depicted in the scheme of Figure 5.1**a** and shown in the SEM image of Figure 5.1**b**, there were three gates below the channel.

---

[1] The NRG calculations which appear in this chapter were made by Rok Zitko, from the University of Ljubljana.

However, gate 1 did not work, and thus only gates 2 and 3 were used throughout the experiment to tune the subbands spatial profile and charge density of this section of the nanowire.

The sample was mounted on a dilution refrigerator equipped with a 2-axis vector magnet, in such a way that the magnetic field was always in-plane. Taking advantage from this possibility, the magnetic field (B) was oriented parallel to the axis of the nanowire and maintained this way unless in most of the measurements presented here, unless otherwise stated. To maintain at a minimum the thermal fluctuations, which would limit our determination of the switching current, the device was measured at T = 15 mK, unless otherwise stated.

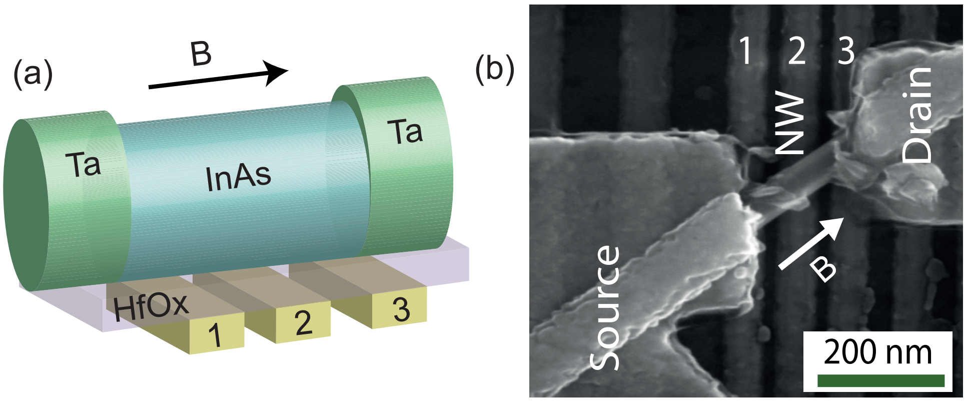

Figure 5.1: **(a)** Scheme of the device and **(b)** corresponding SEM image. A 10 nm layer of hafnium oxide (HfOx) separates the the nanowire from three local gates. The magnetic field (B) orientation -parallel to the nanowire- is indicated by an arrow.

5.3 Formation of a quantum point contact

Sweeping one gate while maintaining the other fixed

To begin this section, I will show two ways in which the gates can be configured to obtain a quantum point contact in the nanowire. These are depicted schematically in Figure 5.1**a** and **b**. In each of these schemes, the edge of the conduction band is depicted in red superposed to the InAs nanowire, to gain a qualitative picture of the spatial variations as a function of the voltages in gates 2 and 3 that can occur. On the sections of the nanowire on top of each gate, a few subbands -drawn as black parabolas- available for transport are sketched. The number of subbands depends, of course, on the spatial distortion of the edge of the conduction band by the gates[2]. For the moment, one can picture these schemes as *two QPCs* in series formed in the nanowire.

---

[2] This is an unorthodox scheme, the parabolic dispersion of subbands -i.e. E vs. k- are plotted on top of an E_{edge} vs. x sketch of the edge of the conduction band, and all of this is superposed to the real space representation of the nanowire.

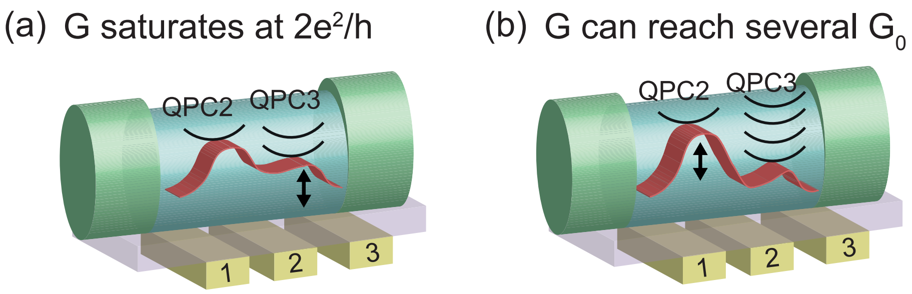

Figure 5.2: Scheme of two quantum point contacts (QPCs) in series inside of a nanowire, named QPC2 and QPC3 for being formed on top of gates 2 and 3, respectively. The edge of the conduction band is represented by a red band. Also represented are the subbands of the nanowire, as black parabolas. Situation **(a)** depicts a nanowire with the number of subbands constrained by QPC2 fixed at one. Situation **(b)** corresponds to QPC3 fixed at several subbands, while QPC2 is unrestrained. The conductance resulting from **(a)** saturates at one quantum of conductance (G_0 = 2 e^2/h), whilst that at **(b)** can reach several quantum of conductance.

In the first gate configuration (Figure 5.2**a**), in which the 0.7 anomaly that is described in the next section was observed, and in which all superconductivity measurements discussed in this chapter were taken, gate 2 is at a fixed voltage of -1 V. The potential produced at this voltage results in the edge of the conduction band being distorted in such a way that only one spin-degenerate subband sits in the section of the nanowire above gate 2. In these conditions, if gate 3 is swept to a negative voltage -i.e. towards pinch-off-, then one would expect that the conductance of the nanowire would decrease to zero, since this would raise the edge of the conduction band and block transport. Else, if gate 3 is swept to a positive voltage, the conductance would raise until it is limited by the constriction in the nanowire section above gate 2. Independently of how much we raise the voltage of gate 3, the conductance of the nanowire would always be that of the single subband in the nanowire section above gate 2. Namely, G = 2 e^2/h at most. The conductance would *saturate* at this value. We can say, if we think of the system as made of two QPCs in series, that if the QPC above gate 2 is fixed at 2 e^2/h, the conductance of the whole system will not raise above 2 e^2/h.

In the second gate configuration (Figure 5.2**b**), the role of the gates is reversed. This time, the maximum conductance is set by gate 3, which in our experiment was fixed at +1 V. Since many subbands sit on top of the edge of the conduction band in the section of the nanowire above gate 3, the conductance will only saturate at several 2N e^2/h, where N is the number of subbands at this position, in contrast to the previous case.

To summarize these two paragraphs, the maximum conductance of a system of two QPCs in series is set by the QPC with the *lowest* number of available subbands. In Figure 5.3, we can see the linear conductance of the device at B = 2.9 T (field large enough to ensure that the device is in the normal state) in the conditions corresponding to the gate configuration of Figure 5.1**a**; i.e. as a function of the voltage of gate 3 (V_{G3}) and with the voltage of gate 2 set at V_{G2} = -1 V. We see that

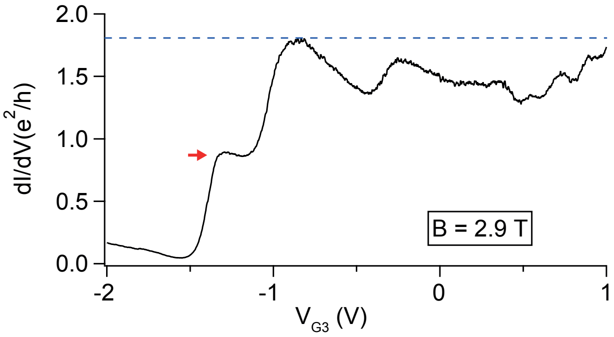

Figure 5.3: Normal-state linear conductance as function of gate voltage 3 (V_{G3}) as a fixed gate voltage 2 (V_{G2} = - 1 V), taken at B = 2.9 T. The conductance of the second plateau saturates at less than 2 e^2/h, as expected for a gate configuration with results in a conduction band profile like the one in Figure 5.2**a**.

the conductance consists of a plateau at around 1 e^2/h (red arrow) and a large wiggly plateau at slightly less conductance than 2 e^2/h. The conductance of this second plateau is saturating at less than 2 e^2/h, just like expected for the case depicted in the scheme of Figure 5.2**a**.

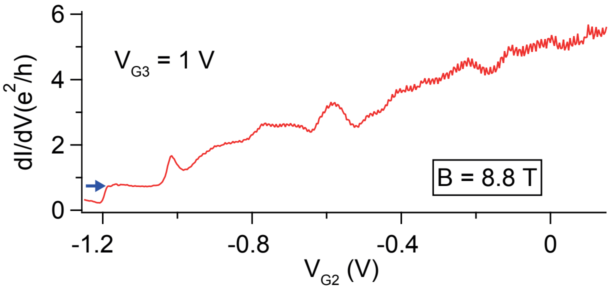

Figure 5.4: Normal-state linear conductance as function of gate voltage 2 (V_{G2}) as a fixed gate voltage 3 (V_{G3} = 1 V), taken at B = 8.8 T. The field in this case was oriented at an angle of 45° with respect to the axis of the nanowire. The conductance increases without boundary, as expected for a gate configuration with results in a conduction band profile like the one in Figure 5.2**b**.

Figure 5.4 shows what happens to the linear conductance when gate 3 is fixed at V_{G3} = 1 V and gate 2 is swept. It is seen that there is a plateau at slightly less than 1 e^2/h, and then the conductance increases without apparent boundary. This situation was depicted in 5.1**b**. It is unclear why the plateaus beyond 1 e^2/h were not clearly seen, but it may have to do with increased localization when V_{G2} is raised.

Figure 5.5**a** shows a map of the magnetic field evolution of the linear conductance as a function of V_{G2}. In this plot, the Zeeman-splitting of the first plateau at 0.8 e^2/h can be observed. Moreover, when we plot cut-lines from this map at a low field (B = 2.2 T) and at a large field (B = 8.8 T), as we did in Figure 5.5**b**, we see that the plateau only increases in width and does not change is conductance from a quantized value. This points to a subband origin for this plateau. Its conductance is lower than 1 e^2/h probably due to the increased backscattering from the greatly distorted band edge in the nanowire section on top of gate 2. This was depicted in the scheme of Figure 5.5**c**. At a conductance above 1.6 e^2/h in the conductance map of Figure 5.5**a**, we find that there are several resonances that move with magnetic field. These resonances could be the result of increased localization from the lowering of the edge of the conduction band edge by an in that we were talking about before in this paragraph. Indeed, as depicted in the scheme of Figure 5.5**d**, when the conduction band edge above gate 2 is lowered as the voltage of gate 2 is raised, the QPC acts more and more as the left barrier of a non-interacting and increasingly-open quantum dot.

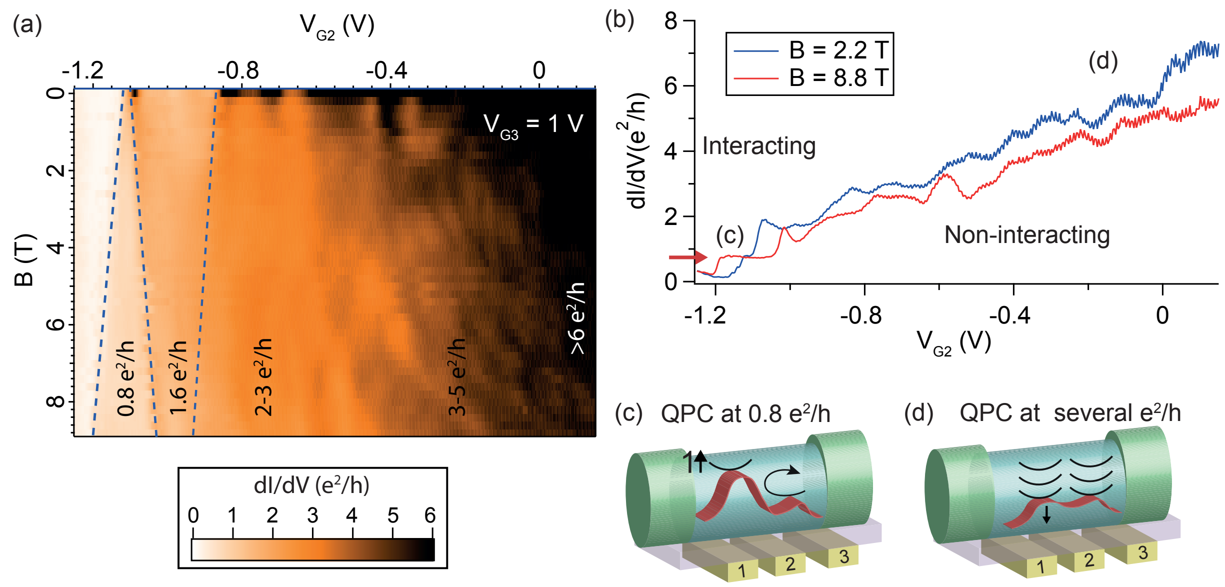

Figure 5.5: **(a)** Map of the magnetic field evolution of the linear conductance as a function of V_{G2}, taken at V_{G3} = 1 V, with a few conductance values indicated. Blue dashed-lines serve as a guide to the eye, to trace the Zeeman splitting of the first plateau. **(b)** Cuts from **(a)** at B = 2.2 T (blue curve) and B = 8.8 T (red curve). A plateau is seen at 0.8 e^2/h, whose width increases with magnetic field. The conductance of the plateau remains quantized at the largest field explored. **(c,d)** Schemes of the spatial variation of the edge of the conduction band for two different values of V_{G3}, indicated in **(b)**. The case in **(c)** is corresponds to a large constriction that only lets one spin-split subband conduct, labeled 1 $\uparrow$ by its orbital number and spin projection to the magnetic field axis. Backscattering reduces the conductance of this subband to less than the ideal 1 e^2/h. The case in **(d)**, on the other hand, corresponds to the other extreme, when the constriction above gate 2 has been reduced up to a degree that it becomes the left barrier of an open quantum dot. In this case, many subbands conduct in parallel with the dot and the conductance is of several G_0.

Sweeping one gate and stepping the other

Let us go back to the configuration depicted in Figure 5.2**a**. From now on, all the discussion will be about this gate configuration, since it was the one used in the experiments that follow in this chapter.

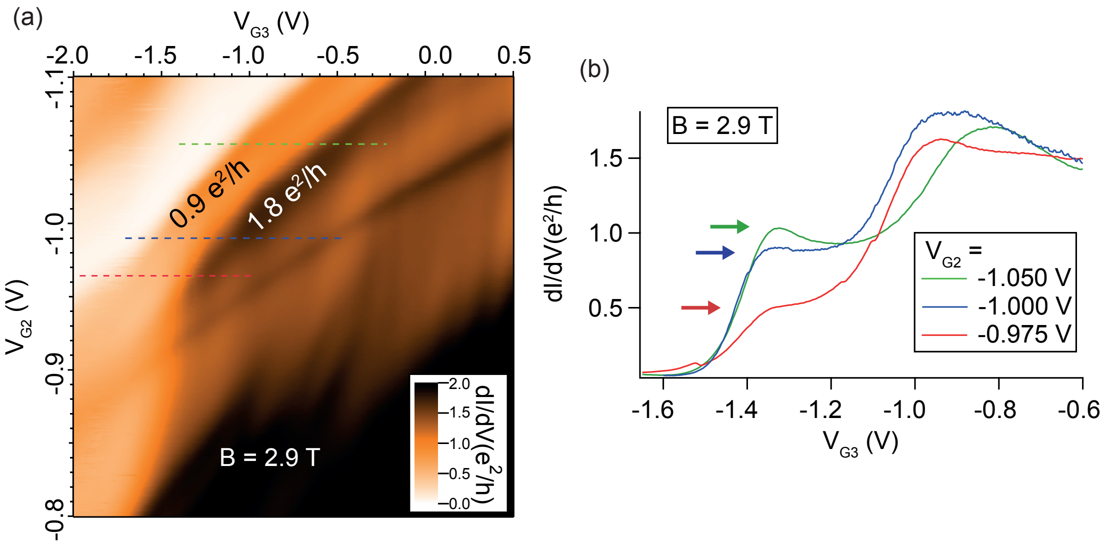

Figure 5.6: **(a)** Map of normal-state linear conductance taken at B = 2.9 T by sweeping V_{G3} and stepping V_{G2}. The conductance of two plateaus is indicated. **(b)** Cuts from **(a)** along the green, blue and red dashed lines. The first conductance plateau is pointed by an arrow of the same color of each of the traces. The trace in blue corresponds to the best plateau from the conductance map in **(a)**, due to its flatness and the closeness of its conductance to 1 e^2/h.

We will now investigate the situation when gate 2 is stepped in the vicinity of the configuration that results in the band profile of Figure 5.2**a**. Figure 5.6**a** shows a conductance map at B = 2.9 T, field which is above the critical field of the Ta contacts (B_c of around 1.8 T). For obtaining this map, V_{G3} swept and V_{G2} was stepped. The need to make this map arose as a way to find a flat and highly transparent plateau of conductance at 1 e^2/h. After this step was found, the goal was to lower the magnetic field for driving the nanowire into the superconducting state and, hopefully, enter the helical states regime and thus see a triplet supercurrent.

Figure 5.6**b** shows cuts taken from this conductance map along the green, blue and red dashed lines, which correspond, respectively, to V_{G2} = -1.05 V, -1 V and -0.975 V. The best ~ 1 e^2/h plateau of the whole map, in terms of flatness and transparency, is the one belonging to the blue curve at V_{G2} = -1 V. This plateau is pointed by a blue arrow. On the other hand, the conductance at the first plateau in the green and red traces shows either a resonance (green curve, green arrow) or it is greatly decreased (red curve, red arrow) from the ideal 1 e^2/h value.

A quantum dot with gate-dependent tunnel coupling

Figure 5.7 shows schemes of the spatial variation of the edge of the conduction band at different V_{G3} values, of the sorts of Figure 5.2**a**. In Figure 5.7**a** and **b**, a camel-shaped band edge results in a localized state -i.e. a quantum dot-. In the scheme 5.7**c**, the system goes from a quantum dot with

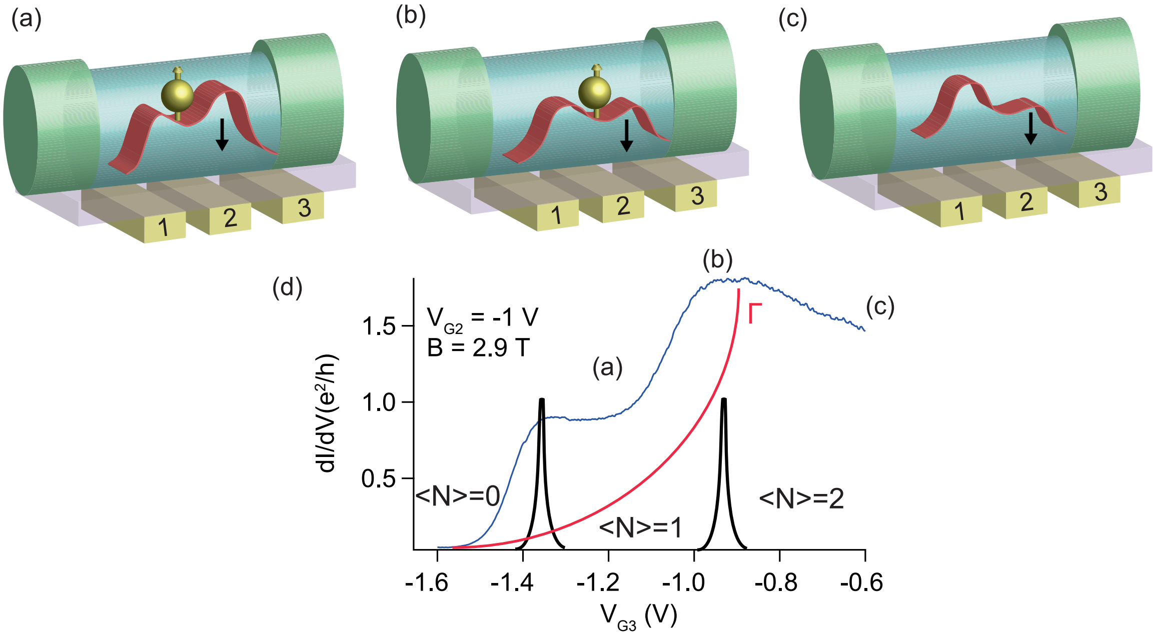

Figure 5.7: (a-c) Schemes of the spatial variation of the edge of the conduction band for three different values of V_{G3}, indicated in the conductance trace of **(d)**. **(a)** and **(b)** correspond to situations when the two QPCs discussed in Figure 5.2**a** turn into the two barriers of a quantum dot, because of the camel-shaped profile of the conduction band. The case in **(c)** depicts a QPC formed above gate 2, that limits the conductance of the system to a maximum of 2 e^2/h, just as described in Figure 5.2**a**. **(d)** Linear conductance trace taken at B = 2.9 T and V_{G2} = - 1 V, corresponding to the blue curve in Figure 5.6**b**. Two Coulomb peaks were drawn in black on top of the plot, as well as the gate-dependence of the tunnel coupling Γ (red line). These Coulomb peaks can morph into a conductance characteristic like this one if their tunnel coupling is increasing quadratically with the gate.

a low left tunnel barrier towards a QPC with one spin-split subband. These gate configurations are marked in the conductance trace at the bottom of Figure 5.7.

We will see in the following a "hand-waving" explanation of how the situation in Figure 5.7**a** may give rise to a conductance plateau at high magnetic field. Let us suppose that the quantum dot that forms in 5.7**a** and **b** has an energy level that can be occupied by either one or two electrons, a charging energy U and level position ε_0. When we change the position of the level with V_{G3}, Coulomb blockade will produce two Coulomb peaks situated at $\varepsilon_0 - U/2 - E_z/2$ and $\varepsilon_0 + U/2 + E_z/2$, where $E_z = g\mu_B B$ is the Zeeman energy that splits the doublet state of mean occupancy $< N > = 1$ between the two peaks. These two peaks are sketched in Figure 5.7**d**. The finite tunnel coupling $\Gamma = \Gamma_L + \Gamma_R$ of the discrete level to the leads will broaden each of the Coulomb peaks. If the two barriers were symmetrical -i.e. $\Gamma_L = \Gamma_R$, the conductance of the peaks would reach 1 e^2/h; if not, it would decrease proportionally to the asymmetry.

Now we have a model to explain why the conductance of the ∼ 1 e^2/h plateau in Figure 5.6**b** changes so drastically when V_{G2} is stepped to lower or larger voltage than V_{G2} = -1 V. Simply put, when V_{G2} changes, the barriers of the quantum dot that forms in Figures 5.7**a,b** will change their absolute and relative height, thus changing Γ_L and Γ_R, and culminating in a difference of conductance for the two Coulomb peaks with respect to the V_{G2} = -1 V case. This change of conductance can produce the versions of the $\sim$ 1 e^2/h plateau observed experimentally in Figure 5.6**b**.

A quantum dot of finite tunnel coupling still does not give rise to a conductance plateau at high magnetic field. What one needs to produce this outcome is to assume that the tunnel coupling of the dot *increases* with the gate voltage. Under this assumption, the broadening of the levels becomes so large as the gate is raised that the peaks overlap and turn into steps. As we will soon see, the dependence of the tunnel coupling with the gate voltage needs to be quadratic for this to happen.

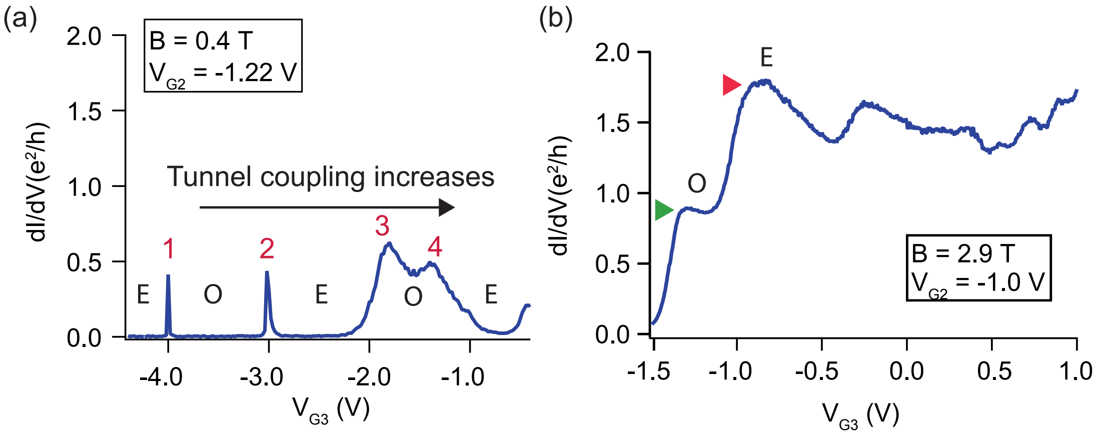

Figure 5.8: **(a)** Linear conductance trace taken at B = 0.4 T and V_{G2} = -1.22 V. The Coulomb peaks have been labeled with numbers for easier identification, while the Coulomb valleys have been labeled according to whether the mean number of electrons $< N >$ in the relevant dot level is even (E) or odd (odd). **(b)** Linear conductance trace taken at V_{G2} = -1 V and B = 2.9 T, show here as a "continuation" of plot **(a)**.

Our sample does indeed show a gate-dependent tunnel coupling, as one can see in Figure 5.8**a**. This plot is a measurement of the linear conductance of the sample at V_{G2} = -1.22 V and B = 0.4 T, in a gate range of V_{G3} just before the 1 e^2/h plateau appears. In this plot, the Coulomb peaks have been labeled with numbers for easier identification, while the Coulomb valleys have been labeled according to whether the mean number of electrons $< N >$ in relevant dot level is even (E) or odd (odd). It can be seen that the *width* of each peak is increasing as V_{G3} is raised. Peak 1 is sharper than peak 2, and peak 2 is sharper than peaks 3 and 4, which together are forming a Kondo resonance. The "continuation" of this plot is in Figure 5.8**b**, for V_{G2} = -1 V and B = 2.9 T. In this other plot, the parity of $< N >$ has also been labeled, as a follow-up of the sequential order E-O-E-O... of the plot 5.8**a**.

One more thing needs to be assumed so that a simple quantum dot produces a plateau at around 1 e^2/h at high magnetic field. The tunnel coupling Γ must also *increase* quadratically with the *magnetic field*. If this second additional assumption is not taken, the valley conductance between the two Coulomb peaks of Figure 5.7**d** would continuously decrease with magnetic field. This conductance decrease is not experimentally observed, as described below.

Figure 5.9**a** shows linear conductance traces at B > B_c, when the magnetic field was applied *parallel* to the nanowire -as it has tacitly been the case so far, unless it was stated otherwise-. It can be seen that the conductance stays quantized at the same value of 0.9 e^2/h over a large range of magnetic field. A way to quantify how large is this range is via the Zeeman energy over charging energy ratio E_z/U. If U is large compared to E_z, then the decrease of the valley conductance may not be observable. However, this is not the case, since E_z/U = 0.88 (for 1.8 T) to 1.42 (for 2.9 T) in the linear conductance traces of Figure 5.9**a**, for U = 1.3 meV and $|g| = 11$. In the next section, we will see how these values for the charging energy U and the g-factor g were obtained.

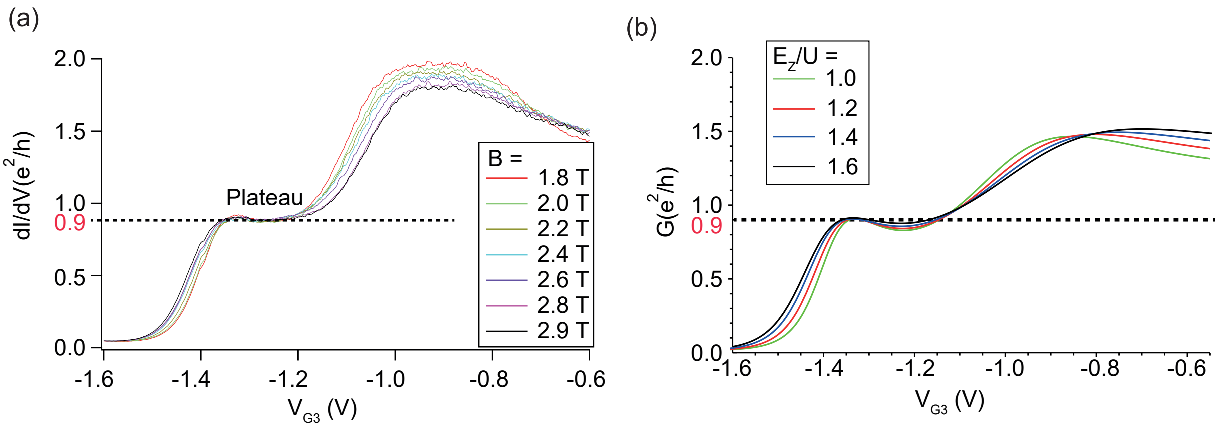

Figure 5.9: **(a)** Linear conductance traces as a function of the gate voltage V_{G3}, taken at different magnetic fields corresponding to the normal state, for a field oriented *parallel* to the nanowire. The plateau at 0.9 e^2/h stays perfectly quantized as the field is varied in a large range of Zeeman energy E_z, with respect to the charging energy U. This range of field corresponds to E_z/U = 0.88 (for 1.8 T) to 1.42 (for 2.9 T), calculated with U = 1.3 meV and $|g| = 11$. **(b)** NRG calculations of the linear conductance done by Rok Zitko, using a model described in the main text, which assumed a quadratic dependence of the tunnel coupling on the gate voltage *and* the magnetic field. The range of E_z/U chosen for these calculations is comparable to the experimental measurements in **(a)**. The experimental parameters U = 1.3 meV, $|g| = 11$ and T = 15 mK were used in these calculations, and the gate voltage was converted from ε_0 to facilitate a comparison with the data

Figure 5.9**b** shows NRG calculations of the linear conductance done by Rok Zitko. The theory that he used corresponds to the single-impurity Anderson model , with the Hamiltonian given by equation 5.1. In this equation, $n = \sum_\sigma d^\dagger_\sigma d_\sigma$ is the dot occupancy operator, δ is the level position, U is the charging energy, $E_z = |g|\mu_B B$ is the Zeeman splitting, $S_z = (d^\dagger_\uparrow d_\uparrow - d^\dagger_\downarrow d_\downarrow)/2$ is the dot spin operator, and $\Gamma = \pi V^2 \rho$ is the tunnel coupling, where $\rho = \sum_k \delta(\omega - \varepsilon_k)$ is the density of states in the contacts. The term x in the Hamiltonian is related to the correlated hopping of electrons, which results in a tunneling rate dependent on dot occupation. x different from zero breaks the electron-hole symmetry in the superconducting regime, as we will see later. A value x = -0.4 gave the best qualitative agreement to the data, and was therefore chosen in all the calculations [3].

$$H = \delta(n-1) + U/2(n-1)^2 + E_z S_z + \sum_{k\sigma} \varepsilon_k c^\dagger_{k\sigma} c_{k\sigma} + \sum_{k\sigma} \left(V_k (1 - x n_{d,\bar{\sigma}}) c^\dagger_{k\sigma} d_\sigma + \text{H.c.} \right). \quad (5.1)$$

In the model, it was assumed that the tunnel coupling was depending quadratically on both the gate *and* the magnetic field $\Gamma = \Gamma_0 + \Gamma_1(c_0 + c_1\delta/U + c_2 E_Z/U)^2$. The term c_2, related to the magnetic effect on Γ, was a small correction to the dominant gate term c_1. It was necessary only when the field was applied parallel to the nanowire, in order to obtain a conductance plateau at 0.9 e^2/h. The range of E_z/U that he chose for these calculations is comparable to the experimental measurements in 5.9**a**, for U = 1.3 meV and g = 11. There is a good qualitative agreement between the data in 5.9**a** and the calculations in 5.9**b**, which reinforces the validity of the assumptions.

A measurement of the linear conductance of the device with the magnetic field applied *perpendicular* to the nanowire -but still in the substrate plane- leads to a surprisingly different outcome with respect to the parallel field case. The measurement, taken at a similar range of magnetic field as the parallel case, is shown in 5.10**a**. This range of field corresponds to E_z/U = 0.76 (for 1.8 T) to 1.35 (for 2.9 T), for U = 1.3 meV and g = 11.5 -the g-factor was larger in this field direction-. In strike contrast to the case when the magnetic field is oriented parallel to the nanowire, the valley conductance in between the two Coulomb peaks strongly decreases as the magnetic field is raised. A quantized plateau is no longer visible.

To replicate qualitatively this experimental result, the quadratic dependence of the tunnel coupling on the magnetic field was discarded for a perpendicular field orientation. Figure 5.10**b** shows NRG calculations of the linear conductance done by Rok Zitko, this time only assuming a quadratic dependence of Γ on the gate voltage (and no dependence on the magnetic field). The valley conductance (black arrow) is strongly suppressed as the field is increased, providing a qualitative agreement with the experimental data.

5.4 Signatures of a 0.7 anomaly

So far, we can conclude that the device behaves like two quantum point contacts (QPCs) in series, and by applying gate voltages one can convert these two QPCs into the two barriers of a quantum dot. In the quantum dot regime, the conductance of the device mimics a well-defined conductance

---

[3] In Ref. [29], x was chosen to be 1 and the hybridization V_k was chosen to be a step-like function of the energy, with a value dependent on the dot occupation.

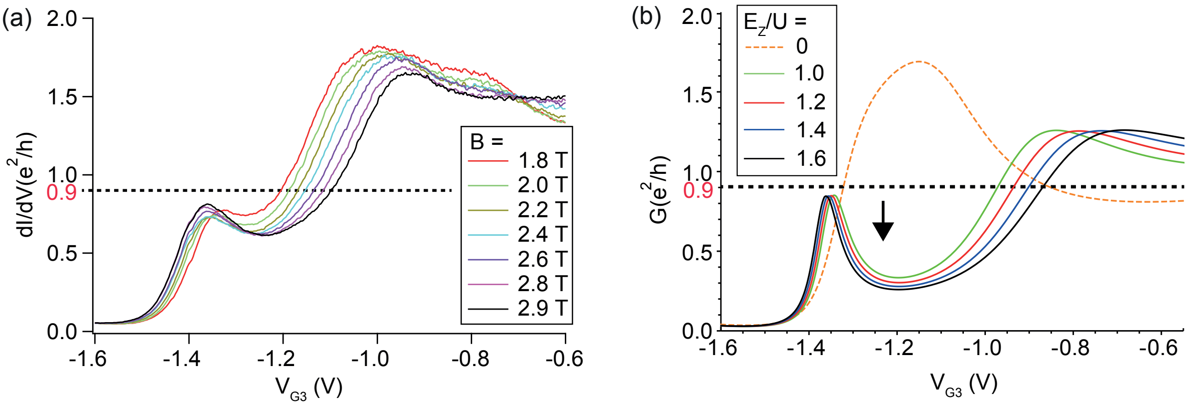

Figure 5.10: **(a)** Linear conductance traces as a function of the gate voltage V_{G3}, taken at different magnetic fields corresponding to the normal state, for a field oriented *perpendicular* to the nanowire. The valley conductance decreases as the magnetic field increases. This range of field corresponds to E_z/U = 0.76 (for 1.8 T) to 1.35 (for 2.9 T), for U = 1.3 meV and $|g|$ = 11.5. **(b)** NRG calculations of the linear conductance done by Rok Zitko, using a model described in the main text, which assumed a quadratic dependence of the tunnel coupling on the gate voltage V_{G3} *only*. The range of E_z/U chosen for these calculations is comparable to the experimental measurements in (a), for U = 1.3 meV and $|g|$ = 11.5.

plateau at 0.9 e^2/h because of gate and field-varying tunnel coupling. This plateau stays quantized at the same value of 0.9 e^2/h for a large range of magnetic field.

In this section, some experimental signatures that link the localized state at the onset of QPC conduction described above with the 0.7 anomaly will be discussed.

Determination of the charging energy and g-factor

Figure 5.11 shows a map of the linear conductance of the device as function of the gate voltage V_{G3} and the magnetic field B. In this map, the blue-dashed lines are a guide to the eye, to trace the Zeeman splitting of the 0.9 e^2/h plateau. Oddly enough, the two blue-dashed lines *do not cross* at zero field. Chronologically speaking, this was the first hint that pointed us to a 0.7 anomaly.

The amount of zero-field splitting in the blue-dashed lines should be roughly equal to the charging energy U of the quantum dot, as indicated in this conductance map. To extract an estimate of U, I derived the conductance with respect to the gate voltage, and in doing so I obtained the transconductance dG/dV_G (where G = dI/dV is the linear conductance and V_G the gate voltage). This is typically done in the field of QPCs in 2DEGs for studying the Zeeman splitting of the plateaus and for finding the value of the zero-field splitting energy [122]. Whenever there are inflection points in the conductance (e.g. in plateaus or in a 0.7 anomaly shoulder), there will be peak in the transconductance. The additional advantage of analyzing the transconductance for our case is that the enhancement of the conductance by superconducting effects, which can

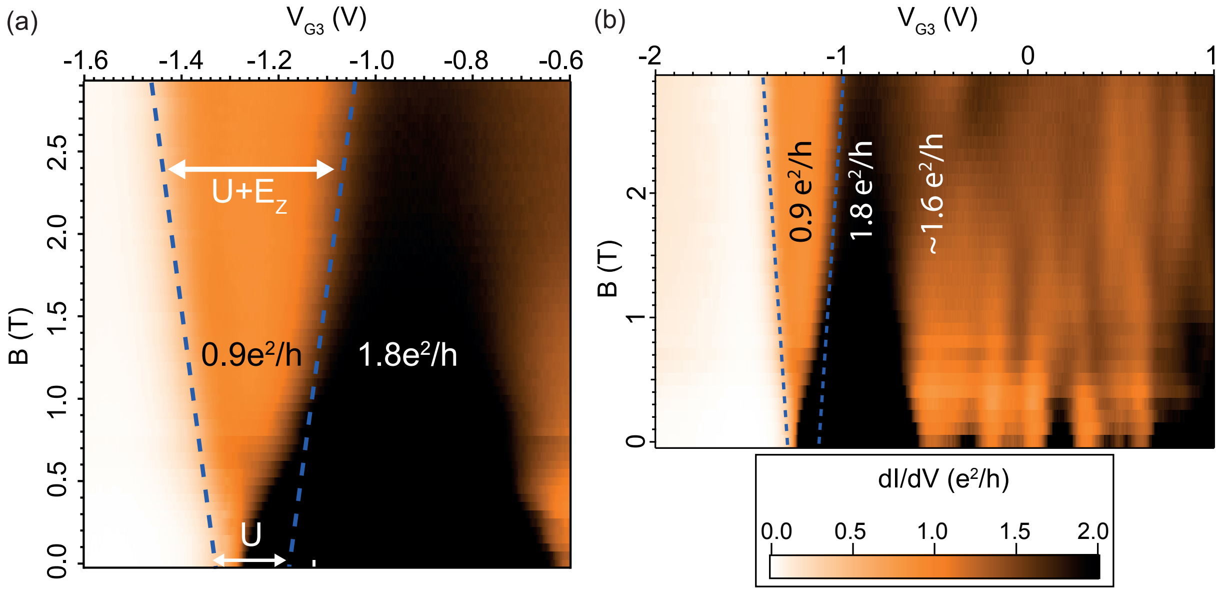

Figure 5.11: **(a)** Map of the evolution of the linear conductance at T = 15 mK with magnetic field B parallel to the nanowire, as a function of the gate voltage V_{G3}. Blue-dashed lines are a guide for the eye for tracing the Zeeman splitting E_z of the 0.9 e^2/h plateau. The charging energy U of the quantum dot is indicated, as well as the amount of splitting $U + E_z$ of the corresponding plateau at high magnetic field. **(b)** Same as **(a)**, but for a larger gate range.

obscure any features at B $\ll B_c$, is lost. Figure 5.12**a** shows the transconductance map obtained from deriving the data belonging to the conductance map in Figure 5.11.

It is natural to assume that the device has Kondo correlations, because of the large tunnel coupling involved to produce a flat plateau at high magnetic field. Kondo correlations will tend to approach the two Coulomb peaks that are separated by U at zero tunnel coupling, by an amount proportional to the tunnel coupling of the quantum dot to the leads.

In the map of Figure 5.12**a**, a wide feature is seen at B < 0.5 T, which splits into two peaks as the field is raised above that value. Those two peaks correspond to the onset of the opening of the first spin-up subband and the onset of the opening of the first spin-down subband, respectively. The wide feature, on the other hand, is made of two overlapped peaks which indicate the two inflexion points of the 0.7 anomaly at a field not large enough to split the associated Kondo state. Figure 5.12**b**, which shows the gate separation δV_{G3} of the two transconductance peaks of Figure 5.12**a** as a function of the magnetic field, fits the description of the approaching Coulomb peaks discussed above (blue arrow).

As calculated by Costi using the NRG model [123], the splitting of the Kondo total spectral density at T = 0 K occurs at a critical field of B = $0.5\kappa_B T_K/2|g|\mu_B S$, where S=1/2 is the spin and κ_B is the Boltzmann constant. In terms of the Zeeman energy E_z, the Kondo energy $E_K = \kappa_B T_K$ is

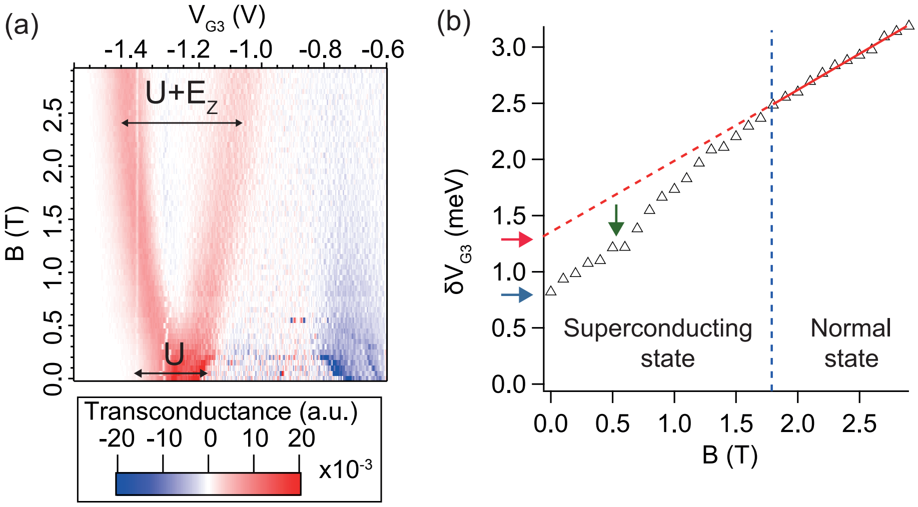

Figure 5.12: (a) Transconductance map as a function of magnetic field and gate voltage V_{G3}. The two read bands in the map come from the Zeeman splitting of the 0.9 e^2/h plateau. **(b)** Gate separation δV_{G3} of the two transconductance peaks of **(a)** as function of magnetic field (open black triangles), converted into energy by using the lever-arm of the device (α_3 = 8×10^{-3}). Also shown is a linear fit of the data in the normal state (red line), as explained in the text. The fit has been prolonged to B = 0 T (red dashed line) to show how U was estimated (red arrow). The black arrow points to the zero-field peak-splitting, while the green arrow points to a kink in the data, which also signals the magnetic field when the peak-splitting becomes visible. The Zeeman energy at which this kink occurs gives an estimation of $T_K \sim 6.5$ K.

$E_K = 2E_z$. In our case, the splitting occurs at B = 0.5 T (marked by a green arrow in Figure 5.12**b**), which sets a Kondo energy of $E_K \sim 0.55$ meV, or $T_K \sim 6.5$ K. The estimation is rough since the moment at which the splitting begins can not be accurately measured through the transconductance and superconducting effects may be playing a role, but it provides at least an order of magnitude for the Kondo energy, which puts it well-above the superconducting gap Δ = 0.08 meV.

A good estimation of the charging energy U is obtained by recognizing that reliable measurements of the Zeeman splitting through the transconductance can only be taken in the normal state, separated at $B_c \sim 1.8$ T from the superconducting state in Figure 5.12**b** by a vertical dashed blue line. By fitting the measurements at B > B_c to the equation $\delta V_{G3} = U + |g|\mu_B B$ (red line), one obtains U = 1.33 meV (red arrow) and $|g|$ = 11.

The existence of a splitting at zero field is in agreement with a bound state interpretation of the 0.7 anomaly.

Measurement of the conductance shoulder

The clearest sign of a 0.7 anomaly is the characteristic shoulder that appears in the linear conductance as a function of gate voltage, at zero magnetic field and at low enough temperature -i.e. lower than the Kondo temperature-. Since the device was Josephson junction, the conductance had to be measured $T > T_c$ or bias $V > 2\Delta$ (where T_c is the critical temperature of superconductivity) to avoid superconducting effects. In a nanowire Josephson junction well-coupled to superconducting reservoirs, such as the one we are discussing here, these effects can comprise supercurrent and multiple Andreev reflection (MAR), which will respectively result in an infinite conductance and in an augmentation of the normal conductance by a value depending on the junction's transparency and the availability of a channel.

These measurements -which display the 'shoulder'-, correspond to the blue and red conductance curves of Figure 5.13. The blue curve was taken at T = 4.2 K and at zero magnetic field, with the bias voltage set at zero. The differential conductance was recorded while the gate voltage V_{G3} was swept. The other gate was kept fixed at a value V_{G2} = -1 V, which was taken at the same gate configuration as the measurements shown in Figures 5.7**d**, 5.9**a**, 5.11 and all the plots to come next.

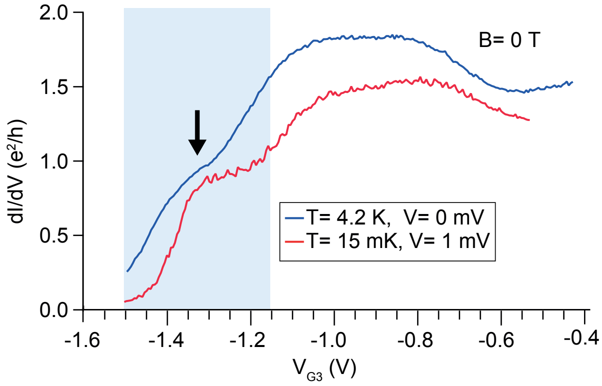

Figure 5.13: Conductance traces that display the 0.7 anomaly conductance "shoulder" (black arrow) taken at zero magnetic field. The blue curve corresponds to a zero-bias conductance measurement at T = 4.2 K -i.e., above the T_c of Ta-. The red curve is a cut-line at V = 1 mV -i.e., above the superconducting gap- from the non-linear conductance map of Figure 5.14**a**. At high parallel magnetic field, the conductance shoulder evolves to the 0.9 e^2/h conductance plateau of Figure 5.9**a**.

The black arrow in Figure 5.13 points to the above-mentioned conductance shoulder. In the blue curve, the conductance on the shoulder reaches a value of around $0.5 \times 2\ e^2/h$, instead of the commonly found $0.7 \times 2\ e^2/h$ in QPCs in 2DEGs. This may happen as a result of the relatively large temperature at which this measurement was taken, which rivals with the previously estimated value of the Kondo temperature. It is well-known that temperature can decrease the enhancement of the linear conductance produced by Kondo correlations.

The red curve in Figure 5.13 is a cut-line at a finite bias (V = 1 mV) above the superconducting gap (2Δ = 0.16 meV) from the non-linear conductance map of Figure 5.14**a**, which was obtained at B = 0 T and T = 15 mK. The conductance "shoulder" is also seen in this curve and its conductance is similarly below $0.7 \times 2\ e^2/h$. In this case, this decrease happens because the Kondo enhancement of the conductance at zero magnetic field decreases as the bias increases, being maximum only at zero bias.

Bias dependence of the 0.7 anomaly

The 0.7 anomaly has a characteristic signature in bias. The anomaly itself produces a zero-bias peak that was one of the early indications of its connection to the Kondo effect. However, at high bias an additional signature is also observed. In a non-linear conductance map as a function of bias voltage and gate, an additional plateau at around 0.8×2 e^2/h is observed [25].

At T = 15 mK, the Josephson effect and MAR greatly enhance the conductance around zero bias inside the gap, obscuring the observation of a zero-bias peak. However, the higher bias plateau at 0.8×2 e^2/h should be in principle observable, because it can fall outside of the superconducting gap.

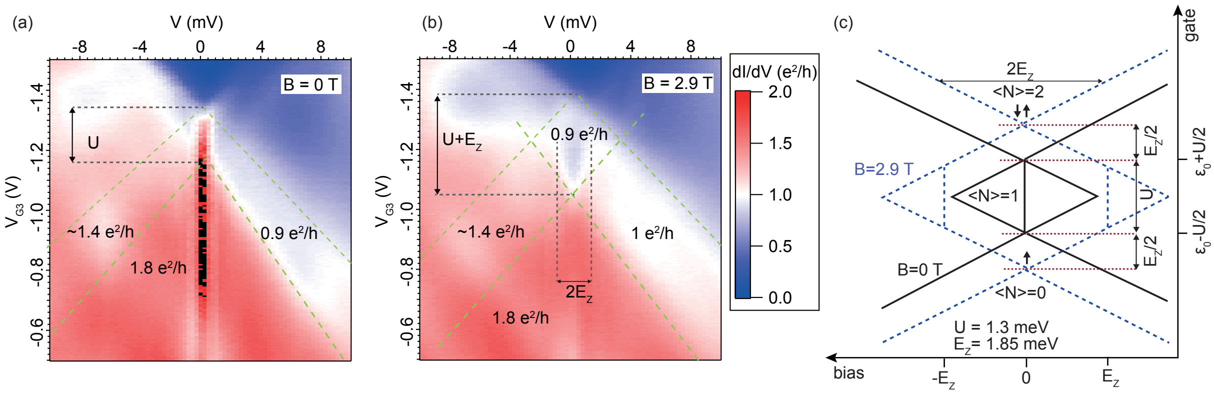

Figure 5.14: Maps of non-linear conductance as a function of bias voltage and gate 3, taken at B = **(a)** 0 T and **(b)** 2.9 T respectively. The green dashed lines are an aid to the eye, for identifying the structures at high bias corresponding to the 0.7 anomaly B = 0 T and the spin-split channel at $B = 2.9T$. **(c)** Scheme of Coulomb diamonds at B = 0 T (black line) superposed on a similar scheme at B = 2.9 T (blue-dashed line) for a weak tunnel coupling that does not depend on the gate. The charging energy U and Zeeman energy E_z values and the mean occupation of the relevant dot level are indicated in the diagram. A Kondo ridge is depicted at zero bias and zero magnetic field as a vertical black line inside of the $< N > = 1$ diamond. It splits into the two peaks at high magnetic field, shown as two vertical blue-dashed lines in the same diamond.

Figure 5.14**a** shows a non-linear conductance map as a function of bias voltage V and the gate voltage V_{G3}, taken at B = 0 T and T = 15 mK, which encompasses the gate region where the 0.7 anomaly was observed in Figure 5.13. In this map, the charging energy U is indicated as a reference of the position of the 0.7 anomaly in gate voltage. Green dashed lines were added to serve as a guide to the eye. Interestingly, for positive bias we see a rather well established plateau at 0.9 e^2/h in-between the two rightmost green-dashed lines. In the case of negative bias, there is a less-defined plateau with a conductance of 1.4 e^2/h. If we adhere to the interpretation of the 0.7 anomaly in this nanowire device as emerging from a discrete quantum dot level with a Kondo resonance, the difference of conductance between positive and negative bias could just come from the way the bias is dropping across the left and right barriers of the dot.

The non-linear conductance of the 0.7 anomaly at high magnetic field has also been found to present some specific signatures [25]. In the spin 1/2 Kondo effect that occurs in a singly-occupied quantum dot level, the magnetic field produces an splitting of the zero-bias peak, but the zero-bias conductance of the split-peak does not reach 1 e^2/h; one needs to recur to a gate-dependent tunnel coupling for this to happen, as we saw before. In ref. [25], both a Zeeman splitting of the zero-bias peak associated with the 0.7 anomaly and a quantized zero-bias conductance in-between the split-peaks are observed. In the Kondo effect in quantum dots, the energy separation between the two split conductance peaks in the bias voltage characteristic is twice the Zeeman energy $E_z = |g|\mu_B B$. This splitting has also been observed for the 0.7 anomaly in QPCs in 2DEGs, but it has been found to depend on the conductance [124].

Figure 5.14**b** shows a non-linear conductance map as a function of the bias V and gate voltage V_{G3}, taken at similar conditions as the map in 5.14**a**, but at a magnetic field of $B = 2.9T$ oriented parallel to the nanowire. In this map, we see a spin-split feature of peak separation $2E_z$, consistent with the interpretation of the 0.7 anomaly as coming from the Kondo effect, as described above. Furthermore, this splitting is seen at different fields. The field dependence of the dI/dV vs. V characteristic at the gate voltage of the 0.7 anomaly is displayed in Figure 5.15. At zero field, a supercurrent -seen here as a prominent and sharp zero-bias peak- obscures the observation of the associated zero-bias peak. However, at higher field, once the superconducting gap is nearly closed (i.e. at $B = 1T$) the measurement shows a zero-bias peak whose width is equal to $2E_z$, indicating that two spin-split peaks are overlapping at this magnetic field. At even higher field, when the gap is fully closed (at B = 2 T and B = 2.9 T) and superconductivity is lost, we can see a clear splitting of $2E_z$.

Figure 5.14**c** is an attempt to compare the maps in Figure 5.14**a,b** with a simple charge stability diagram of a quantum dot with a Kondo ridge in the $< N > = 1$ diamond -where $< N >$ is the mean occupation of the relevant energy level of the quantum dot- at B = 0 T (black line), superposed to a similar diagram at B = 2.9 T of the same dot (blue-dashed line). At high field, the magnetic field splits the Kondo ridge into two peaks separated by $2E_z$. In our case, this simple diagram is complicated by superconductivity (at zero field), stronger Kondo correlations, and a tunnel coupling that depends quadratically on the gate. However, a parallel can be drawn, at least qualitatively.

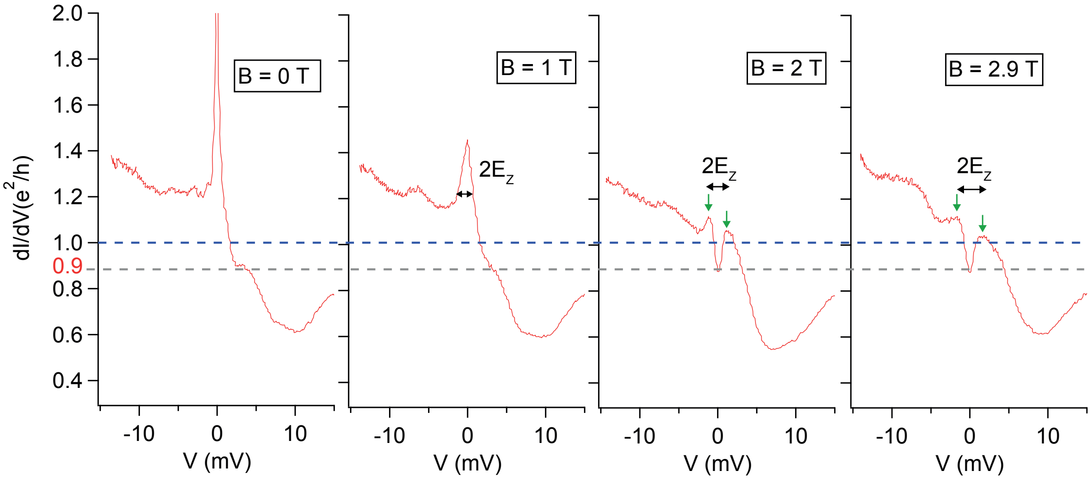

Figure 5.15: Magnetic field evolution of the non-linear conductance in the middle of the gate region where the 0.7 anomaly appears. At B = 0 T, the zero-bias conductance is enhanced by superconductivity, preventing the observation of the zero-bias peak that comes with the 0.7 anomaly. At B = 1 T the peak has a width of $2E_z$; however, superconductivity, though weakened, is still present at this field. At B = 2 T and B = 2.9 T, in the normal state, a peak-splitting (green arrows) of $2E_z$ is clearly visible. These observations are consistent with a Kondo origin of the 0.7 anomaly in this device.

Measurement of the Kondo temperature in near conditions

A definite proof of the the Kondo origin in this device comes from measurement of the temperature dependence of the linear conductance. Unfortunately, the device changed before a temperature dependence of the 0.7 anomaly could be taken, rendering it impossible to obtain a more accurate estimate of the Kondo temperature. The change of the device brought it to a state where a flat plateau with a conductance of 0.9 e^2/h could no longer be seen anymore at T = 15 mK at high parallel magnetic field. However, the device still showed a similar "shoulder" in the linear conductance, and overall, the features where similar. The temperature dependence of this feature is shown in Figure 5.14**a**.

From these temperature measurements, we could extract the Kondo temperature $T_K = 3.7$ K, by fitting the linear conductance in the shoulder with a modified version of the empirical formula for the Kondo effect in quantum dots [25]:

$$G(T) = g_0(T) + G_1 \tag{5.2}$$

In equation 5.2, g_0(T) stands for the traditional empirical formula of the Kondo effect used to fit the conductance in quantum dots $g_0(T) = G_0[1 + (2^{1/s} - 1)(T/T_K)^2]^{-s}$, where G_0 is the saturation conductance, T_K the Kondo temperature and s = 0.22 for a half-spin on the dot. G_1 is an offset constant added to fit the linear conductance background in the absence of a Kondo effect.

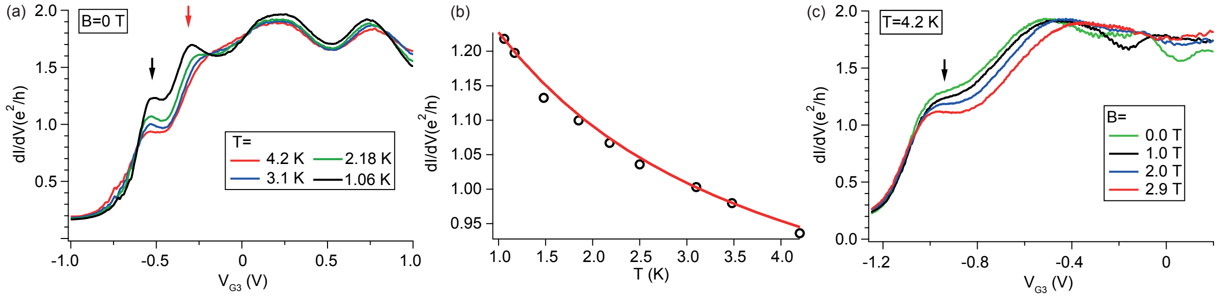

Figure 5.16: Measurements taken after the device changed (as explained in the maint text). **(a)** Temperature dependence of the linear conductance. The black arrow points to a shoulder-like feature whose conductance increases as the temperature decreases. The red arrow points to a peak-like feature that behaves the same. **(b)** Linear conductance (black open circles) taken at a fixed gate value pointed by the black arrow in **(a)**, as a function of temperature, and fitted with equation 5.2 (red line) as explained in the text. **(c)** Magnetic field dependence of the linear conductance, showing a decrease in the conductance of the shoulder feature (black arrow) without saturation at a value $\lesssim$ 1 e^2/h, unlike Figure 5.9**a**.

Figure 5.14**b** shows a fit with this equation (red line) of the linear conductance taken at a fixed gate voltage and at different temperatures (open black circles). To fit the conductance data in the Figure 5.14**b**, I chose G_0 = 0.9 e^2/h, since this is the value that the conductance attained at the first quantized step at high field before the device changed. G_1 = 0.5 e^2/h, together with T_K = 3.7 K, are fitting parameters. T_K in this case has the same order of magnitude as before the device experienced a change.

The parallel magnetic field dependence of the shoulder-like feature of Figure 5.14**a** is displayed in Figure 5.14**c**. It can be seen that, although the feature decreases its conductance, it does not saturate at the highest magnetic field. This is in contrast to what was observed before the device changed: the conductance of the spin-resolved plateau at 0.9 e^2/h saturated at this value and did not change as the field was further increased (as in Figure fig:image9**a**).

5.5 Josephson current through the 0.7 anomaly

In the previous two sections I described measurements of the device mostly taken in the normal state and tried to set an interpretation of the nature of the device in terms that fit the experimental results. In the first section, I concluded that the device was behaving for the two gate configurations presented there as two quantum point contacts (QPCs) in series. Then, I showed that for one of these gate configurations, both QPCs could be turned into the two tunnel barriers of a quantum dot (QD). In this QD regime, at a high magnetic field oriented parallel to the nanowire, the conductance of the device mimicked a well-defined conductance plateau at 0.9 e^2/h because of gate and field varying tunnel coupling.

Afterwards, in the second section, I established a parallel between these and additional

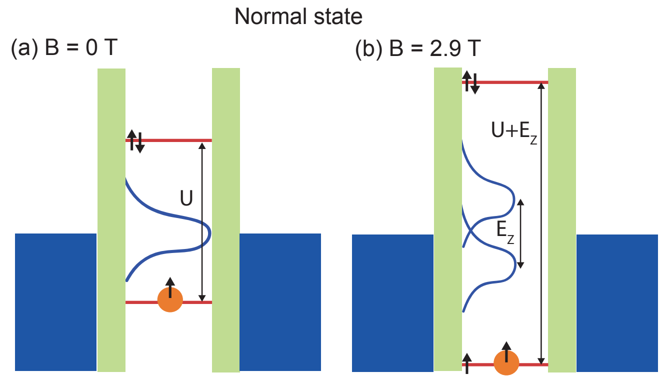

Figure 5.17: Quantum dot schemes of the device in the 0.7 anomaly regime in the *normal* state at zero bias, at zero **(a)** and finite **(b)** field, respectively. At zero field **(a)**, a Kondo resonance (in blue) develops at the chemical potential of the leads. The $< N > = 2$ level is separated by the charging energy U from the $< N > = 1$ level. At large field **(b)**, the Kondo resonance is split by the Zeeman energy. The $< N > = 2$ level is separated now from the $< N > = 1$ by $U + E_z$.

measurements in the quantum dot regime and the observations made in ref. [25] in QPCs in two-dimensional gases (2DEGs), regarding the 0.7 anomaly. There we saw that the Kondo effect was present in the device, giving raise to a conductance shoulder at zero magnetic field and to the previously mentioned 0.9 e^2/h conductance plateau at high magnetic field. These observations were in turn qualitatively reproduced by NRG calculations in a quantum dot model.

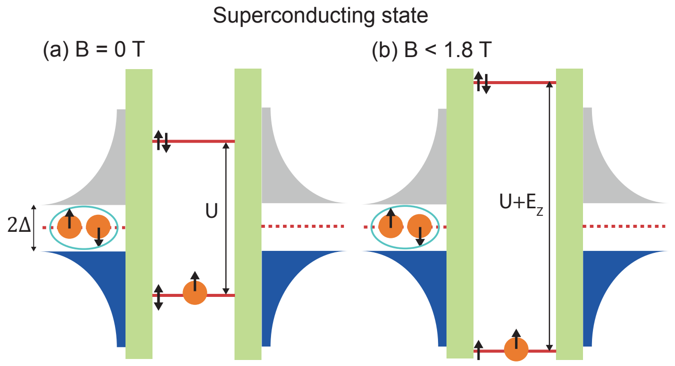

Figure 5.18: Quantum dot schemes of the device in the 0.7 anomaly regime in the *superconducting* state at zero bias, at zero **(a)** and finite **(b)** field, respectively, to be contrasted with Figure 5.17. At zero field **(a)**, Cooper pairs can transit by cotunneling processes not shown here, and a supercurrent develops. At finite field **(b)**, the energy level of the quantum dot is Zeeman-split. In this case, Cooper pairs are also able to transit through cotunneling.

Owing to its two superconducting contacts, the device behave like a Josephson junction at zero magnetic field and sufficiently strong coupling. Thanks to the choice of materials, the Josephson regime could be studied also under a strong magnetic field. Indeed, the Ta contacts had been chosen for their high critical field (~ 1.8 T). This property, combined with the large g-factor of the nanowire ($|g| = 11$), was convenient for investigating the influence of spin effects on the Josephson current, without destroying first the superconductivity of the contacts.

In this section, I will show supercurrent measurements at the gate voltage that displayed the 0.7 anomaly as a function of magnetic field. The schemes of Figure 5.17 represent the constant tunnel coupling limit of the quantum dot model explained in the first section at zero bias, in the normal state. These schemes are to be contrasted with the ones in Figure 5.18. While the situations in Figure 5.17 and Figure 5.18**a** have been studied before in quantum dots [96][110][125], the large magnetic field case of Figure 5.18**b** remained unexplored.

Description of the measurement setup

The two-terminal device was measured in a voltage-biased configuration at a temperature of T = 15 mK. In this configuration, a large enough DC voltage [4] was applied while the differential conductance dI/dV and the current I were both registered simultaneously. To record the dI/dV signal, a small AC excitation of 1 μV at a frequency of 41.3 Hz was applied. Since there was a series resistance of 40 kΩ coming from the filters, plus around 10 kΩ coming from the measuring circuitry -mainly the current amplifier-, the effective AC excitation seen by the sample was less than this value and dependent on the level of conductance through the sample. The real dI/dV was corrected by subtracting the sum of these two known series resistances. After this correction, a non-dissipative supercurrent appeared as a band around zero-bias of divergent conductance. If there was any sort of dissipation, the conductance acquired a finite value.

Besides this correction, there was also a voltage drop through the resistance in series with the sample, which had to be taken into account to obtain the real voltage drop through the nanowire. After this correction, the band of divergent conductance shrinked into a zero-bias divergent peak. If we were dealing with a non-dissipative supercurrent, these two treatments lost all the information that the measurements gave us about the switching current. On the other hand, if the supercurrent was slightly dissipative, the zero-bias peak had a finite width and height which still hold information about the original critical current. I will show later how this information was extracted in this latter case.

Before any of these two corrections, the raw V - dI/dV data appears as a plateau of finite conductance around zero bias, whose value is exactly equal to the conductance of the filters plus the measuring circuitry ($1/R_s$). An example of this is shown in Figure 5.19**b**. The width of the plateau is proportional to the switching current of the device. At a voltage before and after the plateau, the conductance attains a lower value, which is proportional to any channel within the superconducting gap: MAR, ABS, etc. In the raw V-I curves, the plateau corresponds to a line

---

[4] Large enough to see the full non-dissipative branch inside the gap. In the case of dissipative supercurrent, this voltage could be as small as 7 μV and as large as 20 μV.

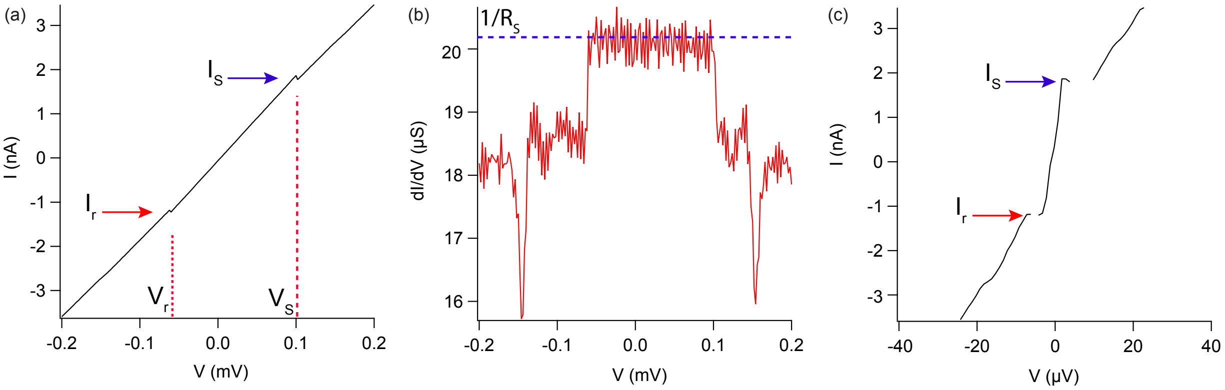

Figure 5.19: **(a)** Raw V-I curve at V_{G3} = -1.235 V, V_{G2} = -1 V and B = 0 T, right within the 0.7 anomaly. The switching (I_s) and retrappring (I_r) current are indicated, together with the quantities V_s and V_r, which appear as a result of the finite series resistance R_s of the filters and the measuring circuitry. **(b)** Raw V - dI/dV recorded simultaneously with **(a)**. The conductance plateau mentioned in the text, which is equivalent to the series conductance $1/R_s$ of the filters and measuring circuitry combined, is indicated by a blue dashed line. **(c)** V-I curve from which the voltage drop at the series resistance R_s was subtracted. Notice the change of units -from mV to μV-.

with a finite slope dI/dV = $1/R_s$, as in Figure 5.19**a**. The raw V-I curves can be corrected by subtracting the voltage drop of around 50 kΩ in the filters and the measuring circuitry. In Figure 5.19**a**, the switching (I_r) and re-trapping (I_s) currents have been identified. Because of the series resistance R_s, the quantities identified as V_r and V_s are proportional to I_r and I_s. The real voltage applied on the sample is then obtained, and the new V-I curves will show a non-dissipative branch between I_r and I_s, which are the re-trapping and the switching currents, respectively, as in Figure 5.19**c**.

At low magnetic field the supercurrent through the 0.7 anomaly was non-dissipative and the switching current was directly extracted following this last method, from corrected V-I curves. At high field, the supercurrent was dissipative -for reasons explained later-, and the critical current could only be extracted by fitting corrected V - dI/dV curves.

Figure 5.20 shows a scheme of the equivalent circuit of the Josephson junction device studied in this chapter. The cold parts of the circuit, which were kept at T = 15 mK during the measurement, are encircled by dashed lines. The voltage source and the ammeter are at room temperature; the latter in series with a resistance $R_{circuitry}$ of about 10 kΩ from the current amplifier.

The cold parts of the circuit consist in a filtering stage (delimited by black-dashed lines), the on-chip leads (blue-dashed lines), and the sample (red-dashed lines). The filtering stage had a two-stage RC circuit, with $R_{filters}$=10 kΩ and $C_{filters}$=10 nF. Since there are four of these resistances in series with the sample, the total series resistance R_s that the sample sees is of about 50 kΩ.

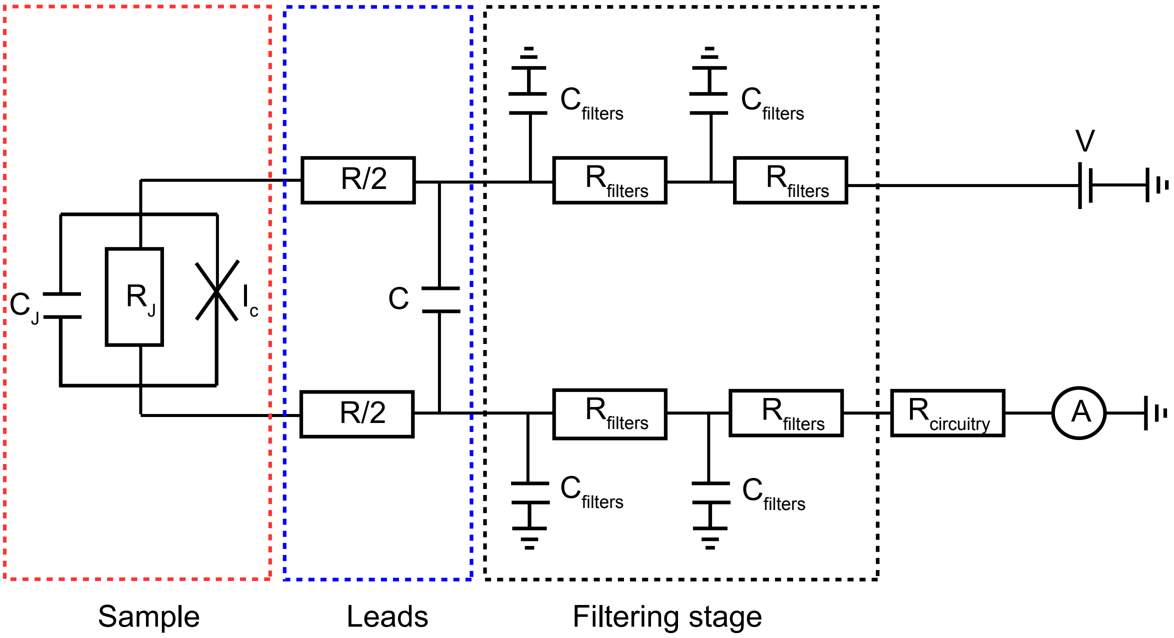

Figure 5.20: Equivalent electric circuit of the measurement setup. The elements relevant for the electromagnetic environment of the sample are depicted.

The on-chip leads had a large capacitance in between them because they ended in large bonding pads -of 150 μm× 150 μm-, as illustrated in the GDS file of the pads in Figure A.8 of the Appendix A. The estimated capacitance between the two neighboring pads was roughly of about C = $1\times10^{-}15$ F. The resistance R of the leads was determined by a fitting of the supercurrent V - dI/dV characteristic, and was found to be R = 1.6 kΩ, as explained later.

The sample itself is modeled as a Josephson supercurrent source I(ϕ) of critical current I_c, in parallel with a junction resistance R_J and a junction capacitance C_J. I_c and R_J depended on the gate voltage and ranged, respectively, from 20 pA to 2 nA, and from 20 kΩ to 100 kΩ. R_J can also depend on the bias voltage V, but for the small bias applied -of less than 20 μV when B ≥ 0.45 T-, this dependency can be dropped. The value of C_J can be estimated from the charging energy U = 1.3 meV measured in the previous section, from which C_J = $6\times10^{-}17$ F.

At low magnetic field

At fields B ≤ 0.4 T, the switching current I_s through the 0.7 anomaly could be directly measured in the way mentioned in the previous section for non-dissipative supercurrents.

Figure 5.21**a** shows a *raw* conductance map -i.e. *as measured*, without any subtraction of the series resistance R_s from the filters and the measuring circuitry- taken at B = 0 T and T = 15 mK, as function of gate 3 and voltage bias. In the map, the gate modulates the voltages V_r and V_s,

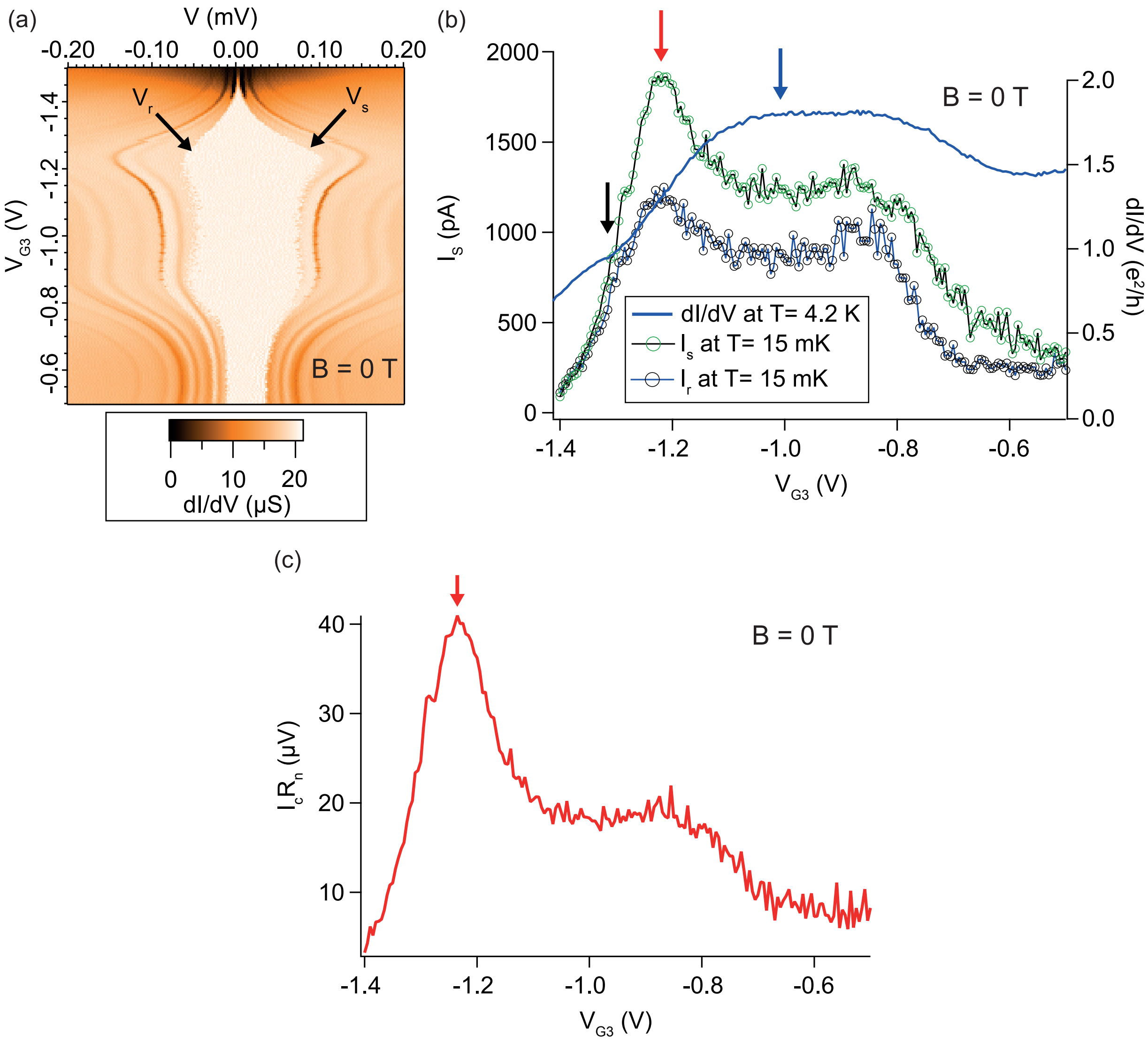

Figure 5.21: **(a)** 2D map of raw conductance data as a function of voltage bias and gate 3, taken at B = 0 T. V_r and V_s, which are proportional to the re-trapping and the switching current, are indicated by black arrows. **(b)** Switching and re-trapping current (green circles and blue circles joined by a black line, respectively) in pA extracted from corrected V-I curves taken from **(a)**, as explained in Section 5.5, for each V_{G3} in the gate range of the 0.7 anomaly. The conductance trace containing the 0.7 anomaly shoulder from Figure 5.13 at T = 4.2 K, also taken at B = 0 T (blue line), is similarly shown. The arrows point, respectively, to the conductance shoulder (black arrow), the maximum of switching current (red arrow) and the maximum of linear conductance (blue arrow). **(c)** I_sR_n product of the normal resistance taken from the blue curve in **(a)** and the switching current, taken also from **(a)**. The I_sR_n product is visibly not constant with the gate voltage.

which are proportional to the re-trapping and the switching currents as explained before. V_r and V_s are clearly not symmetric with respect to zero-bias, with $|V_s| > |V_r|$, but lose this asymmetry near pinch-off.

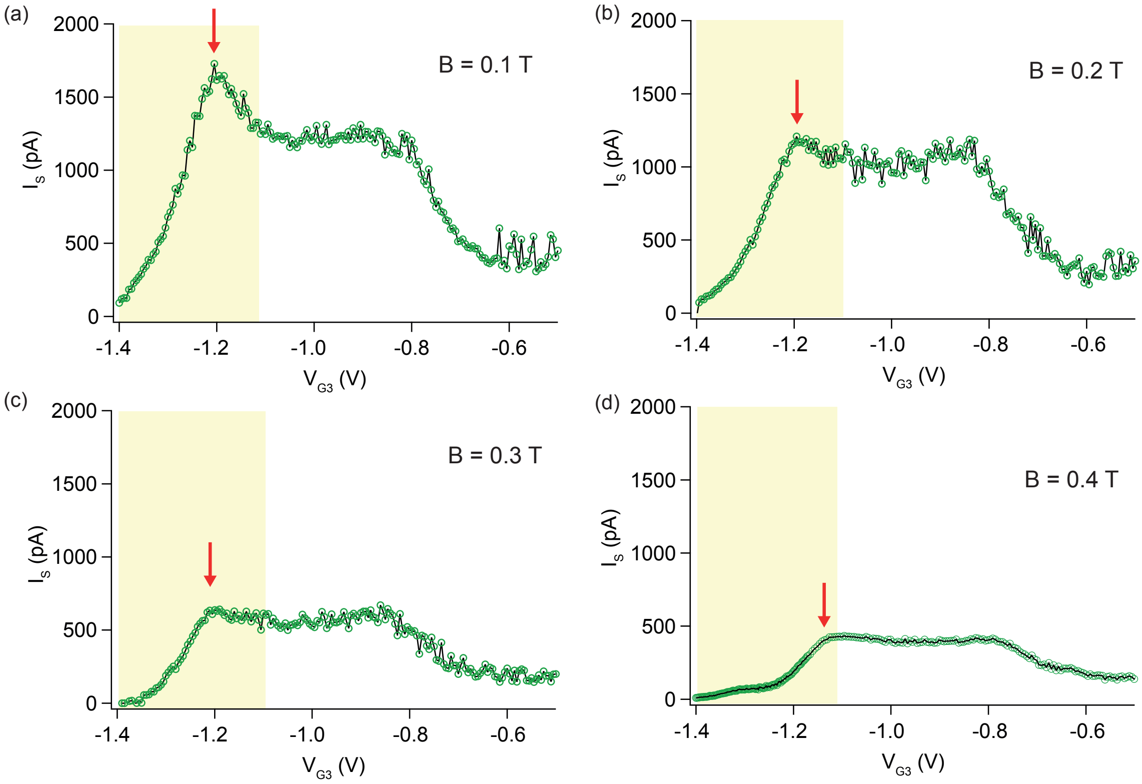

Figure 5.22: Magnetic field dependence of the switching current vs. gate 3 characteristic (I_s vs. V_{G3}), for (a) 0.1 T, (b) 0.2 T, (c) 0.3 T and (d) 0.4 T. The maximum switching current is indicated by a red arrow.

A plot of I_s vs. V_{G3} and I_r vs. V_{G3}, both extracted from the data in 5.21**a**, is given in Figure 5.21**b**, superposed to the linear conductance trace at T = 4.2 K of Figure 5.13, which was also taken at 0 T. $|I_s|$ is clearly larger than $|I_r|$, except at very low normal conductance. Interestingly, the maximum supercurrent at zero magnetic field (red arrow) is not the same as the maximum conductance (blue arrow). The maximum switching current is between the conductance shoulder (black arrow) and the conductance maximum (blue arrow).

This is further evidenced in the I_sR_n product, obtained by multiplying the normal resistance at T = 4.2 K and the critical current at zero field. Plotted in Figure 5.21**c**, the I_sR_n shows a large peak indicated by a red arrow. In the peak, the Is_Rn product is half Δ, or 0.16 times the Ic_Rn product of a tunnel Josephson junction, which is $Ic_Rn = \pi\Delta/e$.

At finite but low magnetic field -oriented parallel to the nanowire-, the switching current quickly decreases in magnitude, but it decreases *faster* at its maximum. Figure 5.22, which corresponds to I_s vs. V_{G3} plots taken at B = **(a)** 0.1 T, **(b)** 0.2 T, **(c)** 0.3 T and **(d)** 0.4 T, shows this tendency (red arrow). In these plots, the gate range of the 0.7 anomaly limited by the higher value of conductance (blue arrow) in Figure 5.21 is shaded in yellow. If the supercurrent is Kondo enhanced at its maximum, then it is natural to see it decreasing faster with magnetic field at this point. This is because the Kondo effect will be progressively destroyed as the electron sitting in the relevant dot level becomes spin-polarized.

At high magnetic field

The switching current is not measurable when the Josephson energy E_J is comparable to the thermal energy $\kappa_B T$, which happens at the gate region in the middle of the 0.7 anomaly starting from B ≥ 0.45 T, and extends to a larger gate region as the magnetic field is increased. In this subsection I will show how this happens in the data and how the critical current can be extracted under these inconvenient circumstances.

Figure 5.23**a** shows a *raw* conductance map -i.e. *as measured*, without any subtraction of the series resistance R_s from the filters and the measuring circuitry- taken at B = 0.45 T and T = 15 mK. In this map, a black line has been added to serve as a guide to the eye for following the gate evolution of the V_r and V_s quantities first described in 5.19**a**, which appear as a result of the finite series resistance R_s, and which are proportional to the re-trapping I_r and the switching current I_s. In this map, the white color corresponds to a conductance of almost $1/R_s$, meaning that the supercurrent is non-dissipative only when the supercurrent branch is of this color. This happens around the black dashed line, as it is also seen in the trace of the same color taken at this gate voltage shown in Figure 5.23**b**. In this trace, the supercurrent branch appears as a plateau of conductance of almost $1/R_s$.

At gate voltages around the green and blue-dashed lines, the supercurrent is clearly dissipative, as can also be seen in the traces of the same color in Figure 5.23**b**, taken at these two gate voltages. In these traces, the supercurrent appears as a zero-bias peak of a conductance much lower than $1/R_s$. Moreover, the zero-bias peak is *smaller* around the green-dashed line as compared to the blue-dashed line, even though the sub-gap conductance is *larger* around the green-dashed line. Not only the sub-gap conductance is larger, but also the *normal* conductance. In the map of Figure 5.23**a**, the normal conductance (blue trace) of the 0.7 anomaly depicted before in Figure 5.13 has been superposed, to show that the conductance is decreasing as the gate goes to negative values, and still the supercurrent is *larger* near pinch-off than in the shoulder of the 0.7 anomaly. This contradicts the usual behavior of a Josephson junction, for which the $I_c R_n$ product is a constant, where R_n is the normal resistance and I_c is the critical current. This is a truly *remarkable* observation; however, it is not the first time that we see it in this device. Figure 5.21, which displayed the switching current vs. gate voltage, also showed this anomalous behavior. In that plot, it happened that at lower normal conductance than the conductance maximum, the supercurrent maximum occurred.

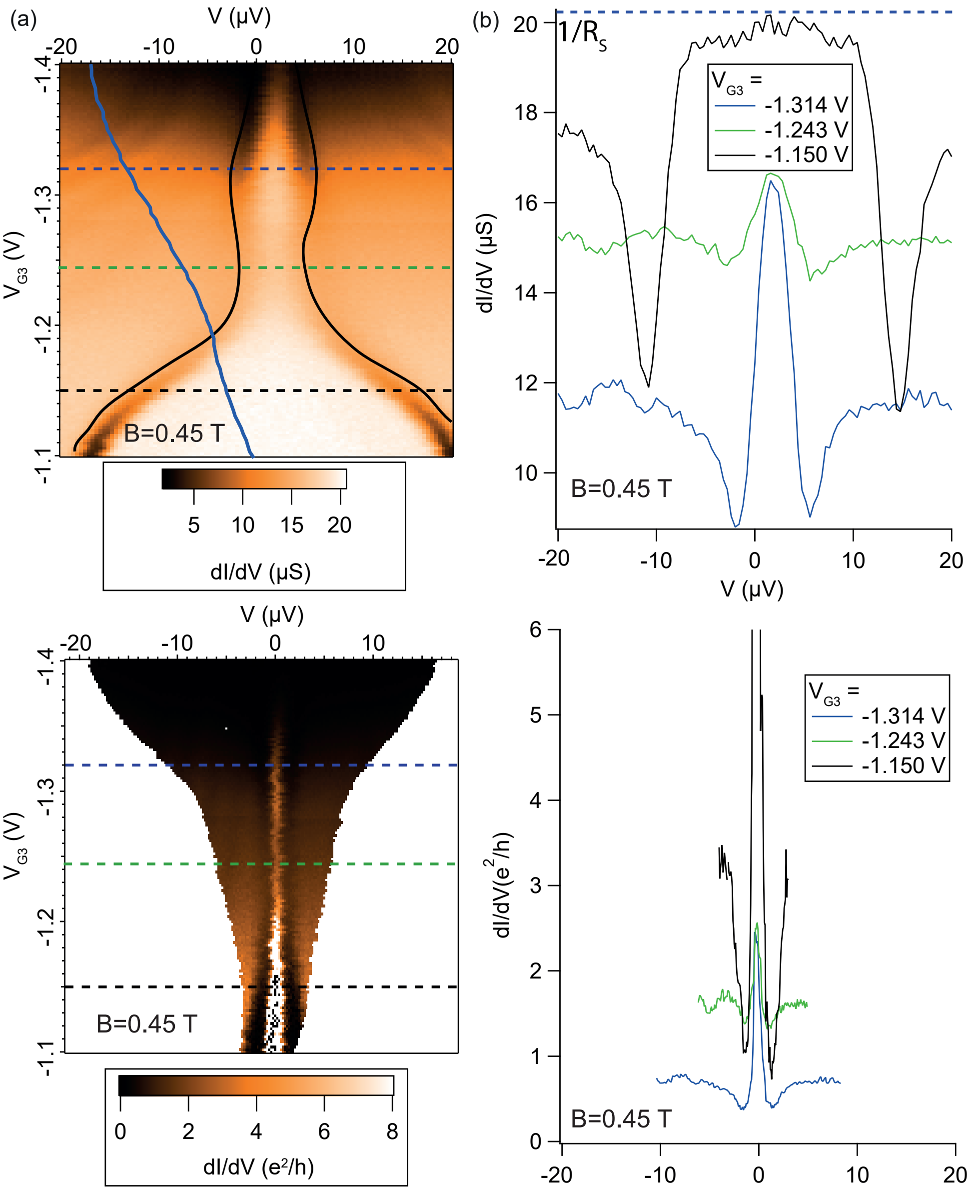

Figure 5.23: **(a)** Maps of raw conductance -i.e., as measured- as a function of gate 3 voltage, taken at B = 0.45 T. Black lines were added as an aid to follow V_r and V_s, which are proportional to the retrapping and the switching currents, respectively. The linear conductance measurement of Figure 5.13 is shown superposed to the map, to demonstrate that V_s is not following monotonically the normal conductance, which is unexpected for a regular Josephson junction. **(b)** Cuts through the dashed lines of the same color in **(a)**. **(c)** Same as **(a)**, but with the conductance and the bias corrected by subtracting R_s. A voltage shift of 1.5 μV coming from the voltage source has also been corrected. **(d)** Cuts through the the dashed lines of the same color in **(c)**.

For the cases in the green and blue dashed lines, the switching current cannot be extracted

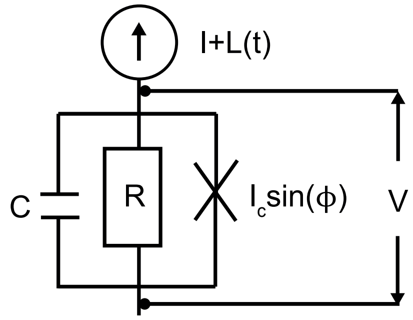

Figure 5.24: Scheme of a current-biased Josephson junction of supercurrent $I_c \sin\phi$ in parallel with a resistance R and a capacitance C. The junction is current-biased by a source I with thermal white noise $L(t)$, generating a voltage drop V across its terminals.

by the procedure used for lower magnetic field. Figure 5.23**c** shows the conductance map of 5.23**a** after the series resistance R_s was subtracted from the conductance and the voltage bias. The supercurrent appears here as a divergent zero-bias peak whenever it is non-dissipative, as in the black trace of Figure 5.23**d**, which was taken at the black dashed line in 5.23**c**. The other two traces -blue and green- of Figure 5.23**d** are zero-bias peaks of finite conductance, and thus correspond to dissipative supercurrents. No switching current can be accurately measure in these conditions, whereas it can definitely be measured in the case of the black curve of Figure 5.23**d**.

A careful look at the the region around the black-dashed line in the map of Figure 5.23**a** also reveals that the V_r and V_s voltages, proportional to the switching and the re-trapping currents, are equal in magnitude -if one corrects for a 2 μV voltage offset from the voltage source-. This indicates that the supercurrent has gone from being underdamped to being *overdamped* [76]. A quantity that points the level of damping in a Resistively and Capacitively Shunted Junction (RCSJ) is the quality factor Q [5]. We can evaluate the quality factor of the sample by the following formula (equation 5.3) [110]:

$$Q = \frac{\sqrt{\hbar[C(1 + R/R_J) + C_J]/(2eI_c)}}{RC + \hbar/(2eI_cR_J)} \tag{5.3}$$

In fact, the Q factor is gate-dependent because of R_J and I_c, which are not inversely proportional to each other for all gate voltages, as we saw. In general, the larger I_c is, the larger the Q factor will be. For a given I_c, the larger R_J is, the larger the Q factor will also be. Since I_c and R_J are also changing with magnetic field, Q will be a function of the gate voltage *and* the magnetic field.

Nevertheless, it is possible to roughly estimate Q for a few values of R_J and I_c and see its tendency, by inserting the values of the junction capacitance $C_J = 6\times10^{-}17$ F, the leads capacitance C = $1\times10^{-}15$ F and the leads resistance R = 1.6 kΩ (obtained in a few moments) in the formula.

---

[5] For a description of the RCSJ model and damping in Josephson junctions, see Ref. [76].

At B = 0 T, at the supercurrent maximum of Figure 5.21**c**, Q = 1.5 and the junction is expected to be slightly *underdamped*, which is the case as one can see by examining the raw data in 5.21**a**, for which $|V_s| > |V_r|$, and the corresponding difference between I_s and I_r in Figure 5.21**b**. At the supercurrent minimum of Figure 5.21**b**, when the normal conductance of the sample is low, Q = 0.8 and the junction is slightly *overdamped*. At this gate voltage, I_s and I_r are nearly equal, as can also be seen in Figure 5.21**b**. Since the magnetic field decreases I_c steadily, one only expects Q to become lower as the magnetic field is raised, and the junction more and more strongly overdamped.

Fitting the conductance curves for extracting the critical current

The supercurrents in the green and blue curves of Figure 5.23**c** appear as finite conductance peaks because of thermal fluctuations that smear-out the switching current, whenever the Josephson energy $E_J = hI_c/2e$ is of the same order as the thermal energy $\kappa_B T$, as was first described in Ref. [126] and extended to a more general case in Ref. [127]. In the more general model, which is also described in Ref. [128], the Josephson junction is treated as a phase-dependent current generator $I_c \sin\phi$ -the junction is assumed very small- connected in parallel with a resistance R and a capacitance C, which is biased by a DC current source I, and across of which a voltage drop V develops -see the scheme in Figure 5.24, adapted from Ref. [128]. So far, this corresponds to the classic RCSJ model at zero temperature [76]. However, Halperin and Ambegaokar also added a white noise source to the current source I, which they described by its time correlation $< L(t+\tau)L(t) >= 2\delta(\tau)\kappa_B T/R$ [127]. Combining this equation with one of the Josephson equations $d\phi/dt = 2eV(t)/\hbar$, the following expression for the phase is found [128]:

$$\frac{\hbar C}{2e}\frac{d^2\phi(t)}{dt^2} + \frac{\hbar}{2eR}\frac{d\phi(t)}{dt} + I_c \sin\phi(t) = I + L(t) \tag{5.4}$$

To solve this equation, Halperin and Ambegaokar assumed that the capacitance of the junction was small, which is a valid assumption for ultra small Josephson junctions such as the device treated in this chapter. In this case, the first term of equation 5.4 can be neglected. Then, they proceeded to solved the equation to find $< V >$, the DC voltage generated by the junction, as a function of I, the applied current. The solution to the equation turns out to be the expression in equation 5.5 [128][110], if the current is written as a function of the voltage.

$$I(V) = \frac{R_J}{R_J + R}\left(Im\left[\frac{I_{1-i\eta(V)}(\beta)}{I_{-i\eta(V)}(\beta)}\right] + \frac{V}{R_J}\right) \tag{5.5}$$

Where $I_\alpha(x)$ is the modified Bessel function of complex order alpha, $\eta(V) = \hbar V/2eR\kappa_B T$, and $\beta = I_c\hbar/2e\kappa_B T$ is the ratio between the Josephson energy and the thermal energy. $Im[]$ indicates that the imaginary part of what is inside the brackets must be taken. This equation additionally contains the resistance of the junction R_J, which does not come from the original expression 5.4.

This term is included to account for an additional multiple Andreev reflection (MAR) channel in parallel with the Josephson current [110]. The resistance R_J provides an ohmic contribution at a current above the critical current.

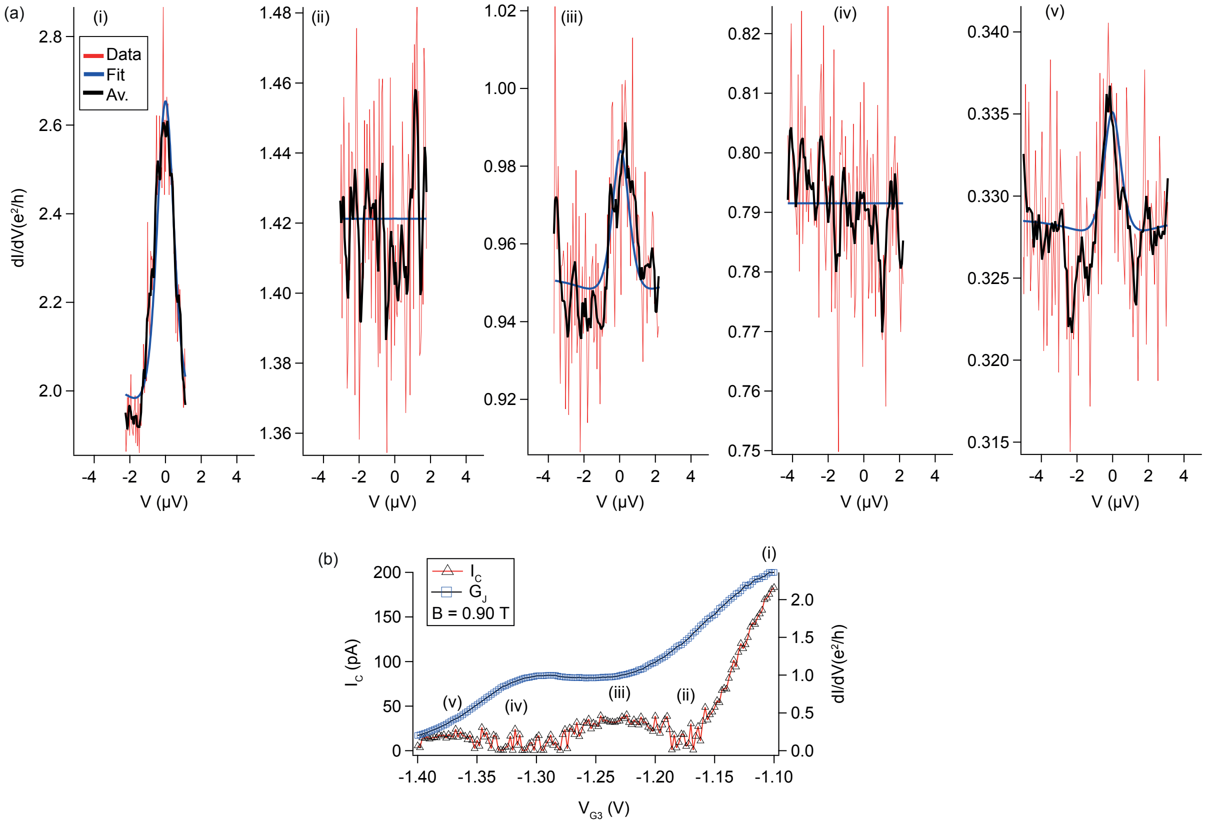

Figure 5.25: (a) Examples of corrected V - dI/dV curves taken at B = 0.9 T, fitted with equation 5.6. They correspond to the gate voltages indicated in **(b)**. The correction in these curves consisted in subtracting the series resistance R_s from the conductance and the bias voltage. **(b)** Critical current I_c and junction conductance G_J as a function of the V_{G3}, extracted by fitting corrected data at B = 0.9 T.

Equation 5.5 has been used in previous works to fit V-I curves, extract the critical current I_c and show $\phi_0 = 0 \rightarrow \phi_0 = \pi$ transitions in overdamped carbon nanotube Josephson junctions [110][125]. In my case, I used V - dI/dV curves to do a similar job. With this purpose, I derived equation 5.5 to obtain an expression that I could use to fit the data:

$$\frac{dI}{dV}(V) = \frac{R_J}{R_J + R}\left(\frac{d}{dV} Im\left[\frac{I_{1-i\eta(V)}(\beta)}{I_{-i\eta(V)}(\beta)}\right] + \frac{1}{R_J}\right) \tag{5.6}$$

The functions $I_\alpha(x)$ in equation 5.6 were numerically found by inserting in the software IGOR the first 65 terms of the following infinite summation for $I_\alpha(x)$ [129], and truncating the series if the difference between the summation of the m and the summation of the $m-1$ terms was smaller than 10^{-10}:

$$I_\alpha(x) = \sum_{m=0}^{\infty} \frac{1}{m!\Gamma(m+\alpha+1)} \left(\frac{x}{2}\right)^{2m+\alpha} \tag{5.7}$$

The derivative of $I_\alpha(x)$, in turn, was found by differentiating equation 5.7 analytically with respect to α, and then proceeding numerically in the same way as for finding the values of $I_\alpha(x)$.

Equation 5.6 leaves as fitting parameters the temperature T; the leads resistance R, the resistance of the junction R_J and the critical current I_c. The temperature was known to be 15 mK throughout the experiment, so it should not really be considered a fitting parameter. In any case, initially I kept these four parameters as free, until I realized that T = 15 mK was indeed obtained by fitting the conductance data at B >∼ 0.45 T with equation 5.6. From these initial fits I also obtained R = 1.6 kΩ. R did not vary as a function of field or gate voltage for fields B >∼ 0.45 T in the overdamped regime. After ruling out these two parameters as constants, I_c and R_J were the only fitting parameters left. The fitting procedure thus provides us with the critical current and the junction resistance -which should not be confused with the normal-state resistance- for each gate voltage.

Figure 5.25**a** shows a series of corrected V - dI/dV curves (i to v; red lines) taken at B = 0.9 T, which were fit with equation 5.6 (blue lines). Since the data was noisy, an eleven-point average done with the software IGOR is also shown (black lines). The gate voltage at which these traces were taken is indicated in Figure 5.25**b**. Figure 5.25**b** is obtained by plotting the critical current I_c and the junction conductance G_J $(= 1/R_J)$ extracted from a fit like the ones in 5.25**a** for each gate voltage V_{G3}. One can see that a large zero-bias peak will give a large I_c -and viceversa-, whereas a flat conductance characteristic will result in $I_c \simeq 0$.

Figure 5.27 shows the magnetic field evolution of the fitted critical current from B = 0.45 T up to 1.3 T. The raw V - dI/dV data used for the fits is displayed in the maps in Figure 5.25. Before fitting the data, it was first corrected by subtracting the series resistance R_s from the conductance and the bias voltage, as explained before. The critical current is represented by black triangles joined by a red line, while the junction conductance is represented by blue squares joined by a black line.

In the first plot (Figure 5.27**a**), taken at B = 0.45 T, the junction conductance is decreasing almost monotonically from right to left, except for the feature pointed by the red arrow, which would correspond to the conductance shoulder of the 0.7 anomaly shown in the blue curve of Figure 5.13. To understand why we also see here the conductance shoulder in the extracted G_J curve, we need to remember that the junction conductance is the sub-gap conductance, which is roughly proportional to the normal conductance. Initially, the supercurrent is also decreasing

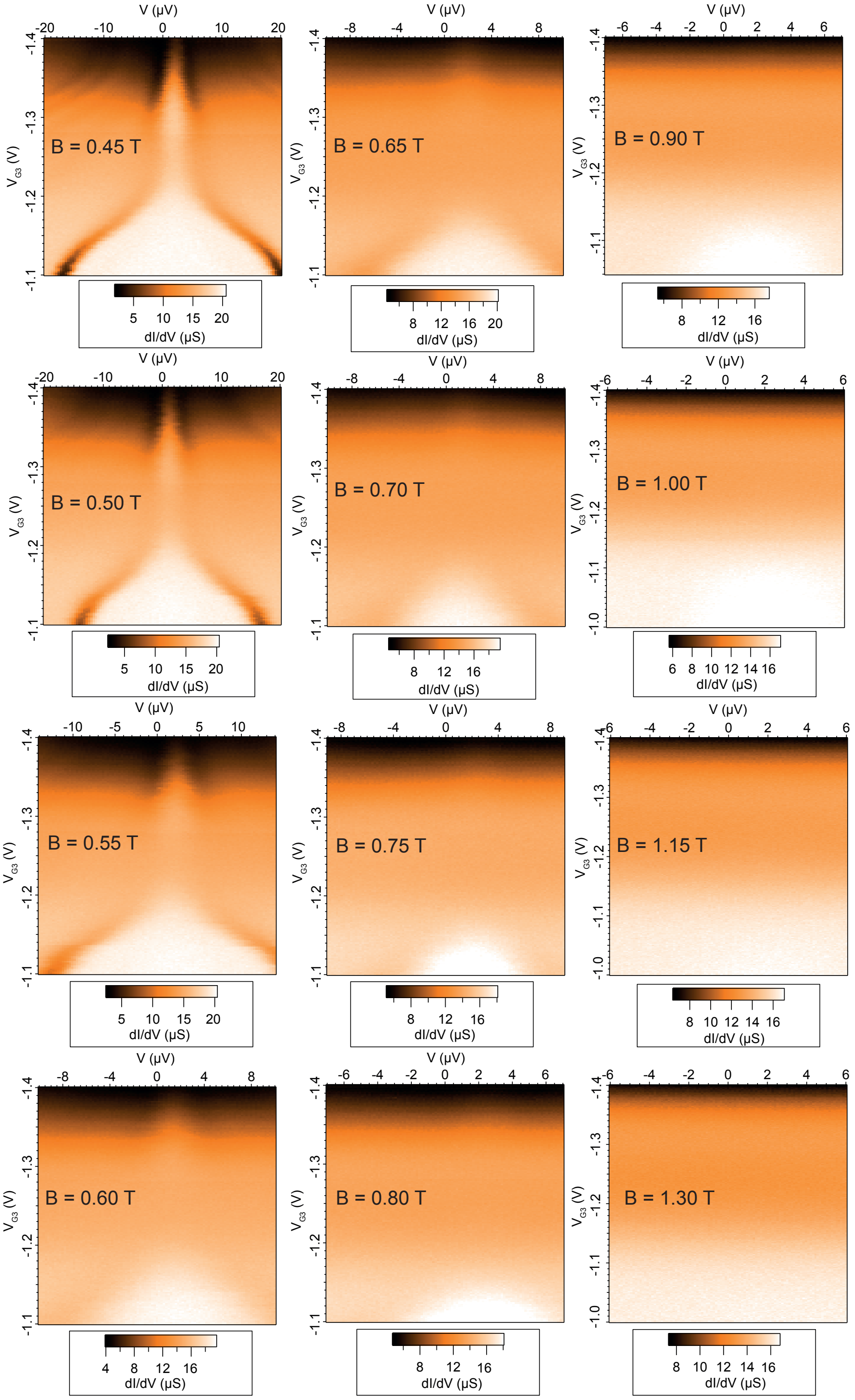

Figure 5.26: Maps of raw conductance data at various magnetic fields from B = 0.45 T to 1.3 T, fitted to obtain the critical current vs. gate plots of Figure 5.27.

monotonically from left to right, until the feature pointed by the red arrow, which is a sort of supercurrent *valley*. Continuing towards lower gate voltage, the supercurrent recovers and then continues to decrease monotonically.

For a larger magnetic field between 0.45 T and 0.65 T, we see the same qualitative gate behavior: the junction conductance continues to display a shoulder feature, and the critical current has a valley *coinciding* in gate voltage with this feature. Additionally, as the magnetic field is increased, the conductance shoulder widens and slowly becomes a plateau. The critical current is overall decreasing and the supercurrent valley is widening with the field. At B = 0.45 T, I_c= 200 pA in the middle of the supercurrent valley, while at B = 0.65 T, I_c is as little as 50 pA.

At B = 0.7 T (Figure 5.27**f**), the critical current in the supercurrent valley has decreased so much that it reaches *zero*. This occurrence is pointed by a black arrow in that plot. Moreover, this is happening at a gate voltage range within the junction conductance shoulder obtained from the same fit. At B = 0.75 T, the zero supercurrent region widens a bit more.

Something spectacular about this measurement must be pointed out. When the junction conductance is around 1.25 e^2/h the supercurrent is *zero*, but at a *lower* conductance of 0.8 e^2/h there is a robust supercurrent peak of about 50 pA. This is in strike contradiction with the constancy of the $I_c R_n$ product for a tunnel Josephson junction -supposing that R_J is proportional to R_n in our case, which is by all lights true-. It implies that there is something happening at the gate voltage pointed by the black arrow that acts as an efficient Cooper pair breaker/scatterer. In the quantum dot model, this corresponds to the spin-polarized impurity sitting in the dot.

When the field is increased to B = 0.8 T, there is a tiny, noisy but clear re-emergence of the critical current, pointed by a blue arrow in the corresponding plot in Figure 5.27**h**. This re-emergent critical current coexists surrounded by a zero-supercurrent region (black arrows). This tells us that the process that makes the supercurrent re-emerge is rather smooth with magnetic field: the first gate points at which the supercurrent disappeared at B = 0.7 T are the same gate points at which it re-emerges at B = 0.8 T [6].

At B = 0.9 T the supercurrent has re-emerged in almost the whole gate range where it had previously disappeared, except in the gate voltage indicated by the black arrows in Figure 5.27**i**. Not only it has re-emerged, but it is slightly stronger. Indeed, I_c is of about 40 pA in the middle of the re-emergence at B = 0.9 T, while it is only of about 20 pA at B = 0.8 T. This behavior is seen all the way until the supercurrent is so little that it can no longer be fit, at B = 1.3 T.

---

[6] As pointed out by Jorgensen et al. [110], the fit given by equation 5.6 ceases to be valid when the current-phase relationship becomes non-sinusoidal at the $0 \rightarrow \pi$ quantum phase transition (QPT). This will tend to produce a broader QPT in the fitted data than the one that the theory predicts. The NRG calculations show an abrupt re-emergence of the supercurrent after the QPT, without reaching zero at any moment -the critical current was defined as the *maximum* Josephson current. In particular, this explains why the supercurrent stays at zero for a long range of magnetic field ($\sim$ 0.1 T) before re-appearing as a π supercurrent in our case.

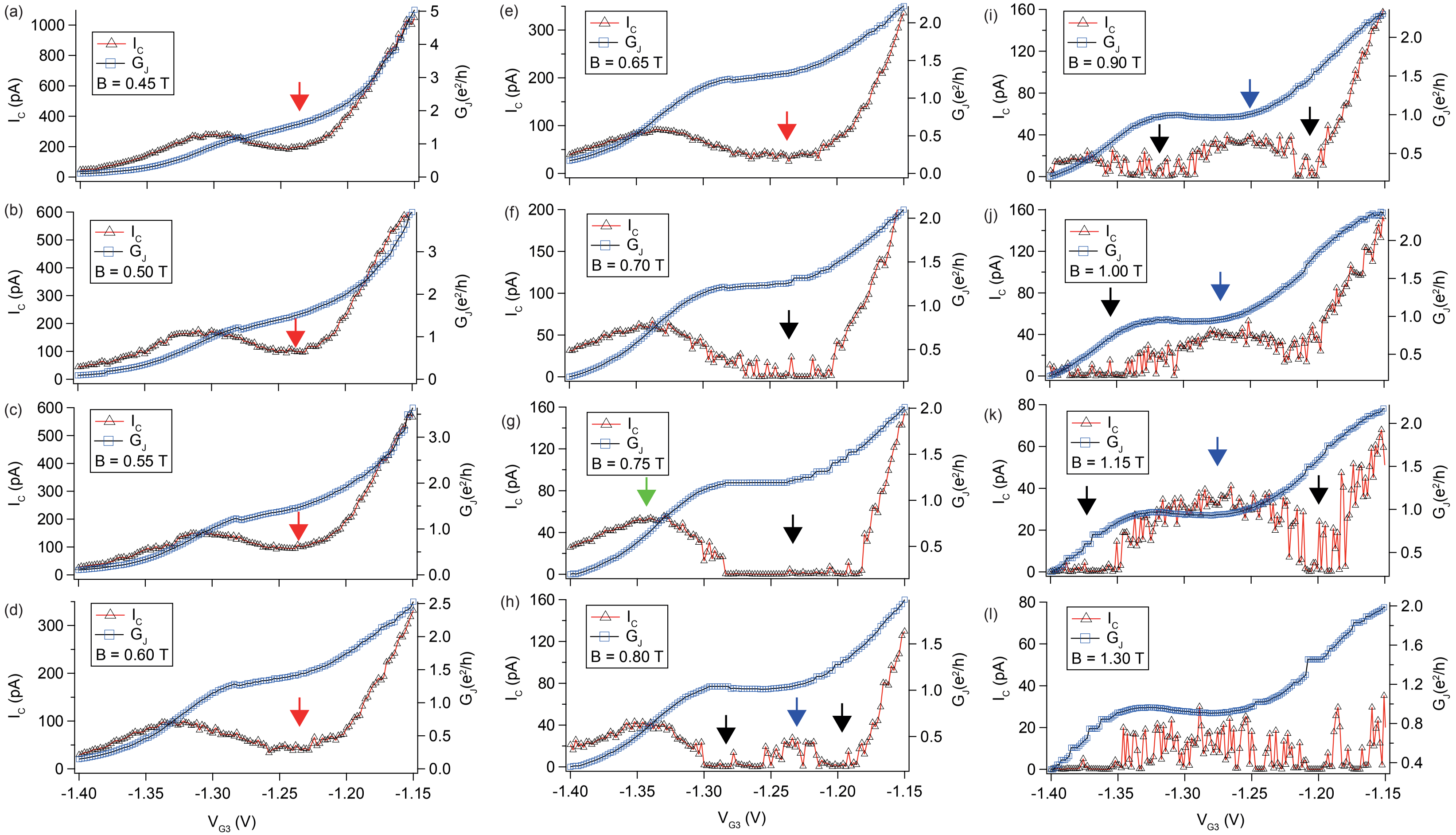

Figure 5.27: Magnetic field evolution of the critical current I_c and the junction conductance G_J as a function of the gate voltage V_{G3}, from B = 0.45 T up to 1.3 T. The red arrows point to supercurrent *valleys*, the black arrows to regions of *zero* supercurrent and the blue arrows to regions of *re-emerging* supercurrent.

Before we finish the description of the data, this last observation must be put in perspective with the fact that the gap closes with magnetic field. The supercurrent has increased for a larger magnetic field, for the *same* -or lower- level of conductance. Figure 5.28 shows the evolution of the gap with magnetic field.

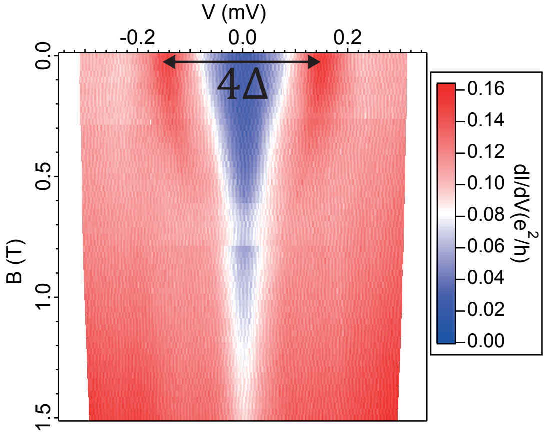

Figure 5.28: Closure of the superconducting gap with magnetic field, measured at V_{G3} = -1.5 V, when $U \gg \Gamma$. Δ is found to be 80 μeV.

5.6 Explanation of the field evolution of the supercurrent

We can bring back the gate and field-dependent tunnel-coupling dot model of Section 5.3 to try to explain this puzzling data. For consistency, it should also be relevant in the superconducting regime, for the *same* normal state parameters.

The Josephson effect in a quantum dot with one level available for transport has been extensively studied at zero magnetic field, both experimentally [110][96][95] and theoretically [120].

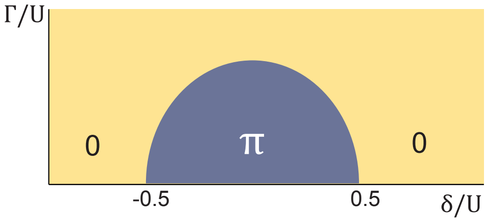

Figure 5.29: Sketch of the phase diagram of the ground state of a single-level quantum dot of charging energy U and energy level ε_d, where δ is defined as $\delta = \varepsilon_d$+U/2. The level is coupled to two superconducting leads of gap Δ with a tunnel coupling Γ, which allows it to carry a Josephson current $I_s = I_c sin(\phi + \phi_0)$. A doublet ground state $|d\rangle$ results in a $\phi_0 = \pi$ phase, which appears as a semi-circle blue shaded region in the diagram. Conversely, a singlet ground state $|s\rangle$ results in a $\phi_0 = 0$ phase, which corresponds to the yellow-shade region outside of the semi-circle region.

Theoretical calculations have demonstrated that a Josephson junction bridged by a single-level quantum dot experiences a quantum phase transition by virtue of the charging energy U of the dot [120]. Four parameters govern the entire physics of the transition: the tunnel coupling (Γ), the difference between the energy level of the dot and the chemical potential of the leads (ε_d), the charging energy U and the superconducting gap Δ, resulting in the zero-field phase diagram sketched in Figure 5.29. In this diagram, the ground state of the dot appears in any of two configurations: a doublet $|d\rangle$ or a singlet $|s\rangle$.

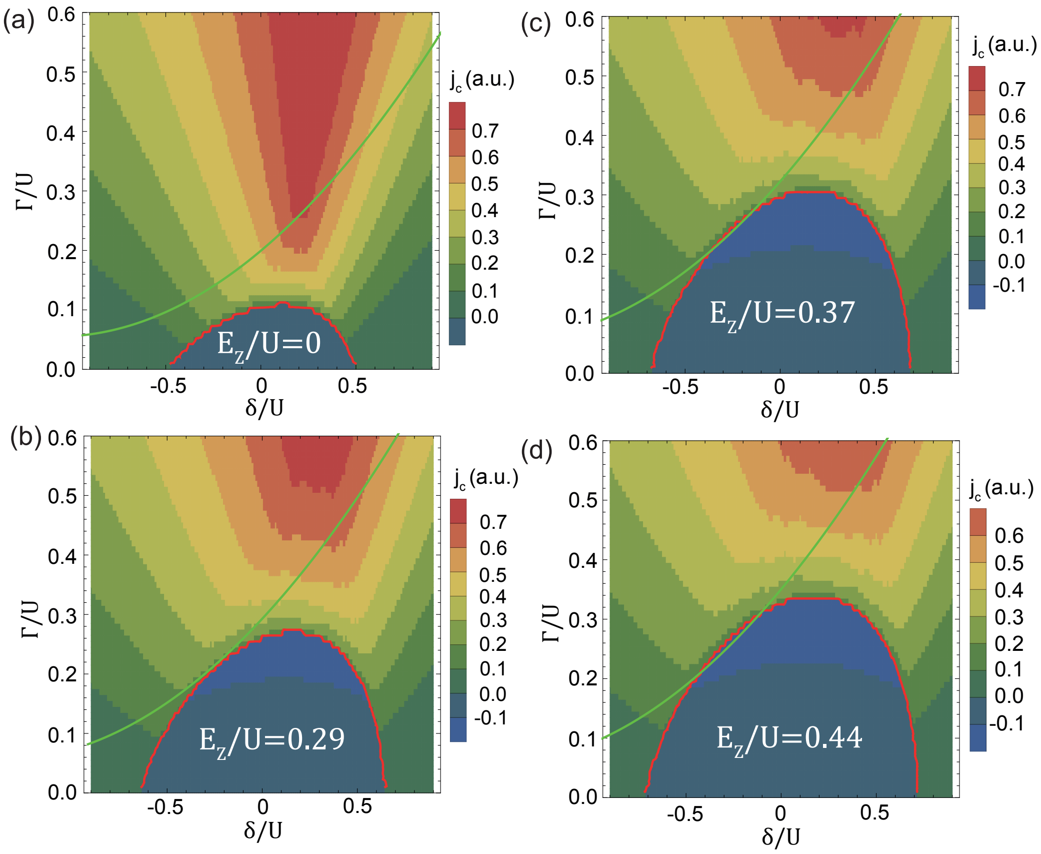

Figure 5.30: Calculated phase diagram of the ground state of a single-level quantum dot of charging energy U and energy level ε_d, where δ is defined as $\delta = \varepsilon_d$+U/2, for four different Zeeman energies: E_z/U = **(a)** 0, **(b)** 0.29, **(c)** 0.37 and **(d)** 0.44. The level is coupled to two superconducting leads of gap Δ with a tunnel coupling Γ, which allows it to carry a Josephson current $I_s = I_c sin(\phi + \phi_0)$. When the phase is $\phi_0 = 0$ ($\phi_0 = \pi$), the Josephson current density j_c is positive (negative). The green curve superposed to all the plots represents the δ dependence of Γ, which was obtained from the normal linear conductance calculations in Figure 5.9**b**. These diagrams come from NRG calculations by Rok Zitko.

The Kondo temperature T_K, which depends on Γ, U and δ, is a good indicator of the ground state when it is compared to Δ. When the values of Γ/U and δ/U are such that $\kappa_B T_K > \Delta$, the quantum dot is in the $|s\rangle$ ground state and it carries a $\phi_0 = 0$ supercurrent, where ϕ_0 is a phase-shift in the current-phase relationship $I_s = I_c sin(\phi + \phi_0)$ of the supercurrent. This corresponds to the yellow region in the diagram of Figure 5.29. Conversely, when these values are such that $\kappa_B T_K < \Delta$, the quantum dot is in a doublet ground state and the phase of the supercurrent is $\phi_0 = \pi$. This in turn corresponds to the blue region in the diagram of Figure 5.29. At $\Gamma = 0$, this latter region extends over $-0.5 < \delta/U < 0.5$, which is also the spacing between the $< N >= 0 \rightarrow 1$ and the $< N >= 1 \rightarrow 2$ Coulomb peaks.

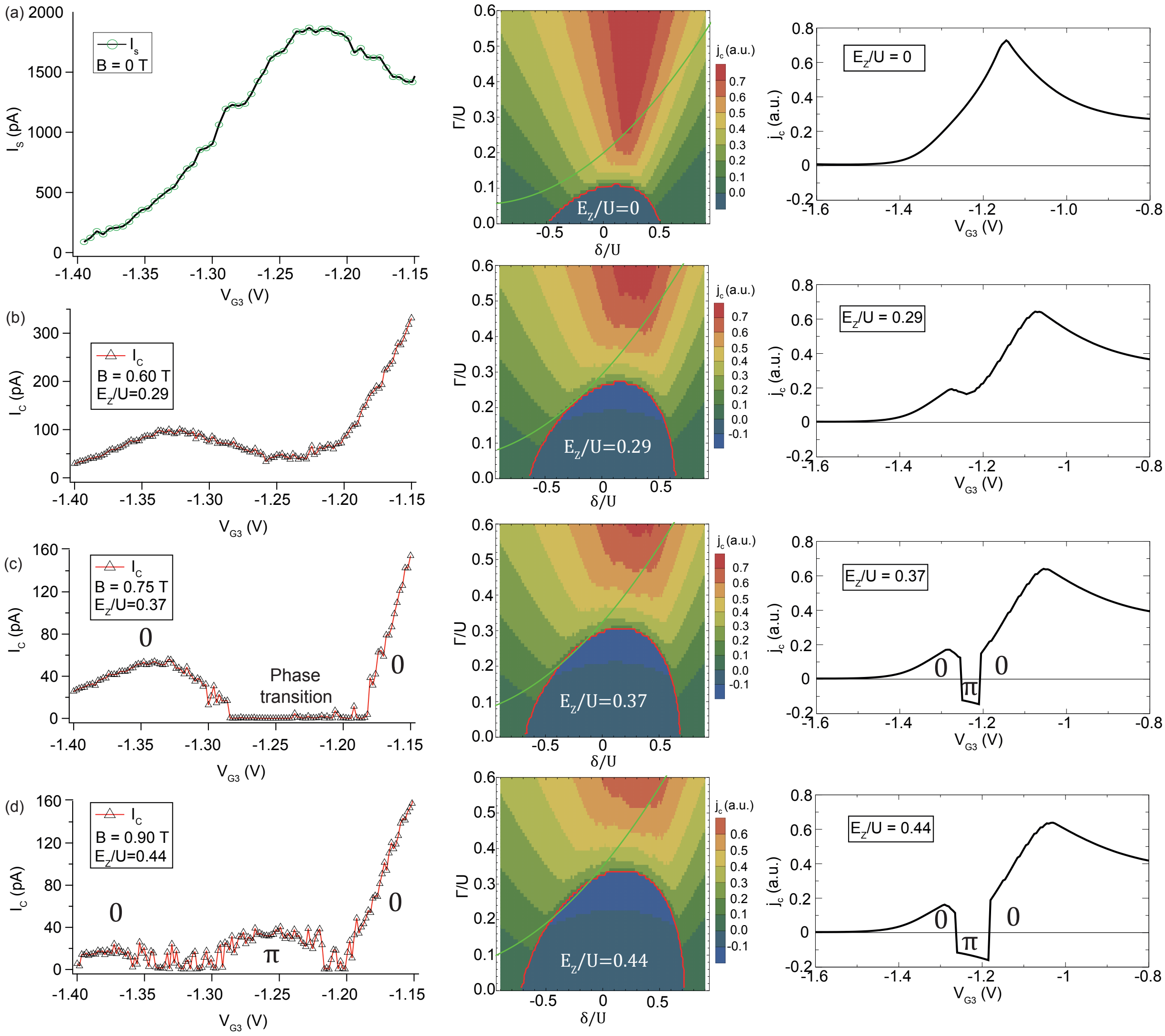

Figure 5.31: Comparison of the experimental data (left panels) for the switching current **(a)** and the critical current **(b-d)** with the calculated phase diagrams (central panels) and cut-lines along the green lines in the phase diagrams (right panels). Data and theory correspond to the same E_z/U ratio: E_z/U = **(a)** 0, **(b)** 0.29, **(c)** 0.37 and **(d)** 0.44. The qualitative agreement is good. Note that in the π region the calculated critical current density j_c (right panels) reaches negative values, and the gate range is larger than in the experiment.

Experimentally, the two ratios δ/U and Γ/U can be conveniently changed by applying a voltage in a plunger gate and in barrier gates, respectively. If one applies a plunger gate voltage on the quantum dot, one can tune δ/U along the red arrows in Figure 5.29, and obtain $\phi_0 = 0$ to $\phi_0 = \pi$ -and viceversa- transitions. By applying voltages on barriers gates, one can tune Γ/U along the green arrow in Figure 5.29, and obtain $\phi_0 = 0$ to $\phi_0 = \pi$ -and viceversa- transitions. What one has to do next is to find a way of *proving* that the phase transition has occurred. People have done this by either directly measuring the phase of the supercurrent in a SQUID configuration [96], or by fitting the critical current and showing that it goes to zero at the $\phi_0 = 0$ to $\phi_0 = \pi$ transition [110][125], without knowing *per se* the phase itself.

However, the influence of a magnetic field, notably by the Zeeman effect, is less known. The Zeeman energy will destroy the Kondo correlations that set the ground state of the quantum dot in the $|s\rangle$ state, by splitting the energy level of the dot in the $-0.5 < \delta/U < 0.5$ range -at mean occupation $< N >= 1$-. Consequently, the $|d\rangle$ region shaded in blue in Figure 5.29 is expected to grow with magnetic field, by an amount at least proportional to the Zeeman energy.

Rok Zitko has made calculations using the NRG model that demonstrate the growth of the $|d\rangle$ ($\phi_0 = \pi$) region which was sketched Figure 5.29. The result of the calculations is shown in Figure 5.30 for four different ratios of the Zeeman energy $E_z = |g|\mu_B B$ to the charging energy U, calculated for the same parameters of the device presented in this chapter. The color code of the map is blue for negative supercurrent ($\phi_0 = \pi$), and green, yellow and red for positive ($\phi_0 = 0$); red being the strongest. The critical current density j_c was extracted by taking j at maximal $|j(\phi)|$. The *ground state* of the sample, and thus the phase of the supercurrent, will depend on the region in which the green curve *lays*. The diagrams are not hole-electron symmetric due to the value x = -0.4 chosen in the Hamiltonian 5.1 to obtain the best qualitative agreement with the normal and superconducting-state data. A negative (positive) x skews the phase boundary towards positive (negative) δ.

The curved green line superposed to each of these diagrams represents the dependency of the tunnel coupling Γ on the level position δ -which depends on the gate voltage-. The dependency of Γ with δ was obtained from the normal linear conductance calculations in Figure 5.9**b**, which connects the normal and the superconducting states and makes both calculations consistent with each other, at least qualitatively.

At zero magnetic field, when E_z/U= 0, the phase diagram is bounded at Γ= 0 by $-0.5 < \delta/U < 0.5$. At this magnetic field, the green curve is always in the $|s\rangle$ region and the phase is accordingly $\phi_0 = 0$, as can be seen in Figure 5.30**a**.

At a finite field of E_z/U= 0.29 (Figure 5.30**b**), the magnetic field has pushed the boundary of the $|d\rangle$ region towards larger Γ/U. This tendency will continue as the magnetic field is increased. At E_z/U= 0.27 (Figure 5.30**c**), the boundary of the $|d\rangle$ region touches the green curve. A phase transition from a $|s\rangle$ to a $|d\rangle$ ground state is happening at this intersection. Finally, at E_z/U= 0.33 (Figure 5.30**d**), a the green curve is intersecting in two point the $|d\rangle$ region of negative supercurrent. In the section of the green curve within the $|d\rangle$ region, the supercurrent will have a π phase and a $|d\rangle$ ground state. In this way, a $\phi_0 = 0$ to $\phi_0 = \pi$ phase transition has been obtained by just cranking up the magnetic field.

In Figure 5.31 I compare the experimental data (on the left) with the calculated phase diagrams (on the right). At E_z/U= 0, a large peak of supercurrent is expected when the green curve intersects the red colored region of the phase diagram. This is indeed seen in the experimental data at B= 0 T in Figure 5.31**a**. For the same gate voltage, as the field is increased, the peak is expected to vanish in the calculations, which is also seen in the data (see Figure 5.22).

At E_z/U= 0.29, which corresponds to B= 0.6 T in the experiment, a small dip in the critical current is expected when the green curve in the phase diagram is nearly touching the phase boundary of the $|d\rangle$ state. The experimental data shows the dip as well.

At a larger magnetic field, the quantum dot will experience a $\phi_0 = 0$ to $\phi_0 = \pi$ transition. At E_z/U= 0.37, in the data of Figure 5.31**c**, the supercurrent becomes zero at a finite gate range. From the way the supercurrent was calculated, it is not zero at this point. The discrepancy may also come from the fact that an I_c of less than 20 pA cannot be extracted from the fit; i.e. any supercurrent of less than 20 pA will effectively appear as zero supercurrent in this fit[7].

At E_z/U= 0.44 (B = 0.9 T, Figure 5.31**d**), the critical current has re-emerged as a $\phi_0 = \pi$ supercurrent in both the measurement and the calculation. In the measurement, since I_c takes only positive values, the supercurrent is seen as a peak when it re-emerges. In contrast, the calculation shows that the supercurrent becomes negative as soon as the green curve crosses the $|d\rangle$ boundary.

5.7 Conclusions

In this chapter, an InAs nanowire Josephson device with two gates -measured in the normal and the superconducting state- was thoroughly studied. In the normal state, the device behaved as two quantum point contacts in series with each other. By tuning the gates, it was possible to balance the conduction band profile in such a way that the two quantum point contacts became the two barriers of a quantum dot.

This quantum dot had a peculiar transport characteristic, which in many ways resembled the data of the 0.7 anomaly observed in quantum point contacts obtained in 2-dimensional electron gases, if the 0.7 anomaly was interpreted as a Kondo resonance. This peculiar transport characteristic comprised the following:

---

[7] One can also say that at this point the junction is *in a limbo* between the 0 and the π regions, and on average the critical current is therefore zero

1. At zero field and at a temperature larger than the critical temperature of the leads, the conductance showed a "shoulder" around 0.9 e^2/h, followed by a long plateau of maximum conductance 1.8 e^2/h
2. At large magnetic field -oriented parallel to the nanowire, above the critical field of the leads- the conductance showed a plateau at 0.9 e^2/h. Big changes in the magnetic field did not decrease the conductance of this plateau.
3. At high magnetic field, the conductance vs. bias characteristic showed a split-peak at zero bias. The peak-to-peak separation increased as twice the Zeeman energy.
4. The non-linear conductance at high bias showed an additional plateau at around 1 e^2/h, at both zero and high magnetic field.

At the end of the discussion of the normal state data, it was concluded that the signatures of the 0.7 anomaly in the device could be reproduced with a single-level spin 1/2 quantum dot model assuming strongly gate dependent tunnel coupling.

In the second part of this chapter, I presented measurements of the supercurrent through the 0.7 anomaly. The large g-factor of the nanowire and the large critical field of the Ta contacts allowed me to measure the Josephson current up to a high magnetic field. At low magnetic field it was possible to directly measure the switching current, but at higher field the supercurrent was so small that the thermal fluctuations prevented this. Luckily enough, the Josephson junction also became overdamped at large field, allowing me to fit conductance traces to extract the critical current.

I found that, at zero field, the Kondo effect enhanced the supercurrent in the 0.7 anomaly and produced a peak of switching current at the corresponding gate voltage. I also found that, at sufficiently high field, the supercurrent was suppressed strongly in the middle of the 0.7 anomaly. Remarkably, the supercurrent was suppressed in a gate region of large conductance, and recovered as a peak in a region of *lower* conductance. At larger field, the critical current dropped to zero and then, at an even larger field, it re-emerged. These observations were all in agreement with the interpretation of the device behaving as quantum dot with gate-dependent tunnel coupling, and were corroborated by calculations based on the single-level Anderson impurity model.

Chapter 6

Tunability of the transition field in a spin-split Josephson-junction nanowire quantum dot

6.1 Introduction

A quantum phase transition (QPT) of the ground-state of a quantum dot strongly coupled to a superconducting (S) lead was recently demonstrated under a magnetic field . In this experiment, the quantum phase transition occurred when spin-resolved Andreev bound states (ABS), coming from the interaction of a localized spin with the superconductor condensate, crossed the Fermi energy [12]. This experiment was proven relevant in the search for Majorana bound states (MBS), as the tunnel spectroscopy of the subgap states by a normal (N) metal could produce a signature in the conductance similar to the expected in a topological nanowire.

The experiment described above was done in an S-NW-N junction. In an S-NW-S junction, the quantum dot will carry a supercurrent [120]. In this chapter, I will first show how the QPT can be revealed by a re-entrant supercurrent under a magnetic field. Then, I will demonstrate how the field at which the QPT happens can be modified by changing the tunnel coupling of the dot to the leads. Finally, the implications of this experiment in the search for MBS will be shown.

6.2 Goal of the experiment

In chapter 5, I presented an InAs device in which a remarkable finding about the Josephson current was made. The critical current through the device showed a strong enhancement at zero magnetic field, followed by suppression, disappearance and finally a re-emergence as the field was increased. This device consisted on a quantum dot with a gate-dependent tunnel coupling Γ to the superconducting leads. The regime in which this device operated was transparent.

After these measurements, I set as a goal to take this experiment to the next level. I wanted to verify that the quantum dot interpretation was the correct one, by fabricating a well-defined quantum dot device with high-impedance and gate-controlled barriers. Moreover, in this next experiment I wanted to show that the magnetic field at which the phase transition was seen -i.e., at which the critical current is zero- could be tuned via the tunnel coupling of the dot to the leads.

In Figure 6.1, the phase diagram of the ground-state / supercurrent phase-shift of a single-level quantum dot of charging energy U and energy level position $\delta = \varepsilon_d$+U/2, is sketched from the calculations of Ref. [120] and the ones of Rok Zitko in chapter 5. The level is coupled to two superconducting leads of gap Δ with a tunnel coupling Γ, which allows it to carry a Josephson current $I_s = I_c sin(\phi + \phi_0)$. A doublet ground-state $|d\rangle$ results in a $\phi_0 = \pi$ phase, which appears as a semi-circle blue-shaded region in the diagram. Conversely, a singlet ground-state $|s\rangle$ results in a $\phi_0 = 0$ phase, which corresponds to the yellow-shade region outside of the semi-circle region. This is just a repetition of what has been described in Chapter 5 for a similar diagram.

As before, the green line in Figure 6.1 represents dependency on δ of the tunnel coupling Γ of the dot to the leads, which is now parallel to the x-axis because Γ is assumed independent of δ in this discussion -in contrast with the case of Chapter 5. At Zeeman energy E_{z1}= 0, which corresponds to the upper diagram of Figure 6.1, the green line is fully in the $|s\rangle$ region, meaning that the ground state of the dot is always a singlet. What Figure 6.1 shows is that when the Zeeman energy increases -by means of an external field-, the $|d\rangle$ region grows and eventually touches the green curve. At this point, when $E_z = E_{z2} > E_{z1}$, there is a *QPT*. At larger Zeeman energy $E_z = E_{z3} > E_{z2}$, the ground-state of the dot changes to a doublet whenever the green line intersects the $|d\rangle$ region. In this case, the ground state becomes δ-dependent.

In an experiment in this system, at $E_{z1} = 0$ one would see an enhancement of the supercurrent in the middle of the $< N > = 1$ diamond, where $< N >$ is the mean-occupation of the relevant dot level [1]. At E_{z2}, the supercurrent would nearly vanish in the middle of this diamond, at $\delta = 0$. At E_{z3}, the supercurrent would re-emerge stronger than at E_{z2} in the same δ point. This scheme summarizes the findings of Chapter 5 regarding the Josephson effect.

The main idea behind the new experiment presented in this chapter is shown in Figure 6.2. In this Figure, the same three cases of Figure 6.1 are presented, with one big difference. We suppose that the device has an additional knob that allows to change the value of Γ while keeping U constant. Experimentally, this could be achieved with a gate that tunes the width/height of the barriers of the dot without changing the Coulomb diamond of interest.

---

[1] In the model, all the other levels are separated by an energy spacing larger than all the relevant energy scales

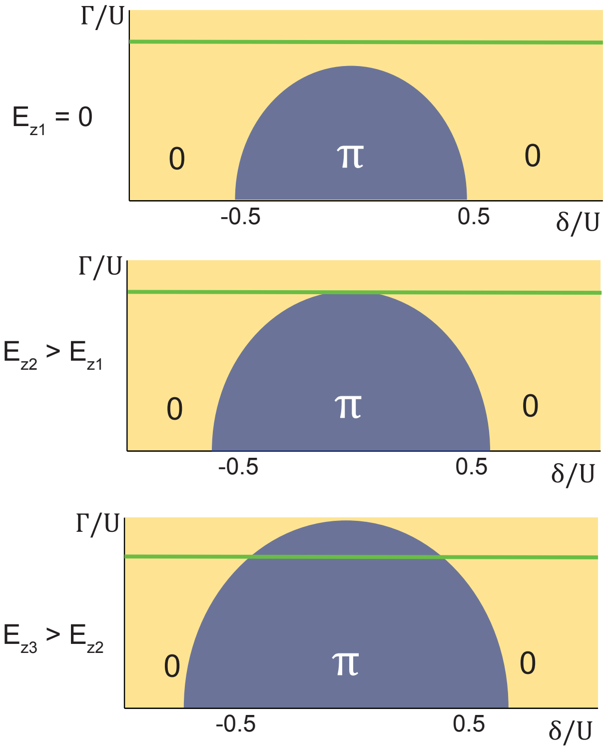

Figure 6.1: Sketch of the phase diagram of a quantum dot as a function of the tunnel coupling/charging energy ratio Γ/U (vertical axis) and the level position/charging energy ratio δ/U (horizontal axis), for three different Zeeman energies: $E_{z1} = 0$, $E_{z2} > E_{z1}$ and $E_{z3} > E_{z2}$. The green line indicates a constant Γ/U ratio. The Zeeman energy makes the $\phi_0 = \pi$ region (in blue) grow, eventually crossing the green line and causing a $\phi_0 = 0 \rightarrow \phi_0 = \pi$ QPT, where ϕ_0 is the phase-shift of the Josephson current $I_s = I_c sin(\phi + \phi_0)$. An experiment to check this transition was shown in chapter 5. However, in that case Γ/U was a quadratic function of δ and the green line was parabola instead of an horizontal line.

Let us suppose that with this additional gate, three distinguishable tunnel couplings can be achieved: Γ_1, Γ_2 and Γ_3, where $\Gamma_1 > \Gamma_2 > \Gamma_3$. If the Zeeman energy is now cranked up, the QPT described before in Figure 6.1 will happen at a *different* magnetic field for each of the three values of Γ.

In the case of Γ_1, the quantum phase transition will occur at the largest Zeeman energy of all (i.e., at E_{z3}), because Γ_1 is the largest of the three tunnel couplings that we are considering here. On the opposite extreme is the case of Γ_3, for which the quantum phase transition will occur at zero Zeeman energy. Experimentally, in this latter case we would see a supercurrent *emerging* with the magnetic field at δ= 0.

In this chapter, I will present experimental measurements that show the tunnel-coupling dependence of the magnetic field at which the quantum phase transition occurs in an InAs nanowire Josephson junction bridged by a quantum dot.

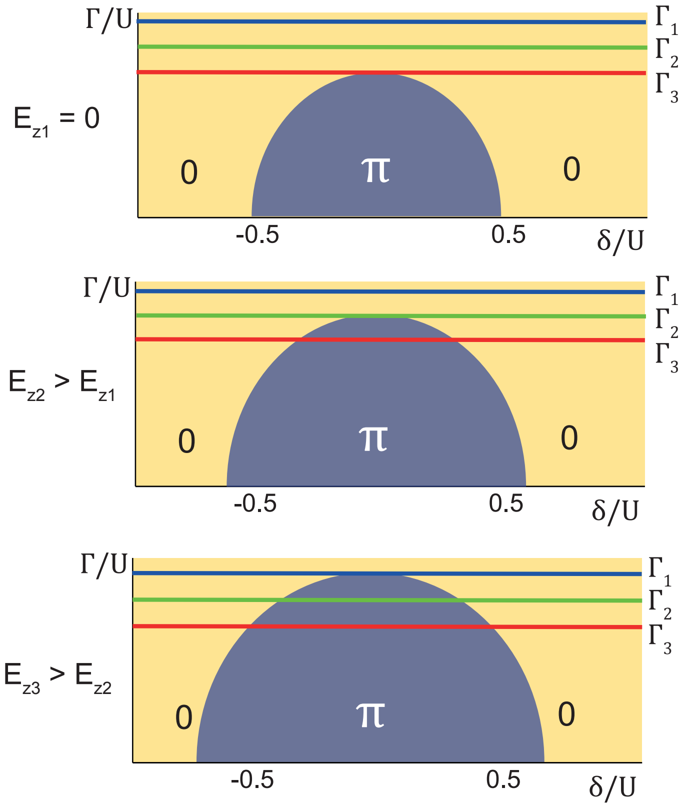

Figure 6.2: Sketch similar to Figure 6.1, but with three different values of Γ indicated: Γ_1 (blue line), Γ_2 (green line) and Γ_3 (red line), where $\Gamma_1 > \Gamma_2 > \Gamma_3$. An experiment which can vary this parameter will have a direct influence on the magnetic field at which the $\phi_0 = 0 \rightarrow \phi_0 = \pi$ QPT is observed. In the extreme case when $\Gamma = \Gamma_3$, the junction will be at the QPT at zero-magnetic field. By increasing the field, a $\phi_0 = \pi$ supercurrent will emerge.

6.3 The device

The device consisted on a two-terminal InAs nanowire contacted by niobium (Nb) / tantalum (Ta) superconducting leads (for a SEM image and a scheme of the device, see Figures 6.3**a,b**, respectively). This Nb/Ta bi-layer (5 nm and 80 nm thickness, respectively) was chosen to increase the superconducting gap of Ta, as discussed at the end of Chapter 4. In that chapter, it was shown that a thin Nb under-layer of 5 nm deposed before depositing a thick layer of Ta of 100 nm, augmented the measured T_c of Ta from 0.7 K to 1.915 K. This significant increase of the T_c of Ta was later confirmed by spectroscopy of the gap in InAs nanowire Josephson junctions. These measurements were also presented in Chapter 4. In these junctions, the Nb under-layer helped to raise the superconducting gap by a factor of 2, from 70 - 80 μeV to 160 μeV, while keeping a high critical field, of around 2 T.

Unfortunately, the device presented here did not show this enlargement of the gap, for reasons probably related to the method of evaporation. Ta or Nb/Ta films were hard to remove by the lift-off method, leading to short-circuited devices. In order to increase the yield of working devices, the 80 nm Ta layer used in making this sample was evaporated in four steps -instead of one single step-, depositing 20 nm in each step. The reasoning behind this was that evaporating the Ta layer in many steps would reduce the baking of the resist, allowing for a better lift-off. While this procedure slightly improved the lift-off yield -from 15 % to 20 %-, the first 20 nm Ta layer on top of the 5 nm Nb layer was not enough to crystallize a significant proportion of bcc-Ta.

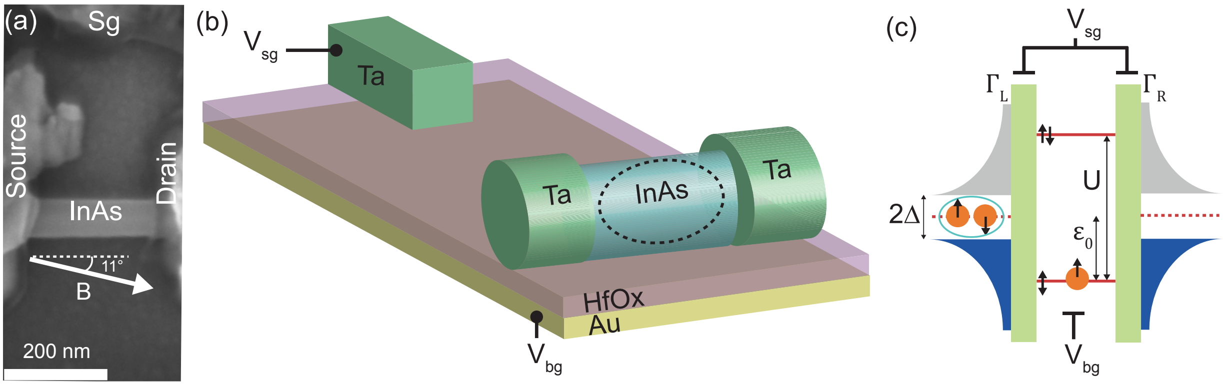

Figure 6.3: **(a)** SEM image of the InAs nanowire two-terminal device. The side-gate (Sg) and the magnetic field orientation are both indicated in this image. **(b)** Scheme of the device. A quantum dot forms naturally in the middle of the nanowire (dashed circle). **(c)** The device behaves as a quantum dot coupled to two superconducting leads by tunnels couplings Γ_L and Γ_R. A spin-degenerate energy level of charging energy U occupied by a single electron is shown. This level is separated from the Fermi energy of the leads by an energy ε. The side-gate voltage V_{sg} tunes $\Gamma = \Gamma_L + \Gamma_R$, while the backgate V_{bg} acts on ε_d.

The device had two gates. One of them was a backgate (of area 1 μm × 2 μm) that acted as a plunger gate, for controlling the δ parameter in Figure 6.2. This gate was separated from the nanowire and the contacts by a 10 nm hafnium oxide (HfOx) dielectric. The other gate was a Nb/Ta side-gate fabricated at the same moment as the contacts, and separated from the nanowire by roughly 300 nm of vacuum. This other gate was used for controlling the Γ parameter of Figure 6.2. The backgate was much better coupled to the nanowire than the side gate. Figure 6.3**c** shows a simple scheme of the quantum dot device and the capacitive coupling of each of the gates to the tunnel barriers and the energy levels for mean occupation $< N > = 1$.

The experiment was performed in a dilution refrigerator of base temperature T = 15 mK. During the whole experiment, the magnetic field was oriented at 11° with respect to the axis of the nanowire, as shown in the SEM image of Figure 6.3**a**.

The Josephson current through the device was measured in a voltage-biased configuration that was thoroughly described in Section 5.5 of Chapter 5. The same considerations discussed there regarding the damping of the junction in the Resistively and Capacitively Shunted Junction

(RCSJ) model and the occurrence of a dissipative supercurrent zero-bias peak in conductance due to thermal fluctuations apply to this device.

6.4 Identification of the Coulomb diamonds of interest

The device had a naturally-occurring quantum dot in the channel of the nanowire. By sweeping the backgate, a number of Coulomb oscillations and Kondo ridges could be observed. With such a large number of Coulomb diamonds to choose from, a way to pick the right one to perform the experiment described in the introduction of this chapter had to be devised. On one hand, if the tunnel coupling Γ in the diamond was too large, the horizontal line in Figure 6.2 would be too far away from the $|d\rangle$ boundary, and the QPT would happen at a magnetic field so high that the critical field of the contacts would be attained before the transition could be seen. An example of this case was shown in Figures 4.22**c,d** of Chapter 4. On the other hand, if Γ was too small, the diamond would always be in the $|d\rangle$ ground-state. An example of this was shown Figures 4.22**a,b** of Chapter 4. Similar arguments could be made about the charging energy U and the g-factor. Having a limited tuning range of Γ, a diamond with an initial Γ/U ratio close to the QPT was a necessary requirement for the experiment to be successful.

I tackled this question by experience. From previous experiments on other devices, I had learned to recognize that for achieving a regime near the QPT, a Kondo ridge with a slightly overdamped supercurrent in its center was to be looked for. A slightly overdamped supercurrent meant that the critical current I_c flowing through the device was small enough -i.e. close to zero-, and that thermal fluctuations would render it dissipative [127]. In these conditions, a zero-bias measurement of the conductance through the Kondo ridge at $T \ll T_c$ leads to an overshoot of the conductance in the associated Coulomb peaks (at $\delta/U \sim \pm 0.5$), because the large Josephson energy conveys a non-dissipative supercurrent. However, in the *center* of the diamond, at the $\delta = 0$ point, the conductance is *finite*, because the Josephson energy is small compared to the thermal energy. In summary, I was looking for this type of Coulomb diamond: 1) of divergent conductance in the Coulomb peaks and 2) of finite conductance in the valley.

This method is more easily understood if we see how it works for the current device. Figure 6.4**a** shows a zero-bias raw-data conductance map as a function of the side-gate voltage V_{sg} (which was stepped) and the backgate voltage V_{bg} (which was swept), taken at B = 0 T and T = 15 mK with a lock-in AC excitation of 1 μV. At this magnetic field and at this temperature, the S-NW-S junction is superconducting and will sustain a Josephson supercurrent. Therefore, in a raw-data map such as this, the conductance will achieve a value of $1/R_s$ (indicated in the color scale) whenever it is non-dissipative -i.e., at zero resistance-, where R_s is a resistance of around 50 kΩ in series with the sample, coming from the RC filters and the current amplifier, as explained in

Chapter 5 [2]. In the same raw-data map, the conductance will have a value slightly below $1/R_s$ whenever the supercurrent is dissipative.

A diamond that fits the characteristics outlined above is the one in between the two yellow-dashed lines of Figure 6.4**a**. In the future, I will name it as Diamond 1. If we follow the evolution of the conductance at the center of this diamond (black arrow), which is more easily done by looking at the traces in Figure 6.4**b** which were taken from Figure 6.4**a**, we notice that it is decreasing as a function of the side-gate voltage V_{sg}. In the black trace, taken at V_{sg} = -3 V, the supercurrent in Diamond 1 is nearly non-dissipative, whereas it turns increasingly dissipative in the green, blue and purple curves. These curves were taken, respectively, at a significantly larger side-gate voltage V_{sg} of -1 V, 0 V and +1 V. In other words, in the black trace, the Josephson energy is much larger than the thermal energy. However, in the green, blue and purple traces, taken at a larger V_{sg} voltage, the Josephson energy is decreasing and getting comparable to the thermal energy.

This measurement implies indirectly that Γ is getting smaller as the side-gate voltage is raised. Indeed, the critical current should get increasingly smaller as the Γ/U green line of the phase diagram in Figure 6.1 (at zero Zeeman energy, upper sketch) approaches the $\phi_0 = 0 \rightarrow \phi_0 = \pi$ phase transition. We will confirm this in what follows.

6.5 Finding the dot parameters

The maps of Figure 6.5 show the magnetic field evolution of the raw-data linear conductance (vs. V_{bg}) at T = 15 mK, taken at V_{sg} = **(a)** -3 V, **(b)** -1 V, **(c)** 0 V and **(d)** 1 V, which correspond to the **(a)** black, **(b)** green, **(c)** blue and **(d)** purple traces of Figure 6.4**b**. Below B_c = 1.8 T, the sample is superconducting. Therefore, as before, whenever the resistance of the sample is zero -i.e. whenever there is a non-dissipative supercurrent-, the conductance goes to $1/R_s$, where $R_s \sim$ 50 kΩ is the series resistance conformed by the RC filters and the measuring circuitry.

In these maps, Diamond 1 is pointed by an arrow. From the splitting of the Coulomb peaks, it is possible to identify if Diamond 1 has a doublet or a singlet ground-state at high magnetic field, corresponding to odd or even mean-occupation $< N >$, respectively (assuming that the Kondo singlet is no longer the ground-state because of the high field). In the former case -i.e, for a doublet-, the Coulomb peaks should move apart driven by the Zeeman energy. Conversely, in the latter case they should come closer. This is a direct result of the Zeeman evolution of the phase diagram in Figure 6.1. In the case of Diamond 1, the Coulomb peaks separate further and further away as the magnetic field is increased, and thus it is possible to deduce that at high magnetic field

---

[2] If I were to subtract $1/R_s$ from the conductance in the way explained in Chapter 5, the conductance would diverge and there would not be any new information provided, so I chose to show raw data here for the point that I want to make.

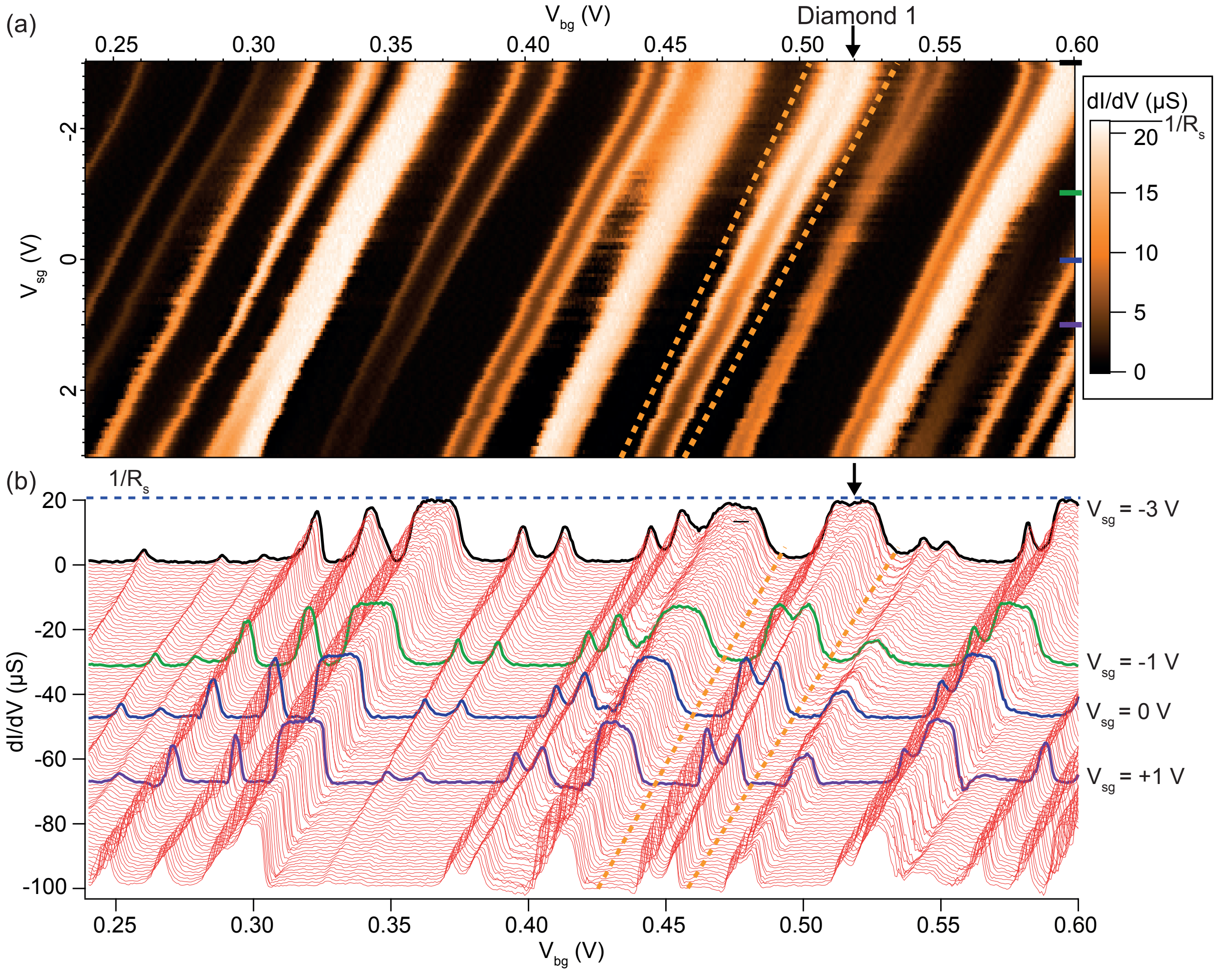

Figure 6.4: **(a)** Raw-data conductance map taken by sweeping the backgate voltage V_{bg} and stepping the side-gate voltage V_{sg}. This map was recorded at zero bias, zero magnetic field and base temperature of 15 mK. The junction is therefore superconducting. A zero-resistance state will attain the conductance $1/R_s$ of the filters plus the internal circuitry of the current amplifier, where $R_s \sim 50$ kΩ, indicated in the color scale in (a) and by a blue-dashed line in (b). Yellow-dashed lines delimit Diamond 1, which was selected to do the supercurrent measurements described in the beginning of this chapter. **(b)** dI/dV traces taken from (a), with an offset of -1 μS starting by V_{sg} = -3 V. The traces colored differently were taken at by V_{sg} = -3 V (black), -1 V (green), 0 V (blue) and 1 V (purple). In both (a) and (b), the $\delta = 0$ point (i.e. the center of the diamond) is pointed by a black arrow.

the ground state inside Diamond 1 is a doublet. Furthermore, it can be deduced that at all fields the energy level of the dot is singly-occupied.

Now that we found that Diamond 1 has a doublet ground-state at high magnetic field, it is important to confirm that at zero field its ground state is a singlet as a result of the Kondo effect. Figure 6.6 shows charge stability diagrams of the quantum dot for Diamond 1 (black arrow), taken in three different conditions (note the different gate and bias scales). The data plotted in

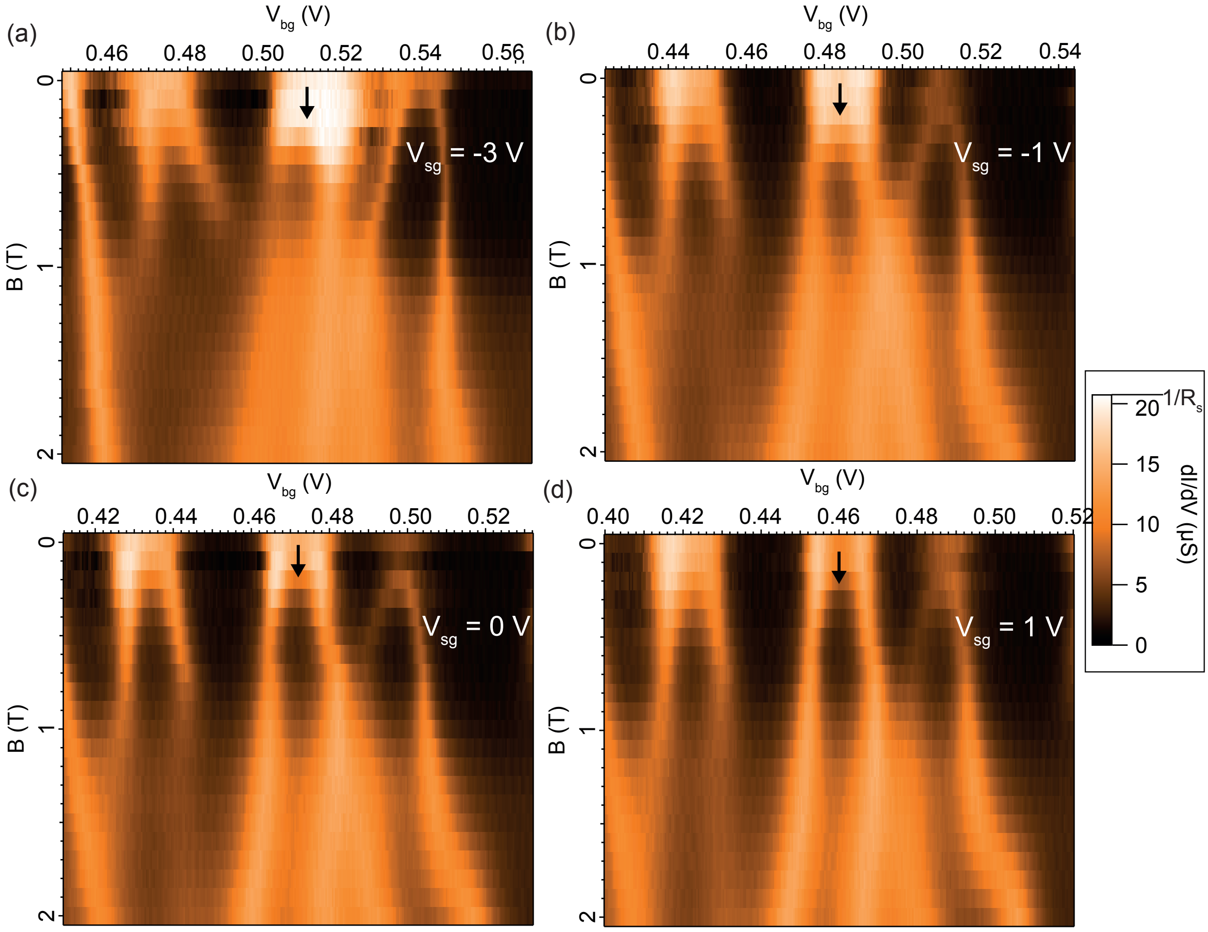

Figure 6.5: Raw-data zero-bias conductance maps vs. backgate voltage and magnetic field, taken at T = 15 mK with a lock-in AC excitation of 1 μV. Each map was recorded at a different value of side-gate voltage: V_{sg} = **(a)** -3 V, **(b)** -1 V, **(c)** 0 V and **(d)** 1 V. In the plots, Diamond 1 is indicated by a black arrow. The color scale of the maps is the same and tops at $1/R_s$, which corresponds to the zero-resistance state of the sample.

the 2D maps is the corrected conductance -R_s subtracted- as a function of backgate voltage and the corrected bias -R_s also subtracted-. At B = 0 T and T = 15 mK (Figure 6.6**a**), the sample is superconducting and the diamonds feature loops inside the superconducting gap (i.e., from -2Δ to 2Δ, between the two horizontal blue lines). These loops are a signature of Andreev Bound states (ABS). From the map, an estimation of the charging energy U from the size of Diamond 1 can be made; however, it will be slightly distorted by the apparent renormalization of the diamond size by the ABS [12]. U is estimated to be 0.5 ± 0.2 meV by this method.

At B = 2 T -above the critical field of Ta- and T = 15 mK (Figure 6.6**b**), superconductivity is lost and the Kondo effect is nearly fully destroyed. In these conditions, there is no renormalization of the Coulomb diamonds neither by superconductivity nor by the Kondo effect, so the lever-arm

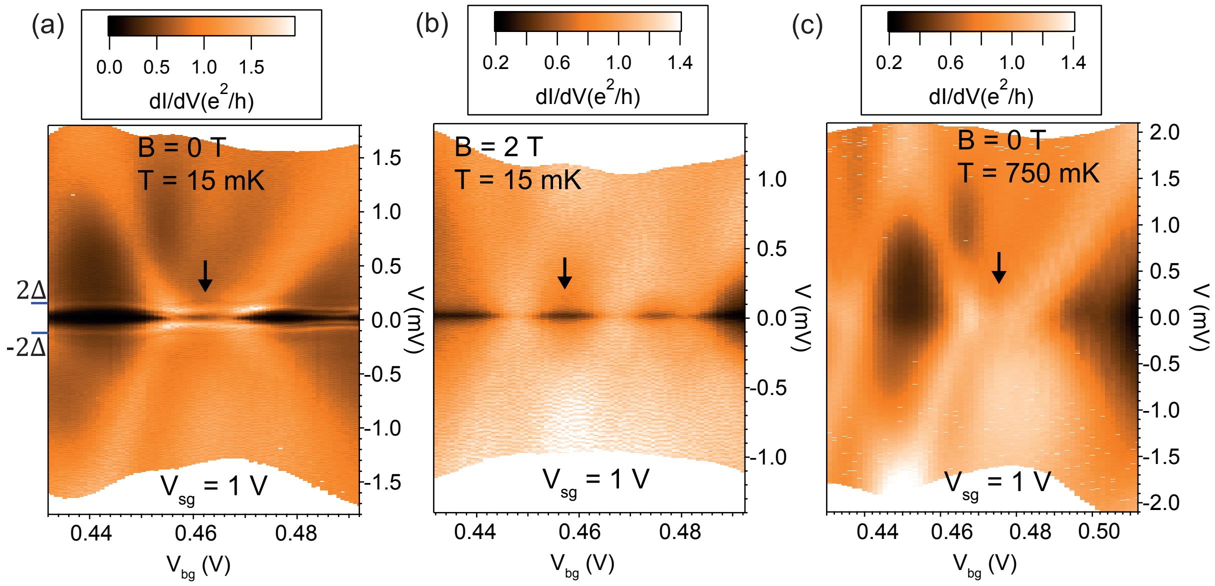

Figure 6.6: Corrected conductace maps -R_s was subtracted- as function of backgate voltage and corrected bias -R_s was also subtracted-, taken at **(a)** B = 0 T and T = 15 mK, **(b)** B = 2 T and T = 15 mK and **(c)** B = 0 T and T = 750 mK. All these maps were taken at V_{sg} = 1 V (purple trace of Figure 6.4**b**). Diamond 1 is indicated by a black arrow. In **(a)**, the superconducting gap (2Δ for the gaps of the two contacts) is indicated by two blue horizontal lines.

of the backgate for Diamond 1 can be estimated without distortions. It is found that $\alpha_{bg} = 0.042 \pm 0.009$. The size of Diamond 1 is equal to $2(E_z + U)$, where $E_z = g\mu_B B$ is the Zeeman energy. By using U = 0.5 meV, it is possible to deduce the g-factor in this way. It is found to be $|g| = 2.8$.

At B = 0 T and T = 750 mK , the sample is no longer superconducting. A Kondo ridge develops inside of Diamond 1 in the charge stability diagram of Figure 6.6**c**. Since superconductivity is gone at this temperature, the Kondo effect is no longer re-normalized by the superconducting gap. The Kondo temperature in Diamond 1 is proportional to the width of the Kondo peak that originates the ridge. The conductance in the peak is around 1.1 e^2/h, showing an enhancement with respect to the doubly-occupied levels -i.e., the diamonds before and after Diamond 1.

An estimation of the g-factor can also be performed by measuring the Zeeman splitting of the Kondo peak of Figure 6.6**c** as a function of magnetic field. At a large field, the peak-to-peak separation was found to be $2E_z$, as expected for a Kondo resonance [38][123]. Figure 6.7**a** shows non-linear conductance vs. bias traces taken at various magnetic fields, from B = 0 T to B = 2.9 T, recorded at V_{sg} = 1 V in the center of Diamond 1. At zero field, a zero-bias peak is seen (blue curve), while at high magnetic field, the peak turns into two steps. The peak is associated with the Kondo effect, while the two steps come from inelastic cotunneling, broadened by $5.44k_BT$ = 0.35 mV [130]. The g-factor found from these measurements is $|g| = 2.8$, confirming the previous measurement.

To confirm this measurement, a similar measurement was performed at V_{sg} = 0 V. This measurement is displayed in Figure 6.7**b**. The Kondo peak at this gate voltage is broader (blue trace at B = 0 T), presumably due to a larger tunnel coupling. The g-factor obtained at this side-gate voltage, by measuring the Zeeman splitting of the cotunneling steps as before, turns to be the same: $|g| = 2.8$.

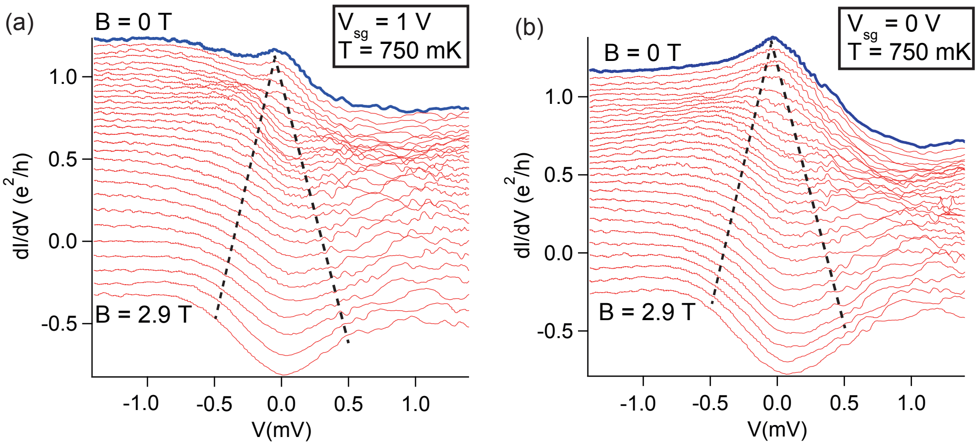

Figure 6.7: Zeeman splitting of the Kondo peak in Diamond 1 at **(a)** V_{sg} = 1 V and **(b)** V_{sg} = 0 V, from B = 0 to B = 2.9 T. To follow the Zeeman splitting, two black dashed lines have been added as a guide for the eye. The trace at 0 T, which showcases the Kondo peak, has been highlighted in blue. The traces have been corrected in bias and conductance by subtracting R_s. They were taken every 0.1 T and offset with respect to each other by -0.025 e^2/h.

6.6 Quantum phase transition revealed by a re-entrant supercurrent in a magnetic field

After confirming that the ground state of Diamond 1 was a Kondo singlet at zero-field (at $T > T_c$) and a spin-doublet at high magnetic field (at $B > B_c$), I proceeded to measure the supercurrent through the singlet as a function of magnetic field, at T = 15 mK $\ll T_c$). In a voltage-biased configuration, I recorded the current (I) and the differential conductance (dI/dV) simultaneously while applying a DC voltage (V) of a few μV superposed to a lock-in AC excitation of 1 μV. Since the chip design, the measurement setup and the material of the contacts are similar to those of the device of Chapter 5, the same considerations detailed there are applicable here. In particular, the Resistively and Capacitively Shunted Junction (RCSJ) model, the gate and field-dependent Q factor, and the overdamped RCSJ regime with thermal fluctuations that forces to do a fit of V - dI/dV curves for extracting the critical current I_c, are all relevant in the current situation.

Figure 6.8**a** is a raw-data map of the conductance as a function of the backgate voltage V_{bg} and the bias V, taken at V_{sg} = -3 V and B = 0 T. In this map, there is a feature around zero-bias that

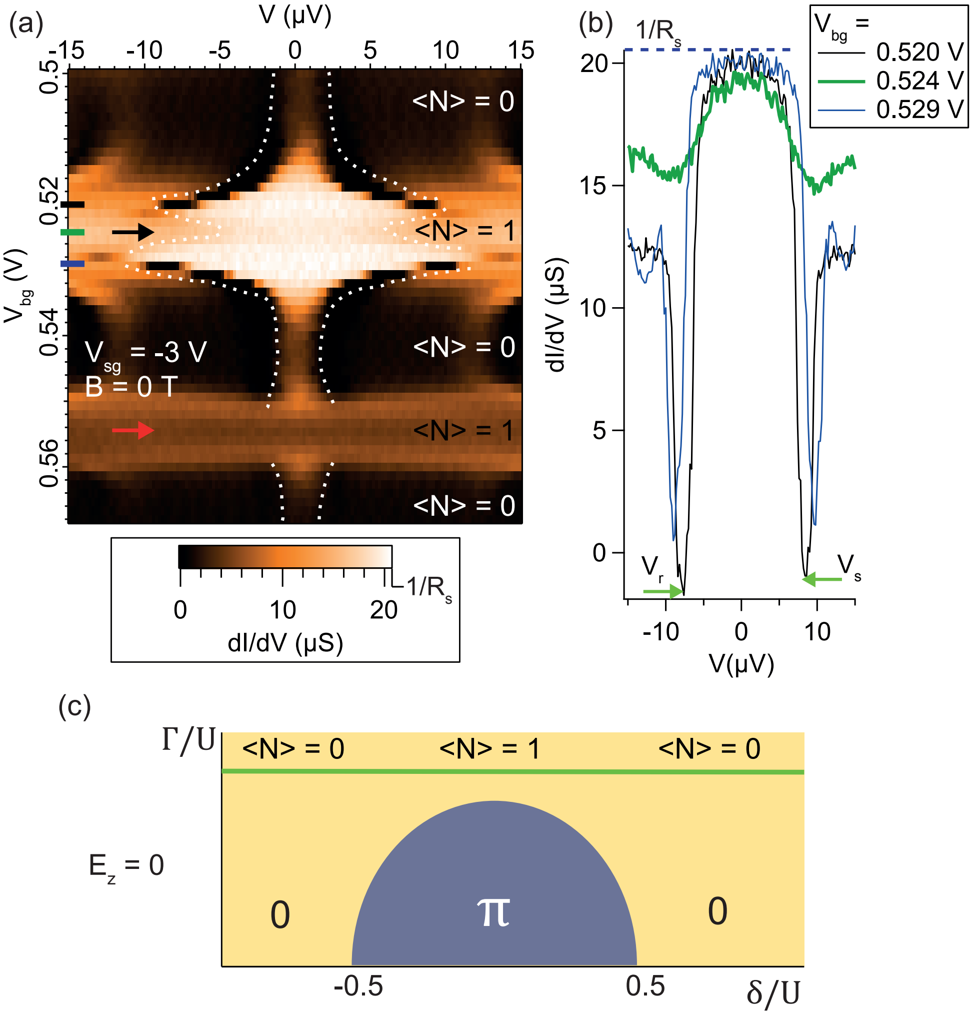

Figure 6.8: **(a)** Raw-data conductance map as a function bias and backgate voltage, taken at B = 0 T and V_{sg} = -3 V. The mean occupation $< N >$ of the respective diamonds is annotated on the right. The center of Diamond 1 is pointed by a black arrow, while the center of another diamond of mean occupation $< N > = 1$ is pointed by a red arrow. In the scale, the conductance $1/R_s$ is indicated. When the conductance reaches this value, the resistance of the sample is zero. The white-dashed lines contour a supercurrent. **(b)** Cuts from (a) taken at the gate points indicated by lines of the same color as the traces. The quantities V_r and V_s, which are proportional to the re-trapping and the switching current because of R_s, are indicated by green arrows. $1/R_s$ is marked by a dashed line. (c) Scheme of the phase diagram at zero field. Diamond 1 is at -0.5<δ/U<0.5 , in the region of mean occupation $< N > = 1$. Since the Γ/U green line is outside of the π region, the junction is a singlet with a $\phi_0 = 0$ supercurrent.

traverses all diamonds and it is gate-dependent. This feature, which is symmetric around zero-bias (if an offset of around 1 μV coming from the voltage source is removed) has been contoured by two white dashed-lines for guidance to the eye. The feature can be attributed to a Josephson current, and its extension in bias is proportional to the critical current. In the color scale of the map, the maximum conductance appears in golden / white and saturates at $1/R_s$. The supercurrent varies significantly depending on the mean level occupation, $< N > = 1$ or $< N > = 0$, which is indicated in the map. In $< N > = 0$ diamonds, the supercurrent is generally weak, whereas in Diamond 1 (whose center is pointed by a black arrow), where $< N > = 1$, the supercurrent is Kondo-enhanced and is strong. In the diamond whose center is pointed by a red arrow, where $< N > = 1$, there is no Kondo effect -the ground state is a doublet- and the supercurrent is very weak.

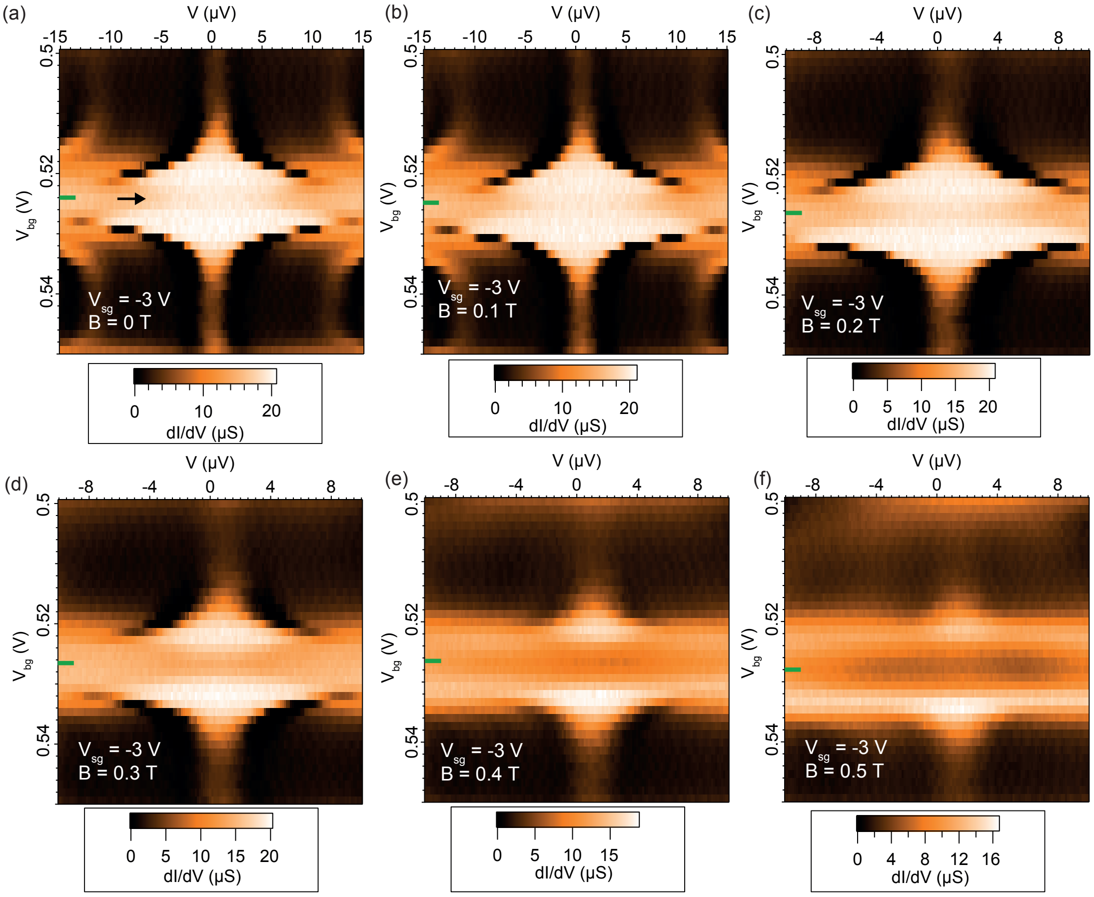

Figure 6.9: Raw-data maps of conductance as a function of the backgate voltage V_{bg} and the bias V, taken at V_{sg} = -3 V and at the magnetic fields indicated in each plot, ranging from B = 0 T to B = 0.5 T. The black arrow points to the center of Diamond 1. The green lines in each map mark the gate point at which a cut shown in Figure 6.10 was made.

Let us focus in Diamond 1 now. Figure 6.8**b** shows V - dI/dV cuts from the map in 6.8**a**, taken at the backgate voltages marked with lines of the same color as the traces (black, green and blue). In raw-data traces such as these ones, as we saw in Chapter 5, a non-dissipative supercurrent appears as a plateau centered at zero-bias, whose conductance reaches $1/R_s$. A dissipative supercurrent, on the other hand, appears as a zero-bias peak whose conductance is below $1/R_s$. Whether a supercurrent will be dissipative or not, in a RCSJ overdamped device with thermal noise such as this one, depends on the ratio of the Josephson energy to the thermal energy, $E_J/\kappa_B T$, where $E_J = I_c\hbar/2e$. If this ratio is much larger than 1, the supercurrent will exhibit a zero-resistance branch. Else, if $E_J/\kappa_B T$ is of the order of 1 or less, the supercurrent will be dissipative.

One can acquire a great deal of qualitative information by just observing the traces of Figure 6.8**b**. In the extremes of the diamond (black and blue traces), the supercurrent is non-dissipative and we can thus assume that I_c is large enough to ensure that $E_J/\kappa_B T$ is much larger than 1. In the center of the diamond (green trace), the supercurrent is dissipative, so $E_J/\kappa_B T$ is of the order of 1 and I_c is consequently smaller. One can also deduce that the junction is overdamped for all gate voltages shown in the map of Figure 6.8**a**, since the quantities V_s and V_r -indicated by green arrows in Figure 6.8**b**- , which are proportional to the re-trapping and the switching current, respectively, are equal[3].

These measurements give us a hint of the Γ/U ratio in Diamond 1. Figure 6.8**c** shows an sketch of the corresponding phase diagram, in which the Γ/U ratio of Diamond 1 ($< N > = 1$) is given by the horizontal green line. For both $< N > = 1$ and $< N > = 0$ mean occupations, the ground state is a singlet and the junction has $\phi_0 = 0$ phase.

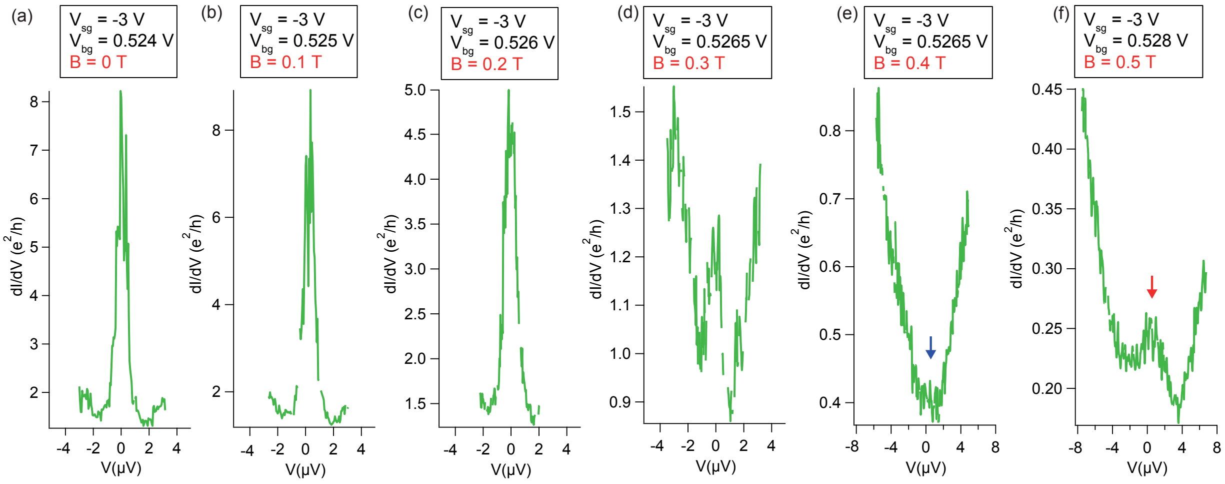

Figure 6.10: V - dI/dV traces corrected in conductance by subtracting R_s, and corrected in bias by subtracting R_s and eliminating an offset of 2 μV from the voltage source. The traces were taken at V_{sg} = -3 V, and at magnetic fields and backgate voltages indicated for each case in the legend on the top. The backgate voltage is also marked by a green line in the raw-data conductance maps of Figure 6.9. In each trace, a zero-bias peak can be associated with a supercurrent, its disappearance (blue arrow) with a $\phi_0 = 0 \rightarrow \phi_0 = \pi$ phase transition, and its re-emergence (red arrow) with a $\phi_0 = \pi$ supercurrent.

I recorded maps similar to the one in Figure 6.8**a** at increasing magnetic fields, with the intention to witness the growth of the doublet region of the phase diagram of Figure 6.8**c** and

---

[3] Taking into account an offset in the voltage source of around 1 μV.

eventually see a phase transition, as it was described in the introduction of this chapter (see Figure 6.1). These raw-data conductance maps, including the B = 0 T case of Figure 6.8**a**, are all shown together in Figure 6.9 for a gate range restricted to show well the supercurrent within Diamond 1 (whose center is pointed by a black arrow). As the magnetic field is increased, the supercurrent in the middle of Diamond 1 decreases in magnitude until the supercurrent *vanishes* at 0.4 T and then *re-emerges* at 0.5 T.

This is more clearly seen in Figure 6.10, which are cuts [4] taken in the center of Diamond 1 in each of the maps explored in Figure 6.9. In these cuts, which were corrected in conductance and bias by subtracting the series resistance R_s from the RC filters and the current amplifier, and by eliminating a small voltage offset from the voltage source, the supercurrent appears as a zero-bias peak of finite conductance as a result of thermal fluctuations. As the magnetic field is increased, this peak vanishes slowly until it is fully suppressed at B = 0.4 T (blue arrow). After completely disappearing, the peak re-emerges at B = 0.5 T (red arrow).

The point where the supercurrent vanishes signals a $\phi_0 = 0 \rightarrow \phi_0 = \pi$ transition, which corresponds to $E_{zc} = E_{z2}$ in Figure 6.1. In this way, I obtained the magnetic field at which the transition occurs, which is B = 0.4 T ± 0.1 T [5] for V_{sg} = - 3 V, corresponding to an E_zc/U ratio of 0.13.

6.7 Tuning the magnetic field of the QPT with a side gate voltage

The purpose of the experiment presented in this chapter was not only to obtain the E_{zc}/U value for a given Γ/U ratio, but to confirm that by varying the Γ/U ratio one could change the E_{zc} critical field at which the $\phi_0 = 0 \rightarrow \phi_0 = \pi$ transition occurs. From the data already presented, one could obtain some clues that Γ is affected by the side-gate voltage. In particular, that Γ was larger at V_{sg} = - 3 V and smaller at V_{sg} = 1 V. The first clue was the variation of the zero-field critical current as a function of side-gate voltage, as evidenced qualitatively by the zero-bias conductance in Figure 6.4. The second one was the larger and wider Kondo peak at V_{sg} = 0 V than V_{sg} = 1 V in Figure 6.7. Thus, by varying V_{sg}, one should be able to vary E_{zc}.

Based on this reasoning, I proceeded to record maps like those in Figure 6.9 at other values of V_{sg}, corresponding to the colored traces in Figure 6.4**b** -i.e., at V_{sg} = -1 V (green), 0 V (blue) and 1 V (purple).

Figure 6.11 shows several raw-data conductance maps taken at V_{sg} = -1 V, at magnetic fields ranging from B = 0 T to 0.6 T. At B = 0 T (Figure 6.11**a**), there is a supercurrent feature around

---

[4] Beware of the change in the scale of each of the plots.

[5] The maps were recorded every 0.1 T.

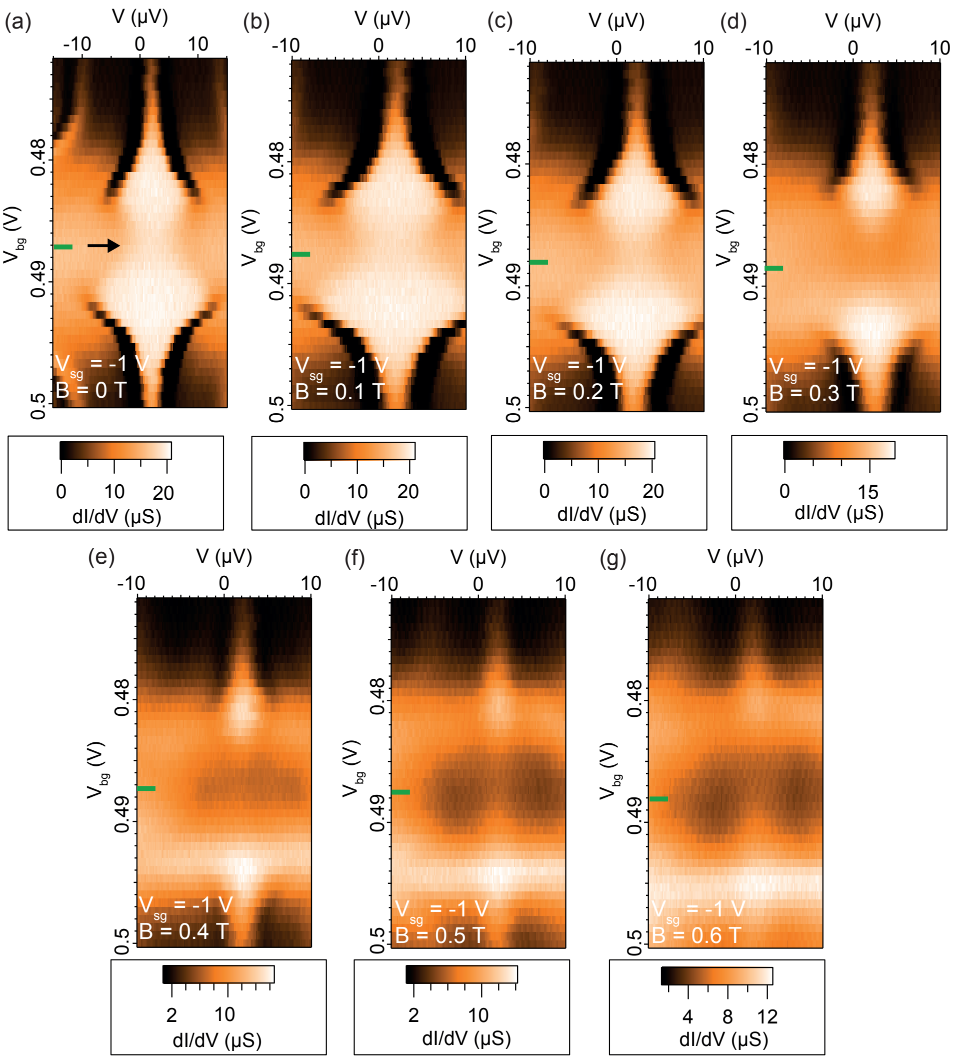

Figure 6.11: Raw-data maps of conductance as a function of the backgate voltage V_{bg} and the bias V, taken at V_{sg} = -1 V and at the magnetic fields indicated in each plot, ranging from B = 0 T to B = 0.6 T. The black arrow points to the center of Diamond 1. The green lines in each map mark the gate point at which a cut shown in Figure 6.12 was made.

zero-bias, if one corrects an offset of 2 μV from the voltage source. The critical current associated along Diamond 1 (pointed by a black arrow) with this supercurrent is weaker than in Figure 6.11**a** at V_{sg} = -3 V, showing that at this gate voltage the zero-field ground state of the dot is closer to the QPT.

As the magnetic field is raised, the supercurrent in the center of Diamond 1 becomes weaker (green line in plots 6.11**b,c** at B = 0.1 T and 0.2 T), until it vanishes at B = 0.3 T (plot 6.11**d**). At larger magnetic field, the supercurrent re-emerges as a zero-bias peak (see plots 6.11**e-g**). This is better seen in the cuts at the center of Diamond 1 (indicated by a green line in each map of

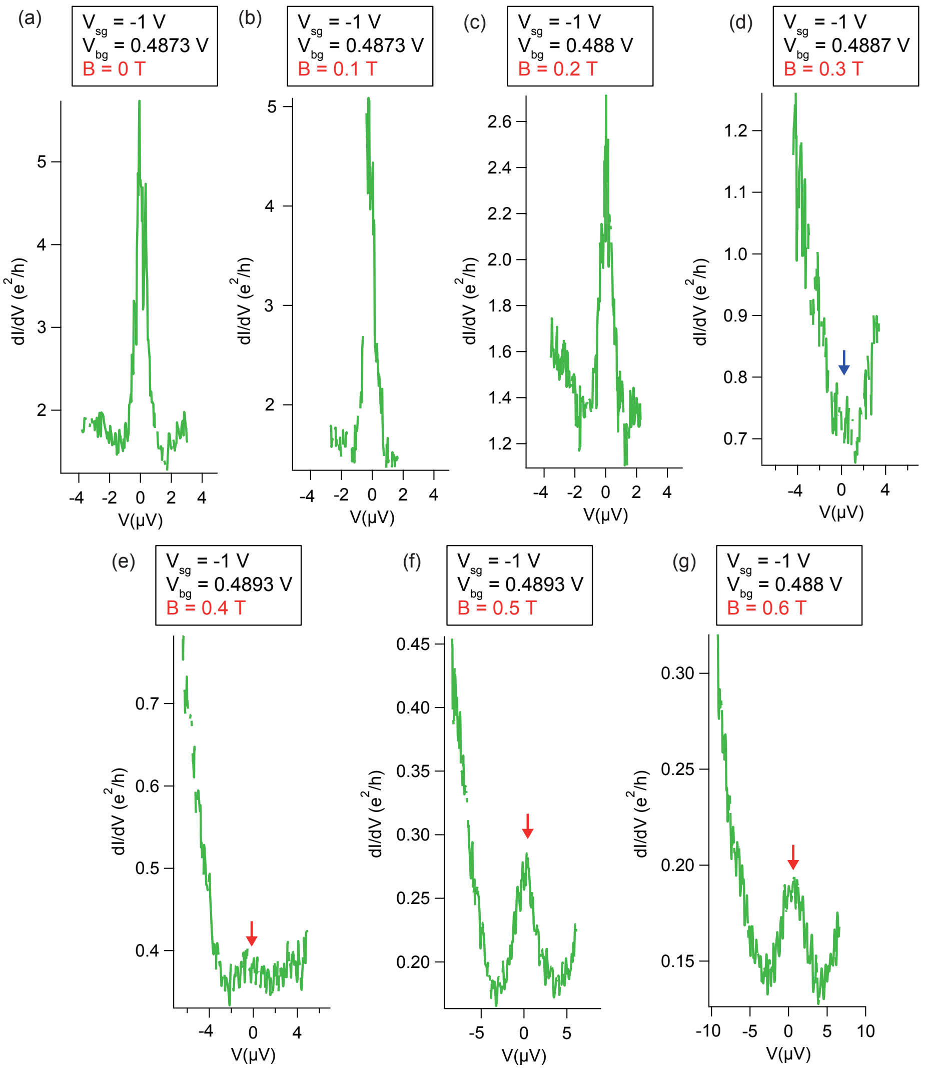

Figure 6.12: V - dI/dV traces corrected in conductance by subtracting R_s, and corrected in bias by subtracting R_s and eliminating an offset of 2 μV from the voltage source. The traces were taken at V_{sg} = -1 V, and at magnetic fields and backgate voltages indicated for each case in the legend on the top. The backgate voltage is also marked by a green line in the raw-data conductance maps of Figure 6.11. In each trace, a zero-bias peak can be associated with a supercurrent, its disappearance (blue arrow) with a $\phi_0 = 0 \rightarrow \phi_0 = \pi$ phase transition, and its re-emergence (red arrow) with a $\phi_0 = \pi$ supercurrent.

Figure 6.11) shown in Figure 6.12. These V - dI/dV traces were corrected by subtracting the series resistance R_s from the bias and the conductance and eliminating a voltage offset from the voltage source.

At B = 0 T (Figure 6.12**a**), the supercurrent appears as a sharp zero-bias peak of large conductance. This peak vanishes at B = 0.3 T (blue arrow, Figure 6.12**d**). After fully disappearing, the peak weakly re-emerges at B = 0.4 T (red arrow, Figure 6.12**e**). Thereafter, it becomes a robust

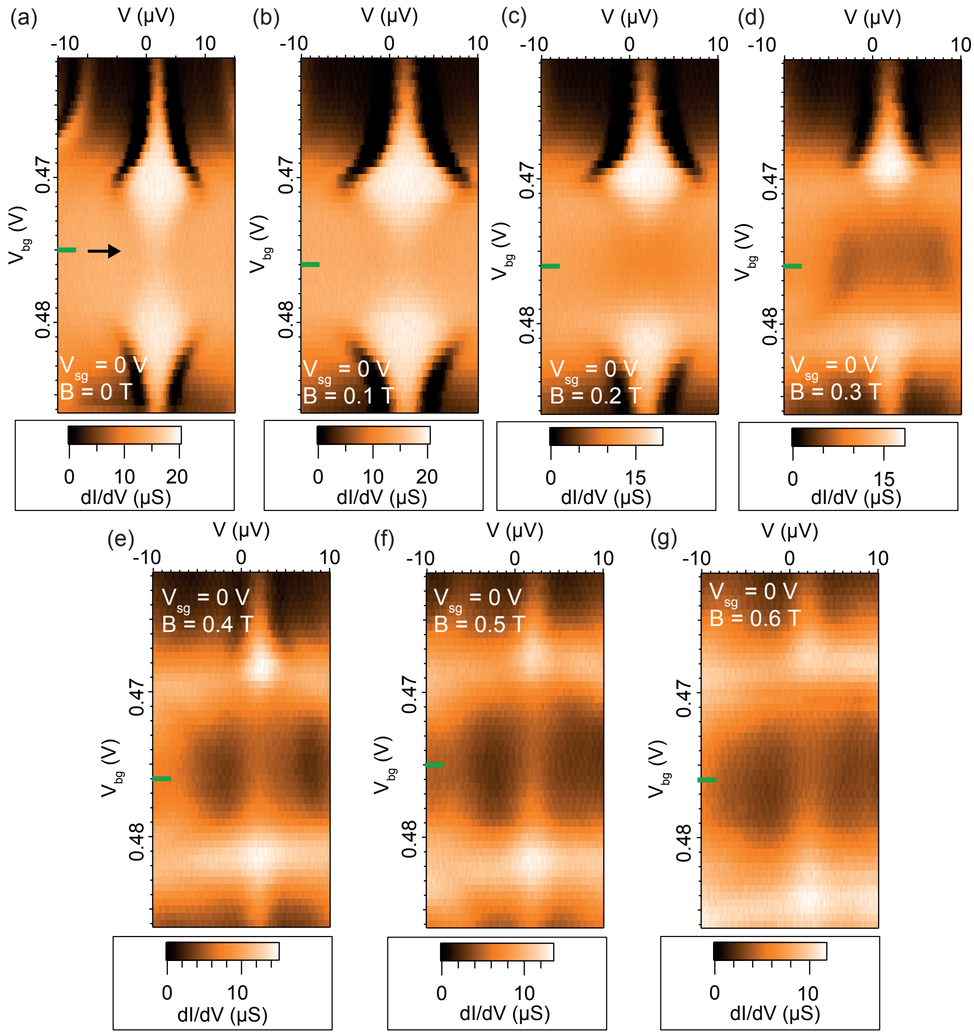

Figure 6.13: Raw-data maps of conductance as a function of the backgate voltage V_{bg} and the bias V, taken at V_{sg} = 0 V and at the magnetic fields indicated in each plot, ranging from B = 0 T to B = 0.6 T. The black arrow points to the center of Diamond 1. The green lines in each map mark the gate point at which a cut shown in Figure 6.14 was made.

zero-bias peak at a larger field of B = 0.5 T and B = 0.6 T (red arrow, Figures 6.12**f,g**).

From these measurements, it is possible to infer that at V_{sg} = -1 V, the field at which the $\phi_0 = 0 \longrightarrow \phi_0 = \pi$ transition happens is B = 0.3 T ± 0.1 T, which corresponds to E_{zc}/U = 0.10. Interestingly, the magnetic field at which the transition occurs in this case is *lower* than at V_{sg} = -3 V (B = 0.4 T). The interpretation that I give for this observation is that, by tuning the side-gate voltage to V_{sg} = -1 V, the Γ parameter has decreased. Such a thing will lower the magnetic field at which the transition $\phi_0 = 0 \longrightarrow \phi_0 = \pi$ occurs, as it was explained before in Figure 6.2.

At V_{sg} = 0 V, the $\phi_0 = 0 \longrightarrow \phi_0 = \pi$ QPT is pushed to an even lower field, as we shall see. Figure

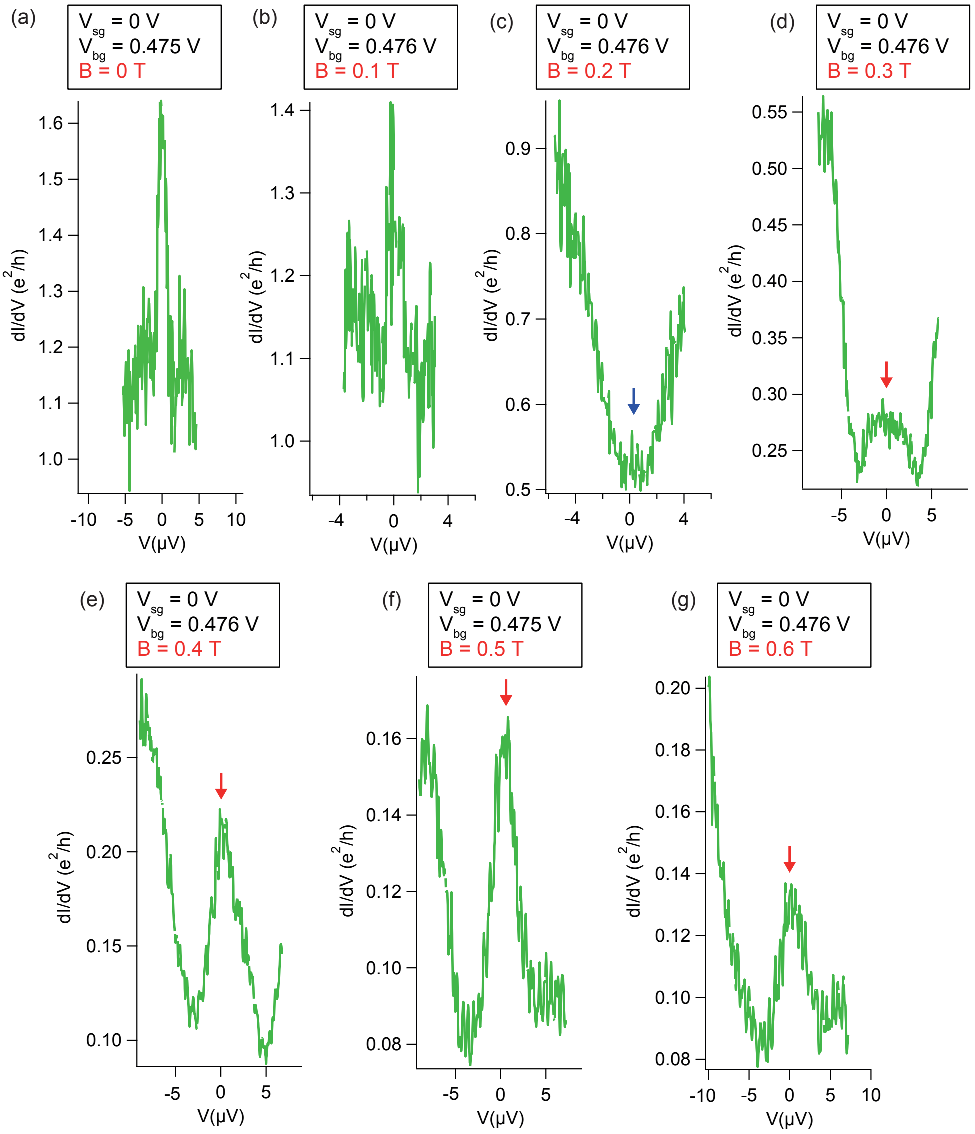

Figure 6.14: V - dI/dV traces corrected in conductance by subtracting R_s, and corrected in bias by subtracting R_s and eliminating an offset of 2 μV from the voltage source. The traces were taken at V_{sg} = 0 V, and at magnetic fields and backgate voltages indicated for each case in the legend on the top. The backgate voltage is also marked by a green line in the raw-data conductance maps of Figure 6.13. In each trace, a zero-bias peak can be associated with a supercurrent, its disappearance (blue arrow) with a $\phi_0 = 0 \rightarrow \phi_0 = \pi$ phase transition, and its re-emergence (red arrow) with a $\phi_0 = \pi$ supercurrent.

6.13 shows raw-data 2D maps of the conductance as a function of bias and backgate voltages for various magnetic fields, ranging from B = 0 T to 0.6 T. The center of Diamond 1 is pointed by a black arrow. At B = 0 T (map 6.13**a**), the supercurrent is weaker than in the zero-field cases of V_{sg} = -1 V (map 6.11**a**) and V_{sg} = -3 V (map 6.9**a**), implying that the Γ parameter is smaller at V_{sg} = 0 V than in these two latter cases.

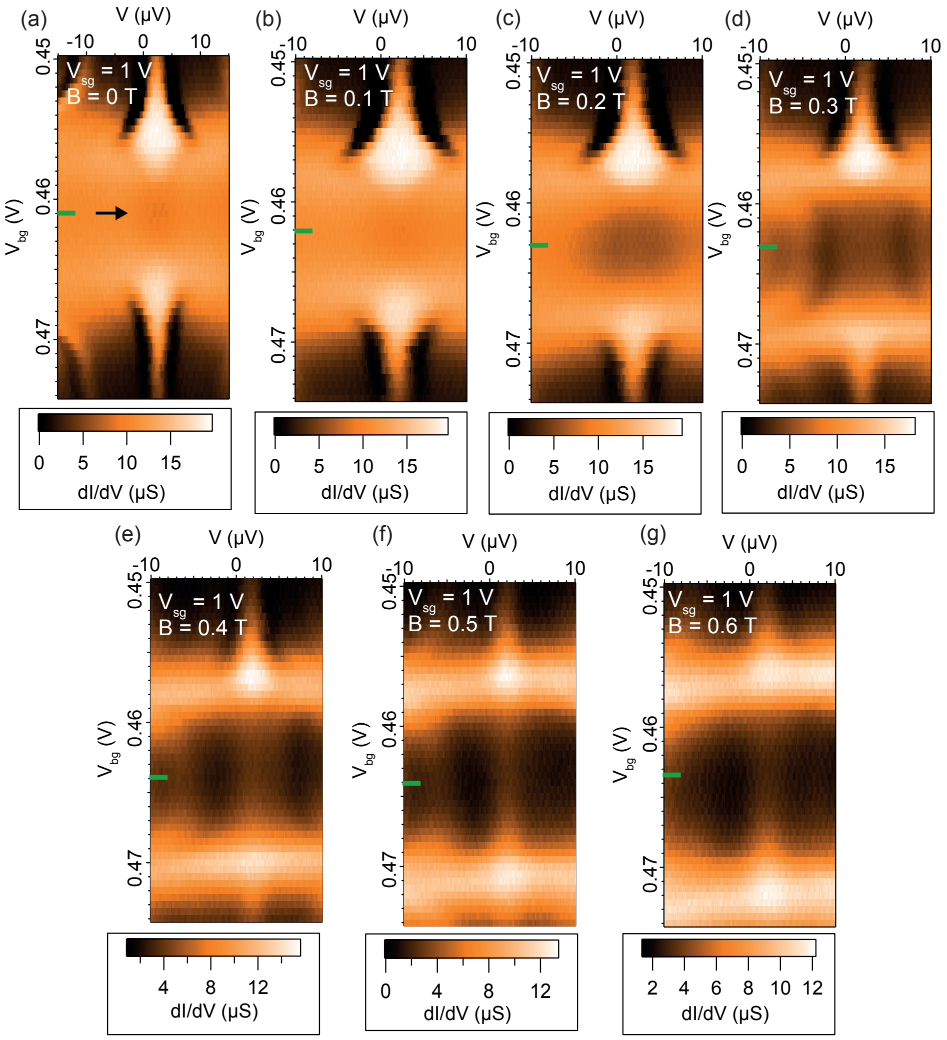

Figure 6.15: Raw-data maps of conductance as a function of the backgate voltage V_{bg} and the bias V, taken at V_{sg} = 1 V and at the magnetic fields indicated in each plot, ranging from B = 0 T to B = 0.6 T. The black arrow points to the center of Diamond 1. The green lines in each map mark the gate point at which a cut shown in Figure 6.16 was made.

Figure 6.14 shows V - dI/dV cuts taken in the center of Diamond 1, in the gate points indicated by a green line in each of the maps of Figure 6.13. In these curves, the conductance and the bias have been corrected by subtracting R_s and eliminating an offset from the voltage source of around 2 μV (this offset is clearly visible in all the maps of Figure 6.13). At B = 0 T (curve 6.14**a**), a small zero-bias peak indicates that a dissipative supercurrent passes through the junction. This peak is fully suppressed at B = 0.2 T (blue arrow, curve 6.14**c**), and re-emerges as a zero-bias peak at B = 0.3 - 0.6 T (red arrow, curves 6.14**d-g**), indicating a phase transition at B = 0.2 T ± 0.1 T (E_{cz}/U = 0.07).

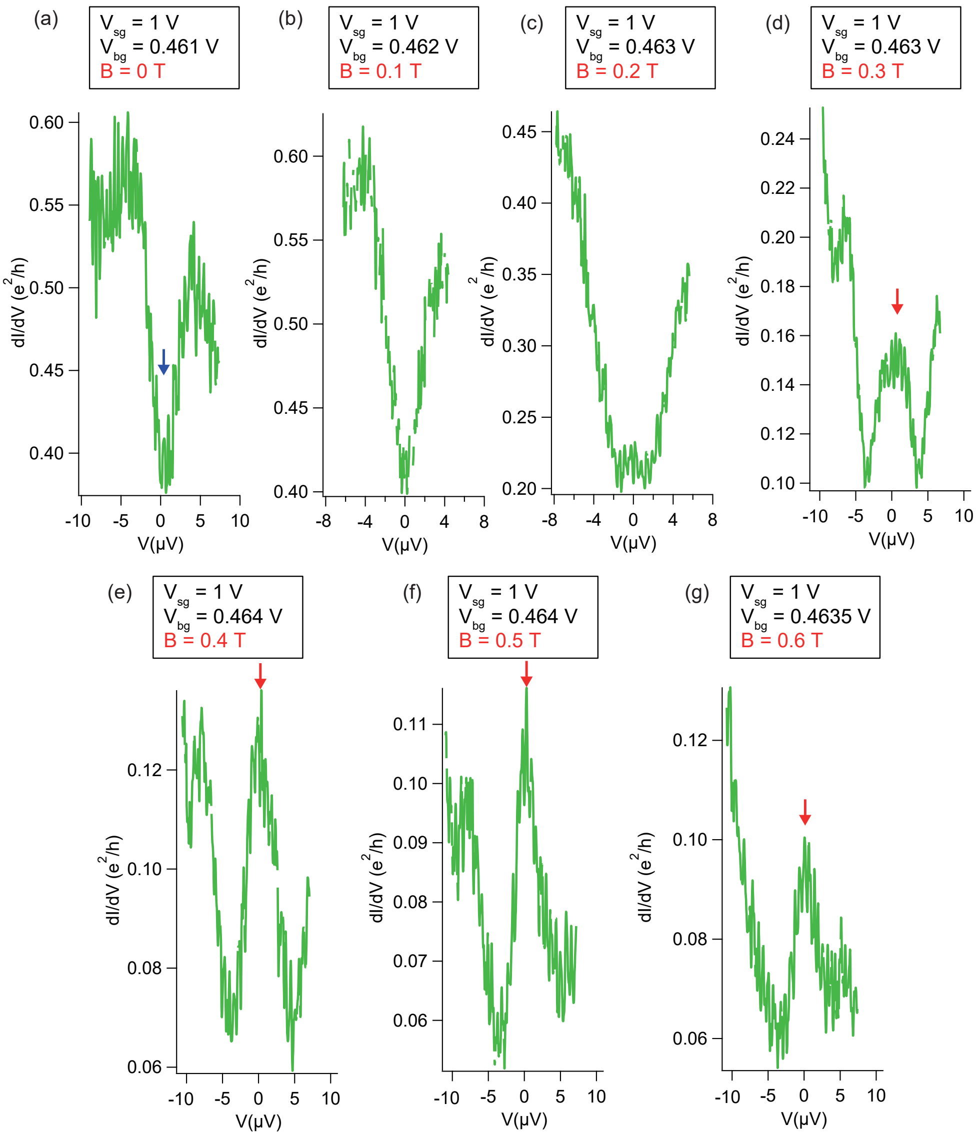

Figure 6.16: V - dI/dV traces corrected in conductance by subtracting R_s, and corrected in bias by subtracting R_s and eliminating an offset of 2 μV from the voltage source. The traces were taken at V_{sg} = 1 V, and at magnetic fields and backgate voltages indicated for each case in the legend on the top. The backgate voltage is also marked by a green line in the raw-data conductance maps of Figure 6.15. The traces **(a)** at B = 0 T and **(b)** at B = 0.1 T show a dip (blue arrow) at zero bias -i.e. an absence of supercurrent-, indicating that a $\phi_0 = 0 \longrightarrow \phi_0 = \pi$ phase transition is occurring at these fields. At larger fields, a zero-bias peak emerges (red arrow), corresponding to a $\phi_0 = \pi$ supercurrent.

So far, the cases V_{sg} = -3 V, -1 V and 0 V followed a consistent trend: the larger V_{sg}, the lower Γ, and the lower the field at which the phase transition happens in the center of Diamond 1. At V_{sg} = 1 V, as we shall see in the next paragraph, the extreme case where the phase transition is happening at B = 0 T occurs.

Figure 6.15 shows raw-data maps of conductance in Diamond 1 as a function of bias and backgate voltage taken at V_{sg} = 1 V, similar to the ones that I presented before at other side-gate voltages. At B = 0 T, contrary to the V_{sg} = -3 V, -1 V and 0 V cases, there is no supercurrent zero-bias peak. This is also confirmed by the cut taken in the middle of Diamond 1 in Figure 6.16**a**. At zero-bias, instead of a peak, there is a *dip* of conductance, indicated by a blue arrow. The situation is similar at B = 0.1 T (map 6.15**b** and curve 6.16**b**). At B = 0.2 T, there is perhaps a tiny peak appearing, but it cannot be clearly discerned from the background noise (map 6.15**c** and curve 6.16**c**).

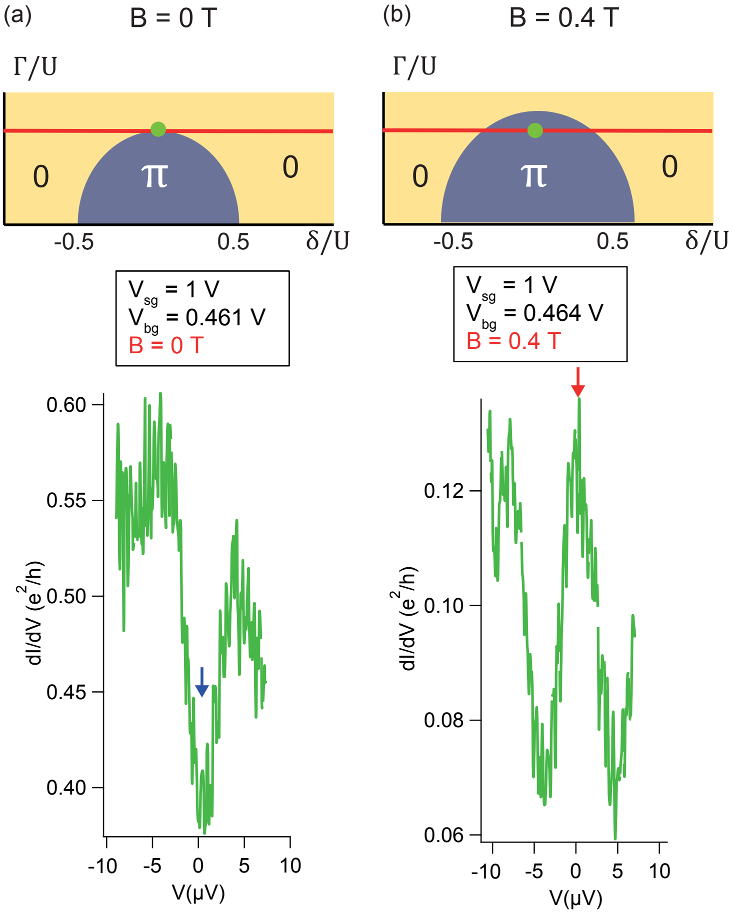

Figure 6.17: Sketches of expected phase diagrams (upper panels), in which the green dot indicates the Γ/U ratio at the $\delta = 0$ point, and corresponding V - dI/dV traces(bottom panels) measured at V_{sg} = 1 V and in the middle of Diamond 1, at **(a)** B = 0 T (in the QPT) and **(b)** B = 0.4 T (in the $|d\rangle$ state, after the QPT).

At a slightly larger field of B = 0.3 T, a robust zero-bias peak appears. Like before, this peak can be interpreted as a re-emerging supercurrent after a phase transition. The peak is present in the maps from B = 0.3 T to 0.6 T (Figure 6.15**d-g**) and in the associated cuts in the middle of Diamond 1 (Figure 6.16**d-g**). This data places the phase transition at B = 0 - 0.1 T, which corresponds to $E_c z/U$ = 0 - 0.03.

Figure 6.17 compares qualitatively the data at **a** B = 0 T and **b** B = 0.4 T (bottom plots) with sketches of the phase diagram of Figure 6.1 at these fields. The green dot in the diagrams is the δ = 0 point, or the center of Diamond 1, at which the data of the bottom curves of Figure 6.17 was acquired. The horizontal red line, as before, indicates a constant Γ/U ratio for all δ values, which is nearly the case in Diamond 1. In the experiment, δ is controlled by the backgate voltage. In the phase diagram of Figure 6.17**a**, at B= 0 T, the δ = 0 point touches the boundary of the π region. In the corresponding data, the supercurrent is so small that it is effectively unmeasurable. In contrast, at B = 0. 4 T, in Figure 6.17**b**, a robust zero-bias peak of supercurrent is measured because the δ = 0 point is well-inside the π region.

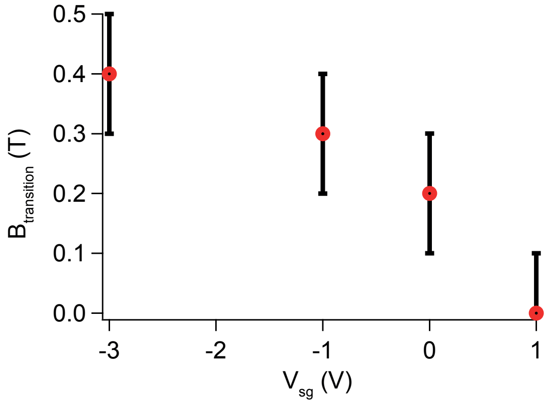

Figure 6.18: Correlation between the side-gate voltage and the magnetic field at which the QPT is seen. Error bars reflect that the conductance maps that generated this data were taken every 0.1 T.

The field $B_{transition}$ at which the $\phi_0 = 0 \longrightarrow \phi_0 = \pi$ transition happens in the center of Diamond 1 is plotted vs. the side-gate voltage in Figure 6.18. In this plot, the error bars are the uncertainty in the magnetic field at which the transition occurs. They are taken in this way because the supercurrent was recorded every 0.1 T. This plot constitutes the main message of this section. It tells us that the field at which the $\phi_0 = 0 \longrightarrow \phi_0 = \pi$ transition happens can be controlled via the side-gate voltage.

All of these findings are qualitatively consistent with the phase diagram sketched in Figure 6.2, given in the introduction to this chapter. They are also qualitatively consistent with the NRG calculations by Rok Zitko shown in Chapter 5. For a quantitative agreement, the Γ coupling needs to be extracted from the normal-state data. As stated in Ref. [89], the best way to do this is to fit the normal-state zero-bias conductance data with curves from NRG calculations. After extracting the Γ values for each V_{sg}, the phase diagrams will be calculated for the exact charging energy and g-factor of Diamond 1. This work is under progress.

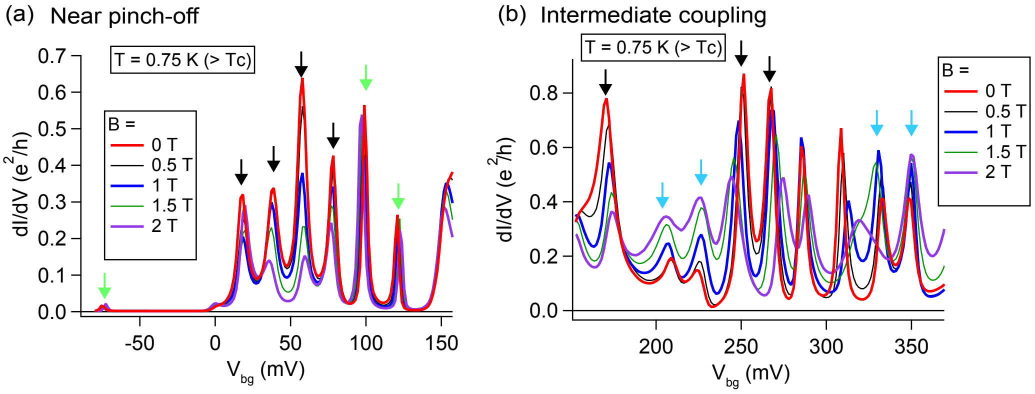

Figure 6.19: Linear conductance traces at different magnetic fields (from 0 T to 2 T) at T = 0.75 K (above the critical temperature of beta-phase Ta), portraying Coulomb peaks after the charge state of the device changed. The green arrows point to peaks whose conductance was not modified by the field. The black arrows point to peaks whose conductance was decreased by the field. Finally, the blue arrows point to peaks whose conductance was *enhanced* by the field. The latter is a sign of the dependence of the tunnel coupling of these states to the leads. Notice that the peaks come in pairs, implying that the same dot level originates them. **(a)** Near pinch-off. **(b)** Intermediate coupling regime.

One needs to be aware that Γ may depend on the magnetic field applied, as it was the case of the device of Chapter 5 when the magnetic field was applied parallel to the nanowire. In Diamond 1 of the device presented in the current chapter, the conductance decreased with the magnetic field as a result of the destruction of Kondo correlations. This is expected for a Γ that remains constant with magnetic field. However, after the measurements discussed here were completed, the same device switched to another charge state in which a different set of Coulomb peaks was observed. In this new regime, the conductance of some of the Coulomb peaks increased with the magnetic field, as seen in Figure 6.19 (blue arrows). To deal with this potential issue, the normal-state conductance of Diamond 1 will be fitted at different magnetic fields, in order to rule-out a dependence of Γ on the magnetic field. This is also work under progress.

6.8 Conclusions

A quantum dot with gate-tunable parameters and coupled to high-critical-field superconducting leads was presented. In the Josephson junction dot, a supercurrent was measured as a function of magnetic field. Due to thermal fluctuations and the overdamped regime of the junction, the supercurrent could only be observed as a zero-bias peak (ZBP). A re-entrant effect in the supercurrent was observed, and it was linked with a field-induced quantum phase transition (QPT) of the ground state of the dot. By varying the Γ coupling with a side-gate voltage, it was demonstrated that the field at which the QPT was observed could be changed.

Tuning Γ to be at the QPT at zero field resulted in a vanishing supercurrent-related ZBP at this field. In this condition, applying a finite field provoked the re-emergence of the supercurrent ZBP. This observation is of particular interest in the context of the ZBP signature of Majorana bound states, as it provides a mechanism for the observation of emergent ZBPs in nanowire Josephson junctions not previously known. In contrast with peaks emerging from the QPT of Andreev bound states [12], this supercurrent-related ZBP stays pinned to zero-energy as the magnetic field is increased.

Chapter 7

Conclusion

Low-temperature transport in InSb and InAs nanowires coupled to superconducting leads was explored, motivated by the need to understand the frontiers of the search for helical liquids and Majorana bound states in these systems, within the most basic two-terminal Josephson junction device design.

It was found that one-dimensional (1D) transport in InSb and InAs nanowires could be affected by serendipitous quantum dots in the channel of the devices. In InSb nanowires, they may appear in parallel to the 1D conduction. In both InSb and InAs nanowires, they can show at the onset of the 1D conduction, when the charge density is low. Their existence poses a threat on the interpretation of the various signatures surrounding Majorana bound states physics, including conductance quantization and helical states in the normal state, and zero-bias peaks emerging with magnetic field in the superconducting state.

In the normal state, a quantum dot in an InAs nanowire can imitate the plateaus of quantized conductance that are expected from a 1D nanowire, when its tunnel coupling and its chemical potential are simultaneously affected by one gate voltage. Quantum dots in parallel to the 1D conductor in an InSb nanowire can also replicate signatures of helical states in two different ways. A first way is when a Kondo resonance conducting in the unitary limit Zeeman-splits before the onset of the first plateau of the parallel 1D path, ending as a peak on top of a 1 e^2/h plateau. A second way, more subtle, happens when a localized state at the onset of one of two parallel 1D channels produces a Coulomb resonance on top of a 1 e^2/h plateau.

It was proposed that two 1D conductors in parallel in a single InSb nanowire, with different g-factors and affected differently by the orbital effect of the field, could lock their subbands together, resulting in degeneracies that persisted over a large range of magnetic field. The observation of two 1D wires in the same nanowire opens the door for other interesting experiments, including fractional helical states.

A variety of superconductor / nanowire hybrids were investigated, gaining knowledge on the factors that improve or detriment the hardness of the gap, the critical field, the magnitude of the Josephson current, and the occurrence of ballistic transport. It was found that Ar^+ etching, nominally considered a harsh surface treatment, could be used to obtain hard gaps with Aluminum and with Vanadium contacts having a 20 nm Aluminum under-layer. Evaporated Tantalum was found to be a good alternative for large-critical field Josephson junctions, and its gap size and gap hardness were found to be improved by a 5 nm Niobium under-layer, albeit under strict deposition conditions.

A nanowire could possess deteriorated signs of superconductivity and still be in the ballistic regime. Conversely it could behave as a quantum dot and still maintain superior superconducting properties. This implies that a pristine channel was mostly responsible for 1D transport, while a pristine interface was to be thanked for a hard gap and a large Josephson current.

In the superconducting state, the formation of quantum dots at low charge density prevented a proper tunnel spectroscopy of the 1D state in InSb and InAs nanowires. In a regime with a slightly larger charge density, in which supercurrent could be observed, localization still prevented the study of the truly 1D superconducting state in an InAs nanowire. Instead of revealing the physics of the 1D system, the supercurrent measurements showed the ground-state transitions of the underlying quantum dot as a function of gate voltage and magnetic field.

This novel observation was confirmed in a second InAs nanowire Josephson junction with a well-defined quantum dot. In this new device, the field at which the transition of the ground-state of the dot happened was tuned with a side-gate voltage, which acted upon the tunnel coupling of the dot to the leads.

7.1 Perspectives

Independent gating of the 1D electron gases of an InSb nanowire

Figure 7.1 shows a proposed type of device for gating independently the 1D conduction paths that form in an InSb nanowire. This scheme involves split side-gates on top of the nanowire, separated by a layer of hafnium oxide dielectric. A side-effect of a dielectric on direct contact with the nanowire is that it may affect the natural formation of the 1D gases by altering the charge landscape in the native oxide of the nanowire. Side-gates separated by vacuum may be a good replacement, provided that their capacitive coupling to the nanowire is kept large by approaching them. If independent side-gating is achieved, novel experiments with double quantum wires can be performed [13].

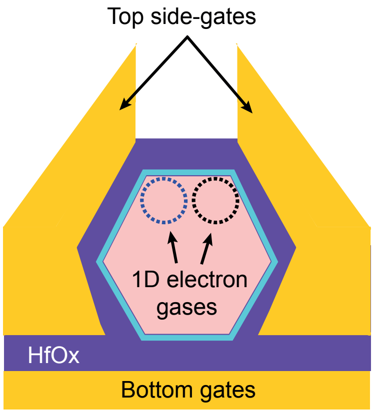

Figure 7.1: Sketch of a device conceived for independent gating of the 1D electron gases of an InSb nanowire. The split top side-gates are separated by 50 nm.

Avoiding localization in InSb nanowires

If it is confirmed that the charges trapped in the native oxide of an InSb nanowire or in the substrate produce undesired quantum dots, then surface treatments such as sulfur passivation could be used to remove the native oxide and replace it by electrically neutral molecules. If this is achieved, the 1D properties of the wire should be accessible without spurious quantum dots. However, it may also be the case that the native oxide is essential in confining 1D electron gases near the surface of the nanowire, as it is being investigated through simulations. This method may then lead to a rearrangement of the charge density in the wire, with the wavefunction moving away from the surface and towards the center, as expected for oxide-free InSb [131].

Obtaining signatures of helical states in III-V nanowires

Signatures of helical states are currently been searched by direct transport through nanowires, but this may suffer from some drawbacks when low-energy features are probed, specially if the spin-orbit gap is of sub-meV size. Direct transport through nanowires is affected by localization at any point in the nanowire. The finite tunnel coupling of localized states can be of the same order of magnitude than the spin-orbit gap, and so can other quantities such as the charging energy and the Kondo enhancement of the conductance. Therefore, two-terminal conductance measurements may not be the most suitable for the purpose of determining the existence of helical states in nanowires.

Tunnel spectroscopy can be a better option, since it is sensitive only to local features (a few nm away from the tunnel probe) and to the density of states. In the helical regime, the density of states of the nanowire would show an additional Van Hove singularity, as shown in Figure 7.2. A tunnel-barrier can be obtained in the nanowire by heterostructuring it during its growth or by a adding a weakly-coupled contact. A third possibility is to set a quantum dot weakly coupled to

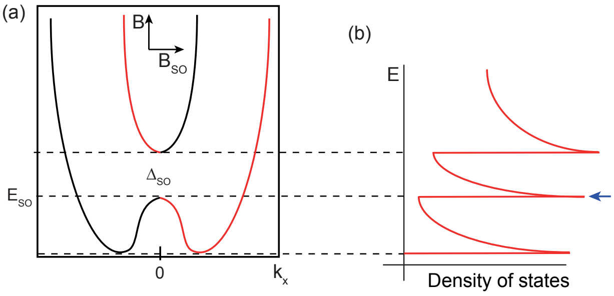

Figure 7.2: **(a)** Sketch of the band dispersion of a 1D nanowire with a helical gap Δ_{SO}. **(b)** The density of states will show an additional Van Hove singularity (blue arrow) when the extrema point at energy E_{SO} is reached, which would not appear in the absence of a strong spin-orbit Rashba interaction under Zeeman splitting.

a one-dimensional nanowire by electrostatic means. In this case, the dot level could be used to probe the 1D density of states in an asymmetric tunnel configuration. These three possibilities are sketched in Figure 7.3.

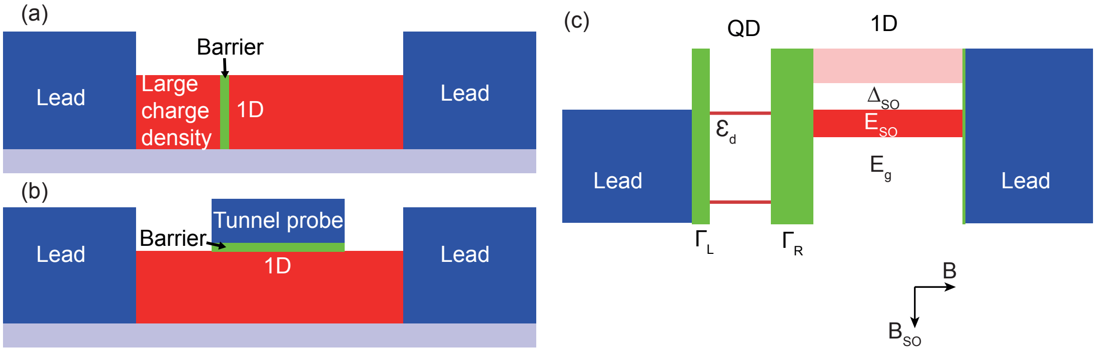

Figure 7.3: Sketches of devices that can be used to perform tunnel spectroscopy on the 1D density of states of a nanowire. **(a)** A nanowire with an epitaxial barrier grown along the axial direction is used. By gating it is possible to accumulate electrons in one section of the nanowire and use it as a lead to probe the subbands of another section, via the tunnel barrier. **(b)** A tunnel probe weakly coupled to the nanowire probes 1D states near surface of the nanowire. **(c)** Semiconductor scheme of a nanowire with a quantum dot (QD) embedded ($\Gamma_R \ll \Gamma_L$). By biasing the leads attached to the dot - 1D nanowire, one can use an excited level of the dot (ε_d) to probe the density of states of the nanowire in the helical regime. Alternatively, if one can use a gate to compensate the shift of the 1D subbands, it is possible to use a dot level at zero-bias, at the degeneracy point. In this simplified scheme, the Zeeman splitting of the state of the dot is not taken into account.

We tested these three approaches in my thesis, with inconclusive results. In the first approach, we measured InAs nanowires intercalated with thin InP barriers such as to establish an InAs quantum dot coupled to a 1D InAs section. Unfortunately, the InP barriers were discovered to be short-circuited by lateral overgrowth of InAs. In the second approach, bare InAs and InSb nanowires were deposited on top of bottom contacts to use them as local tunnel probes, and then contacted by the usual two-terminal method. Unfortunately, the nanowire oxide was too thick to be able to measure a finite current. Wet-etching did not improve this due to other issues. In the third approach, we measured a gate-defined quantum dot in an InSb nanowire to use it as a probe of the density of states of a 1D section of the nanowire. Using gate voltages, we tuned asymmetrically this dot. Yet again, this experiment was unsuccessful because of the inability to pinch-off the 1D section of the nanowire via biasing.

These circumstantial misadventures could eventually be circumvented in other ways. Different nanowire heterostructures could be investigated. The weakly-coupled probe could be set in a different way, by mildly and locally etching a section of the native oxide, or by replacing the native oxide by a different a oxide barrier, without locally creating quantum dots. Finally, a 1D nanowire with lower charge density could be used to ensure a pinch-off.

Testing of Ta, Nb/Ta and Al/V in InSb nanowires

Tantalum, tantalum with a 5 nm niobium under-layer, and vanadium with a 20 nm aluminum under-layer remain to be tested in InSb nanowires. Alternatively, a thin layer of vanadium (<45 nm) could also be tested, to falsify the hypothesis of strain-related issues with thicker vanadium films.

Confirmation of the Josephson current phase transition with a SQUID

In my thesis, I fabricated SQUIDs (Superconducting Quantum Interference Device) with InAs nanowire quantum dots in order to confirm the change in the phase of the supercurrent when a magnetic field-induced ground-state transition occurred. In doing so, I noticed the need to couple the nanowires to a superconductor with a larger gap, supporting a stronger Josephson current. Even if this material requirement is achieved, the experiment still remains challenging. A field transverse to the SQUID is needed to alter its flux, but it will also change the magnetic state of the dot. To prevent this from happening, the SQUID needs to be fabricated with the largest area possible, in order to phase-bias the quantum dot with small variations of magnetic field. In those circumstances, a field parallel to the plane of the SQUID can be used to force a quantum phase transition in the dot.

Josephson current phase transition in large g-factor InSb nanowire quantum dots

The large g-factor of InSb nanowires should allow seeing the quantum phase transition of the ground-state of Josephson-junction quantum dots at a magnetic field 5 to 10 times lower than InAs nanowires, improving significantly the resolution and the size of the supercurrent after the transition. If this is achieved, even aluminum contacts will suffice to observe the transition before destroying superconductivity.

Appendix A

Device fabrication and testing

During the length of my PhD, I fabricated many types of devices, which include two and four-terminal devices, SQUIDS, Cooper-pair splitters and others. In turn, I fabricated these devices on top of various types of substrates with various gate configurations, whose design I evolved according to my needs. However, for the sake of clarity, here I will only present the fabrication steps of a generic type of device -a nanowire Josephson junction-, which was also the type of device that was used in the four chapters of this thesis that contain experimental results (Chapters 3 - 6). The credit for developing the fabrication processes that I used or that I was inspired by goes to Eduardo J. H. Lee and Jean-Pierre Cleuziou. Their help, training and advice was essential to develop my own fabrication processes and to lighten the number of spent cleanroom hours.

I did nearly all the steps of device fabrication at the cleanroom installations of the "Plateforme Technologique Amont" (PTA, CEA Grenoble), except for the atomic layer deposition, which I did in the Neel Institute (Grenoble) with the help and supervision of Laurent Cagnon, and the chip bonding and nanowire deposition, which I did in the PROMES cleanroom at CEA Grenoble.

The InAs nanowires that I used in the fabrication of some of the devices were provided by Lucia Sorba's group at NEST Pisa, while the InSb nanowires were grown by Erik Bakkers' group at TU Eindhoven. Their high quality was essential for my work.

The fabrication of a nanowire Josephson junction device involves the following steps:

1. Patterning of the substrate with gates.
2. Deposition of the nanowire with a micro-manipulator.
3. Patterning of the superconducting contacts.
4. Testing and bonding of the finalized chip to a chip-carrier.

In this appendix, I will detail each of these steps.

A.1 Substrate patterning

The fabrication of gates requires at least four electron beam lithography steps, for patterning the following:

1. Alignment marks on a Silicon wafer.
2. Gates.
3. Dielectric.
4. Bonding pads.

Figure A.1 shows a sketch of the final outcome of each step for an individual writing field after lift-off. In a 2-inch wafer (sketched in Figure A.4**a**), there were typically 25 chips of 5x5 mm with 8 writing fields each.

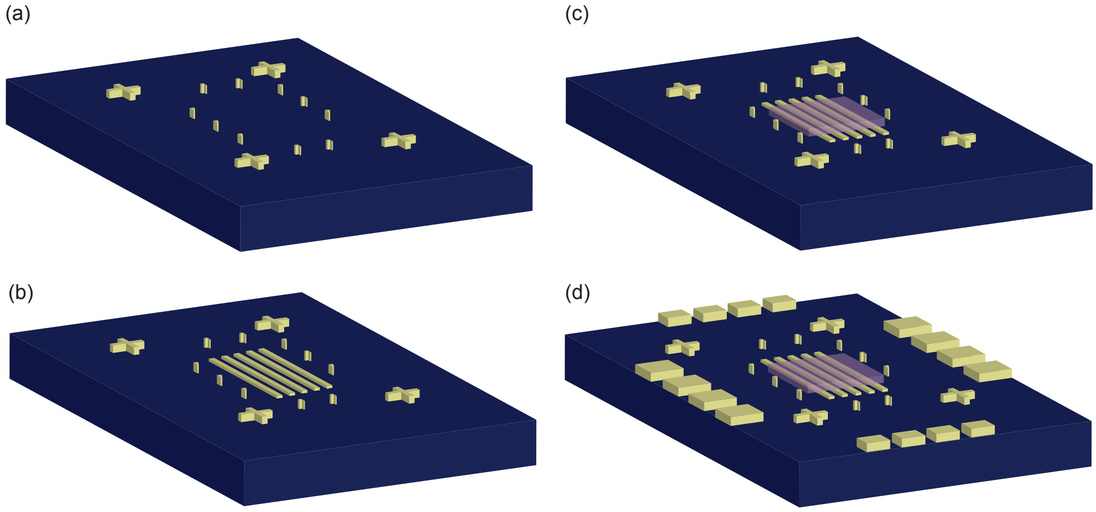

Figure A.1: Scheme of the outcome of each step in substrate patterning. **(a)** Alignment marks. **(b)** Gates. **(c)** Dielectric. **(d)** Bonding pads.

Patterning of alignment marks

Alignment marks are needed for several reasons. We use two types of alignment marks: 1) for the lithography itself (of gates and nanowire contacts) and 2) for aligning scanning electron microscopy (SEM) images of nanowires. In a JEOL masker system, which I used in my work, the first type of marks are divided into two subtypes: global marks and chip marks. The so-called "global marks" are employed to automatically detect local marks, also called "chip marks", which in turn are used to obtain the best focus of the electron beam locally. This information is acquired automatically with a laser beam that detects their height, and it is used to correct for beam deflection and field deformation. When writing fine gates (width and spacing < 40 nm), these corrections are essential for a successful pattern. The arrows in the sketches in Figures A.2 and in Figure A.4 point to each type of alignment marks.

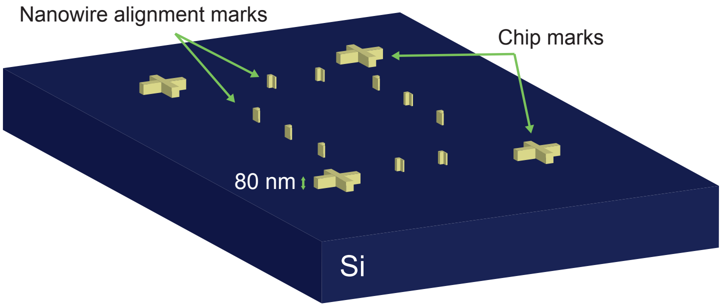

Figure A.2: Sketch of the final outcome of a writing field after lift-off of the alignment marks. Arrows point to two types or alignment marks: lithography "chip marks" and marks for aligning SEM images of nanowires.

As starting substrate, we use a 2-inch Silicon (Si) wafer nominally non-doped. These wafers have the advantage of being non-conductive and, contrary to heavily-doped Si wafers with a thermal oxide -that I used as backgates in the first year of my thesis-, they do not pose any problems at the moment of bonding. The disadvantage is that, evidently, they cannot be used as a global backgate.

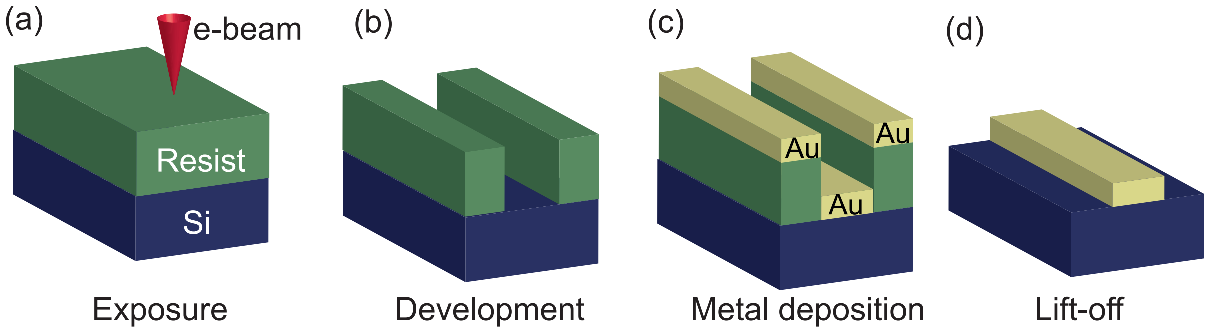

Figure A.3: Scheme of the patterning of a nanostructure by lift-off. **(a)** After spin-coating it on top of the Si wafer, the resist is exposed by e-beam lithography. **(b)** Inmmersion of the wafer in a solution that makes the exposed resist soluble leaves an opening with the shape of the desired pattern. **(c)** Then, a thin film of metal is deposited. **(d)** Immersion of the wafer in acetone removes the resist and leaves the desired gold pattern intact.

Before depositing the resist for the lithography, the wafer is cleaned of any organic residues by rinsing in acetone, followed by ultrasound and rinsing in isopropanol. The patterning of alignment marks and nearly all other structures (i.e. gates, contacts) was done via a lit-off process, which is schematically depicted in Figure A.3.

First, I spin-coated one layer of PMMA 4% (dissolved in ethyl lactate) with a molecular weight of 950 KDa. To keep things simple, I kept the same spin-coating parameters for all the types of resist mentioned in this work: a speed of 4000 rpm and an acceleration 2000 rpm/s^2 during a time of 60 s. The baking temperature for PMMA and ZEP resists was always 180 °C (for 5 minutes), done in a hotplate protected by a silicon wafer for cleanliness. The e-beam exposure of the resist (dose = 1500 $\mu C/cm^2$, current = 5 nA) and its development in MibK (Methyl isobutyl ketone)/Isopropanol 1:3 (during 30 seconds) followed by 60 seconds of Isopropanol rinsing and blow-drying leads to the desired pattern of alignment marks.

Afterwards, 10 nm of Titanium (Ti) and 70 nm of Gold (Au) are evaporated on top of the developed resist. The evaporation was done in an PLASSYS electron-gun machine, preceded by in-situ Argon etching at 250 V for 48 seconds to remove resist residues. Ti aids in the adherence of Au to the Si substrate, while Au in itself is chosen by its high atomic number, which ensures a large contrast and eases its detection by the electron beam.

Finally, a lift-off in acetone with ultrasound is performed. After the lift-off, the final pattern shown in the sketch in Figure A.2 is obtained in an individual writing field. The GDS file that produces this pattern and all patterns shown in this work is made with the software Klayout. Screenshots of the pattern at three zooms are shown in Figures A.4**b-d**, from a (A.4**b**) 5x5 mm individual chip to a (A.4**d**) 3 µm −long field of nanowire alignment marks, passing by a (A.4**c**) 50 x 50 µm writing field. At the same time that alignment marks are written, a T-shaped mark is written on each chip to distinguish the top from the bottom of the wafer with the naked eye. In the 2-inch wafer, the chip pattern described before is repeated 25 times in a 5x5 array and four large global marks are added as indicated in the sketch in Figure A.4**a**, for global alignment in the succeeding lithography steps concerning the substrate.

Patterning of the gates

The patterning of the gates is the most demanding process of all. The typical gates that I fabricated had a width of 40 nm and a separation of 40 nm as well, with a length of about 4 µm   Sixteen fine gates of these characteristics were sprayed across 1.2 µm of wafer. The electron beam writing conditions needed to achieve this level of miniaturization are stringent. As explained in the previous subsection, the gates are written using the chip marks shown in the GDS file of Figure A.4**c** to obtain the best focus and correct accordingly the beam deflection and field distortion. The proximity of the chip marks to the gates (20 - 25 μm) is key for this to work properly.

The gates were fabricated through a lift-off process as the one shown in Figure A.3. First, a layer of resist ZEP 1:1 (dissolved in anisole) was spin-coated on top of the wafer. Then, the

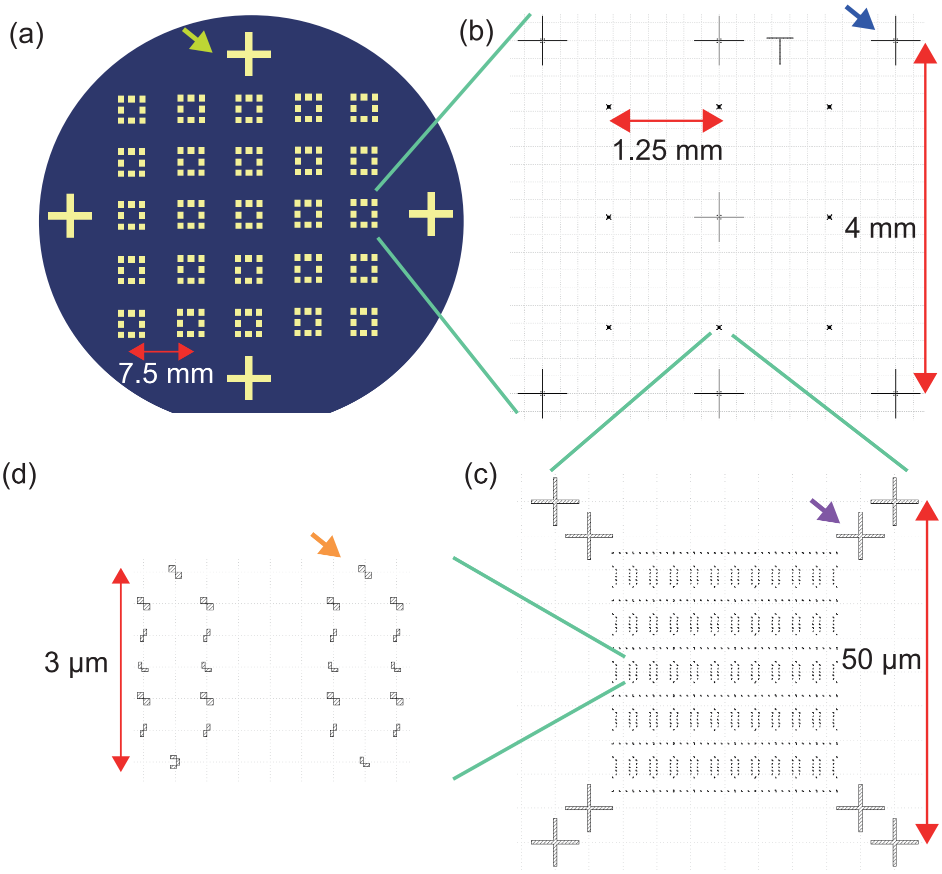

Figure A.4: Alignment marks at different zooms. **(a)** Scheme of the 2-inch Si wafer, containing an array of 5x5 chips. One of the four global marks used during substrate patterning is indicated by a light green arrow. **(b)** GDS file used to pattern the alignment marks of one chip in a real wafer. The blue arrow points to a global mark that is used for alignment during contact patterning -of nanowires and gates- in each individual chip. **(c)** GDS file zoom of one the eight writing fields of a chip. The purple arrow points to one of the chip marks used during gate patterning and, later on, during contact patterning. **(d)** GDS file zoom of one field of nanowire alignment marks. Notice that the bottom marks of each field are different.

resist was exposed through electron beam lithography with an area dose of 800 $\mu C/cm^2$ for the pads of the gates and a linear dose of 5000 $\mu C/cm$ for the gates themselves, at a current of 1 nA. Figure A.5 shows a screenshot of the typical GDS file employed in the patterning. Following exposure, the resist was developed during 60 seconds in 1:1 Isopropanol/MibK followed by 20 seconds in 89:11 Isopropanol/MibK and blow-drying. After the development, the resist residues were removed via Argon etching for 54 seconds, followed by in-situ evaporation of a thin film of 7.5 nm of Ti and 12 nm of Au. This was followed by lift-off in acetone under ultrasound and rinsing in isopropanol. To remove resist residues on top of the gates, the wafer was put under mild oxygen plasma for 90 seconds in a Reactive Ion Etching ICPS machine.

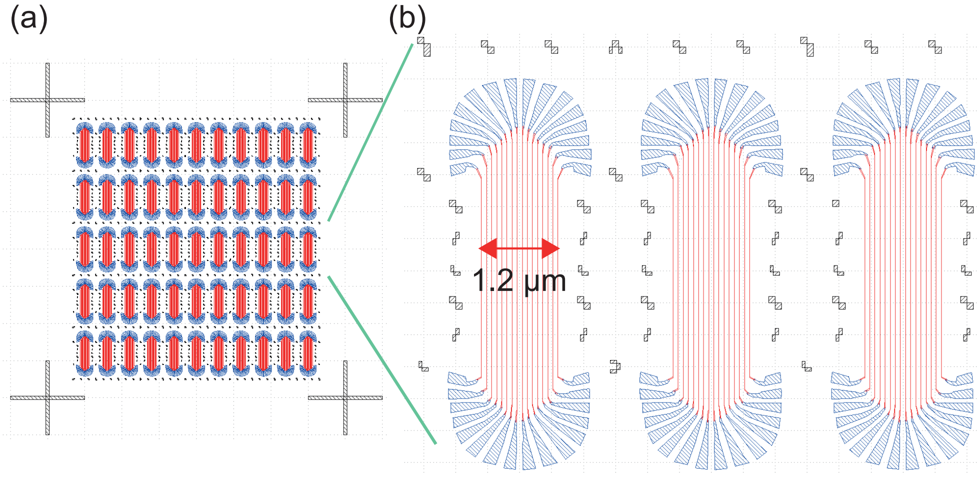

Figure A.5: GDS file of the gates. **(a)** Typical gate design on a writing field. The red lines were written with a line dose, while the blue pads were written with an area dose, as explained in the text. Alignment marks appear in black. **(b)** Zoom into a gate field.

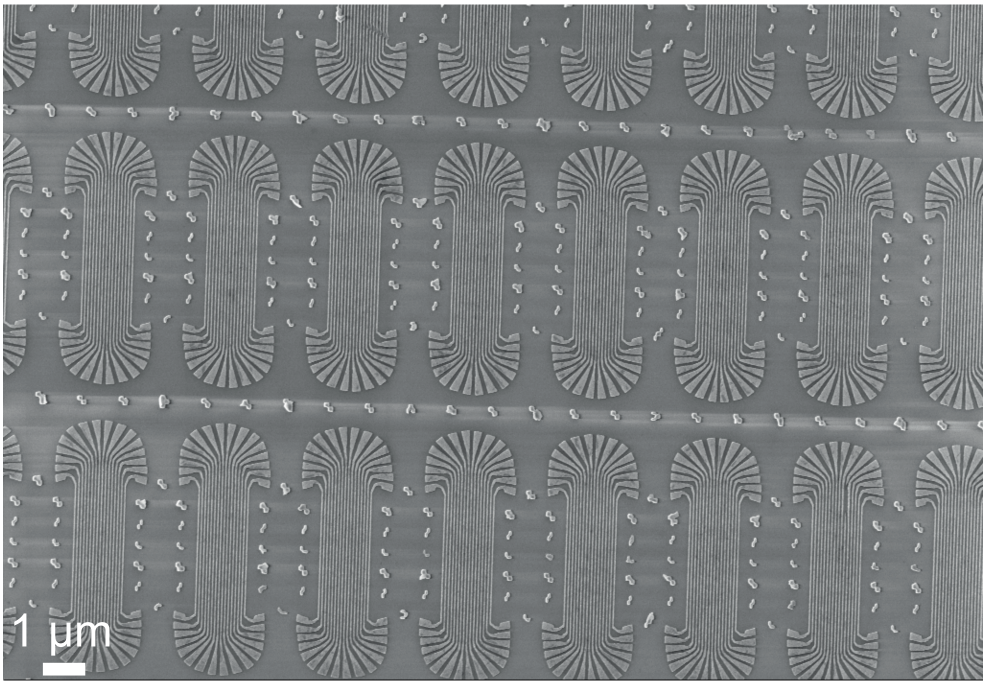

Figure A.6: SEM image of finished gates.

A SEM image of a successful example of the final product is shown in Figure A.6.

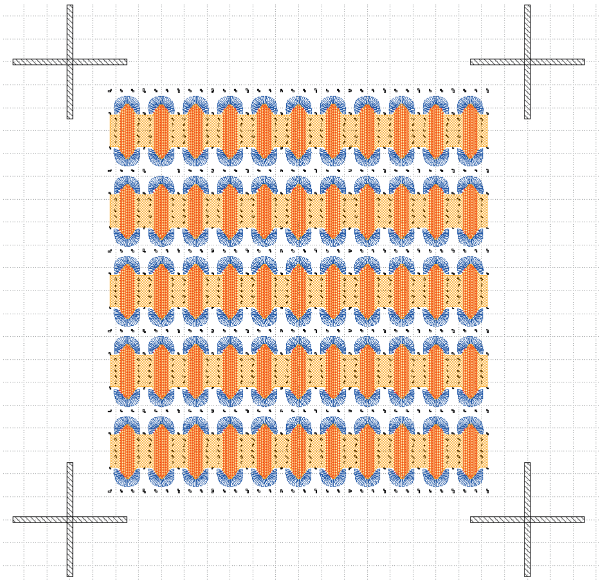

Figure A.7: GDS file of the dielectric pattern, colored in orange. Gate pads are shown in blue and alignment marks in black.

Patterning of the dielectric

In most wafers, I patterned the dielectric via a lift-off process similar to the one in Figure A.3. First, a layer of pure ZEP resist was spin-coated on top of the wafer. This was followed by electron beam lithography of resist openings at a current of 5 nA and a dose of 800 μC/cm^2 , with the GDS pattern shown in Figure Figure A.7. The development of the pattern was made by dipping during 60 seconds in 1:1 MibK/Isopropanol followed by 20 seconds in 89:11 Isopropanol/MibK.

After development, 10 nm of hafnium oxide were deposited by atomic layer deposition (ALD) in a Cambridge machine, at a chamber temperature of 120 °C [1]. The ensuing lift-off was carried out in acetone under ultrasound.

Gates with 10 nm hafnium oxide as dielectric break down at roughly 8 - 10 V half of the time. During low-temperature electron transport, gate shifts (called in the transport jargon "switches") will not increase significantly up to that voltage. Hysteresis, on the other hand, will depend on the device. Typical lever-arm values measured on real devices fabricated on top of these gates range from 0.01 to around 0.1, indicating a moderately good coupling of the gate to the device. Compared to silicon nitride (50 nm) and highly-doped Si substrates with a thermal silicon oxide (300 nm) on top, devices made with hafnium oxide as gate dielectric had the lowest low-temperature noise.

---

[1] This relatively low temperature had to be used to avoid baking the resist. To compensate for the lower temperature, longer pulse times of the precursors were used.

Patterning of the bonding pads

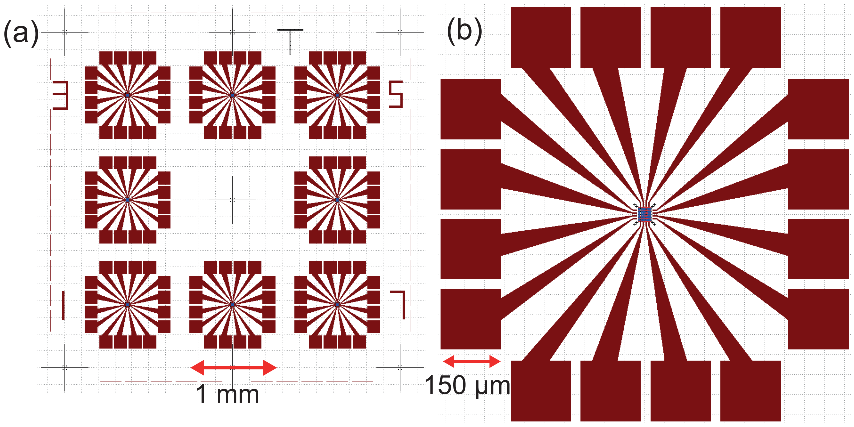

Figure A.8: (a) GDS file of the bonding pads, colored in dark red. Numbers (1, 3, 5, 7) are written in the same exposure for easier identification by the naked eye of each writing field. Alignment marks are shown in black. **(b)** Zoom of one writing field, showing the finer structure of the bonding pads.

The bonding pads, being large structures (150 μm × 150 μm), were fabricated by using a sensitive resist and a large beam current. The resist chosen for this task was the photoresist UV5, which is also sensible to electrons. In a typical run, the UV5 was spin-coated and then baked in a hotplate at 130 °C for 1 minute. Immediately after this, the resist was exposed with a dose of 60 $\mu C/cm^2$ and a current of 25 nA by e-beam lithography. After exposure, the resist was baked once more at 135 °C for another minute, for its stabilization. Following this, it was developed in the base MF26. Then, a mild oxygen plasma of 30 seconds was employed for resist residue removing. After the bottom of the resist openings was stripped of resist, 10 nm of Ti and 60 nm of Au were evaporated on top. Lift-off in acetone under ultrasound was performed as usual, followed by another round of oxygen plasma for total removal of the resist -this time, for 2 minutes-. Resist residues on top of the dielectric affect nanowire mobility [132].

Figure A.8 shows the GDS file used for the patterning of the bonding pads. In each writing field, the pads go all the way to the vicinity of the gates. This shortens the length of the nanowire contacts written in an upcoming step, preventing stitching errors in their lithography.

Cleaving of the wafer

After I finish the last processing step, I cleave the wafer in chips of at least 7 x 7 mm by hand with a diamond pen. At this point, each chip is ready to receive nanowires on its surface.

A.2 Nanowire deposition

The deposition of nanowires was done manually using a homemade micromanipulator. Although its design evolved with time, we developed it initially with the collaboration of Patrick Torresani and Moira Hocevar. Here I will describe the final design that we adapted and used in the last two and a half years of my PhD. In basic terms, a sharp tungsten tip was used to pick a nanowire from a growth substrate -provided by either Bakker's or Sorba's group- and place it on top of a gate field of one of the chips whose fabrication I described in the previous section.

InAs nanowires used

The InAs nanowires used in this thesis had a wurzite crystalline structure. They were growth by Daniele Ercolani and Lucia Sorba from NEST Pisa by the chemical beam epitaxy method, described elsewhere [133]. Figure A.9 shows SEM and TEM images of these nanowires, provided by Valentina Zannier and Jérémy David from NEST Pisa. The growth substrate is depicted in the SEM image of Figure A.9**a**. The as-growth InAs nanowires are long (<5 μm), thin (diameter ~ 60 - 70 nm) and densely positioned.

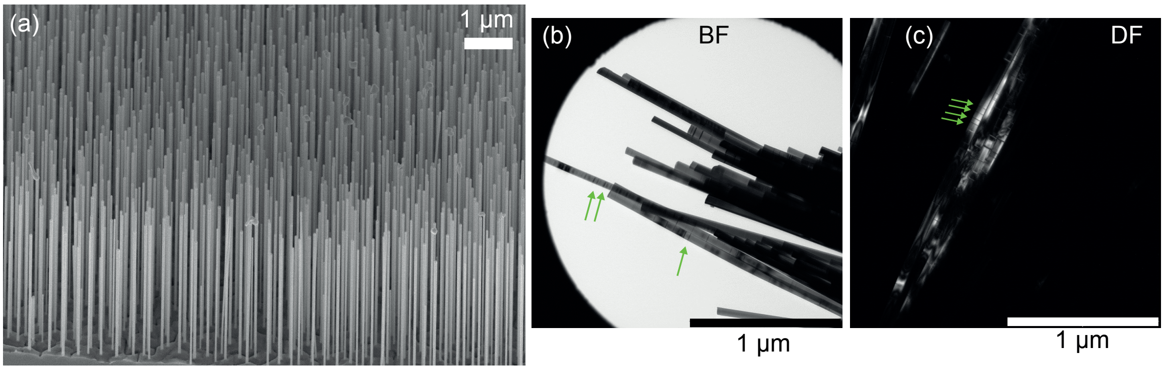

Figure A.9: **(a)** SEM image of a growth substrate with InAs nanowires used in this thesis. The nanowires are standing straight and densely packed. **(b,c)** TEM images in bright **(b)** and dark **(c)** field of the InAs nanowires used in this thesis. A few stacking faults are pointed by green arrows. Credits: Growth done by Daniele Ercolani and Lucia Sorba; SEM and TEM images provided by Valentina Zannier and Jérémy David.

The nanowires had a few stacking faults, with random spacing in between each of them. In the TEM images in Figures A.9**b,c**, some of these planar defects are pointed by green arrows.

InSb nanowires used

The InSb nanowires used in this thesis had a zinc-blende defect-free crystalline structure. They were growth by Diana Car, Sébastien Plissard and Erik Bakkers from TU Eindhoven by the molecular beam epitaxy technique. The growth technique and characterization of these nanowires has been extensively discussed in the PhD thesis of Diana Car [134].

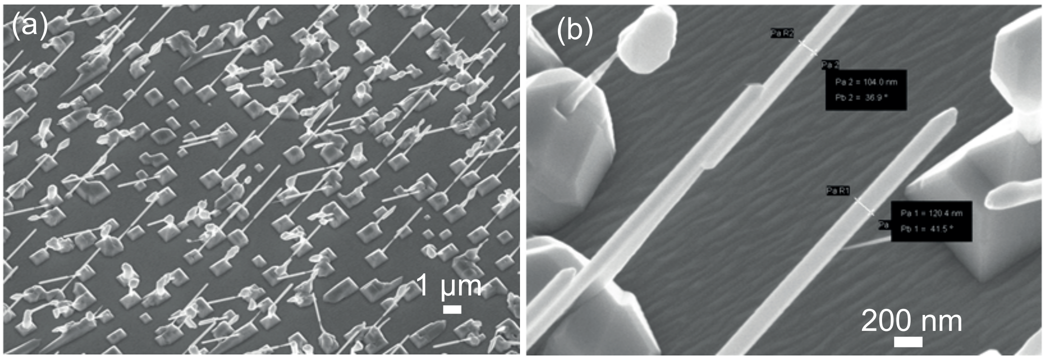

Figure A.10: **(a)** SEM image of a growth substrate with InSb nanowires used in this thesis. The nanowires are not sparsely positioned. **(b)** Zoom on a few nanowires. . Credits: Growth done by Diana Car, Sébastien Plissard and Erik Bakkers; SEM images provided by Diana Car.

Figure A.10**a** shows a SEM image of a growth substrate made with InSb nanowires. The substrate was made of InP, whilst the nanowires were grown from InP stems with 40 nm gold colloids. Figure A.10**b** shows a SEM image zoomed on a few nanowires. The nanowires are short (<2.5 μm), thick (diameter ~90 - 130 nm) and sparsely positioned.

Description of the micromanipulator

The micromanipulator was composed of a tungsten tip attached to a low-vibration mechanical arm. The mechanical arm was made by assembling the following components:

- As a base, a heavy planar plate with mounting screw-holes was used, to reduce vibrations. This plate was placed on top of a heavy table.
- A Thorlabs "Lab Jack" Z-stage for rough vertical displacements (maximum range of 56 mm) was screwed onto the heavy plate. This component was used to adjust the height of the tungsten tip with respect to the sample.
- On top of the Z-stage, a Thorlabs "Adjustable Angle Plate" tilting stage was screwed. The tilt angle was kept fixed at 15° with respect to the vertical.
- On top of the tilting stage, a Thorlabs "3-axis Microblock Stage" with X,Y,Z degrees of freedom was screwed. This stage allowed for micrometer-precise motion of the tugnsten tip with respect to the sample, in a range of 50 µm per revolution of the adjuster screw in fine mode, with a total travel range of 4 mm in coarse mode.

- A homemade metal piece with axial rotation freedom was screwed to one side of the microblock stage to enable the axial rotation of the tip. This was useful when the picked nanowire was stuck to a side of the tungsten tip that was not the bottom one.

- A SUSS Microtek probe station tip holder was screwed to the center of the rotating metal piece.

- On the tip holder, an American Probe tungsten tip (diameter at the sharpest edge = 350 nm) was secured.

Figure A.11 shows a picture of the micromanipulator at current status, with all its main parts indicated.

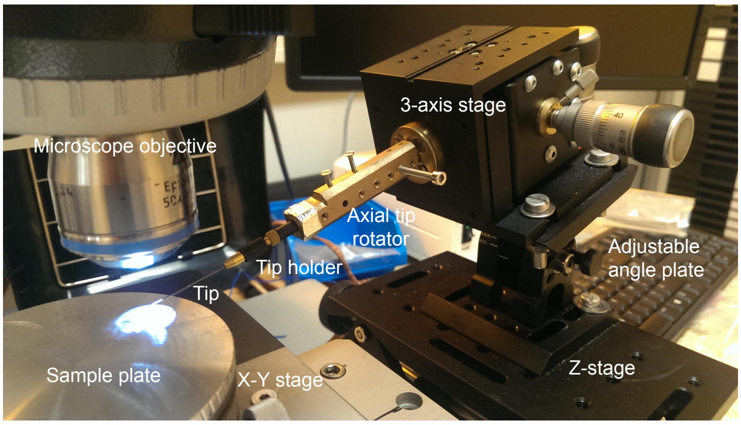

Figure A.11: Picture of the micromanipulator. Parts are indicated in white.

A Zeiss optical microscope with x50 magnification and long working distance (0.55 cm), equipped with a CDD camera, was used for observing the manipulation of the nanowire. The base of the microscope was screwed to the same heavy plate where the mechanical arm previously described was screwed. Even though the smaller nanowires that I deposited had a diameter of 60 nm and a length of a few micrometers, individual nanowires could be discerned at this magnification.

The microscope was equipped with its own X-Y stage of in-plane motion. This was sufficient for switching between the nanowire growth substrate for picking a nanowire and the chip with gates for depositing the nanowire.

Description of the process of nanowire deposition

Nanowire deposition is a kind of art that requires patience, calmness and a steady arm. It is aided by a low-vibration environment. Each substrate of nanowires that I deposited required a different technique (due to different density of nanowires and different nanowire length/diameter). In this subsection I will describe what steps are needed in general, and what are the particularities of the two most common cases that I encountered: low density, large diameter and short length nanowires (i.e. InSb nanowires; which I will call *the scarce type*), and large density / medium diameter and long length nanowires (i.e. InAs nanowires; which I will call *the bundle type*).

As explained in the introduction of this section, nanowire deposition entails the picking of a nanowire with a tugnsten tip and its deposition on a substrate with gates. The process in more detail is the following:

1. First of all, check the tip for its cleanliness and suitability. On one hand, a dirty tip will prevent nanowire sticking. If this is the case, it can sometimes be cleaned in acetone under ultrasound. On the other hand, a tip that is not sharp enough (round shape as opposed to an ideal conical shape) will not allow picking an individual nanowire.

2. Once you are sure the tip is in good conditions, focus the microscope on the nanowire growth substrate. At at x50 magnification, you will only see a field of a few micrometers across. The way to proceed from this point varies depending on the type of nanowire growth substrate you have.

   Scarce type. Once you identify a suitable nanowire -still standing, as opposed to toppled-, you can gently lower the tip until you reach it. I recommend you to switch focus between the tip and the growth substrate to see how far is your tip from the substrate. The nanowire will stick without touching the substrate, since the tilt angle of the tip with respect to the substrate plane ensures that only its lowest point will touch the nanowire. If after a few tries, not a single nanowire has stuck to the tip, then it is time to rotate the tip by its axis, to try better luck with another side. I typically rotate the tip by 90° and retry.

   Bundle type. In this case, after gently lowering the tip until it nearly touches the substrate, it needs to be scanned on the plane of the substrate until a bundle of nanowires adheres [2].

3. Once the nanowire(s), is (are) picked, the tip is raised, in order to safely switch position from the growth substrate to the gates chip -which are not necessarily at the same height.

4. Focus on the gate field that you want to target. The x50 magnification allows you to see the whole writing field plus a small section of the bonding pads. Focus again on the tip to be sure that it is still where you think it is, and to get a feeling of the distance that separates it from the gate field.

5. Start lowering gently the tip until you see its unfocused image. Then, select a good landing spot in one of the 1.3 µm gate fields, and lower the tip very gently until you touch the

---

[2] In a large density growth substrate, the nanowires cannot be picked individually.

substrate. Since the tip is roughly of the same size as the field gate, do not expect a lot of precision in positioning in the first try.

6. After deposition, the angle of the nanowire with respect to the gates can be controlled by rubbing the tip along the axis of the nanowire. This will slightly change its position as well. Although this is valid for both types of nanowires, the *Bundle type*, since it consists of a spaghetti-type bundle of nanowires, first needs to be dispersed in the writing field. This is done by scratching the tip in a direction perpendicular to the bundle, starting on its center. In principle, the mere fact of touching the bundle on its center with the tugnsten tip while it is laying on the gates chip will suffice to disentangle it slightly, but a more energetic scratching may be needed for obtaining single nanowires in different gate fields. Unfortunately, this may also scratch the dielectric off the gates and deposit dirt from the tugnsten tip, as well as from the nanowires themselves (gold seeds, pieces of growth substrate, broken nanowire segments, etc.).

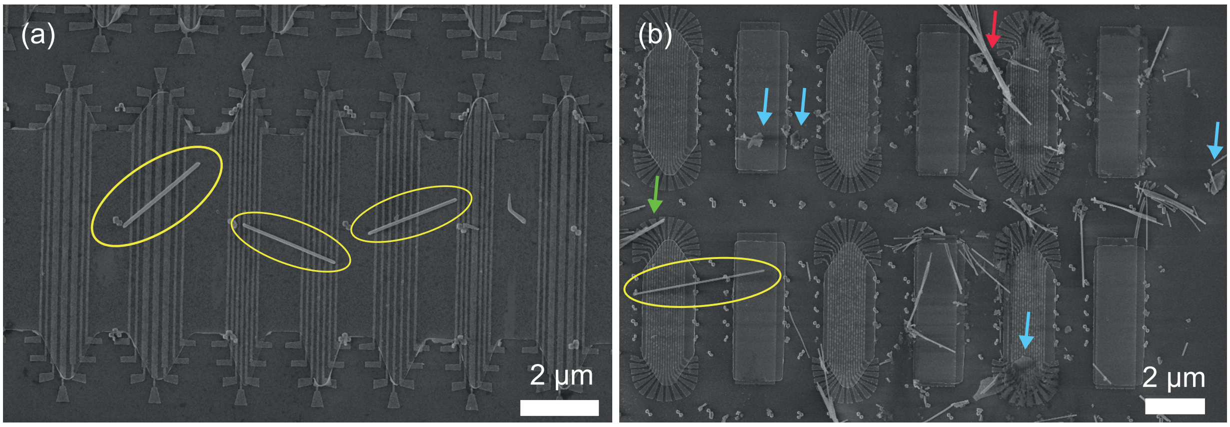

Figure A.12: SEM images of the final result of nanowire deposition for two types of growth substrate. **(a)** *Scarce type*. The low density of InSb nanowires allows to place them individually in a gate field. Three suitable nanowires for contacting are encircled in yellow. **(b)** *Bundle type*. InAs Nanowire bundles (red arrow) must be dispersed for placing individual nanowires on gate fields, leaving behind residues from the tip (light-blue arrows) and hundreds of extra nanowires. These extra nanowires must be avoided because they can short-circuit or break contacts. Sometimes, they can also short-circuit adjacent gates (green arrow). Occasionally, the surface of the substrate will be scratched in the effort of dispersing a bundle, removing alignment marks and damaging gates. A suitable nanowire for contacting is encircled in yellow.

Figure A.12 shows SEM images of examples of the result of nanowire deposition for both the scarce and the bundle type. With a growth substrate containing nanowires of the scarce type, a writing field can be populated with less than ten nanowires. This is impossible to achieve with a growth substrate of the bundle type. After a deposition of this type of wires, I typically had writing fields filled with a few hundreds of nanowires. As we will see in the next section, the design of contact leads in the latter case is much more complicated, because nanowires in excess can short-circuit or break contacts -and gates- and must be avoided.

A.3 Contact patterning

In a nanowire Josephson junction, the contacting of the nanowire and the local bottom gates -and, sometimes, the fabrication of side gates- are all done in one processing step, for simplicity. The fabrication involves a lift-off process as the one shown in Figure A.3. First, a bi-layer of PMMA 4% (in ethyl lactate) 250 KDa and PMMA 4% (in ethyl lactate) 950 KDa is spin-coated on the chip. Each layer is baked at 180 °C after it has been deposited. Then, the resist is exposed by electron beam lithography at a dose of 1700 $\mu C/cm^2$ and a current of 1 nA. Later on, the sample is developed on MibK/Isopropanol 1:3 for 30 seconds followed by Isopropanol rinsing during 60 seconds.

Following development, and before metal deposition, the sample is subjected to in-situ Argon ion etching at an angle of 90° to the substrate at 250 V for 45 seconds for removal of the native oxide of the nanowires -without substrate rotation. Surprisingly, the same conditions give a good contact resistance for both InAs and InSb nanowires.

However, the Argon etching disturbs greatly the surface of the nanowire below the oxide. Figure A.13 shows two SEM images of InSb nanowires after being bombarded with Ar ions during 150 seconds at 250 V. For this test, electron beam lithography was performed to have resist windows along sections of the nanowires in which the Argon etching would be effective, while covering the rest of the nanowire for an effective comparison. After the etching, the resist was removed with acetone. In these SEM images, the surface of the nanowire appears damaged in the sections uncovered by resist.

After Argon etching comes in-situ metal deposition. Since the refractory metals Nb, Ta and V are rather sensitive to vacuum conditions and rate deposition -both parameters being specially critical for Nb underlayers-, I deposited these metals at a high vacuum of 1×10^{-7} mbar and relatively high rate depositions of 0.75 nm/s for the 5 nm underlayer Nb films and 0.5 nm/s for Ta. Al and Au contacts were deposited at standard conditions of 1×10^{-6} mbar and rate depositions which vary between 0.1 nm/s for layers below a 10 nm thickness to 0.5 nm/s for layers above that.

After metal deposition, I immerse the sample in hot acetone (T = 40 °C) for 1 hour and then leave it overnight in the solvent at room temperature for lift-off. The temperature is chosen to accelerate the reaction of the solvent with the resist. After this step, the sample is ready to be tested.

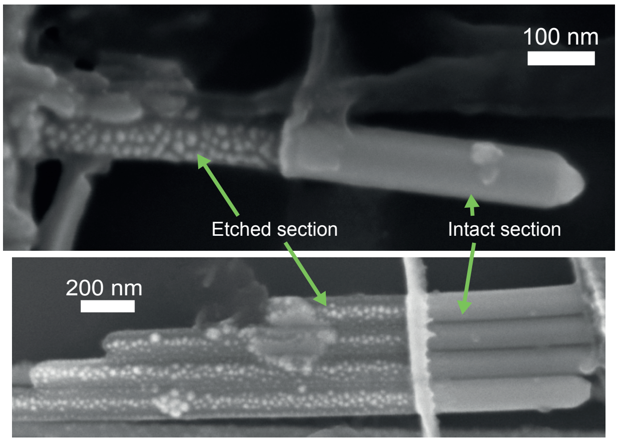

Figure A.13: SEM images of the outcome of Argon etching on InSb nanowires, after 150 seconds of exposure to a 250 V Ar ion beam. The non-etched section of the nanowire appears pristine, while the etched section is populated by grains. These grains could be In islands [135].

A.4 Testing and bonding of the chip

Once the chip has left the cleanroom [3], I test it in a probe station (SUSS Microtek) at room temperature to determine the resistance of each nanowire junction, with a 100 kΩ resistance in series for protecting the nanowire from sudden discharges. Since neither InAs nor InSb nanowires showed a strong and consistent gate effect at room temperature, I did not systematically measure the gate effect.

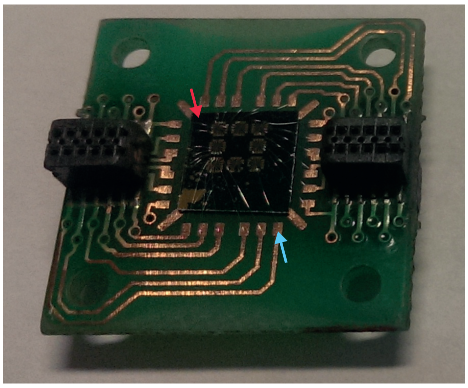

Figure A.14: Picture of a chip (red arrow) bonded to a chip carrier. The light-blue arrow points to one of the twenty-four bonding pads of the chip carrier.

After testing, a few devices with the lowest resistances -typically below 10 kΩ- were selected for bonding. I also checked gate leakage in these devices as another way to discriminate the ones to be bonded from the ones to be discarded.

---

[3] If the chip was not going to be immediately tested, I kept it inside of a vacuum box to protect the nanowire and the contacts from dust and oxidation.

Before bonding, the chip was first glued with silver paste to a homemade chip carrier with twenty-four available bonding pads. Figure A.14 shows a picture of the chip carrier with a sample glued and bonded to it. The chip carrier comes with a removable shunt that short-circuits the twenty-four pads, thus keeping them at the same potential and avoiding transient currents that may damage the devices. Bonding is done with a standard wedge-bonding machine. To protect the nanowires -once again- from sudden discharges, I ground myself but I keep the sample floating during the bonding procedure. For the same reason, once I bond the sample to the chip carrier, I immediately place it in a Faraday-cage box while keeping myself grounded. Given that nanowires cannot withstand large current densities due to their nanometric size, each of these precautions is absolutely necessary.

Right after bonding, I plug the device in the cryostat which will be used. Four cryostats were used in this thesis: 1) a 4K dipstick; 2) a He 3 refrigerator with 250 - 330 mK base temperature and equipped with a 9 T coil; 3) a He 3 refrigerator with a 3 T split-coil and 250 - 300 mK base temperature; and 4) a dilution refrigerator with a 15 mK base temperature and a 2-axis vector magnet (3 T and 9 T). Pumping of the cryostat is carried overnight or over the weekend, to remove absorbants from the surface of the devices [132].

References

[1] V. Mourik, K. Zuo, S. M. Frolov, S. R. Plissard, E. P. a. M. Bakkers, and L. P. Kouwenhoven. Signatures of Majorana Fermions in. Science, 336(6084):1003, 2012.

[2] MT Deng, S Vaitiekėnas, EB Hansen, J Danon, M Leijnse, K Flensberg, J Nygård, P Krogstrup, and CM Marcus. Majorana bound state in a coupled quantum-dot hybrid-nanowire system. Science, 354(6319):1557–1562, 2016.

[3] Jason Alicea, Yuval Oreg, Gil Refael, Felix Von Oppen, and Matthew PA Fisher. Non-abelian statistics and topological quantum information processing in 1d wire networks. Nature Physics, 7(5):412–417, 2011.

[4] Yuval Oreg, Gil Refael, and Felix Von Oppen. Helical liquids and Majorana bound states in quantum wires. Phys. Rev. Lett., 105(17):1–4, 2010.

[5] Ettore Majorana and Luciano Maiani. A symmetric theory of electrons and positrons. In Ettore Majorana Scientific Papers, pages 201–233. Springer, 2006.

[6] Werner Rodejohann. Neutrino-less double beta decay and particle physics. International Journal of Modern Physics E, 20(09):1833–1930, 2011.

[7] Frank Wilczek. Majorana returns. Nature Physics, 5(9):614–618, 2009.

[8] A Yu Kitaev. Unpaired majorana fermions in quantum wires. Physics-Uspekhi, 44(10S):131, 2001.

[9] Tudor D Stanescu, Roman M Lutchyn, and S Das Sarma. Majorana fermions in semiconductor nanowires. Physical Review B, 84(14):144522, 2011.

[10] Benoit Voisin, Viet-Hung Nguyen, Julien Renard, Xavier Jehl, Sylvain Barraud, Franccois Triozon, Maud Vinet, Ivan Duchemin, Yann-Michel Niquet, Silvano De Franceschi, and Marc Sanquer. Few-electron edge-state quantum dots in a silicon nanowire field-effect transistor. Nano letters, 14(4):2094–2098, 2014.

[11] Eduardo JH Lee, Xiaocheng Jiang, Ramón Aguado, Georgios Katsaros, Charles M Lieber, and Silvano De Franceschi. Zero-bias anomaly in a nanowire quantum dot coupled to superconductors. Physical review letters, 109(18):186802, 2012.

[12] Eduardo JH Lee, Xiaocheng Jiang, Manuel Houzet, Ramón Aguado, Charles M Lieber, and Silvano De Franceschi. Spin-resolved andreev levels and parity crossings in hybrid superconductor-semiconductor nanostructures. Nature nanotechnology, 9(1):79–84, 2014.

[13] Yuval Oreg, Eran Sela, and Ady Stern. Fractional helical liquids in quantum wires. Physical Review B, 89(11):115402, 2014.

[14] A Srinivasan, KL Hudson, D Miserev, LA Yeoh, O Klochan, K Muraki, Y Hirayama, OP Sushkov, and AR Hamilton. Electrical control of the sign of the g factor in a gaas hole quantum point contact. Physical Review B, 94(4):041406, 2016.

[15] Supriyo Datta. Electronic transport in mesoscopic systems. Cambridge university press, 1997.

[16] JM Krans, CJ Muller, IK Yanson, Th CM Govaert, R Hesper, and JM Van Ruitenbeek. One-atom point contacts. Physical Review B, 48(19):14721, 1993.

[17] JM Krans, JM Van Ruitenbeek, VV Fisun, IK Yanson, and LJ De Jongh. The signature of conductance quantization in metallic point contacts. Nature, 375(6534):767, 1995.

[18] B. J. Van Wees, H. Van Houten, C. W J Beenakker, J. G. Williamson, L. P. Kouwenhoven, D. Van Der Marel, and C. T. Foxon. Quantized conductance of point contacts in a two-dimensional electron gas. Phys. Rev. Lett., 60(9):848–850, 1988.

[19] Jakob Kammhuber, Maja C. Cassidy, Hao Zhang, Önder Gül, Fei Pei, Michiel W. A. de Moor, Bas Nijholt, Kenji Watanabe, Takashi Taniguchi, Diana Car, Sébastien R. Plissard, Erik P. A. M. Bakkers, and Leo P. Kouwenhoven. Conductance Quantization at Zero Magnetic Field in InSb Nanowires. Nano Letters, page acs.nanolett.6b00051, 2016.

[20] Ilse van Weperen, Sébastien R. Plissard, Erik P. A. M. Bakkers, Sergey M. Frolov, and Leo P. Kouwenhoven. Quantized conductance in an insb nanowire. Nano Letters, 13(2):387–391, 2013. PMID: 23259576.

[21] Simon Abay, Daniel Persson, Henrik Nilsson, H. Q. Xu, Mikael Fogelström, Vitaly Shumeiko, and Per Delsing. Quantized conductance and its correlation to the supercurrent in a nanowire connected to superconductors. Nano Letters, 13(8):3614–3617, 2013. PMID: 23898893.

[22] Florian Vigneau, Önder Gül, Yann-Michel Niquet, Diana Car, Sebastien R Plissard, Walter Escoffier, Erik PAM Bakkers, Ivan Duchemin, Bertrand Raquet, and Michel Goiran. Revealing the band structure of insb nanowires by high-field magnetotransport in the quasiballistic regime. Physical Review B, 94(23):235303, 2016.

[23] Florian Vigneau, Vladimir Prudkovkiy, Ivan Duchemin, Walter Escoffier, Philippe Caroff, Yann-Michel Niquet, Renaud Leturcq, Michel Goiran, and Bertrand Raquet. Magnetotransport subband spectroscopy in inas nanowires. Physical review letters, 112(7):076801, 2014.

[24] AP Micolich. What lurks below the last plateau: experimental studies of the 0.7× 2e2/h conductance anomaly in one-dimensional systems. Journal of Physics: Condensed Matter, 23(44):443201, 2011.

[25] S. M. Cronenwett, H. J. Lynch, D. Goldhaber-Gordon, L. P. Kouwenhoven, C. M. Marcus, K. Hirose, N. S. Wingreen, and V. Umansky. Low-temperature fate of the 0.7 structure in a point contact: A kondo-like correlated state in an open system. Phys. Rev. Lett., 88:226805, May 2002.

[26] MJ Iqbal, Roi Levy, EJ Koop, JB Dekker, JP De Jong, JHM van der Velde, D Reuter, AD Wieck, Ramón Aguado, Yigal Meir, et al. Odd and even kondo effects from emergent localization in quantum point contacts. Nature, 501(7465):79–83, 2013.

[27] Boris Brun, Frederico Martins, Sebastien Faniel, Benoit Hackens, Guillaume Bachelier, Antonella Cavanna, Christian Ulysse, Abdelkarim Ouerghi, Ulf Gennser, Dominique Mailly, et al. Wigner and kondo physics in quantum point contacts revealed by scanning gate microscopy. Nature communications, 5, 2014.

[28] Jan Heyder, Florian Bauer, Enrico Schubert, David Borowsky, Dieter Schuh, Werner Wegscheider, Jan Von Delft, and Stefan Ludwig. Relation between the 0.7 anomaly and the Kondo effect: Geometric crossover between a quantum point contact and a Kondo quantum dot. Physical Review B, 92(19), 2015.

[29] Yigal Meir, Kenji Hirose, and Ned S Wingreen. Kondo model for the "0.7 anomaly" in transport through a quantum point contact. Phys. Rev. Lett., 89(19):196802, 2002.

[30] P Středa and P Šeba. Antisymmetric spin filtering in one-dimensional electron systems with uniform spin-orbit coupling. Physical review letters, 90(25):256601, 2003.

[31] Yuriy V Pershin, James A Nesteroff, and Vladimir Privman. Effect of spin-orbit interaction and in-plane magnetic field on the conductance of a quasi-one-dimensional system. Physical Review B, 69(12):121306, 2004.

[32] Diego Rainis and Daniel Loss. Conductance behavior in nanowires with spin-orbit interaction: A numerical study. Physical Review B, 90(23):235415, 2014.

[33] Jakob Kammhuber, Maja C Cassidy, Fei Pei, Michal P Nowak, Adriaan Vuik, Diana Car, Sèbastien R Plissard, Erik PAM Bakkers, Michael Wimmer, and Leo P Kouwenhoven. Conductance through a helical state in an insb nanowire. arXiv preprint arXiv:1701.06878, 2017.

[34] CHL Quay, TL Hughes, JA Sulpizio, LN Pfeiffer, KW Baldwin, KW West, D Goldhaber-Gordon, and R De Picciotto. Observation of a one-dimensional spin–orbit gap in a quantum wire. Nature Physics, 6(5):336–339, 2010.

[35] Leo P Kouwenhoven, Charles M Marcus, Paul L McEuen, Seigo Tarucha, Robert M Westervelt, and Ned S Wingreen. Electron transport in quantum dots. In Mesoscopic electron transport, pages 105–214. Springer, 1997.

[36] Ronald Hanson, Leo P Kouwenhoven, Jason R Petta, Seigo Tarucha, and Lieven MK Vandersypen. Spins in few-electron quantum dots. Reviews of Modern Physics, 79(4):1217, 2007.

[37] S De Franceschi, S Sasaki, JM Elzerman, WG Van Der Wiel, S Tarucha, and Leo P Kouwenhoven. Electron cotunneling in a semiconductor quantum dot. Physical review letters, 86(5):878, 2001.

[38] D Goldhaber-Gordon, Hadas Shtrikman, D Mahalu, David Abusch-magder, U Meirav, and M A Kastner. Kondo effect in a single-electron transistor. Nature, 391(January):1996–1999, 1998.

[39] WG Van der Wiel, S De Franceschi, T Fujisawa, JM Elzerman, S Tarucha, and LP Kouwenhoven. The kondo effect in the unitary limit. Science, 289(5487):2105–2108, 2000.

[40] Ania C Bleszynski, Floris A Zwanenburg, RM Westervelt, Aarnoud L Roest, Erik PAM Bakkers, and Leo P Kouwenhoven. Scanned probe imaging of quantum dots inside inas nanowires. Nano Letters, 7(9):2559–2562, 2007.

[41] I Shorubalko, A Pfund, R Leturcq, MT Borgström, F Gramm, E Müller, E Gini, and K Ensslin. Tunable few-electron quantum dots in inas nanowires. Nanotechnology, 18(4):044014, 2006.

[42] Karl Weis, Stephan Wirths, Andreas Winden, Kamil Sladek, Hilde Hardtdegen, Hans Lüth, Detlev Grützmacher, and Thomas Schäpers. Quantum dots in inas nanowires induced by surface potential fluctuations. Nanotechnology, 25(13):135203, 2014.

[43] Jesper Wallentin, Martin Ek, L Reine Wallenberg, Lars Samuelson, and Magnus T Borgstrom. Electron trapping in inp nanowire fets with stacking faults. Nano letters, 12(1):151–155, 2011.

[44] Mikael T Björk, Claes Thelander, Adam E Hansen, Linus E Jensen, Magnus W Larsson, L Reine Wallenberg, and Lars Samuelson. Few-electron quantum dots in nanowires. Nano Letters, 4(9):1621–1625, 2004.

[45] Stefano Roddaro, Andrea Pescaglini, Daniele Ercolani, Lucia Sorba, and Fabio Beltram. Manipulation of electron orbitals in hard-wall inas/inp nanowire quantum dots. Nano letters, 11(4):1695–1699, 2011.

[46] JWG Van den Berg, S Nadj-Perge, VS Pribiag, SR Plissard, EPAM Bakkers, SM Frolov, and LP Kouwenhoven. Fast spin-orbit qubit in an indium antimonide nanowire. Physical review letters, 110(6):066806, 2013.

[47] S Nadj-Perge, SM Frolov, EPAM Bakkers, and Leo P Kouwenhoven. Spin-orbit qubit in a semiconductor nanowire. Nature, 468(7327):1084–1087, 2010.

[48] Sami Sapmaz, Pablo Jarillo-Herrero, Leo P Kouwenhoven, and Herre SJ van der Zant. Quantum dots in carbon nanotubes. Semiconductor science and technology, 21(11):S52, 2006.

[49] Neil P Dasgupta, Jianwei Sun, Chong Liu, Sarah Brittman, Sean C Andrews, Jongwoo Lim, Hanwei Gao, Ruoxue Yan, and Peidong Yang. 25th anniversary article: semiconductor nanowires–synthesis, characterization, and applications. Advanced materials, 26(14):2137–2184, 2014.

[50] Yue Wu, Jie Xiang, Chen Yang, Wei Lu, and Charles M Lieber. Single-crystal metallic nanowires and metal/semiconductor nanowire heterostructures. Nature, 430(6995):61–65, 2004.

[51] Ke Xu and James R Heath. Long, highly-ordered high-temperature superconductor nanowire arrays. Nano letters, 8(11):3845–3849, 2008.

[52] L Mohaddes-Ardabili, H Zheng, SB Ogale, B Hannoyer, W Tian, J Wang, SE Lofland, SR Shinde, T Zhao, Y Jia, et al. Self-assembled single-crystal ferromagnetic iron nanowires formed by decomposition. Nature Materials, 3(8):533–538, 2004.

[53] Oliver Hayden, Ritesh Agarwal, and Wei Lu. Semiconductor nanowire devices. Nano Today, 3(5):12–22, 2008.

[54] Feng Chen, Hongquan Jiang, Arnold M Kiefer, Anna M Clausen, Yuk-Hong Ting, Amy E Wendt, Bingjun Ding, and Max G Lagally. Fabrication of ultrahigh-density nanowires by electrochemical nanolithography. Nanoscale research letters, 6(1):444, 2011.

[55] WuXia Li, Jun Zhang, TieHan Shen, Grenville A Jones, and Philip J Grundy. Magnetic nanowires fabricated by anodic aluminum oxide template—a brief review. Science China Physics, Mechanics and Astronomy, 54(7):1181–1189, 2011.

[56] Yat Li, Fang Qian, Jie Xiang, and Charles M Lieber. Nanowire electronic and optoelectronic devices. Materials today, 9(10):18–27, 2006.

[57] John Bardeen. Surface states and rectification at a metal semi-conductor contact. Physical Review, 71(10):717, 1947.

[58] TC McGill and DA Collins. Prospects for the future of narrow bandgap materials. Semiconductor Science and Technology, 8(1S):S1, 1993.

[59] Neil W Ashcroft and N David Mermin. Solid state physics (holt, rinehart and winston, new york, 1976). page 403, 2005.

[60] William Shockley and GL Pearson. Modulation of conductance of thin films of semiconductors by surface charges. Physical Review, 74(2):232, 1948.

[61] Hideo Kosaka, Andrey A Kiselev, Filipp A Baron, Ki Wook Kim, and Eli Yablonovitch. Electron g factor engineering in ili-v semiconductors for quantum communications. Electronics Letters, 37(7):464–465, 2001.

[62] S Csonka, L Hofstetter, F Freitag, S Oberholzer, C Schonenberger, Thomas Sand Jespersen, Martin Aagesen, and Jesper Nygård. Giant fluctuations and gate control of the g-factor in inas nanowire quantum dots. Nano letters, 8(11):3932–3935, 2008.

[63] Henrik A Nilsson, Philippe Caroff, Claes Thelander, Marcus Larsson, Jakob B Wagner, Lars-Erik Wernersson, Lars Samuelson, and HQ Xu. Giant, level-dependent g factors in insb nanowire quantum dots. Nano letters, 9(9):3151–3156, 2009.

[64] B Odom, D Hanneke, B d'Urso, and G Gabrielse. New measurement of the electron magnetic moment using a one-electron quantum cyclotron. Physical Review Letters, 97(3):030801, 2006.

[65] S Nadj-Perge, VS Pribiag, JWG Van den Berg, K Zuo, SR Plissard, EPAM Bakkers, SM Frolov, and LP Kouwenhoven. Spectroscopy of spin-orbit quantum bits in indium antimonide nanowires. Physical review letters, 108(16):166801, 2012.

[66] S Heedt, N Traverso Ziani, F Crépin, W Prost, J Schubert, D Grützmacher, B Trauzettel, Th Schäpers, et al. Signatures of interaction-induced helical gaps in nanowire quantum point contacts. Nature Physics, 2017.

[67] I Van Weperen, B Tarasinski, D Eeltink, VS Pribiag, SR Plissard, EPAM Bakkers, LP Kouwenhoven, and M Wimmer. Spin-orbit interaction in insb nanowires. Physical Review B, 91(20):201413, 2015.

[68] C. Fasth, A. Fuhrer, L. Samuelson, Vitaly N. Golovach, and Daniel Loss. Direct measurement of the spin-orbit interaction in a two-electron inas nanowire quantum dot. Phys. Rev. Lett., 98:266801, Jun 2007.

[69] Mircea Trif, Vitaly N Golovach, and Daniel Loss. Spin dynamics in inas nanowire quantum dots coupled to a transmission line. Physical Review B, 77(4):045434, 2008.

[70] Shunta Maeda, Satoru Miyamoto, Mohammad H Fauzi, Katsumi Nagase, Ken Sato, and Yoshiro Hirayama. Fabry-pérot interference in a triple-gated quantum point contact. Applied Physics Letters, 109(14):143509, 2016.

[71] HA Nilsson, MT Deng, Philippe Caroff, Claes Thelander, Lars Samuelson, L-E Wernersson, and HQ Xu. Insb nanowire field-effect transistors and quantum-dot devices. IEEE Journal of Selected Topics in Quantum Electronics, 17(4):907–914, 2011.

[72] MD Schroer and JR Petta. Correlating the nanostructure and electronic properties of inas nanowires. Nano letters, 10(5):1618–1622, 2010.

[73] Gregory W Holloway, Chris M Haapamaki, Paul Kuyanov, Ray R LaPierre, and Jonathan Baugh. Electrical characterization of chemical and dielectric passivation of inas nanowires. Semiconductor Science and Technology, 31(11):114004, 2016.

[74] Gregory W Holloway, Yipu Song, Chris M Haapamaki, Ray R LaPierre, and Jonathan Baugh. Trapped charge dynamics in inas nanowires. Journal of Applied Physics, 113(2):024511, 2013.

[75] Joe Salfi, Nicola Paradiso, Stefano Roddaro, Stefan Heun, Selvakumar V Nair, Igor G Savelyev, Marina Blumin, Fabio Beltram, and Harry E Ruda. Probing the gate- voltage-dependent surface potential of individual inas nanowires using random telegraph signals. ACS nano, 5(3):2191–2199, 2011.

[76] Michael Tinkham. Introduction to superconductivity. Courier Corporation, 1996.

[77] B Pannetier and H Courtois. Andreev reflection and proximity effect. Journal of low temperature physics, 118(5-6):599–615, 2000.

[78] Yasushi Nagato, Katsuhiko Nagai, and Jun'ichiro Hara. Theory of the andreev reflection and the density of states in proximity contact normal-superconducting infinite double-layer. Journal of low temperature physics, 93(1):33–56, 1993.

[79] N Moussy, H Courtois, and B Pannetier. Local spectroscopy of a proximity superconductor at very low temperature. EPL (Europhysics Letters), 55(6):861, 2001.

[80] S Guéron, H Pothier, Norman O Birge, D Esteve, and MH Devoret. Superconducting proximity effect probed on a mesoscopic length scale. Physical review letters, 77(14):3025, 1996.

[81] GE Blonder, M Tinkham, and TM Klapwijk. Transition from metallic to tunneling regimes in superconducting microconstrictions: Excess current, charge imbalance, and supercurrent conversion. Physical Review B, 25(7):4515, 1982.

[82] So Takei, Benjamin M Fregoso, Hoi-Yin Hui, Alejandro M Lobos, and S Das Sarma. Soft superconducting gap in semiconductor majorana nanowires. Physical review letters, 110(18):186803, 2013.

[83] Hao Zhang, Önder Gül, Sonia Conesa-Boj, Kun Zuo, Vincent Mourik, Folkert K de Vries, Jasper van Veen, David J van Woerkom, Michał P Nowak, Michael Wimmer, et al. Ballistic majorana nanowire devices. arXiv preprint arXiv:1603.04069, 2016.

[84] Önder Gül, Hao Zhang, Folkert K de Vries, Jasper van Veen, Kun Zuo, Vincent Mourik, Sonia Conesa-Boj, Michał P Nowak, David J van Woerkom, Marina Quintero-Pérez, et al. Hard superconducting gap in insb nanowires. arXiv preprint arXiv:1702.02578, 2017.

[85] W Chang, SM Albrecht, TS Jespersen, Ferdinand Kuemmeth, Peter Krogstrup, J Nygård, and CM Marcus. Hard gap in epitaxial semiconductor–superconductor nanowires. Nature nanotechnology, 10(3):232–236, 2015.

[86] Silvano De Franceschi, Leo Kouwenhoven, Christian Schönenberger, and Wolfgang Wernsdorfer. Hybrid superconductor-quantum dot devices. Nature Nanotechnology, 5(10):703–711, 2010.

[87] Jong Soo Lim, Rosa López, Ramón Aguado, et al. Shiba states and zero-bias anomalies in the hybrid normal-superconductor anderson model. Physical Review B, 91(4):045441, 2015.

[88] RS Deacon, Yoichi Tanaka, A Oiwa, R Sakano, K Yoshida, K Shibata, K Hirakawa, and S Tarucha. Tunneling spectroscopy of andreev energy levels in a quantum dot coupled to a superconductor. Physical review letters, 104(7):076805, 2010.

[89] Eduardo JH Lee, Xiaocheng Jiang, Rok Zitko, Ramon Aguado, Charles M Lieber, and Silvano De Franceschi. Scaling of sub-gap excitations in a superconductor-semiconductor nanowire quantum dot. arXiv preprint arXiv:1609.07582, 2016.

[90] J-D Pillet, P Joyez, MF Goffman, et al. Tunneling spectroscopy of a single quantum dot coupled to a superconductor: From kondo ridge to andreev bound states. Physical Review B, 88(4):045101, 2013.

[91] Brian Møller Andersen, Karsten Flensberg, Verena Koerting, and Jens Paaske. Nonequilibrium transport through a spinful quantum dot with superconducting leads. Physical review letters, 107(25):256802, 2011.

[92] JD Pillet, CHL Quay, P Morfin, C Bena, A Levy Yeyati, and P Joyez. Andreev bound states in supercurrent-carrying carbon nanotubes revealed. Nature Physics, 6(12):965–969, 2010.

[93] Bum-Kyu Kim, Ye-Hwan Ahn, Ju-Jin Kim, Mahn-Soo Choi, Myung-Ho Bae, Kicheon Kang, Jong Soo Lim, Rosa López, and Nam Kim. Transport measurement of andreev bound states in a kondo-correlated quantum dot. Physical review letters, 110(7):076803, 2013.

[94] Pablo Jarillo-Herrero, Jorden A Van Dam, and Leo P Kouwenhoven. Quantum supercurrent transistors in carbon nanotubes. Nature, 439(7079):953–956, 2006.

[95] Jorden a van Dam, Yuli V Nazarov, Erik P a M Bakkers, Silvano De Franceschi, and Leo P Kouwenhoven. Supercurrent reversal in quantum dots. Nature, 442(7103):667–670, 2006.

[96] Romain Maurand, Tobias Meng, Edgar Bonet, Serge Florens, Laëtitia Marty, and Wolfgang Wernsdorfer. First-order 0-π quantum phase transition in the kondo regime of a superconducting carbon-nanotube quantum dot. Physical Review X, 2(1):1–11, 2012.

[97] CWJ Beenakker and H Van Houten. Josephson current through a superconducting quantum point contact shorter than the coherence length. Physical review letters, 66(23):3056, 1991.

[98] MT Deng, CL Yu, GY Huang, M Larsson, P Caroff, and HQ Xu. Parity independence of the zero-bias conductance peak in a nanowire based topological superconductor-quantum dot hybrid device. Scientific Reports, 4:7261, 2014.

[99] L Martin-Moreno, JT Nicholls, NK Patel, and M Pepper. Non-linear conductance of a saddle-point constriction. Journal of Physics: Condensed Matter, 4(5):1323, 1992.

[100] Craig E Pryor and Michael E Flatté. Landé g factors and orbital momentum quenching in semiconductor quantum dots. Physical review letters, 96(2):026804, 2006.

[101] Yinlong Sun and George Kirczenow. Energy level locking in quantum conductors. Physical review letters, 72(15):2450, 1994.

[102] Ji-Rong Shi and Ben-Yuan Gu. Magnetoconductance oscillations of two parallel quantum wires coupledthrough a potential barrier. Physical Review B, 55(15):9941, 1997.

[103] SK Lyo. Magnetic quenching of back scattering in coupled double quantum wires: giant mobility enhancement. Journal of Physics: Condensed Matter, 8(46):L703, 1996.

[104] SF Fischer, G Apetrii, U Kunze, D Schuh, and G Abstreiter. Energy spectroscopy of controlled coupled quantum-wire states. Nature Physics, 2(2):91–96, 2006.

[105] SF Fischer, G Apetrii, U Kunze, D Schuh, and G Abstreiter. Magnetotransport spectroscopy of spatially coincident coupled electron waveguides. Physical Review B, 71(19):195330, 2005.

[106] Anindya Das, Yuval Ronen, Yonatan Most, Yuval Oreg, Moty Heiblum, and Hadas Shtrikman. Zero-bias peaks and splitting in an al-inas nanowire topological superconductor as a signature of majorana fermions. Nature Physics, 8(12):887–895, 2012.

[107] W Chang, VE Manucharyan, Thomas Sand Jespersen, Jesper Nygård, and Charles M Marcus. Tunneling spectroscopy of quasiparticle bound states in a spinful josephson junction. Physical review letters, 110(21):217005, 2013.

[108] ST Gill, J Damasco, D Car, EPAM Bakkers, and N Mason. Hybrid superconductor-quantum point contact devices using insb nanowires. Applied Physics Letters, 109(23):233502, 2016.

[109] HA Nilsson, Peter Samuelsson, Philippe Caroff, and HQ Xu. Supercurrent and multiple andreev reflections in an insb nanowire josephson junction. Nano letters, 12(1):228–233, 2011.

[110] H. Ingerslev Jörgensen, T. Novotný, K. Grove-Rasmussen, K. Flensberg, and P. E. Lindelof. Critical current 0-?? transition in designed josephson quantum dot junctions. Nano Letters, 7(8):2441–2445, 2007.

[111] Nikolai M Chtchelkatchev, Gordey B Lesovik, and Gianni Blatter. Supercurrent quantization in narrow-channel superconductor–normal-metal–superconductor junctions. Physical Review B, 62(5):3559, 2000.

[112] Jie Xiang, Andy Vidan, Michael Tinkham, Robert M Westervelt, and Charles M Lieber. Ge/si nanowire mesoscopic josephson junctions. Nature nanotechnology, 1(3):208–213, 2006.

[113] S Li, N Kang, DX Fan, LB Wang, YQ Huang, P Caroff, and HQ Xu. Coherent charge transport in ballistic insb nanowire josephson junctions. Scientific reports, 6, 2016.

[114] PM Tedrow and R Meservey. Spin-dependent electron tunneling in superconducting vanadium and vanadium-titanium thin films. Physics Letters A, 69(4):285–286, 1978.

[115] BJ Van Wees, P De Vries, P Magnée, and TM Klapwijk. Excess conductance of superconductor-semiconductor interfaces due to phase conjugation between electrons and holes. Physical review letters, 69(3):510, 1992.

[116] LI Glazman and KA Matveev. Resonant josephson current through kondo impurities in a tunnel barrier. JETP Lett, 49(10):659–662, 1989.

[117] Kasper Grove-Rasmussen, H Ingerslev Jørgensen, and Poul Erik Lindelof. Kondo resonance enhanced supercurrent in single wall carbon nanotube josephson junctions. New Journal of Physics, 9(5):124, 2007.

[118] Newton Schwartz, WA Reed, P Polash, and Mildred H Read. Temperature coefficient of resistance of beta-tantalum films and mixtures with bcc-tantalum. Thin Solid Films, 14(2):333–346, 1972.

[119] DW Face and DE Prober. Nucleation of body-centered-cubic tantalum films with a thin niobium underlayer. Journal of Vacuum Science & Technology A: Vacuum, Surfaces, and Films, 5(6):3408–3411, 1987.

[120] Tobias Meng, Serge Florens, and Pascal Simon. Self-consistent description of Andreev bound states in Josephson quantum dot devices. Phys. Rev. Lett., pages 38–41, 2009.

[121] Francesco Giazotto, Panayotis Spathis, Stefano Roddaro, Subhajit Biswas, Fabio Taddei, Michele Governale, and Lucia Sorba. A josephson quantum electron pump. Nature Physics, 7(11):857–861, 2011.

[122] K.J. Thomas, J.T. Nicholls, M. Y. Simmons, M. Pepper, D. R. Mace, and D. a. Ritchie. Possible Spin Polarization in a One-Dimensional Electron Gas. Phys. Rev. Lett., 77(1):135–138, 1996.

[123] T. A. Costi. Kondo effect in a magnetic field and the magnetoresistivity of Kondo alloys. Physical Review Letters, 85(7):1504–1507, 2000.

[124] S. M. Cronenwett. Coherence, charging, and spin effects in quantum dots and point contacts. PhD thesis, Stanford University, 2002.

[125] A. Eichler, R. Deblock, M. Weiss, C. Karrasch, V. Meden, C. Schönenberger, and H. Bouchiat. Tuning the Josephson current in carbon nanotubes with the Kondo effect. Physical Review B, 79(16):2–5, 2009.

[126] Yu M Ivanchenko and L A Zil 'berman. the Josephson Effect in Small Tunnel Contacts. Soviet Physics Jetp, 28(6):1272–1276, 1969.

[127] Vinay Ambegaokar and B. I. Halperin. Voltage due to thermal noise in the dc josephson effect. Phys. Rev. Lett., 23:274–274, Aug 1969.

[128] William T Coffey and Yuri P Kalmykov. The Langevin equation: with applications to stochastic problems in physics, chemistry and electrical engineering, volume 27. World Scientific, 2012.

[129] Boris Grigorevich Korenev. Bessel functions and their applications. CRC Press, 2003.

[130] A Kogan, S Amasha, D Goldhaber-Gordon, G Granger, MA Kastner, and Hadas Shtrikman. Measurements of kondo and spin splitting in single-electron transistors. Physical review letters, 93(16):166602, 2004.

[131] PDC King, Tim D Veal, Martin J Lowe, and Chris F McConville. Surface electronic properties of clean and s-terminated insb (001) and (111) b. Journal of Applied Physics, 104(8):083709, 2008.

[132] Önder Gül, David J Van Woerkom, Ilse van Weperen, Diana Car, Sébastien R Plissard, Erik PAM Bakkers, and Leo P Kouwenhoven. Towards high mobility insb nanowire devices. Nanotechnology, 26(21):215202, 2015.

[133] Daniele Ercolani, Francesca Rossi, Ang Li, Stefano Roddaro, Vincenzo Grillo, Giancarlo Salviati, Fabio Beltram, and Lucia Sorba. Inas/insb nanowire heterostructures grown by chemical beam epitaxy. Nanotechnology, 20(50):505605, 2009.

[134] D Car. Synthesis of InSb nanowire architectures: building blocks for Majorana devices. PhD thesis, Eindhoven University of Technology, 2016.

[135] M Bouslama, C Jardin, and M Ghamnia. The insb (100) surface change during the argon ion bombardment and the electron stimulated oxidation. Vacuum, 46(2):143–146, 1995.

Résumé long

Ettore Majora a prédit en 1937 l'existence des Fermions de Majorana [5], dont les caractéristiques principales sont : une masse nulle et une absence de charge. Notamment, ces particules élémentaires sont égales à ces propres antiparticules, ce qui les rend fascinantes. Pour ce motif, elles sont assidument recherchées dans les accélérateurs de particules, sans succès pour autant [6].

Le couplage d'un nanofil semiconducteur à un supraconducteur a retrouvé un intérêt notable dans les derniers cinq années, grâce à la possibilité de retrouver des états liés de Majorana dans ces nanostructures [4]. L'émergence de ces quasiparticules est prédite dans des nanofils avec des états hélicoïdaux couplés à un supraconducteur de type conventionnel. Ces quasiparticules reçoivent leur nom des Fermions de Majorana, même si elles ne sont pas tout à fait des fermions [7]. Leur statistique plus exotique, et leurs protection du phénomène de décohérence par la présence du gap supraconducteur, leur rend utiles pour ce qu'on appelle la computation quantique topologique [3].

Activement recherchés, une première signature de ces états a été trouvée dans un nanofil d'InSb en 2012 [1]. Cette signature correspond à un pic à biais nul qui émerge au milieu du gap supraconducteur, quand un champ magnétique perpendiculaire à l'interaction Rashba est appliqué [9].

La recherche expérimentale des quasiparticules de Majorana a poussé les limites d'optimisation des matériels et interfaces, notamment l'interface supraconducteur / semiconducteur [85][84]. Des interfaces propres sont souhaitées, pour éviter la présence dans le gap des états non liés à ces quasiparticules, qui pourraient rendre obscure la signature à biais nul.

D'autres expériences ont suivi et ont arrivé à démontrer la même signature [83][2]. Pourtant, dans aucune de ces expériences la condition nécessaire pour la présence des états liés de Majorana a été montré : l'existence des états hélicoïdaux. Les états hélicoïdaux apparaissent grâce à l'interaction Rashba dans un nanofil unidimensionnel, ce qui couple le moment des électrons avec leur spin, et les rendent sans-spin (de façon effective) lorsque le potentiel chimique du nanofil est positionné dans une plage d'énergie interdite généré par l'interaction Zeeman [4].

Pour obtenir un nanofil unidimensionnel, il est nécessaire d'avoir un transport balistique dans l'axe du nanofil, sans aucun confinement [19][20][21]. Dans ces conditions, le confinement transversal donné par les parois du nanofil le rend quasi-unidimensionnel. Cependant, dans la vie réelle les nanofils peuvent héberger une boite quantique lorsque les électrons sont localisés par des défauts dans le canal, des barrières tunnel dans les contacts, et des charges dans l'oxyde des grilles et l'oxyde native du nanofil [10][40][42][43]. Des boites quantiques peuvent aussi être localisées de façon intentionnelle par l'utilisation des voltages de grille [41].

Des expériences ont montré que la présence de ces boites dans un nanofil peuvent générer des signatures sous champ magnétique dans l'état supraconducteur qui ressemblent les signatures attendues lorsque des états liés de Majorana sont présents [11][12].

Dans ma thèse, j'avais pour but d'étudier les réquisits pour la présence des quasiparticules de Majorana dans un nanofil semiconducteur. J'ai choisi d'utiliser des nanofils d'InAs et d'InSb, qui ont un fort facteur gyromagnétique, un fort couplage Rashba et une masse effective petite, ce qui les rendent attractives pour ce type de recherches. J'ai fabriqué des jonctions Josephson à deux terminaux avec ces nanofils, et j'ai étudié leur transport unidimensionnel et j'ai cherché des signatures des états hélicoïdaux. Lors de leur fabrication, j'ai choisi en plus d'utiliser des supraconducteurs à fort champ critique, à fin de pouvoir étudier les effets supraconducteurs dans un champ magnétique élevé, sans tuer la supraconductivité.

De manière inattendue, j'ai trouvé que ces systèmes simples présentaient des signatures de localisation qui pouvaient ressembler la signature de l'unidimensionnalité, des états hélicoïdaux et même des états liés de Majorana. Cela a une signification profonde pour la recherche des états liés de Majorana dans des systèmes à base de nanofils d'une complexité supérieure, puisque les signatures de localisation y seraient mieux cachées.

Ma thèse est organisée de la façon suivante.

Dans le premier chapitre, je présente une introduction au sujet des quasiparticules de Majorana. Je raconte les défis et les atouts, et puis je décris le contenu de ma thèse. Dans le deuxième chapitre, je présente la théorie sur les systèmes unidimensionnels et zéro-dimensionnels dans l'état normal et supraconducteur. Notamment, je détaille les concepts que je vais utiliser au long de ma thèse. Parmi ces concepts, on trouve les contacts de point quantiques, l'anomalie 0.7, les états hélicoïdaux, les effets Zeeman et orbital du champ magnétique, l'effet de proximité, les états d'Andreev dans une boite quantique, les jonctions Josephson, et finalement quels effets on peut s'atteindre dans une jonction portant des quasiparticules de Majorana. J'explique aussi les défis pratiques reliés à l'obtention de l'état unidimensionnel dans un nanofil, et les conditions sous lesquelles une boite quantique pourrait se développer dans le canal d'un nanofil.

Dans le troisième chapitre, je décris mes premiers résultats expérimentaux. Ce chapitre est dédié à deux observations inédites dans le domaine, faites sur des nanofils uniques d'InSb. La première annonce de la découverte des états liés de Majorana (en 2012) a été faite sur des nanofils d'InSb poussés par le même groupe qui nous a donné ces nanofils [1]. En 2016, les mêmes chercheurs ont aussi démontré du transport unidimensionnel à champ nul dans ces nanofils, et récemment (en avril 2017), encore sur les mêmes systèmes, ils ont annoncé la découverte des états hélicoïdaux.

La première des observations que j'ai fait a été la coexistence d'un canal unidimensionnel avec un canal zéro-dimensionnel dans un nanofil unique d'InSb. J'appris cela grâce à des mesures qui ont montré des pics de Coulomb super-imposés à des plateaux quantifiés en conductance. L'évolution en champ magnétique de ces deux caractéristiques était indépendante. Il m'a été possible de faire une de-convolution des deux, afin d'extraire des paramètres des deux systèmes, tels que le factor gyromagnétique.

La boite quantique en parallèle au fil quantique peut produire des signatures de conductance qui ressemblent à celles qui sont attendues pour un gap hélicoïdal ouvert par des interactions à champ nul, et ouvert par l'effet Zeeman à fort champ. Le premier de ces effets est dû à un effet Kondo à conductance unitaire dû à la boite quantique. Le deuxième est reproduit par le splitting Zeeman d'un des pics de Coulomb de la résonance Kondo, qui se développent avec le champ magnétique sur un plateau à la conductance demi-quantifié. Les deux signatures ressemblent la chute de conductance attendue dans le premier plateau à la conductance quantifié quand on a des états hélicoïdaux dans le nanofil.

La deuxième des observations décrite dans ce chapitre correspond à un nanofil qui portait deux canaux unidimensionnels en parallèle. C'est à dire, deux fils quantiques l'un à côté de l'autre sur un même nanofil. Pour affirmer cela, j'ai mesuré la conductance du système en fonction du champ magnétique. S'il s'agit d'un seul canal, on s'attend à voir des plateaux à la conductance quantifié en multiples du quantum de conductance quand le champ magnétique est nul. Si on monte le champ, on verra que des plateaux quantifiés en multiples d'un demi-quantum de conductance font leur apparition. Ces derniers se produisent grâce à l'effet Zeeman, qui partitionne les sous-bandes du nanofil en deux, selon leur spin.

Pourtant, dans ce nanofil j'ai observé une absence totale du premier demi-plateau jusqu'à un champ très forte. En plus, cet effet était dépendent de la grille. A faible voltage de grille et à champ fixe, le demi-plateau était présent comme s'il s'agissait d'un effet Zeeman courant. Par contre, à forte voltage de grille, le demi-plateau disparaissait progressivement.

Dans un premier instant, j'ai interprété cette observation comme le résultat d'un factor gyromagnétique qui dépendait de la taille du canal (un canal unique, dans ce cas) par intermédiaire de la grille. Quand le canal était plus petit que la longueur magnétique, le facteur gyromagnétique était presque nul. Quand le canal était plus grand, le facteur gyromagnétique attendait une valeur proche à ce du InSb bulk, ce qui veut dire -50.

Dans l'interprétation des deux canaux unidimensionnels en parallèle, cette observation était vue depuis une autre optique. Les grilles agissaient sur les tensions de seuil des chaque canal, en sorte que quand les deux conduisaient à la même tension, les demi-plateaux de chacun donnaient lieu à un plateau de conductance entière. Par contre, quand les tensions de seuil n'étaient pas égales, le premier demi-plateau faisait son apparition.

Une observation ultérieure appuyé cette dernière interprétation. On a vu que pour certaines valeurs de grille, un pic de Coulomb apparaissait au seuil du premier demi-plateau à la conductance quantifié. Et pour d'autres, le pic de Coulomb apparaissait au milieu du deuxième demi-plateau. Cette dernière signature pouvait être expliquée d'une façon naturelle si, dans ce cas-là, ce qu'on voyait été le pic de Coulomb correspondant à la premier sous-band résolu en spin du deuxième canal. Dans un canal unique 1D, ce pic n'a pas d'explication, puisque la densité de charge dans le canal à ce stade-là est trop élevée pour avoir un pic de Coulomb. Cette dernière signature peut aussi être confondue avec la signature attendue lorsqu'on a des états hélicoïdaux.

La possible observation de deux fils quantiques dans un même nanofil pourrait donner lieu à des expériences qui visent des états hélicoïdaux et des états liés de Majorana à nature fractionnel [13].

Dans le quatrième chapitre, j'explique des mesures de l'effet de proximité supraconducteur dans des nanofils à deux contacts supraconducteurs. D'abord, je me concentre sur l'effet Josephson dans l'état unidimensionnel. Dans un nanofil unidimensionnel d'InSb, je montre une corrélation entre un courant Josephson et la quantification de la conductance. Dans un nanofil unidimensionnel d'InSb ayant des modulations de Fabry-Pérot sur un fond de conductance quantifié, je montre une corrélation entre les résonances de Fabry-Pérot et des résonances dans le courant Josephson.

Puis, je décris des mesures du gap supraconducteur induit dans les nanofils quand la densité de charge est basse. Je montre que des gaps avec une faible densité d'états de quasiparticules –connu comme un gap « dur »- peuvent être obtenus avec une combinaison d'aluminium et vanadium. Je montre qu'un gap dur peut être obtenu avec une gravure à base d'ions d'Argon de l'oxyde du nanofil avant le dépôt des métaux peut être suffisante pour avoir un gap dur, même si à la basse cette méthode est supposé d'être trop brusque pour l'interface.

J'aussi montre des mesures du gap induit dans un nanofil avec un canal 1D en parallèle avec une boite quantique, quand le canal 1D est fermé. On découvre que la boite peut donner lieu à un pic à biais nul dans le gap induit quand le champ magnétique est augmenté, ce qui constitue la signature des états liées de Majorana. Cette observation pourrait être confondue facilement avec l'obtention de l'état topologique dans le nanofil, puisque on voit aussi du transport balistique.

Finalement, je fais une comparaison entre toutes les mesures du gap induit présentés dans le chapitre. J'ai étudié le couplage de cinq supraconducteurs différents avec des nanofils d'InAs et InSb : Al, V, Al / V, Ta et Nb / Ta. Le but été de montrer qu'on peut avoir du transport unidimensionnel avec des courants Josephson élevés et un gap induit dur. L'exploration de ces matériaux constitue un important pas vers ce but, qui est nécessaire pour l'observation des états liées de Majorana dans des systèmes à base de nanofils.

Dans le cinquième chapitre, je montre comment une boite quantique dans un nanofil d'InAs peut avoir une conductance quantifié, ce qui peut jeter un doute sur la caractéristique principale que les chercheurs utilisent pour savoir si un système est unidimensionnel. Le caractère unidimensionnel du nanofil est essentiel pour l'expérience de Majorana. Je appui ma découverte avec des mesures du courant Josephson dans l'état supraconducteur sous un champ magnétique.

Ces mesures, inédites elles-mêmes, montrent que la boite quantique peut subir des transitions de phase quantiques à un champ donné. Lorsque cette transition arrive, le courant Josephson devienne nul. Après la transition, à un champ plus élevé, le courant Josephson re-émerge.

Des calculs faites par Rok Zitko sur une boite quantique à un seul niveau, selon le model d'Anderson, arrivent à reproduire les observations dans l'état normal –c'est-à-dire, la quantification de la conductance-, et dans l'état supraconducteur.

Dans le sixième chapitre, je montre des mesures de cette transition de phase dans un autre échantillon. Cet échantillon était un nanofil d'InAs contenant une boite quantique bien définie, équipé avec deux grilles. Cette fois, j'aussi montre que le champ magnétique auquel la transition de phase se produit peut être modifié par un voltage de grille, en agissant sur le couplage tunnel du niveau de la boite aux réservoirs supraconducteurs.

Quand la transition de phase quantique se produise à champ nul, on peut avoir un pic de courant Jospehson à biais nul qui fait son apparition lorsque le champ est augmenté. Ce pic reste à biais nul quand le champ change, est puisque il apparait dans le gap supraconducteur, il peut aussi être confondu avec une signature des états liées de Majorana. Ce mécanisme n'était pas connu dans les jonctions Josephson.

Dans le septième et dernier chapitre, je présente mes conclusions et les perspectives de mes travaux. Parmi les perspectives, je discute sur la possibilité de contrôler les deux gaz unidimensionnels qui coexistent dans un nanofil unique d'InSb, en utilisant des grilles.

J'aussi propose de faire un SQUID avec deux jonctions Josephson à base des nanofils pour prouver qu'un changement de phase de la courant Josephson se produit lorsqu'on arrive à la bonne valeur du champ magnétique. J'aussi propose de faire les mêmes expériences dans de nanofils d'InSb au lieu d'InAs, puisque la transition devrait arriver à un champ 5 à 10 fois plus petit.

Finalement, je propose de faire une spectroscopie tunnel des états hélicoïdaux pour démontrer leur existence, au lieu des mesures à deux terminaux qui sont beaucoup plus sensibles à la localisation.